Automated Microassembly Using an Active Microgripper with Sensorized End-Effectors and Hybrid Force/Position Control

Bilal Komati

To cite this version:

Bilal Komati. Automated Microassembly Using an Active Microgripper with Sensorized End-Effectors and Hybrid Force/Position Control. Engineering Sciences [physics]. Université de Franche-Comté, 2014. English. <tel-01133926>

HAL Id: tel-01133926
https://hal.archives-ouvertes.fr/tel-01133926

Submitted on 20 Mar 2015

HAL is a multi-disciplinary open access archive for the deposit and dissemination of scientific research documents, whether they are published or not. The documents may come from teaching and research institutions in France or abroad, or from public or private research centers.

L'archive ouverte pluridisciplinaire **HAL**, est destinée au dépôt et à la diffusion de documents scientifiques de niveau recherche, publiés ou non, émanant des établissements d'enseignement et de recherche français ou étrangers, des laboratoires publics ou privés.

SPIM

Thèse de Doctorat

école doctorale sciences pour l'ingénieur et microtechniques

UNIVERSITÉ DE FRANCHE-COMTÉ

Automated Microassembly Using an Active Microgripper with Sensorized End-Effectors and Hybrid Force/Position Control

Bilal KOMATI

SPIM

Thèse de Doctorat

école doctorale sciences pour l'ingénieur et microtechniques

UNIVERSITÉ DE FRANCHE-COMTÉ

THÈSE présentée par

Bilal KOMATI

pour obtenir le

Grade de Docteur de
l'Université de Franche-Comté

Spécialité : **Automatique**

Automated Microassembly Using an Active Microgripper with Sensorized End-Effectors and Hybrid Force/Position Control

Unité de Recherche : FEMTO-ST, UMR CNRS 6174

Soutenue le 12 Décembre 2014 devant le Jury :

Skandar BASROUR	Président	Professeur, Université Joseph Fourier, Grenoble
Gabriel ABBA	Rapporteur	Professeur, ENI de Metz, Metz
Eric BIDEAUX	Rapporteur	Professeur, INSA, Lyon
Stéphane RÉGNIER	Examinateur	Professeur, UPMC, Paris
Dan POPA	Examinateur	Professeur, UTA, Arlington TX USA
Philippe LUTZ	Directeur de thèse	Professeur, UFC, Besançon
Cédric CLÉVY	Co-encadrant de thèse	Maître de Conférences, UFC, Besançon

To my loving parents Ahmad and Hiyam, for everything I am now.
To my beloved wife Zeinab for her support, and to my lovely daughter Tasnim.

Acknowledgments

*At the beginning, a Ph.D. is never an individual work. Several factors cooperate to achieve the final goal: **being a doctor**. These factors are the key for the success and the main source of motivation. It starts from the personal life going to the professional career and in between scientific contributions becomes a result.*

I would like to thank all the members of the AS2M department of FEMTO-ST, starting from the director Michaël Gauthier and to all the permanents, non-permanents, post-docs, Ph.D. students and graduate students for their support and the good environment in the department.

I would like to express my special appreciation and thanks to my advisors Professor Philippe Lutz and Associate Professor Cédric Clévy, you have been tremendous mentors for me. I would like to thank you for encouraging my research and for allowing me to grow as a research scientist. Your advices on both research as well as on my career have been invaluable.

I would like to thank my committee members, Professor Skandar Basrour, Professor Gabriel Abba, Professor Eric Bideaux, Professor Stéphane Réginer and Professor Dan Popa for serving as my committee members even at hardship. I also want to thank you for letting my defense be an enjoyable moment, and for your brilliant comments and suggestions, thanks to you. I would like to thank Professor Dan Popa for the enjoyable time I have spent in his research team at the University of Texas at Arlington Research Institute.

A special thanks to my family. Words cannot express how grateful I am to my mother and father for all of the sacrifices that you have made on my behalf. Your prayer for me was what sustained me thus far. I would also like to thank my brother Ali who has had an important impact on my personal and professional career. I would also like to thank my uncle for his support and all of my friends who supported me in writing, and incented me to strive towards my goal.

I would like to express appreciation to my beloved wife Zeinab who spent sleepless nights with me and was always my support in the moments when there was no one to answer my queries. I would also like to express my special appreciation to my lovely beautiful princess Tasnim for the great ambiance she has given to our lovely family.

Finally I thank my God, for giving me all the capabilities and helping me throughout all the difficulties to achieve my goals. I have experienced Your guidance day by day. You are the one who let me finish my degree. I will keep on trusting You for my future.

Bilal Komati

Contents

General introduction **1**

1 Microrobotic Systems for the Assembly of MOEMS **5**

1.1 MOEMS and their fabrication . . . 5
1.1.1 The need of MOEMS . . . 6
1.1.2 The contribution of the microassembly to the fabrication of MOEMS . 11
1.1.3 Microassembly of hybrid MOEMS components on Reconfigurable-Free-Space Micro-Optical-Bench (RFS-MOB) . . . 12
1.2 Challenges raised by the microassembly . . . 14
1.2.1 Microscale specificities and their consequences for the microassembly . 15
1.2.2 Technological limitations . . . 20
1.3 Methods and principles for the microassembly . . . 21
1.3.1 Type of end-effectors for the microassembly . . . 21
1.3.2 Serial and parallel microassembly . . . 23
1.3.3 Microassembly modes . . . 27
1.3.4 Choice of a robotic system for the microassembly . . . 35
1.4 Towards an automated robotic microassembly of MOEMS using hybrid force/position control . . . 37
1.4.1 Interest of force control for the assembly of MOEMS . . . 38
1.4.2 Automated microassembly of MOEMS using hybrid force/position control 40
1.5 Conclusion . . . 40

2 Piezoresistive Force Sensor for Microscale Applications **41**

2.1 Introduction . . . 41
2.2 Force sensors integrated in microgrippers . . . 43
2.2.1 Non contact force measurement techniques . . . 44
2.2.2 Thermal Force sensing technique . . . 44
2.2.3 Electrostatic sensing . . . 45
2.2.4 Piezoelectric sensing . . . 47
2.2.5 Piezoresistive sensors . . . 49

2.2.6 Choice of the force sensing principle 51
2.3 Piezoresistive Force Sensor Theory and Design 53
2.3.1 Working principle of the piezoresistive force sensor 53
2.3.2 Piezoresistive Force Sensor Design 56
2.4 Simulations studies of the force sensor 58
2.5 Microfabrication 59
2.6 Experimental sensor Calibration 60
2.6.1 Experimental Setup 61
2.6.2 Mechanical Characterization 63
2.6.3 Resistance variation and sensor's sensitivity relative to the applied stress 64
2.6.4 Resolution 65
2.6.5 Dynamic Characterization 66
2.6.6 Discussions about experimental results 67
2.7 Conclusion 69

3 Fabrication and Dynamic Nonlinear Model of Two-Smart-Fingers Microgripper (TSFM) 71
3.1 Introduction 71
3.2 Realization of the Two-Smart-Fingers-Microgripper (TSFM) 72
3.3 Model of an active piezoelectric microgripper 74
3.3.1 Nonlinearities in the piezoelectric actuators 75
3.3.2 Dynamic nonlinear model of a 2-DOF duo-bimorph piezoelectric actuator 81
3.4 Model of the Two-Smart-Fingers Microgripper (TSFM) 86
3.4.1 Model of the sensorized end-effector 87
3.4.2 Micromanipulation sequence and related modeling 87
3.4.3 Model of the free motion of the TSFM 89
3.4.4 Model of the constrained motion of the TSFM 92
3.5 Experimental investigations 95
3.5.1 Experimental setup 96
3.5.2 Identification of the parameters of the piezoresistive force sensors . . . 96
3.5.3 Identification of the actuator parameters 96
3.5.4 Experimental investigations of the model of the TSFM 99
3.6 Conclusion 103

4 Dynamic Force Control for the automation of the grasp and release steps at the microscale 105
4.1 Introduction 105
4.2 Automation at the microscale 106
4.2.1 Open-loop based automation 106
4.2.2 Closed-loop based automation 107
4.3 Scaling issues in robot force control 109
4.3.1 Explicit force control 110
4.3.2 Indirect force control 115
4.3.3 Choice of the force control technique 124

4.4 Proposed control technique 125
4.4.1 Sliding mode impedance control (SMIC) 125
4.4.2 Force tracking in impedance control 128
4.4.3 Force tracking despite estimation errors 129
4.4.4 Strategy to deal with pull-off force 130
4.4.5 Experimental results for the proposed control technique 131
4.5 Conclusion 131

5 Hybrid Force/Position Control for a Full Automated Microassembly 135
5.1 Introduction 135
5.2 Microassembly strategy 135
5.2.1 Automated grasping and release of the micropart 136
5.2.2 Automated guiding and grasp stability 137
5.2.3 Grasp stability 137
5.2.4 Guiding strategy 141
5.2.5 Lateral contact force estimation 142
5.3 Control for the automation of the microassembly 144
5.3.1 Hybrid force/position control 144
5.3.2 Final control diagram combining both position and force diagrams . . . 147
5.4 Experimental investigations 148
5.4.1 Experimental setup used for the automated microassembly 148
5.4.2 Automated microassembly of a rigid micropart 150
5.4.3 Automated microassembly of a flexible micropart 153
5.5 Conclusion 156

Conclusion and Future Works 157

Bibliography 165

A Appendix - Transfer Functions for the Model defined in Chapter 3 183

Publications 185

List of Figures

1.1 (a) Two mirror-pixels: one mirror-pixel is turned on and reflects incoming light through a projection lens to the screen and the other mirror-pixel is turned off reflecting the light away from the lens, (b) Integration of DMD inside a one-chip DLPTM projection system [44]. 8
1.2 Schematic of the MEMS-based endoscopic OCT system. CM is the collimator. The OCT signal is the combination of the reference source and the reflected light from the sample, which creates the interference pattern. The external reference mirror moves for axial scan of the sample [185]. 9
1.3 Two different configurations of a Michelson interferometer used in Fourier spectroscopy [105]: (a) with scan configuration, (b) configuration stationary. 10
1.4 (a) Concept of Fourier transform spectrometer (FTS). In the real setup, the beam splitter (BS) and the fixed mirror are macroscopic. The movable mirror was driven by a push-pull configuration. (b) The MEMS mirror is much larger than in the OXC and the V OA to increase the reflecting area [114]. 11
1.5 Individual components of the RFS-MOB and their assembly concept as presented in [10]: (a) details of the silicon bulk-micromachined baseplate and silicon holder (with the ball microlens as a micro-optical component), (b) holder assembled into the central rail of the silicon baseplate. 13
1.6 General concept of holder assembly based on the use of a robotic active microgripper as presented in [10]. The geometry of a gripping tool, performing the insertion and displacement of the holder within the rail of the baseplate, is illustrated. 14
1.7 Images during the microassembly of the holder and after the microassembly of two holders onto the rail of the baseplate as presented in [10]: (a) Picking the holder on the flexible part, (b) SEM picture of two assembled holders. 15
1.8 The predominance of surface forces at the microscale. 17
1.9 Typical curve for approach/retract between two planar surfaces [128] allowing to quantify pull-off forces. 18
1.10 A scheme showing two cantilever beams: (a) a cantilever beam B_1 with dimensions L, W, T; (b) Cantilever beam B_2 with dimensions $\frac{L}{10}$, $\frac{W}{10}$, $\frac{T}{10}$. 18

1.11 (a) Two passive fingers microgripper using the compliance to handle the micropart [32], (b) the assembly steps and the locking of the micropart to the substrate [33]. 23
1.12 The handling steps of the micropart using the passive finger [32]. 23
1.13 PRONOMIA microassembly station [62] and the assembled microcow. 24
1.14 Hybrid handling technique [138]. (a) Assembly site is on top of a micropart. (b) Droplet of water is dispensed on the bottom part. (c) Microgripper approaches the release site with a part. (d) Droplet contacts with the top part and wets between the parts, which forms a meniscus. (e) Microgripper releases the part and the capillary force aligns the parts. (f) Water between the two parts evaporates, which leaves the two parts aligned. (g) Image sequence of the actual experiment, as viewed from the top side. 25
1.15 Parallel microassembly by flip-chip method. 26
1.16 Parallel microassembly: Multiple microscale components (e.g. electronics, photonics and MEMS) are built in parallel using standard fabrication processes. They are positioned and combined with other components on a hybrid *pallet*. Note that the fabrication density is high, while the pallets may have a larger size and lower density [13]. 27
1.17 The method of the fabrication proposed by super-chip integration technology [87]. 28
1.18 Parallel assembly of 6 pairs of microchips with size 200 μm × 200 μm × 30 μm [20]. 29
1.19 The different approaches for the automation of robotic microassembly tasks. . . 30
1.20 The passive *jammer* gripper and some figures showing the manipulation and the insertion of the micropart into the substrate. 31
1.21 (a) The robotic station of the system and (b) the results of the automated open loop microassembly of 12 microparts using a passive microgripper (*jammer*) and calibrating the robotic station. 32
1.22 (a) Microaasembly robotic station illustrating the global view of the station and the zooming view in the MMOC and (b) the complete view of the MMOC and the microparts used for the microassembly [161]. 32
1.23 (a) Some shots during the different microassembly steps and (b) zooming picture of the complex 3-D structure assembled [161]. 33
1.24 (a) Closeup view of the robotic microassembly station, (b) (1) Initial part position, (2) Part rotated and probes moved close to part, (3) Probes gripping part after automated sequence, (4) Part at start of out of plane rotation, (5) Part after out of plane rotation, (6) Part and slot prealigned, (7) Part inserted [178]. 34

1.25 Structure and manipulation schemes of the 3D Micromanipulation System (3DMS) [186]. (a) A photo of the developed 3DMS. (b) System configuration of the 3DMS, which mainly consists of two sets of devices used in a commercially available AFM, including two cantilevers and the corresponding two sets of nanopositioning devices and optical levers. (c) A microscopic image captured during the pick-up operation of a microsphere using the gripper constructed by tip I and tip II. The bottom inset shows a side view of the pick-and-place scheme with a gripper. The scale bar represents 20 µm. (d) Close-up figure showing the scheme for grasping a microsphere with the nanotip gripper. 35
1.26 The 3D microassembly results under magnification of 100× [186]. 36
1.27 Summary of microassembly techniques. 38

2.1 Manipulation of the holder (presented in chapter 1 section 1.1.3) from the flexible part and showing the small gap of the holder where the microgripper fingers should be inserted to perform manipulation of the holder. 43
2.2 (a) The structure of a MEMS Micro-gripper presented in [119], (b) a simplified sensor model as presented in [119]. 45
2.3 Parallel plate capacitor. 46
2.4 Differential capacitors used in electrostatic sensors. 47
2.5 Examples of microgrippers with integrated capacitive force sensors: (a) Microgripper from FemtoTools [54] showing one capacitive sensing finger and one electrostatic comb-drive based actuated finger, (b) Microgripper presented in [81] showing two axis capacitive sensors and one electrothermal actuated finger, (c) Microgripper presented in [90] showing one electrostatic based sensing finger and one electrostatic based actuated finger. 48
2.6 The range of some existing force sensors versus the resolution. The details of the force sensors are presented in the Table below. 52
2.7 Strain distribution inside a cantilever with two bulk strain gauges where a force is applied at its tip: (a) no cavity and (b) with cavities. 57
2.8 (a) Sensing beam structure and (b) its Wheatstone bridge. 57
2.9 Microfabrication process flowchart. 61
2.10 SEM pictures of the force sensor showing: (a) complete force sensor with the strain gauges ,the ohmic contact and the test body (b) closed view on the ohmic contacts part and the strain gauges of the three beams structure of the sensing part: (1)&(2) fixation of the three beam, (3)&(4) zoom on one beam. (1)&(3) are side photos while (2)&(4) are top view. 62
2.11 Experimental setup used for the characterization of the piezoresistive force sensor. A calibrated force sensor (CalibFS) is fixed on a robotic system consisting of a fine positioning stage and rotation stage. The piezoresistive force sensor (PiezoFS) is fixed. Two cameras are used to see the contact. 63
2.12 Force measurement of the CalibFS with respect to the position of the fine positioning stage in order to measure the stiffness of the force sensor. 64

2.13 (a) The variation of the strain gauges resistances relative to an applied force on the tip of the force sensor. R_{1m} and R_{2m} are the measured values of resistances in experiments and R_{1f} and R_{2f} are the approximated linear variation of the resistances and (b) The variation of the readout voltage from the Wheatstone Bridge, V_{out}, for a referenced voltage of $V_{ref} = 5$V and amplification gain, $A = 100$, relative to an applied force. 65
2.14 The force sensor signal measured while applying small displacement of the positioning stage in order to determine the resolution of the sensor: (a) resolution of 800 nN without filtering, (b) resolution of 100 nN with a low pass filter with a cut-off frequency of 10 Hz. 66
2.15 The time signal and the FFT signal of the signal measured by the force sensor when free vibrations are applied to the force sensor. 67
2.16 The time signal of the force sensor compared to the model after fitting the damping coefficient. 68

3.1 Organization of this chapter showing the steps to model the TSFM. 72
3.2 Integration of the sensorized end-effectors into a piezoelectric actuator to realize TSFM. 73
3.3 Complete scheme of the two-smart-fingers microgripper (TSFM). 73
3.4 The procedure for the integration of the force sensor into the piezoelectric actuator showing five main steps which are detailed in section 3.2. 75
3.5 Two-smart-fingers microgripper (TSFM). 76
3.6 A typical curve showing the internal loop and external loop hysteresis for piezoelectric actuators. 76
3.7 A block diagram showing the Preisach operators and the output of the hysteresis model, h_P, as sum of all the Preisach operators with weight functions. 78
3.8 A block diagram showing the Prandt-Ishlinskii operators and the output of the hysteresis model, h_{PI}, as sum of all the Prandt-Ishlinskii operators with weight functions. 79
3.9 (a) An elasto-slide element, (b) its input-output relationship and (c) the physical interpretation of the Maxwell-resistive-capacitor hysteresis model. 80
3.10 A scheme of a 2-D duo-bimorph piezoelectric actuator showing the two layers of piezoelectric materials, the elastic layer which is connected to the ground and the electrodes. 82
3.11 A scheme of a 1-D bimorph piezoelectric actuator where a voltage U, a force F, a moment M and a pressure load p are applied. 83
3.12 A top view of Figure 3.11 showing the displacement of the bimorph piezoelectric actuator and showing the output variables: the bending angle α, the deflection δ, the volume displacement V and the charge Q. 83
3.13 Dynamic hysteresis could be decomposed in a static part followed by a dynamical part. 84
3.14 Complete scheme of the two-smart-fingers microgripper (TSFM). 86
3.15 Equivalent scheme of the sensorized end-effector. 88

3.16 Four cases for the manipulation of a rigid micropart: (a) the micropart is placed between the fingers of the microgripper, (b) a voltage is applied to move the two fingers, (c) a contact appears between one of the fingers and the micropart and (d) a contact between the two fingers and the micropart appears. 88
3.17 The equivalent scheme of microgripper manipulating a rigid micropart: (a) the mass of finger (m_{s_2}) is separated of the mass of the micropart (m_p) and (b) the mass of the finger is combined with the mass of the micropart ($m_e = m_{s_2} + m_p$). 89
3.18 Equivalent scheme of the free motion of one smart finger: (a) without any applied voltage ($U = 0$), (b) voltage is applied (quasi-static behavior), (c) voltage is applied (dynamic behavior). For each of the three cases, at left the scheme of the gripper and at right the scheme of gripper after replacing the force sensor by a lever system connected to a mass-spring-damper system. 90
3.19 Bloc diagram to show the method to determine the free motion model of the TSFM. 90
3.20 Equivalent dynamic scheme of the constrained motion of one of the TSFM fingers in four cases: (a) no motion without contact and without any applied voltage ($F_s = 0$ and $U = 0$) (b) free motion with an applied voltage to the finger ($F_s = 0$ and $U \neq 0$ the same case considered in Figure 3.18-(c)), (c) just at the transition between free motion and constrained motion ($F_s = 0$) and (d) constrained motion after contact ($F_s \neq 0$). 92
3.21 Bloc diagram to show the method to determine the constrained motion model of the TSFM. Notice that y_A and α_A are coupled but their separation is done to clarify the parameters needed for the model. 93
3.22 Bloc diagram showing the final model of the TSFM. 95
3.23 (a) Experimental setup used for the identification of the static parameters of the actuators; (b) Comparison between the Bouc-Wen static hysteresis model and experimental results for many sine voltages with three different amplitudes 30V, 60V and 100V at a frequency 0.1 Hz. 97
3.24 Comparison between the normalized step responses of the model of the displacement of Y_B given in Equation (3.15) and the experimental measurements of Y_B. 98
3.25 Experimental setuo and results of the identification of the actuator's elastic constant s_p: (a) experimental setup used including TSFM, FemtoTools force sensor, nanocub and rotation stage, (b) comparison between the measurement and the model of the force relative to the displacement leading to the identification of s_p, (c) comparison between the model and the experimental results of the displacement of the tip B y_B when a force is applied at the tip B after identifying s_p. 101
3.26 Comparison between the displacement model of the tip B y_B given in Equation (3.15) and experimental results for many sine voltages with an amplitude of 100V and with different frequencies where no force is applied: (a) 10Hz, (b) 50Hz, (c) 100Hz and (d) 500Hz. 102
3.27 Experimental setup showing the TSFM end-effectors, the flexible micropart and a vacuum gripper to hold the flexible micropart. 103

3.28 Comparison between the model of the force given in Equation (3.34) and the experimental measurements. The model of the displacement given in Equation (3.31) is also shown. 104

4.1 The different approaches for the automation of the microassembly tasks. 106
4.2 The figure showing the experimental setup showing the TSFM end-effectors, the flexible micropart and the vacuum gripper. 110
4.3 Force-based explicit force control diagram. 111
4.4 Experimental results of the explicit force control using PI controller for four different values of proportional and integral gains K_p and K_i: (a) $K_p = 0.3$ and $K_i = 0.6$, (b) $K_p = 0.4$ and $K_i = 1$, (c) $K_p = 0.2$ and $K_i = 0.5$, (d) $K_p = 0.3$ and $K_i = 0.7$. 114
4.5 Admittance control diagram. 116
4.6 Position-based impedance control diagram as proposed by [64]. 117
4.7 Force tracking position-based impedance control diagram where the part of the diagram inside the box is the same as the diagram shown in Figure 4.6. 119
4.8 Experimental results for the position-based impedance control with offline environment parameter estimation: (a) force response compared to the reference force, (b) position response compared to y_r and y_d. 122
4.9 Experimental results for the position-based impedance control with online estimation of the environment parameters: (a) force response compared to the reference force, (b) position response compared to y_r and y_d. 124
4.10 Diagram of the sliding-mode impedance control with force tracking. 129
4.11 Experimental results for the Sliding Mode Impedance Control (SMIC) with online estimation of the environment parameters: (a) force response compared to the reference force, (b) position response compared to y_r. 132

5.1 General concept of holder assembly based on the use of a robotic active microgripper as presented in [10]. 136
5.2 Guiding task based on two-sensing-fingers microgripper with coordinate frames: $O_{rail}X_{rail}Y_{rail}Z_{rail}$ and $O_mX_mY_mZ_m$. 138
5.3 Perturbated grasp with each component of the contact force: F_x, F_y, and F_z. . . 138
5.4 A scheme showing the simplified model of the system when a micropart is grasped between the fingers of the microgripper. 140
5.5 Experimental results of gripping forces evolution F_{y1} and F_{y2} according to an applied contact forceF_y for: (a) a rigid micropart and (b) a flexible micropart . . 140
5.6 (a) TSFM initial scheme showing tips A, B and C of the two fingers, (b) a scheme showing the micropart between the fingers of the microgripper and a perturbation force F_y applied on the micropart, F_{y_1} and F_{y_2} being the gripping forces applied on the micropart. 143
5.7 (a) Experimental setup for the contact lateral force estimation and (b) experimental results comparing the estimated contact force to the measured contact force. 144
5.8 Hybrid force/position control diagram as defined in [53]. 145

5.9 Force Control Law (FCL) used for the guiding task. 147
5.10 Hybrid force/position control diagram used for the automation of three microassembly tasks where $F_g = (f_{g_1}, f_{g_2})$ and $F_r = (f_{r_1}, f_{r_2})$. 147
5.11 Robotic microassembly station used to investigate the experimental results of the automation of the microassembly tasks using the microassembly strategy defined in section 5.2 and the hybrid force/position control developed in section 5.3. 149
5.12 Experimental results for the automated grasp and release of a rigid micropart using Sliding Mode Impedance Control (SMIC) with online estimation of the environment parameters: (a) force response compared to the reference force, (b) position response compared to y_r. 151
5.13 Experimental results for the automated guiding of a rigid micropart inside a rail showing the estimation of the lateral contact force, $\hat{f}_y$, and the gripping forces, the Nanocube displacement along the X axis, D_x, and the NanoCube displacement along the axis of correction Y, D_y. 152
5.14 Experimental results for the automated guiding of a rigid micropart inside a rail showing the estimation of the contact force $\hat{f}_y$ and the gripping forces. 153
5.15 An image showing the rigid micropart handled between the two fingers of the microgripper and while the guiding task along of one sided rail. 154
5.16 Experimental results for the automated guiding of a rigid micropart inside a rail showing the estimation of the contact force $\hat{f}_y$ and the gripping forces. 155
5.17 (a) Image showing the micropart in the guiding task, (b) an image of the assembled holder. 155

List of Tables

1.1 Advantages and disadvantages of MOEMS switching devices as presented in [160]. 6
1.2 Force summary according to the interaction distance [92]. 17

2.1 Comparison of different microgripper designs. 51
2.2 Details of the force sensors presented in the above Figure. 52
2.3 Comparison between the force sensing techniques. 54
2.4 Formula for transverse and longitudinal gauge factors for various commonly encountered resistor configurations. 55
2.5 Silicon parameters used in the simulations using COMSOL MULTIPHYSICS. . 58
2.6 Comparison between theoretical model and microfabrication results. The dimensions are measured using SEM and the other variables are measured through experiments. The error is between experimental results and the theoretical parameters with taking into consideration the dimensions error in the microfabrication process. 69

3.1 Identified parameters of the TSFM including the parameters of the two piezoelectric actuators and the two piezoresistive force sensors. The powers l and r correspond to the left and right fingers respectively. 100

4.1 Comparison between open-loop based and closed-loop based automation at the microscale. 108
4.2 Comparison between the PI controller performances relative to different gains. . 115
4.3 Comparison between explicit force control and impedance control schemes. . . 125

General introduction

Nowadays, the miniaturization of systems provides new challenges for scientists, industrial and sales representatives. This miniaturization takes place in computers, mobile phones, GPS, medical and surgical products and many other systems which integrate several complex functions in a small volume. The advantages of miniaturized systems are the improved performances, the reduction of the energy consumption, their low cost due to batch fabrication, their storage and transport.

This interest in miniaturization has led to the introduction of Micro-Electro-Mechanical Systems (MEMS) and their fabrication techniques. After tens years of research, well known MEMS products have appeared including MEMS accelerometer of BOSCH and printheads of Hewlett Packard. Then, optical function has been added to MEMS to form MOEMS (Micro-Opto-Electro-Mechanical Systems) where the most known applications are optical routers [166], DMD (Digital Micromirror Device) [107], OCT (Optical Coherence Tomography) [66] and microspectrometers [166].

The fabrication of MOEMS using an approach combining advanced microfabrication techniques and robotic microassembly has been presented in several works [10, 32, 26] and has shown its effectiveness in the fabrication of three-dimensional (3D) complex MOEMS structures. The contribution of the microassembly notably relies on the cost reduction, the amelioration of the flexibility of the design, the optimization of the design in order to guarantee an optimized final component with the desired performances.

Robotic microassembly has raised several challenges such as the need of microrobots with high performances, taking into account physical phenomenon that are predominant at the microscale and some technological limitations. The physics of the microscale is mainly manifested by the predominance of surface forces, the high dynamics of the systems, the small inertia and the fragility of the microsystems. In order to overcome these specificities, introduction of force and position sensors with wide bandwidth is required in order to understand what is happening at this scale and to automate the microassembly in both static and dynamic cases. However, integrating sensors inside the microassembly robotic station is a big challenge at this scale. As a result of microscale limitations and challenges, solutions need to be proposed to perform high yield microassembly with high precision and low process time.

The Automatic Control and Micro-Mechatronic Systems (AS2M) department of the FEMTO-ST [1] Institute in Besançon has been interested in the micromanipulation and the fabrication of MEMS and MOEMS using robotic microassembly for several years [2]. AS2M department is divided in four research teams where the main research topics are control, micromechatronics, microrobotics, nanorobotics, biomedical robotics, microassembly, micromanipulation, sensors, actuators, prognostics and health management. This PhD has been done inside the research team CODE (COntrol and DEsign) of the AS2M department since October 2011. The CODE team considers the design, modeling and control of micromechatronic and microrobotic structure and notable investigates inovative control solutions well adapted for microsystems.

This PhD work has been funded by the Franche-Comté region in the framework of MIOP [2] project. The two departments MN2S [3] and AS2M of the FEMTO-ST institute are both involved in this project. The objective of this project is to design and develop three-dimensional (3D) reconfigurable micro-optical benches using microfabrication technology for the fabrication of silicon-based MOEMS and robotic microassembly. Robotic microassembly enables to assemble several MOEMS, called hybrid MOEMS, issued from different microfabrication processes which enables to optimize each fabrication process and consequently to increase the performances of the resulting MOEMS structure.

The objective of this PhD work is to perform automated robotic microassembly of the hybrid MOEMS. The use of an active microgripper with sensorized end-effectors is proposed in order to measure both of the gripping forces applied by the microgripper to grasp a microcomponent and to estimate the contact forces between the microcomponent and the substrate of microassembly. Then, full automation of the microassembly is performed using hybrid force/position which enables to position the microcomponent in its final position while controlling the gripping forces and reducing the contact forces.

In chapter 1, the need of MOEMS is presented firstly based on examples of main applications. The methods of their fabrication are also discussed. The contribution of the microassembly to the fabrication of MOEMS is highlighted with related scientific and technological challenges considering the microscale specificities. Existing microassembly techniques are also presented and compared, one being chosen for the rest of the work. The interest of using hybrid force/position control for the microassembly is also highlighted.

In chapter 2, the state of the art of microforce sensors integrated in microgrippers is presented showing the lack of powerful and high sensitive sensors which can be integrated in microgrippers. A piezoresistive force sensing principle is adopted for the design of the sensor according to the required specifications where it should be able to measure the forces at the microscale and notably pull-off forces. The force sensor is designed to be integrated inside a microgripper and to present innovative performances compared to existing force sensor notably the ability to measure big range of force. Then, a novel piezoresistive force sensor and the prototyping of its fabrication are proposed. The performances of the fabricated force sensor are also analyzed.

[1] Franche-Comté Electronique, Mécanique, Thermique et Optique - Sciences et Technologies

[2] Microsystems for instrumented optical chips

[3] Micro Nano Sciences and Systems

In chapter 3, The force sensor presented in chapter 2 is integrated into an active piezoelectric microgripper. The whole system is composed of two piezoelectric active fingers with sensorized end-effectors. The whole system is called Two-Smart-Fingers Microgripper (TSFM). A dynamic nonlinear force/position model of the complete gripper while manipulating a micropart is developed. Non-contact and contact scenarios are studied and also modeled. Finally, the model is validated experimentally.

In chapter 4, the automation of grasp/release of microcomponents is investigated as a case to study the force control. Existing force control techniques are detailed and their use at the microscale is also considered. Theoretical and experimental studies are performed in order to compare the performances of main existing force control techniques taking into consideration the microscale specificities. An impedance control technique is chosen taking into consideration microscale specificities notably pull-off force and high dynamics of the microscale objects. A new nonlinear force control scheme based on force tracking sliding mode impedance control with online parameter estimation is proposed. Using this control technique, the dynamics of the contact can be controlled and a strategy to deal with pull-off force is proposed. Finally, the control technique is tested experimentally for the automation of the grasp/release of microcomponents.

In chapter 5, full closed-loop based automation of the microassembly is performed using hybrid force/position control. The considered microassembly tasks are grasping, releasing and guiding tasks for the microcomponent. In this chapter, the focus will be on the guiding task because the rest has been investigated in chapter 4. In the hybrid force/position control formulation, some axes are controlled in position and others are controlled in force. For the force controlled axes, the force control technique developed in chapter 4 is used. The stability of the grasp during manipulation is studied and a guiding strategy is defined taking into consideration microscale specificities. The automated tasks are tested for rigid and flexible microparts. The final objective of this chapter is to achieve a full automated microassembly process.

After presenting the works, the results will be discussed and future works are proposed.

Chapter 1

Microrobotic Systems for the Assembly of MOEMS

In this chapter, a study of MOEMS (Micro-Opto-Electro-Mechanical Systems) and their fabrication is presented. The need of MOEMS in different fields of applications is identified. The contribution of the microassembly to the fabrication of complex 3D microsystems is discussed. Microassembly techniques are presented, classified and illustrated through examples. Automation of micro-assembly tasks is also discussed notably highlighting the interest of force based control. Based on that analysis, the objectives of the PhD thesis are formulated and the choice of a robotic system is done.

1.1 MOEMS and their fabrication

Microsystem manufacturing is a growing field that deals with fabrication and packaging of micro-components to be used in a variety of domains: automotive industry, IT peripherals and telecommunications, biomedical, medical, instrumentation, etc. The miniaturization of microsystems leads to the reduction of the product's price due to the batch fabrication techniques. Microsystems are smaller in size, lighter in mass allowing high capabilities of integration in one packaged substrate (such as silicon) [194].

The MOEMS are microsystems combining mechanical, electrical and optical functions. They are widely used for many applications such as sensors, accelerometers or optical switches. The effect of adding the optical options to microsystems has many advantages:

1. the optical signal carries a lot of information including light intensity, the frequency or the wavelength, the difference of phases, the polarization and the propagation velocity;

2. the light beams are not perturbed by the electromagnetic perturbations or others which is of great interest for using it inside a perturbed environment especially at the microscale;

Advantages	Disadvantages
• Low loss • Low cross-talk • Polarization insensitive • Wavelength sensitive • Compact and scalable • Low holding power	• Complex manufacture • Vibration sensitive (if non-latching) • Temperature sensitive • Poor power handling • Low speed • High voltage (if electrostatic)

TABLE 1.1: Advantages and disadvantages of MOEMS switching devices as presented in [160].

3. the MOEMS is the only technology present nowadays to meet the growing need for data flow transferred required by internet networks;

4. the signal to noise ratio of the optical signal is very promising compared to electrical signals which facilitates the information processing.

The advantages and disadvantages of MOEMS switching devices, compared to bulk optics and guided wave form, are summarized in Table 1.1 by Professor Richard Syms from Imperial College London [160].

These advantages have recently motivated researches in several domains and cover a wide scope of applications: systems such as Optical Coherence Tomography [4], endomicroscopy [179], microspectrometers [59], implantable optical sensors [52], optical interconnects [35], photon counters [113], etc. Several of these applications have been commercialized due to the pertinence, small size, low cost, high efficiency of these systems which have leaded to an increase in the market of MOEMS. A recent market analysis conducted by Yole development and Fairchild semiconductor forecasts MOEMS growth of 80% between 2012 and 2018.

1.1.1 The need of MOEMS

The MOEMS are used in many applications. These applications can be divided in three main categories as cited below: communication systems and data storage, display and imaging systems, and sensors. Some examples of MOEMS are presented. Many of these MOEMS are commercialized where others remain at the research level.

Communication systems and data storage

MOEMS technology is used for optical communications and for data storage of type CD/DVD. Optical switches define the essentials of the world network and communication. From the time of Alexander Graham Bell invented telephone to today, switching technology has changed dramatically from manual to electronic and recently to optical with the use of optical fibers in telecommunications. Increasing demand for larger bandwidth in telecommunication forced technology to explore new alternatives in switching and routing of data. Bell Laboratories, the research and development arm of Lucent Technologies, demonstrated an all Optical Cross-Connect (OXC) optical switch using MOEMS. This MEMS technology for fabricating optical switches presents the best value in terms of size, form factor, durability, and cost. Lucent and

other companies selected MOEMS for building OXC because it yields small size, more durable and lower cost devices and that can be incorporated with very large scale integrated circuits. OXC is an example of device used by telecommunications carriers to switch high-speed optical signals in a fiber optic network, such as an optical mesh network. A 2×2 OXC has two inputs and two outputs fibers. The light of either one of the input fibers can be switched to either one of the output fibers. In practice, to direct a wavelength along a pathway in the network, the MOEMS switch uses tiny micro-mirrors positioned so that each is illuminated by one or more of the optical wavelengths carrying a stream of information within a single fiber. For example, a stream of photons in a wavelength coming in through an input port hits series of micro-mirrors that send it out through one of many output ports, depending on which route it is supposed to take. Sophisticated controllers that mange the motion of the mirrors make decision when a stream of light arrives on how the mirror needs to tilt in order to bounce the beam to appropriate output [144]. The LambdaRouter is based on the above principle. The incoming lightwave gets filtered into separate wavelengths, each of which hits one of the 256 tilted input mirrors. The wavelengths bounce off the input mirrors and get reflected off another mirror onto output mirrors that then direct the wavelength into another fiber. The entire process lasts a few milliseconds which is fast enough for the most demanding switching applications [40].

Display and imaging systems

MOEMS technology combining MEMS and micro-optics is well suited for manipulating light. Electromechanical structures can be used to scan, steer or modulate light beams. MOEMS display and imaging products have been used for defense, aerospace, medical, industrial in the form of wearable displays, projection displays, imaging devices, barcode readers and infrared imaging cameras.

Three of most advanced MOEMS display technologies are (1) retinal scanning display (RSD) which is a 2D scanner-based display technology, (2) grating light valve (GLV) technology, which is an example of a 1D scanner and 1D pixel-array technology and (3) digital micromirror device (DMD) technology, which is a 2D pixel-array technology. Each of the three has a different system architecture and employs a different optical principle for light modulation. The DMD is a good example of a successful MOEMS display product. It is used in the fabrication of videoprojectors. The first DMD product was launched by the Texas Instruments in 1996. It has probably the largest number of moving mechanical components of any product (1.5 millions in 2002 [114, 44]). It is a matrix of actuated micromirrors which steer the light beams inside the high resolution videoprojectors. Figure 1.1-(a) shows an elementary of the DMD which is composed of two mirror-pixels where one mirror-pixel is turned on and reflects incoming light through a projection lens to the screen and the other mirror-pixel is turned off reflecting the light away from the lens. Figure 1.1-(b) shows the integration of a DMD chip inside one chip DLPTM projection system from Texas Instruments.

MOEMS have not only achieved to miniaturized projection systems but they have also allow researchers to develop new imaging methods. MOEMS have enhanced and enrich the capacities of computational imaging and have define a new era in digital imaging. The OCT (Optical Coherence Tomography) is a good example of an established medical imaging technique that benefits form MOEMS technology. OCT is a relatively new optical imaging modality [66].

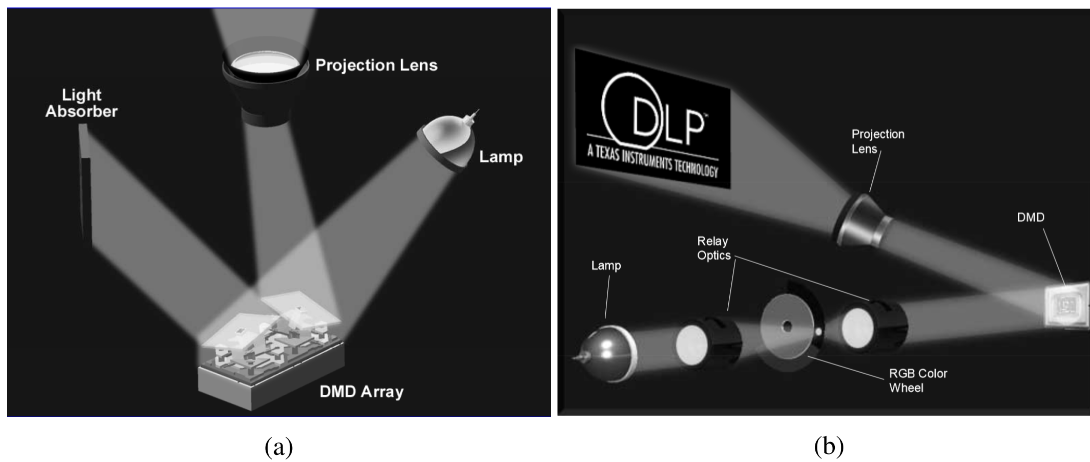

(a) (b)

FIGURE 1.1: (a) Two mirror-pixels: one mirror-pixel is turned on and reflects incoming light through a projection lens to the screen and the other mirror-pixel is turned off reflecting the light away from the lens, (b) Integration of DMD inside a one-chip DLPTM projection system [44].

Since its introduction in the early 1990s, it has been employed extensively in dermatology and ophthalmology [126, 182, 55, 164]. It has also been used for imaging internal organs such as the GI tracts, bladders, and esophagus [148, 71]. It enables the early stages detection of cancer due to its micron-scale resolution which can reach 1 to 15 μm depending on the light source employed. In addition to that, OCT is an optical fiber-based system, and thus it is compact, portable, free of radiation, and affordable. With the development of MEMS technology, Pan et al. introduced the first MEMS-based OCT endoscope by employing a one-dimensional (1D) electrothermally actuated MEMS mirror [116]. Two-dimensional (2D) porcine bladder cross-sectional imaging was demonstrated. After that various forms of MEMS mirrors have been developed as the scanning engine in endoscopic probes for OCT systems including electrostatic [76], magnetic [82], piezoelectric [58], electrothermal [185] and pneumatic actuated mirrors [5]. Figure 1.2 shows a 5 mm diameter endoscopic OCT system equipped with an actuated micromirror [185]. A broadband light source is guided equally into two single-mode fibers through a beam splitter to form a Michelson interferometer. The light in the sample arm is collimated by a fiber-optic aspherical lens, deflected by a conventional mirror and the beam steering micromirror. It is then focused on the detecting biological sample, which reflects part of the incident light back to the sample arm. The light in the reference arm is linearly scanned in the axial direction by an optical delay line. Because broadband light has short temporal coherence, this will permit detection of backscattering from different depth within the biological sample.

Sensors

MOEMS are widely used for the fabrication of sensors such as accelerometers, control of distance in cars, automatic wiper activation, reading of barcodes, health care, medical instruments, etc. Accelerometers are an example of MOEMS-based sensors. They are used in automo-

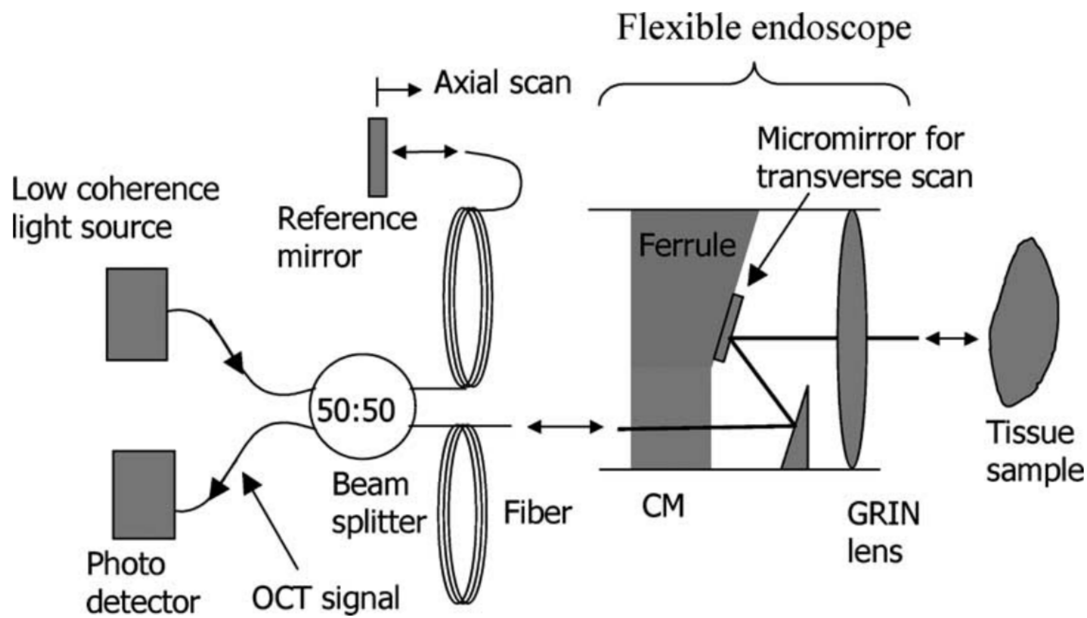

FIGURE 1.2: Schematic of the MEMS-based endoscopic OCT system. CM is the collimator. The OCT signal is the combination of the reference source and the reflected light from the sample, which creates the interference pattern. The external reference mirror moves for axial scan of the sample [185].

tive, aerospace applications and recently in smartphones. A MOEMS-based accelerometer is proposed in [114, 196]. The latter is used for aerospace applications. MEMS-based optical accelerometers provide higher sensitivity and better reliability, which are key factors in sensor performance, compared to those based on piezoelectric or capacitive effects. Since these types of sensors use optical power instead of electrical power, they are immune to electromagnetic interference.

Another example of MOEMS-based sensors is the optical microspectrometer. It enables the decomposition of light beams in its different wavelengths in order to determine its spectrum. The measurement of the sensor (the medical diagnostic, the presence of a gas, the measurement of colors, the quality of a food product, etc) is performed by comparing the initial spectrum with the other which has passed the sample (modified by absorption of a part of the spectrum or a shift in spectrum). Two configurations for the fabrication of microspectrometer exist: the first using time dependent scanning to modify the path difference δ (difference between the optical path of the two beams) and the second stationary using the diffraction phenomena. Figure 1.3 shows the two configurations based on a Michelson interferometer where A is the source; B is a collimator ; C is the beam splitter; D_1 is the fixed mirror; the optical path difference is generated by a displacement of the mirror D_2; F and H are collimators; G and I are photodectector or array of photodectectors. For a symmetric interferogram, use of compensator E is required. In the stationary case, the path difference is generated by a tilt of the mirror D_2 and therefore

interferogram spreads in the space. A row of photodectectors I is required. The lens H is used to minimize the effect of the size of the source and thereby to obtain the interference on I.

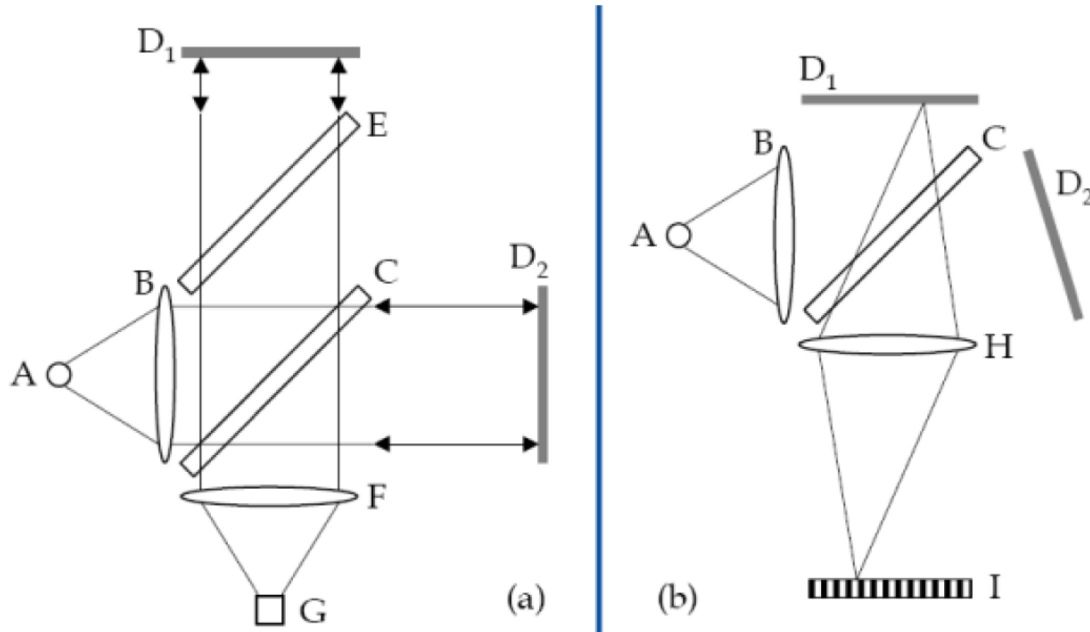

FIGURE 1.3: Two different configurations of a Michelson interferometer used in Fourier spectroscopy [105]: (a) with scan configuration, (b) configuration stationary.

The time dependent microspectrometer must have a system for realizing a mobile variation of the path difference. In the case of Michelson interferometer, it is often observed that one of the mirrors is driven to scan. The travel range of the mirror defines the spectral resolution achieved by the spectrometer at a given wavelength. Figure 1.4 shows a movable mirror driven by push-pull configuration using interdigitated comb drive actuation. The mirror is used in the spectrometer presented in [105, 114]. The push pull configuration of the actuator reduces the nonlinearities of moving the mirror. In this spectrometer, a displacement of 80 µm of the mirror (generating a path difference $\delta_{max} = 160$ µm) allows to obtain a resolution of 2.5 nm at a wavelength of 633 nm (the resolution is calculated by $\Delta\lambda = \frac{\lambda^2}{\delta_{max}}$). The system is fabricated using SOI wafer. Mastering microfabrication techniques is the main key to the operation of this microspectrometer.

An approach for 3D microassembly of microspectrometer has been presented in [27]. The microassembly has enabled to build 3D microspectrometer. The detail of the microassembly technique will be presented later.

After this presentation of some MOEMS products issued from batch microfabrication techniques, the contribution of the microassembly to the fabrication of MOEMS will be presented.

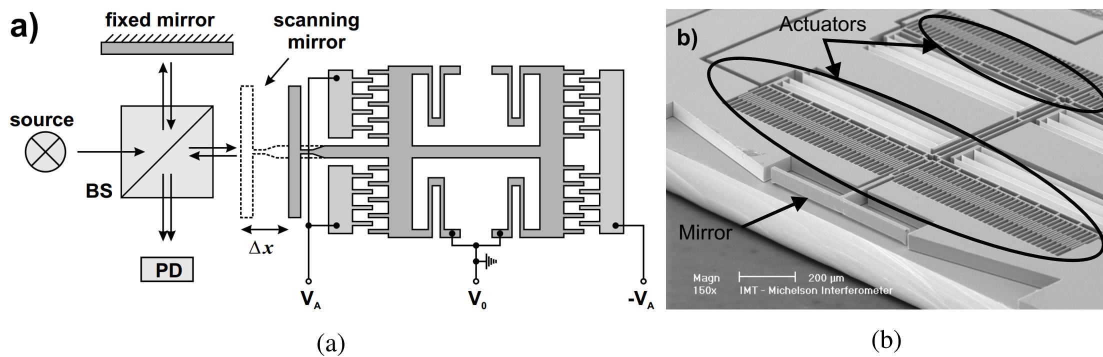

(a) (b)

FIGURE 1.4: (a) Concept of Fourier transform spectrometer (FTS). In the real setup, the beam splitter (BS) and the fixed mirror are macroscopic. The movable mirror was driven by a push-pull configuration. (b) The MEMS mirror is much larger than in the OXC and the V OA to increase the reflecting area [114].

1.1.2 The contribution of the microassembly to the fabrication of MOEMS

There are several ways to fabricate MOEMS. One of the most successful techniques is the monolithic fabrication which facilitates the packaging, reduces the unit cost for large series of product due to the batch fabrication of MOEMS, enables precise alignment of multiple materials and pieces and avoids the manipulation of fragile microparts. This technique relies on using the standard MEMS microfabrication techniques to fabricate the electrical, mechanical and optical functions on the same substrate. Thus, successive etching and sputtering processes are done after aligning the photolithography masks in order to fabricate a final component. Several MOEMS have been fabricated using MEMS technology including movable micromirrors for OCT [204, 51], microspectrometers [115, 151, 137] and others. This technique enables to reduce increasingly the size of the optical components such as microlenses and micromirrors.

The major difficulty in the fabrication of MOEMS is the incompatibility of fabrication processes that leads to compromise on the quality of the system. Indeed, it is difficult to achieve integration of semiconductor materials like alloys, polymers, glass, silicon and others on the same microsystem without compromise on the fabrication steps. On the other hand, MOEMS tend to be increasingly complex, integrating more functions using a variety of miniaturized microcomponents. The microassembly offers the opportunity to optimize the fabrication of microcomponents in order to integrate them on the final system. The fabrication of hybrid 3D MOEMS based on optical elements outside the plane seems to be unavoidable to produce optical functions with a beam propagating in free space. It is difficult even impossible to produce monolithic microsystems especially with complex 3D shapes. The intervention of an assembly step becomes therefore necessary to fabricate hybrid 3D MOEMS. Recent results confirm the relevance of microsystems obtained by microassembly [21, 34, 27, 10, 26]. For example, the use of microassembly to fabricate MEMS Fourier Transform microspectrometer enables to avoid some of the drawbacks of the monolithic approach such as reduced spectral range and fixed resolution [27, 26]. Many advances have allowed for teleoperated and automated microassembly.

Consequently, the fabrication of MOEMS using an approach combining advanced microfabrication techniques and the contribution of microassembly is an interesting topic that deserves to be investigated. This interest notably relies on the cost reduction, the amelioration of the flexibility of the design, the optimization of the design in order to guarantee an optimized final component with the desired performances.

Several microassembly techniques will be presented in Section 1.3.4.

1.1.3 Microassembly of hybrid MOEMS components on Reconfigurable-Free-Space Micro-Optical-Bench (RFS-MOB)

The fabrication of microsystems by microassembly is an alternative to monolithic approach. Several microassembly techniques have been presented in the past years where we can notice that dedicated tools are required for each assembly process depending on the desired application and the fabricated micro-objects. A technique allowing the assembly of various sizes, shapes and types of micro-objects is not fully developed in literature. The various optical elements made of incompatible microfabrication processes will be the basic building blocks of a new generation of MOEMS called hybrid MOEMS.

Hybrid MOEMS have been presented during the project MIAAMI (Flexible micromanipulation cell for the assembly of hybrid MOEMS: Application to micro-optical benches) in collaboration between the two departments AS2M and MN2S of FEMTO-ST institute. During this project, a technology platform for the hybrid integration of MOEMS components on a reconfigurable silicon free-space micro-optical bench (RFS-MOB) has been presented as shown in Figure 1.5. In this approach, a desired optical component (e.g. micromirror, microlens) is integrated with a removable and adjustable silicon holder, with spring-based snap connectors, which can be manipulated, aligned and fixed in the precisely etched rail of the silicon baseplate by use of a robotic micro-assembly station. An active-based gripping system allows modification of the holder position on the baseplate with nanometre precision. Thus, modification of the components position on the baseplate can be possible by making the reconfiguration of the complex microsystem easy and reducing manufacturing costs. The micro-optical elements can be fabricated independently on a dedicated holder using various materials (glass, polymer), other than the bench substrate (silicon), and using optimized technologies (e.g. bulk or surface micromachining, solgel, replication techniques). Based on the active gripping principle, generic holders with spring-based snap connectors have been developed enabling the insertion, guiding and fixing of various micro-optical components on the silicon baseplate. Figure 1.5 illustrates the concept of assembly of the holder into the rail of the silicon baseplate.

Teleoperated microassembly has been used in order to perform the microassembly of RFS-MOB using a robotic microassembly station. This work has been presented in [10] and the microassembly position accuracy characterization has been presented in [23] where a position accuracy of 1 μm and 1° of error on the tilting angle of mirrors have been performed. A strategy to achieve the microassembly of the RFS-MOB has been presented in [10] and is summarized in the following steps and in Figure 1.6:

- picking up of the holder by active opening and closing motions of the microgrippers fingers and pre-positioning of the holder in front of the rail,

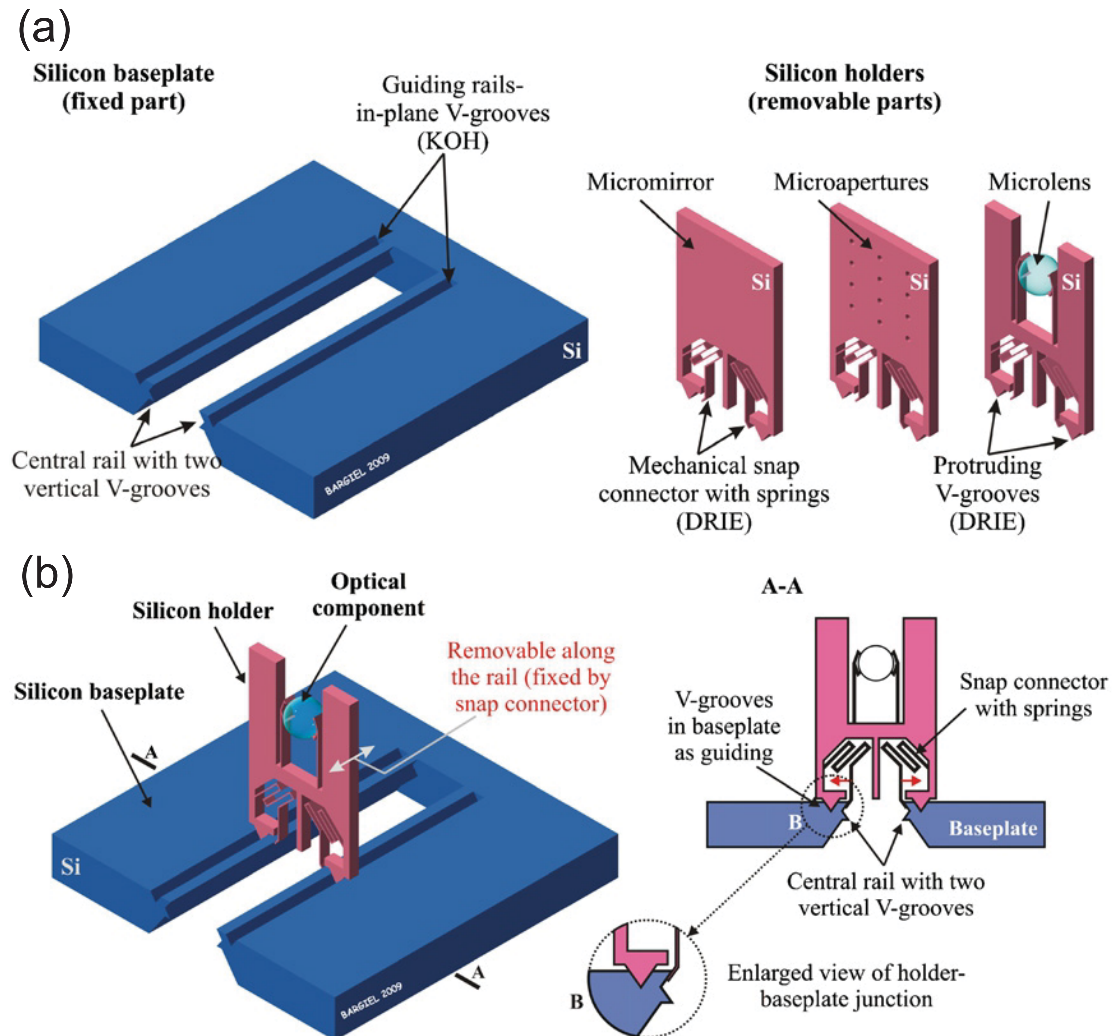

FIGURE 1.5: Individual components of the RFS-MOB and their assembly concept as presented in [10]: (a) details of the silicon bulk-micromachined baseplate and silicon holder (with the ball microlens as a micro-optical component), (b) holder assembled into the central rail of the silicon baseplate.

- insertion of the holder into the baseplate,
- guiding of the holder within the guiding rails to get the fine positioning of the holder,
- releasing of the snap connector springs through opening motion of the microgripper, which enables the fixing of the holder onto the baseplate,
- moving back motion of the microgripper.

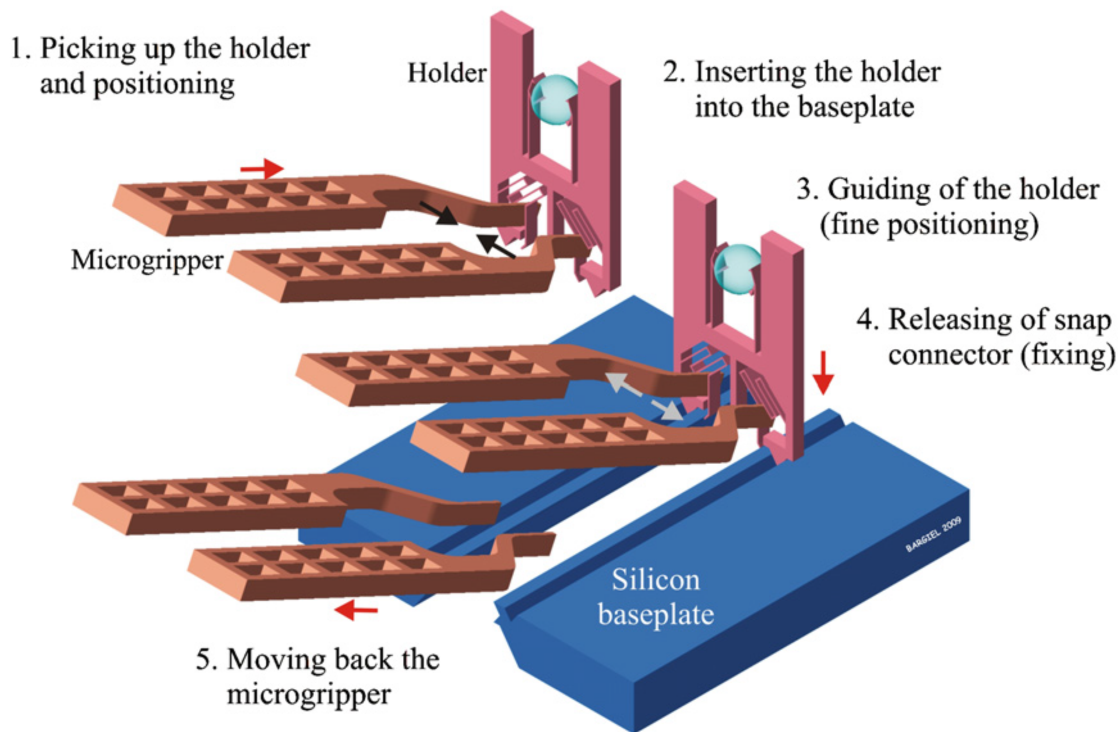

FIGURE 1.6: General concept of holder assembly based on the use of a robotic active microgripper as presented in [10]. The geometry of a gripping tool, performing the insertion and displacement of the holder within the rail of the baseplate, is illustrated.

Some results of the microassembly are presented in Figure 1.7 where in Figure 1.7-(a) a holder is handled between the two fingers of the active microgripper from the flexible part of the holder. In Figure 1.7-(b), a SEM picture of the two holders assembled onto the rail of the baseplate.

In order to improve the position accuracy of the microaseembly, to ensure large production series and cost reduction, automation of the microassembly is required. The automation of the microassembly is the objective of the ongoing project MIOP (Microsystems for instrumented optical chips) where our work is a part of this project. In this rest of the chapter, the challenges raised by the microassembly and the methods and principles of the microassembly are presented in order to determine a method to automate the microassembly of these systems. The integration of sensors is also discussed in order to perform the automation.

1.2 Challenges raised by the microassembly

The microassembly offers a good flexibility in the design and the fabrication of MOEMS. It offers the possibility to fabricate complex 3D MOEMS structure by assembling several 2D structures while optimizing each of the 2D structures. However, many challenges exist on the microassembly including the microscale specificities and the technological limitations to en-

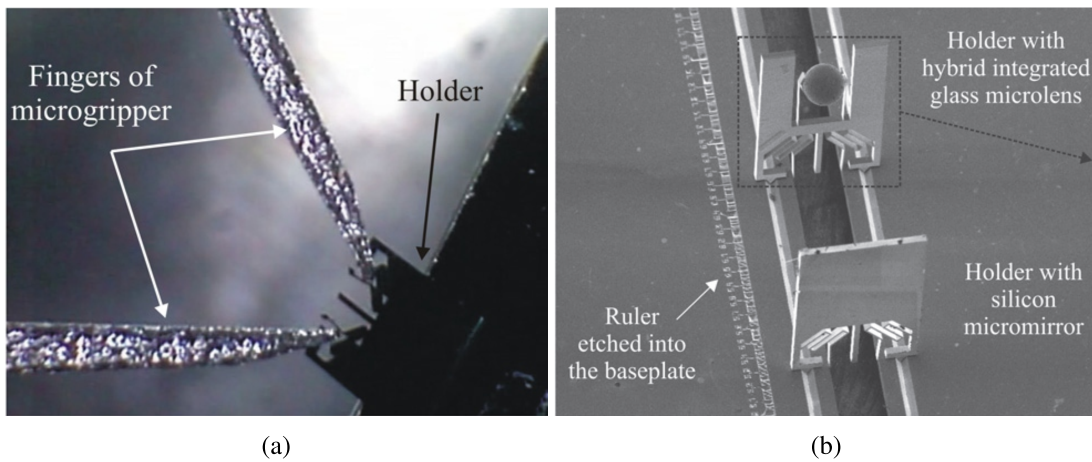

(a) (b)

FIGURE 1.7: Images during the microassembly of the holder and after the microassembly of two holders onto the rail of the baseplate as presented in [10]: (a) Picking the holder on the flexible part, (b) SEM picture of two assembled holders.

counter in the system. In this section, some of the microscale specificities, the technological limitations and their consequences for the microassembly are presented.

1.2.1 Microscale specificities and their consequences for the microassembly

Microscale has many specificities which can be convenient for many applications but can also complicate the task to be done. These specificities are detailed in [19]. The main microscale specificities can be summarized by:

- predominance of surface and contact forces,
- very high dynamics of the microsystems,
- fragility of the microparts,
- dependency of the microsystems to environment parameters,
- very small size inducing many difficulties to act and sense efficiently and especially for multi-DOF actuation and sensing.

Predominance of surface and contact forces

At the microscale, surface forces are predominant. Indeed, when downscaled, volume forces (e.g. gravity) tend to decrease faster than other kinds of forces such as surface forces. Volume forces become negligible at the micro/nano-scale. Contrary to the term volume forces, which represent forces proportional to the volume of the object (e.g. gravity), the term surface force is misleading since all these forces does not really depend on the square of the characteristic

length. Nevertheless, this term conveys the idea that these forces decrease more slowly than the weight, which leads to some cut-off sizes below which these forces disturb some microscale tasks such as a handling task because they generate the sticking of the micropart to the tip of the gripper (the weight is no longer sufficient to overcome them and ensure release). Some examples exist in the nature, showing the predominance of surface forces, including an ant which carries a load greater than his weight.

Surface forces have adhesive effect on objects. They are manifested by three large classes at the microscale: van der Waals forces, capillary forces and electrostatic forces.

- Van der Waals forces: they are manifested by the molecular level interaction. These forces represent the sum of the attractive and repulsive forces inside the molecule or between different molecules. They are named after a Dutch scientist Johannes Diderik van der Waals (1837-1923) who won the Nobel Prize in physics in 1910. These forces depend on the geometry of the contact and the characteristics of materials.

- Capillary forces: they appear when a liquid bridge, known as meniscus, exist between two solids. They depend on the liquid involved through the surface, on the material used, on the volume of liquid in the bridge, on the distance between the two solids and on the geometry of the solids. Their existence is determined by the environmental humidity conditions.

- Electrostatic forces: they occur through the Coulomb interactions in presence of charged particles or caused by the appearance of charges generated through triboelectrification. The electrostatic forces are inversely proportional to the separation distance which increases their effects when small distances exist. When triboelectrification occurs, these forces may have an uncontrolled impact on the system and some displacements may occur.

Figure 1.8 and Table 1.2 show the predominance of surface forces relative to the distance of interaction between two objects at the microscale.

Surface forces can disturb some microscale tasks. However, these forces can be useful for other applications and are used to perform many microscale tasks such as micromanipulation and microassembly tasks. Indeed, capillary forces are used in some works in order to align and fix the components for a self-assembly task [152]. Furthermore, electrostatic forces are used to manipulate microparts to perform positioning and alignment of the microparts for microassembly in [13].

Contacts forces appear when a contact between two surfaces exists. They are generated by the local deformations, known as *plastic* deformation, and are characterized by the required energy to break contact [19]. These forces are notably manifested by the *pull-off* force which is the minimum force needed to break contact between two objects. These forces are in fact a combination of the three types of surface forces (van der Waals, capillary and electrostatic). Several models have been developed for a contact between a sphere and a planar surface. They are mainly based on Johnson-Kendall-Roberts (JKR) [73] or Derjaguin-Muller-Toporov (DMT) formulations [37]. Physical phenomena are complex and researchers still have great difficulty in identifying them and quantifying their effects. Nevertheless, microassembly commonly requires

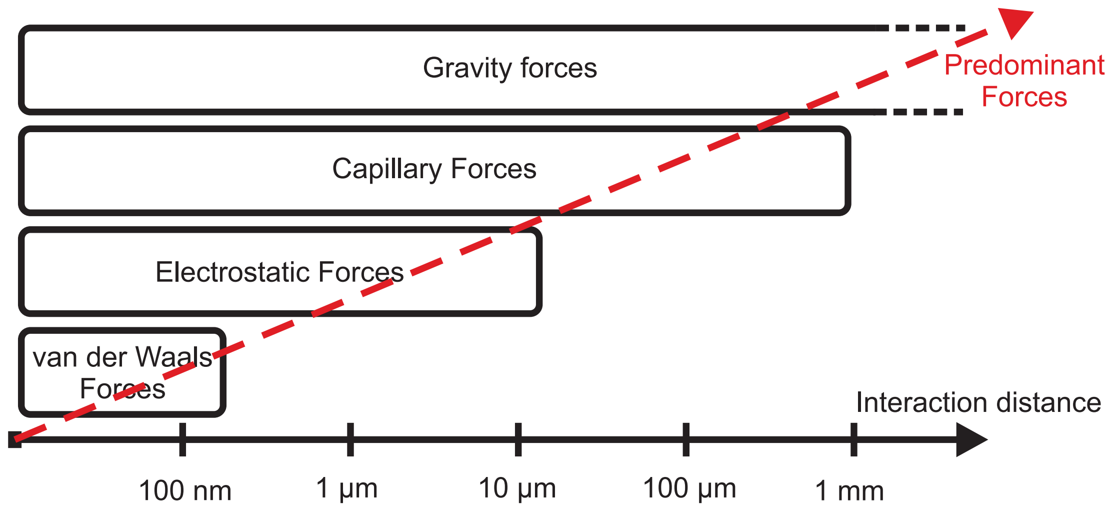

FIGURE 1.8: The predominance of surface forces at the microscale.

Interaction distance	Predominant force
• Up to infinite range	• Gravity
• From a few nm up to 1 mm	• Capillary forces
• > 0.3 nm	• Electrostatic forces
• Between 0.3 nm and 100 nm	• van der Waals
• < 0.3 nm	• Molecular interaction
• 0.1-0.2 nm	• Chemical interactions

TABLE 1.2: Force summary according to the interaction distance [92].

planar contacts and surfaces are often made of silicon. Models for contact between two planar surfaces is not studied in literature. An experimental study and measurement of the pull-off force has been performed in [128]. Figure 1.9 shows a typical curve for approach/retract between two planar surfaces where the force appears when a contact exists and while the retract part the pull-off force appears. The pull-off force depends on several parameters including the preload force, the contact angle, the environmental conditions (temperature, humidity), the materials, the roughness of the surfaces, etc. It was shown in [128], that the pull-off force can reach 196 µN for a contact surface of 50 µm $\times$ 50 µm.

During the microassembly, pull-off forces appear whenever a contact appears between a micropart and the microgripper or between a micropart and the substrate. Due to their adhesive effects, pull-off forces increase the complexity of the task when a separation of contact is needed. For example, if a micropart is manipulated using a microgripper and the micropart needs to be released, the presence of pull-off force causes adhesive effect between the microgripper fingers and the micropart which can lead to a disturbance of the release task and consequently a disturbance which can change the final desired position of the micropart. The same argument can be done once an undesired contact between the manipulated micropart and the substrate appears, an adhesive force also appears preventing the easy separation of the undesired contact.

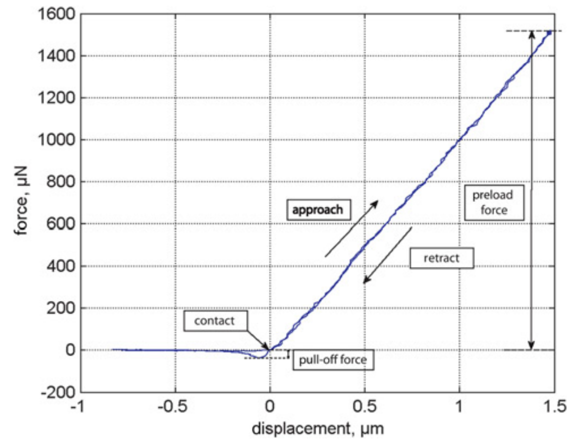

FIGURE 1.9: Typical curve for approach/retract between two planar surfaces [128] allowing to quantify pull-off forces.

In order to be able to deal with pull-off forces, we need first to identify their presence. Their presence can be measured using a convenient force sensor. Then, a convenient strategy can be defined to deal with these forces. Thus, integrating force sensors inside the microassembly station is required. In addition, the effect of pull-off forces has to be considered in the microassembly and the control strategies to be used.

Dynamics of the microsystems

The dynamics of a system depends on the geometry and the scale of the system. A simple example, illustrated in Figure 1.10, will be given in order to emphasize the dynamics of the system related to the size of the system. Considering two silicon cantilever beams, whose one

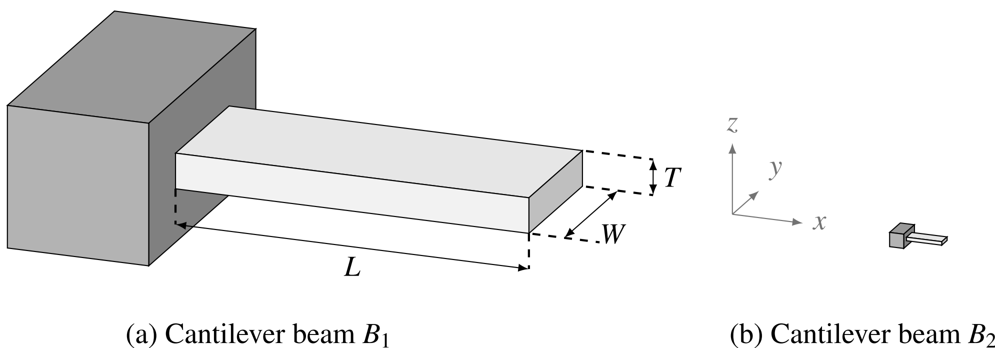

(a) Cantilever beam B_1 (b) Cantilever beam B_2

FIGURE 1.10: A scheme showing two cantilever beams: (a) a cantilever beam B_1 with dimensions L, W, T; (b) Cantilever beam B_2 with dimensions $\frac{L}{10}$, $\frac{W}{10}$, $\frac{T}{10}$.

end is fixed and the other end is free, with the same geometry but with different sizes. The first

beam, B_1, has L in length, W in width and T in thickness where the other, B_2, has $\frac{L}{10}$ in length, $\frac{W}{10}$ in width and $\frac{T}{10}$ in thickness. The natural frequency of a cantilever beam is given by:

$$f_n = \frac{\omega_n}{2\pi} = \frac{\beta_n^2}{2\pi L^2}\sqrt{\frac{EI}{\rho A}} \tag{1.1}$$

where f_n is the natural frequency in Hz of the nth vibration mode, ω_n is the natural frequency in rad/s of the nth vibration mode, β_n is a constant corresponding to the nth vibration mode, E is the Young Modulus of the material, I is the moment of inertia of the beam cross-section, ρ is the density of the material and A is the area of the cross section. Considering a rectangular cross-section, the area and the moment of inertia of the cross-section, I_x along the X axis (Figure 1.10), can be given as follows:

$$\begin{cases} A = W \cdot T \\ I = \dfrac{W \cdot T^3}{12} \end{cases} \tag{1.2}$$

Replacing Equation (1.2) in Equation (1.1), the frequency in Hz of a cantilever beam is given as follows:

$$f_n = \frac{\beta_n^2 \cdot T}{2\pi L^2}\sqrt{\frac{E}{12\rho}} \tag{1.3}$$

The frequencies of beam B_1 and beam B_2 are given as follows:

$$\begin{cases} f_n^{B_1} = \dfrac{\beta_n^2 \cdot T}{2\pi L^2}\sqrt{\dfrac{E}{12\rho}} \\ f_n^{B_2} = \dfrac{\beta_n^2 \cdot \frac{T}{10}}{2\pi \left(\frac{L}{10}\right)^2}\sqrt{\dfrac{E}{12\rho}} = 10 \cdot f_n^{B_1} \end{cases} \tag{1.4}$$

Equation (1.4) shows that if each dimension of the system is divided by 10, the natural frequency of the system is multiplied by 10. Consequently, dynamics of microsystems are much greater than dynamics of macrosystems due to the scale effect.

A the microscale, the acceleration of a microcomponent can reach thousands of the gravitational acceleration g. Thus, fine and rapid control is required to control the evolution of forces during pick and place steps of the microassembly in order not to loose the microcomponent. Otherwise, the microcomponent can easily be lost due to the big accelerations generated by the contact between the micropart and one finger of the microgripper. In the case of robotic microassembly, the dynamic control of the robotic station and the microgripper is the key for high speed and high dynamics microassembly. The dynamic control requires the presence of high dynamics sensors and to choose a well adapted control scheme. Thus, high dynamics position and force sensors are required in addition to an efficient control law.

Fragility of the microparts

The microparts are often fragile and could be broken when small forces are applied on them. These facts increase the complexity of doing some manual tasks in the system because the

forces that human can apply are big enough to break the microparts. An example of fragile microparts, the force sensors of FemtoTools [54] which can be deformed of 2 μm for the maximal force measurement range. Using micropositioning stages, 2 μm of displacement error can be easily generated (due to backlash, nonlinearity, perturbations, etc) which can lead to break the force sensor. Using this argument, even position control can not guarantee the safety of the microparts. Consequently, the use of force sensors and force control is appreciated if the safety of the microparts needs to be ensured.

Dependency of the environment conditions

Most of the materials are influenced by the environmental conditions. However, at the microscale, the influence becomes greater and significant. Indeed, a microsystem can have a thermal elongation in the μm range with an environmental temperature change of 1°C [162] which is a typical variation within a controlled environment such as a clean room. These changes have important consequences at the microscale. Furthermore, some materials, such as piezoelectric materials or piezoresistive sensors, are widely influenced by temperature change and the experiments can change from one day to other due to environment change. This dependency influences the choice on the automation of the microassembly where closed-loop based automation is more appreciated to overcome these effects than open-loop based automation. Indeed, it is required to integrate sensors to evaluate these changes in the system as a result of the difficulty of their modeling.

1.2.2 Technological limitations

In addition to these microscale specificities, there are several technological limitations at the microscale. The lack of suitable actuators and sensors remain the main challenge:

- in the actuators design at the microscale, trade-off corresponding to the resolution, range and blocking force of the actuator design are considered. This trade-off limits the capability of having precise micropositioning stage with big displacement range. Using this fact, the user should choose between having a micropositioning stage with big range or with low resolution which has effect on the task especially in applications such as microassembly where both big displacements and high precision are needed to perform precise microassembly. Indeed, some micropositioning stages with big positioning range are based on DC motors and have backlash of several μm (for example Physik Instrumente srie M-11x.1DG et M-11x.1xS positioning stage) and precise positioning stages with nm resolutions have displacement range of several hundreds of μm and are based on piezoelectric actuators (for example PIMars XYZ piezostage).

- the lack in suitable microsensors is another limitation. In order to measure the displacement at the microscale, laser sensors or vision based sensors are often used. Some dynamics issues exist on the use of cameras to measure the displacement. Most of the works using vision are limited to the quasi-static approach which limits the benefit of the dynamics at the microscale. The Scanning Electron Microscope (SEM) offers good precision in the

measurement at the microscale. However, its response time is in the range of several milliseconds [19]. Laser sensors have good precision and good dynamic behavior. However, their size is relatively big and they are expensive (such as laser sensors form Keyence and laser interferometer form SIOS Meβtechnik GmbH). In addition, this big size increases the difficulty of measuring multi-DOF displacements. Another lack is the measurement of angles and velocities at the microscale. In order to overcome the problem of size and cost of sensors, extensive researches exist on integrated displacement/force sensors in the system for example adding some strain gauges to the system to measure the displacement/force or working on some microfabricated force sensors by MEMS manufacturing techniques.

1.3 Methods and principles for the microassembly

Microassembly allows the construction of complex microsystems which can not be fabricated using micromanufacturing processes alone [57]. It also allows the fabrication of out-of-plane microstructures that require microparts issued from two or more different microfabrication processes. To perform microassembly, several steps have to be realized on the microcomponents to assemble: take, remove, displace, insert, release, etc. These steps can be done manually or through robotic systems. Several microassembly approaches have been studied and can be classified into several categories depending on the considered approach. Classifications can be based on the throughput of fabrication (serial or parallel), type of end-effectors (contact or non-contact) or level of human intervention (manual, teleoperated or automated). All these approaches will be detailed with examples in this section.

1.3.1 Type of end-effectors for the microassembly

Several methods exist on the manipulation of the microcomponents including non-contact and contact manipulation. The non-contact manipulation or self-assembly can be done by the use of an external driving force and the contact manipulation can be done by the use of a microgripper which is convenient to the application. Many researches have been done on the microgrippers [93]. The choice of microgripper is done relatively to the application and to the microassembly constraints. The microgrippers can be divided into two parts: passive and active. Passive microgrippers do not have actuators. Generally, the compliance in the passive fingers is introduced either in the microgripper [32, 169, 177] or the micropart [29, 26]. The active microgrippers have integrated actuators. Several types of actuators have been presented in the past years including electrostatic actuators [12, 119], electrothermal actuators [81, 157], piezoelectric actuators [118, 175] and others.

Self assembly

Self assembly consists of assembling microparts together spontaneously by subjecting them to the influence of an external driving force such as electrostatic force [13], heat [46], magnetic [205], centrifugal force [91], capillary forces [152], dielectrophoresis [80] or other. The use of self-assembly limits the effect of contact forces in the microassembly which is an important issue

at the microscale and take benefit form surface forces which are predominant at the microscale (electrostatic forces or capillary forces). Their advantages is the capability of producing large quantity of microparts in a small operating time and with high precision.

The self-assembly techniques will not be detailed because the use of self-assembly techniques is often used to make 2D assembly and the capacity of performing complex 3D assembly still limited. However, in several cases, the self-assembly techniques are combined with serial or parallel assembly techniques as will be shown in section 1.3.2.

Manipulation using passive fingers

Several works using passive microgrippers are presented in [8, 169, 28, 26]. A two orthogonal passive fingers microgripper has been proposed in [165] where two orthogonal fingers are used to manipulate and rotate a micropart.

One of the works using two passive fingers microgripper is presented in [32, 33] where a passive microgripper composed of two flexible silicon fingers is used. The initial gap between the two fingers is 14 µm.The microgripper is bonded to a 5-DOF robotic workstation via *contact head* as shown in Figure 1.11a in order to assemble 3D microparts in many steps. In the design of the microparts, some interfaces are fabricated in order to manipulate the micropart using these interfaces. The microgripper is pushed into contact with the component and when a contact happens the compliant fingers of the gripper deforms and the micropart enters between the two fingers and finally the micropart is fixed between the two fingers of the microgripper as shown in Figure 1.12. After handling the micropart and manipulating it to the final position, some *T-Slots* are fabricated on the base structure and two *Keys* are fabricated on the micropart in order to fix definitively the micropart on the substrate as shown in Figure 1.11b. Once the micropart is inserted in the base structure, the *Keys* enter two *T-Slots* to create *Key-Lock joints*. In order to fix a micropart on another one, *slits* and *lock slits* are fabricated on the microparts as shown in Figure 1.11b.

The use of a passive microgripper is unique for each application and each micropart. Indeed, if the micropart design changes, the microgripper design needs to be changed in order to fit to the new application.

Manipulation using active fingers

These microgrippers are widely used for micromanipulation and microassembly [119, 191, 175, 14, 6, 62, 12, 118]. Their advantage is that they can be used to manipulate several objects with different shapes and sizes. A two piezoelectric fingers microgripper is proposed in the AS2M departement of FEMTO-ST institute. Several microassembly station were developed to achieve 3D microassembly. PRONOMIA (Principes et Outils Nouveaux pour le Micro-Assemblage Automatisé) station was used to assemble a microcow using five microfabricated pieces where each piece has 5 µm of thickness. The microcow has 830 ng of weight, 500 µm of length and 300 µm of height. Figure 1.13 shows PRONOMIA microassembly station and the assembled cow.

The same presented active microgripper has been used to perform the microassembly of the microparts of the MIAAMI project presented in section 1.1.3. The same microgripper has en-

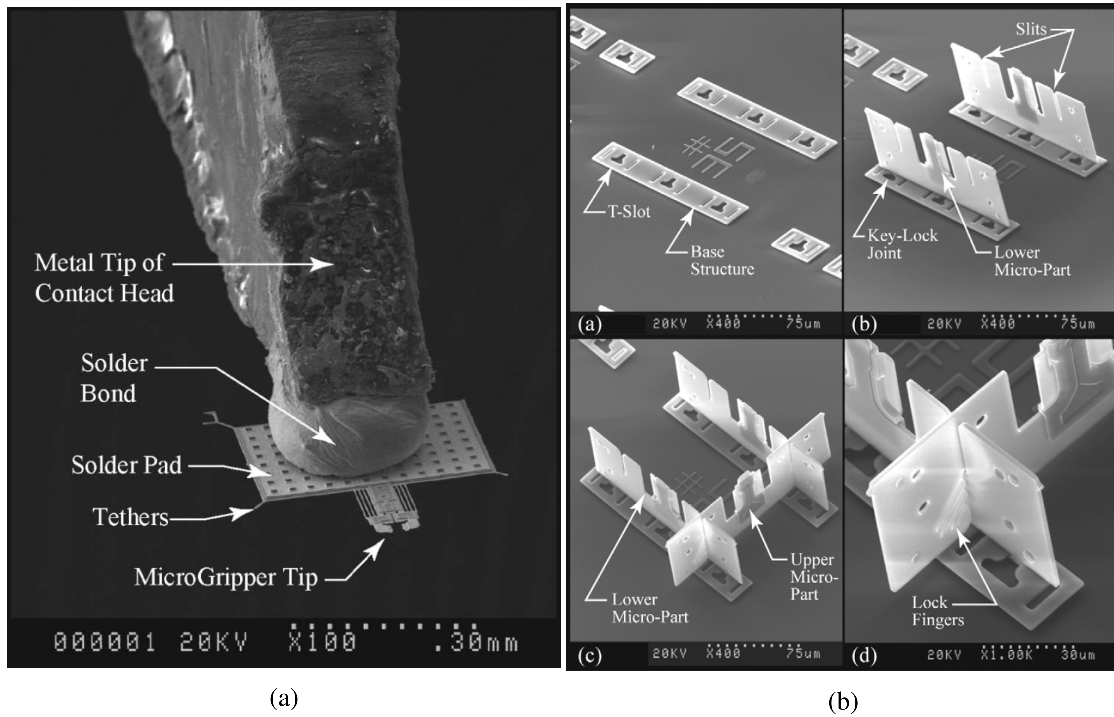

(a) (b)

FIGURE 1.11: (a) Two passive fingers microgripper using the compliance to handle the micropart [32], (b) the assembly steps and the locking of the micropart to the substrate [33].

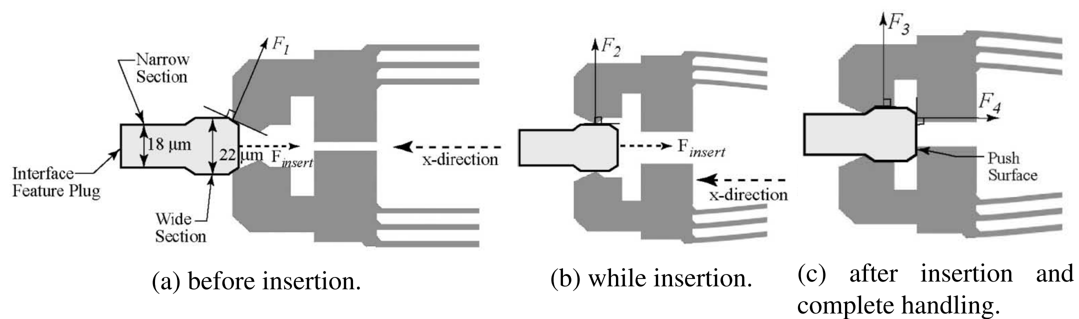

(a) before insertion. (b) while insertion. (c) after insertion and complete handling.

FIGURE 1.12: The handling steps of the micropart using the passive finger [32].

abled to successfully perform the microassembly of two different shapes and sizes of microparts. Hence, the main advantage of using an active microgripper is the versatility of the microgripper enabling the use of the microgripper for several applications.

1.3.2 Serial and parallel microassembly

The microassembly can be classified based on robot structure into two categories: serial and parallel. The two categories will be detailed with examples in the following.

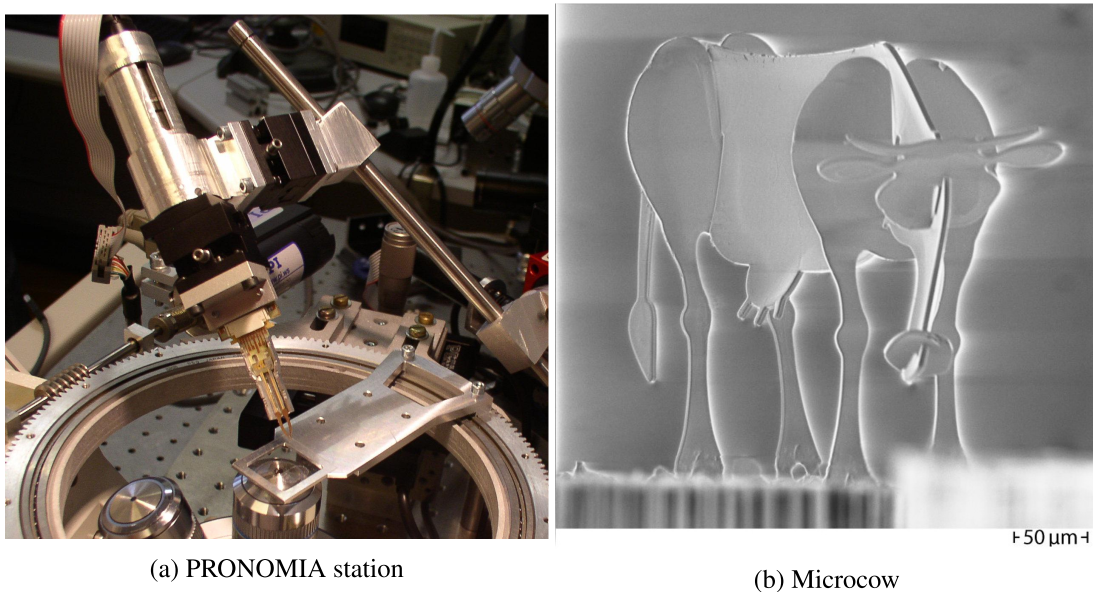

(a) PRONOMIA station

(b) Microcow

FIGURE 1.13: PRONOMIA microassembly station [62] and the assembled microcow.

Serial microassembly

Serial Microassembly is a sequential process in which assembly tasks are performed one after the other. To complete one microassembly, series of subtasks are required, such as grasping microparts, manipulating them, and joining them to other microparts, etc. It requires the use of a microgripper which is convenient to the application. Both types of microgrippers (passive and active) can be used to perform serial microassembly. The examples given in section 1.3.1 for the microassembly using passive and active microgrippers are considered as serial microassembly. The example of MIAAMI project given in section 1.1.3 is also considered as serial microassembly.

Serial microassembly can also be performed with self-assembly. In some applications robotic serial microassembly is combined with self-assembly using capillary forces as presented in [138, 201]. In [138], a microgripper is used to position the micropart near the desired position and the fine positioning (self-positioning) is performed by a water droplet. The positions of the water droplets are microfabricated which reduce the positioning error. Water droplets compensate the errors induced by a non precise robotic system. The microassembly steps and the handling techniques are shown in Figure 1.14. This method enables to perform 2D½ microassembly. The dimensions of the tested micropart go from 50 μm $\times$ 50 μm $\times$ 40 μm up to 300 μm $\times$ 300 μm $\times$ 70 μm. The yield of the assembly can reach more than 99% and the duration of self-alignment process was measured to range from 50 to 500 ms.

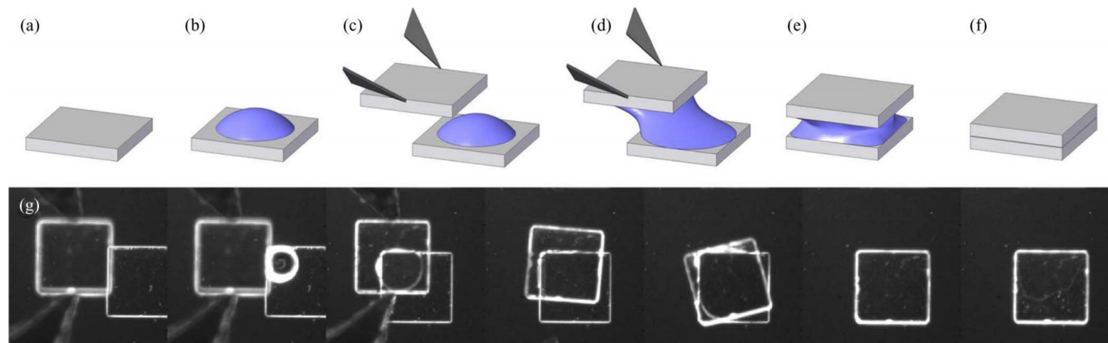

FIGURE 1.14: Hybrid handling technique [138]. (a) Assembly site is on top of a micropart. (b) Droplet of water is dispensed on the bottom part. (c) Microgripper approaches the release site with a part. (d) Droplet contacts with the top part and wets between the parts, which forms a meniscus. (e) Microgripper releases the part and the capillary force aligns the parts. (f) Water between the two parts evaporates, which leaves the two parts aligned. (g) Image sequence of the actual experiment, as viewed from the top side.

Parallel microassembly

The main objective of Parallel microassembly is to simultaneously assemble microdevices or multiple assembly sites and includes *flip-chip* [146] and *batch transfer* [104] methods. This method is also called wafer-to-wafer. The steps of the flip-chip method are the following:

- two different set of microparts are fabricated on each wafer,
- one wafer is flipped and aligned with the other,
- the two components are bonded in order to fix them together.

This method is widely used in microelectronics and it enables 2D microassembly. Parallel assembly avoids the drawbacks of a sequential one for small devices: time consuming and low throughput. The drawbacks of parallel assembly are less flexibility compared to sequential assembly and the success rate of the microcomponents. Indeed, it is known that in the microfabrication process, some percentage (it can reach 20%) of fabricated microcomponents are not functional due to some technological limitations, non homogenous behavior of some machines and several source of imperfections. If the components issued from two different wafers are bonded, then non-functional microcomponents of wafer 1 can be bonded with functional microcomponents of wafer 2 leading to a non-functional resulting component. Thus, the success rate can be divided by two, *e.g.* if the success rate of one process is 80% then, the success rate of the bonded system can reach 40%. If ten wafers are used in the wafer-to-wafer approach, the success rate of the microfabrication can be so small.

One example of parallel microassembly is the parallel microassembly with electrostatic force fields that has been proposed in [13]. In this paper, a new approach to microassembly using (1) ultrasonic vibration to eliminate friction and adhesion and (2) electrostatic forces to

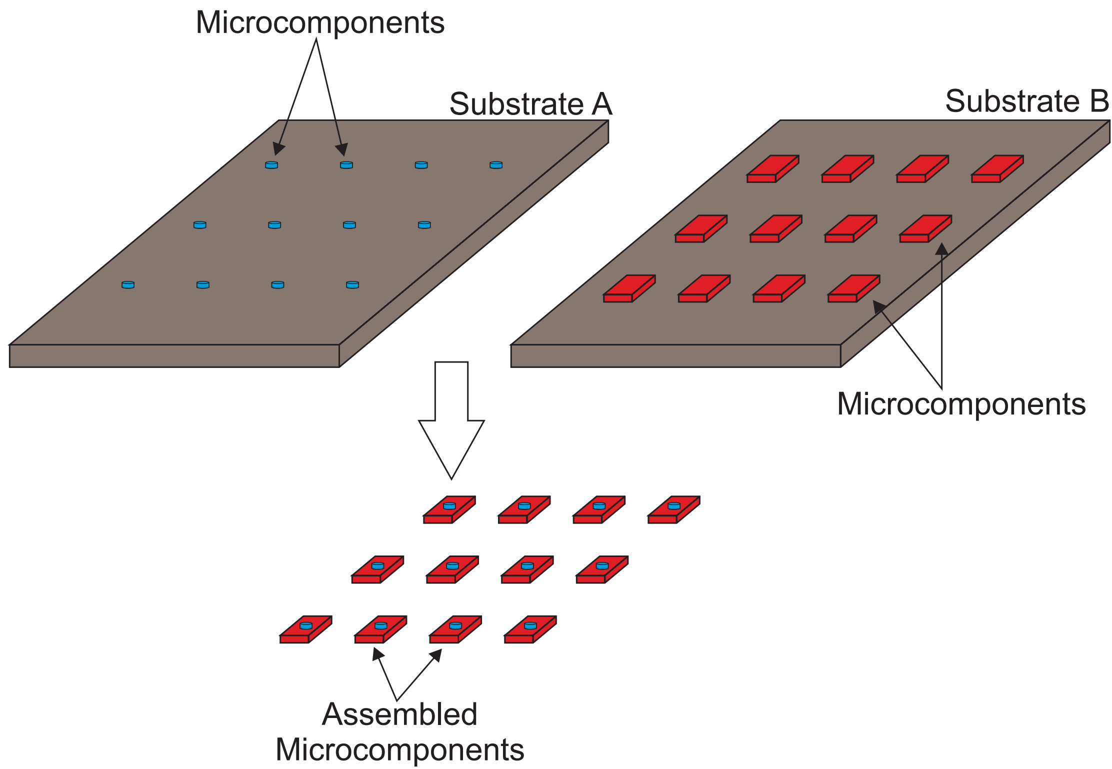

FIGURE 1.15: Parallel microassembly by flip-chip method.

position and align parts in parallel. The experiments show that friction and adhesion between small parts can be overcome by ultrasonic vibration. Consequently, in such frictionless environment, an accurate positioning of the small parts can be performed in parallel with electrostatic traps. Figure 1.16 shows the parallel microassembly techniques where multiple microscale components (e.g. electronics, photonics and MEMS) are built in parallel using standard fabrication processes.

Another example of parallel microassembly is an example where parallel robotic microassembly is combined with self-assembly by capillary forces. This work is proposed by a team of the Bioengineering and Robotics departement in Tohoku University, Japan. Many researches have been performed in order to achieve 3D integration technology by combining parallel microassembly to the self-assembly by capillary forces [56, 87]. A 3D image sensor chip, 3D shared memory chip, 3D artificial retina chip and 3D microprocessor test chip have been fabricated by using this technology. The microassembly steps are summarized in Figure 1.17. A number of known good dies (KGDs see Figure 1.17) are simultaneously aligned and bonded onto lower chips or wafers with high alignment accuracy by using a self-assembly technique in a super-chip integration.

Another work proposes a hybrid microassembly technique for parallel assembly of 200 µm × 200 µm × 30 µm SU-8 chips [20]. The hybrid microassembly technique combines the

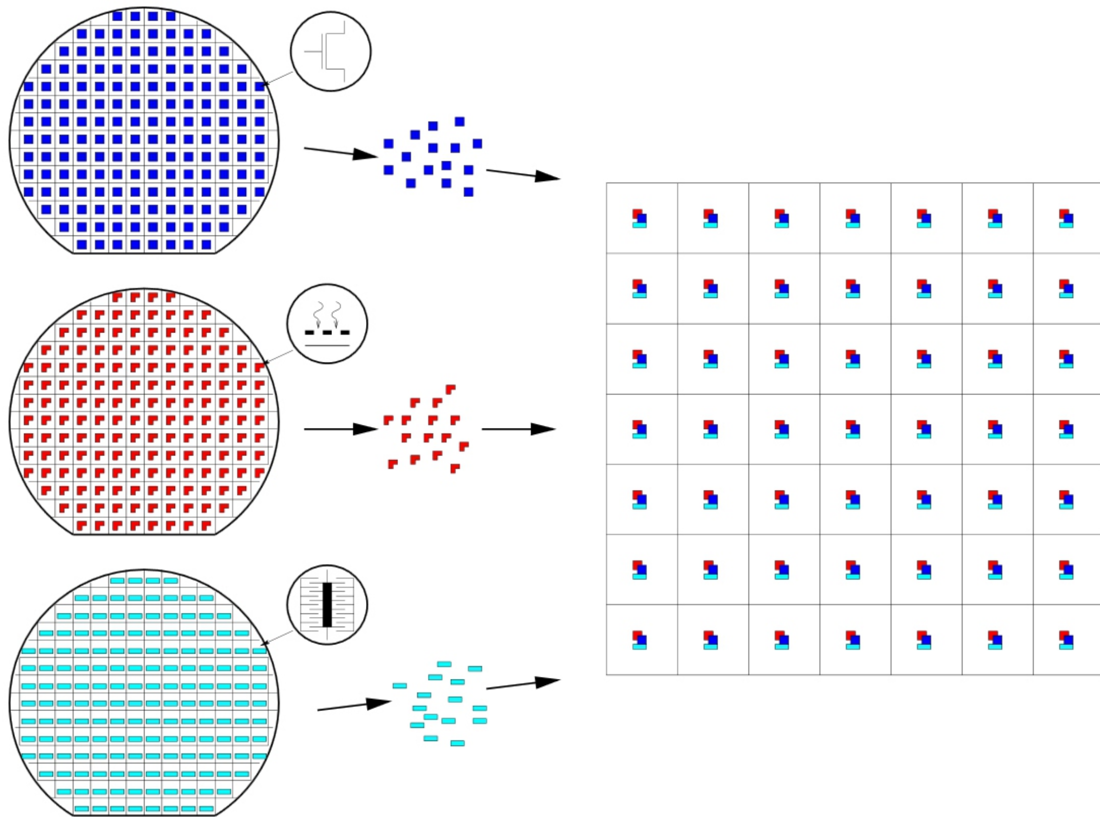

FIGURE 1.16: Parallel microassembly: Multiple microscale components (e.g. electronics, photonics and MEMS) are built in parallel using standard fabrication processes. They are positioned and combined with other components on a hybrid *pallet*. Note that the fabrication density is high, while the pallets may have a larger size and lower density [13].

robotic pick-and-place technique and water mist induced self-assembly technique. The chips are prepositioned using the robotic station and the precise positioning and alignment are performed using the water mist. The results of the microassembly technique are shown in Figure 1.18. The results show that the alignment can reach submicrometer accuracy [20].

1.3.3 Microassembly modes

The microassembly can also be classified in terms of level of human intervention into three categories: manual, teleoperated and automated. Both teleoperated and automated microassembly requires robotic station. Robotic microassembly is used to perform complex 3D assembly tasks with high precision thanks to the use of microgrippers, robotic systems, sensors, cameras, human-machine interface, etc. Many robotic micropositioning stages can be used in order to move the microgripper to the object to be manipulated or vice versa. These stages add some degrees-of-freedom to the microassembly station. In addition, some position sensors can be

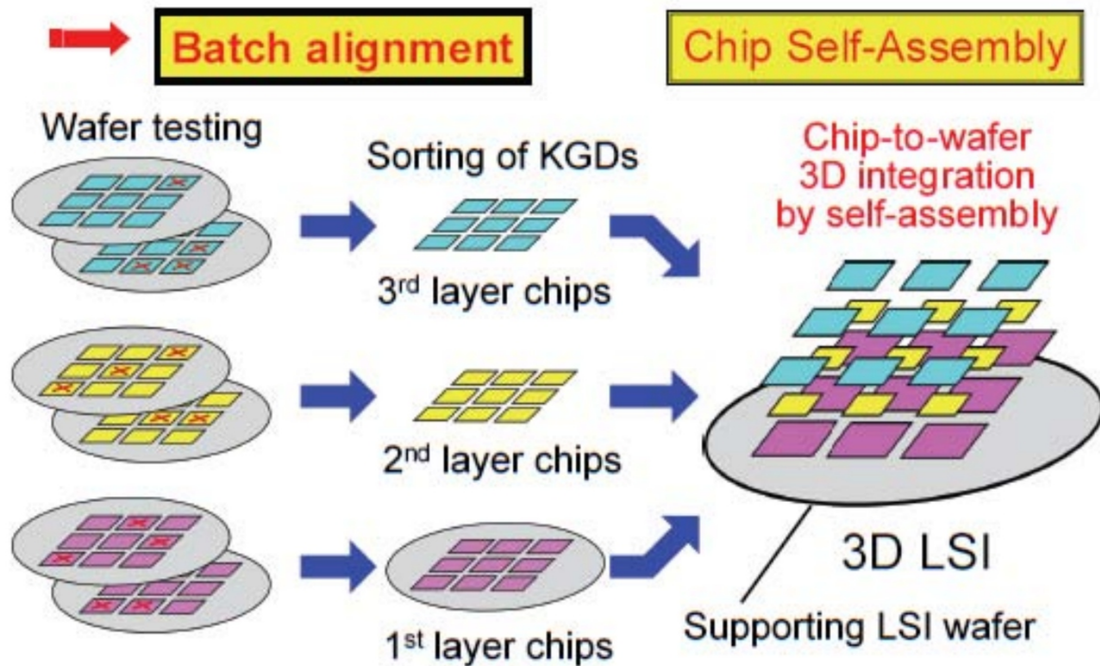

FIGURE 1.17: The method of the fabrication proposed by super-chip integration technology [87].

used in order to measure the positions of the object and microgripper and some force sensors to sense the interaction forces. Vision systems are also used in order to visualize what is happening. Sensors and vision systems can be used for both approaches of serial microassembly but their presence for the automation of the microassembly is essential.

Manual microassembly

It consists of a human who uses some tools such as mechanical tweezers and uses microscope or binocular in order to see what's happening. It requires dexterity and skills of the operator and a lot of precision and attention which is a tired task for the operator. Furthermore, due to the involuntary hand tremor (bigger than 30 µm [153]), the precision of the assembly may reach some µm but at a high cost due to the training of the human operator and the long time needed to achieve the task. In addition, the forces involved by human are big because human can not sense forces lower than mN. Consequently, the microparts can easily be broken when manual microassembly is performed.

Teleoperated microassembly

In teleoperated microassembly, a human operator controls a robotic station to perform the microassembly tasks. The operator uses different types of sensors and visual systems in order

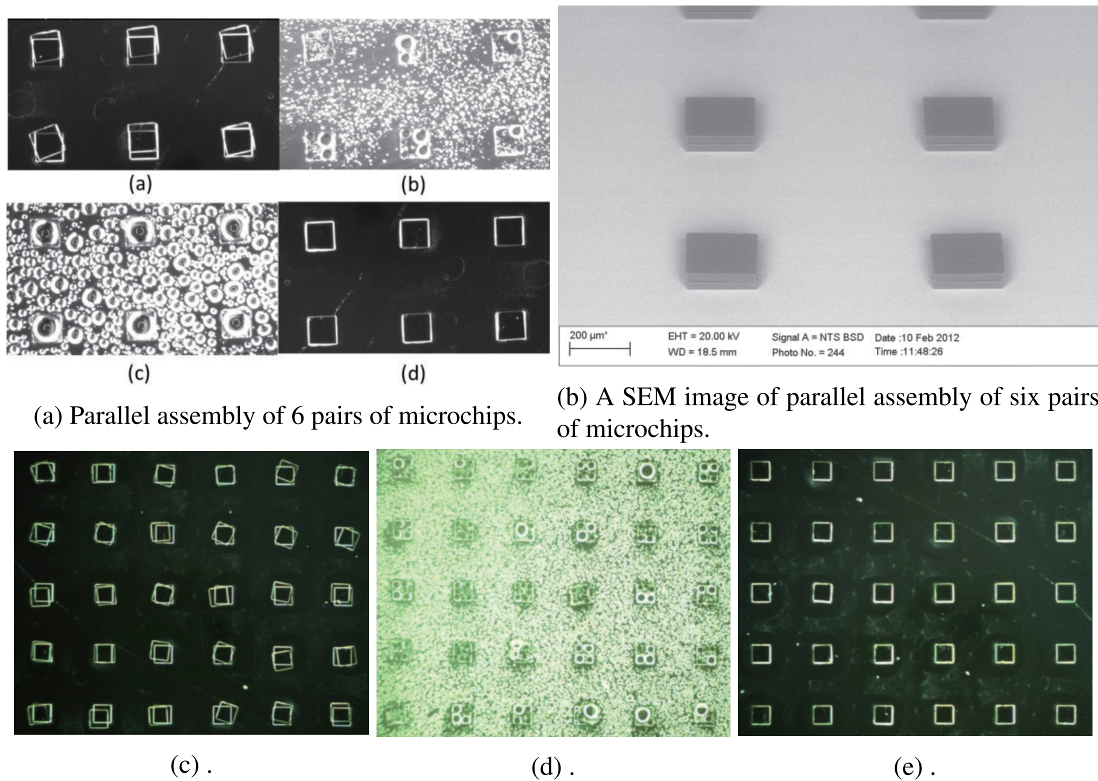

(a) Parallel assembly of 6 pairs of microchips.

(b) A SEM image of parallel assembly of six pairs of microchips.

(c) .

(d) .

(e) .

FIGURE 1.18: Parallel assembly of 6 pairs of microchips with size 200 µm × 200 µm × 30 µm [20].

to grasp the micropart and to position it in the desired position. Teleoperated microassembly enables to perform complex 3D microassembly. Once the micropart is positioned at the final position, this position should be maintained by fixing the micropart using several techniques (compliant mechanical techniques, grooves, holes, UV glue, etc).

The examples given in section 1.3.1 for the microassembly using passive and active microgripper and the example given in section 1.1.3 are performed in the teleoperated mode. Complex 3D microassembly can be performed using teleoperated microassembly. However, teleoperated microassembly requires dexterity of the operator and long time to achieve each assembly process.

Automated microassembly

Automated microassembly is used to achieve more precise and faster microassembly process. The automation can be done using two principles:

- open loop automation which consists of calibrating the robotic system in order to compensate the static and dynamic errors, nonlinearities, temperature drift, etc. [123, 122].

- closed loop automation using position and/or force feedback [178, 161, 88]. Position sensors and/or vision feedback are used to measure the positions of the micropart to be manipulated, the microgripper and the substrate. The force sensor measures the interaction forces between the micropart and the substrate as well as gripping forces. Hybrid force/position assembly uses the information of both the force and the position sensors.

Figure 1.19 summarizes the methods of performing automated robotic microassembly. Some examples are given in the following to the main existing works of automated microassembly.

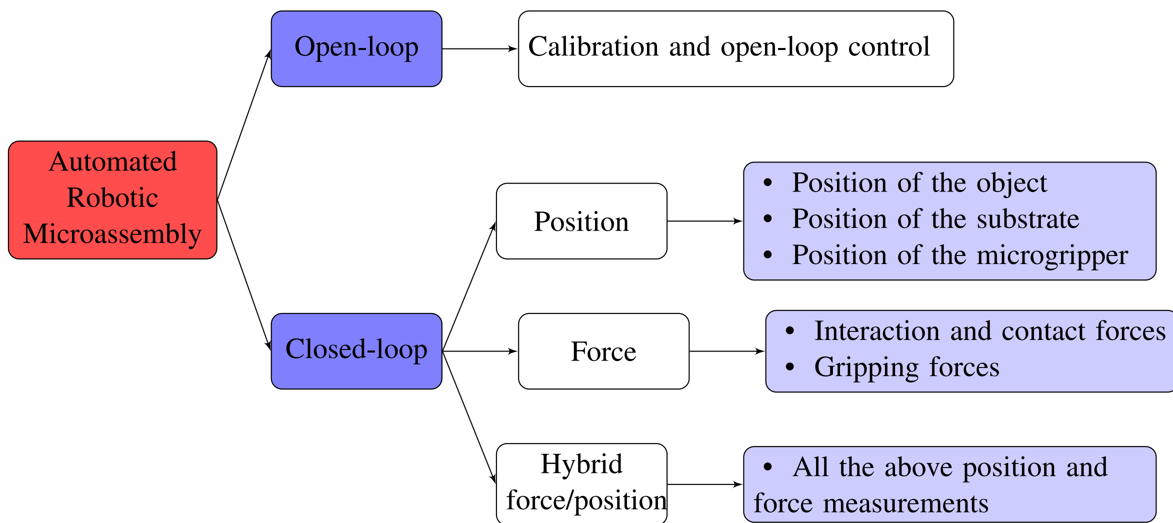

FIGURE 1.19: The different approaches for the automation of robotic microassembly tasks.

Example 1 - Open loop automated microassembly using passive microgripper: An open loop automated microassembly has been presented in [29] in UTARI in Texas. A passive gripper, called *jammer*, is used to manipulate the microparts. The design was originally proposed by the research department of Zyvex Corporation [170] where the *jammer* and the microparts where fabricated. Figure 1.20 shows the *jammer* and the manipulation of the microparts during the microassembly. The *jammer* is rigid and is used to handle the micropart through a flexible zone in the micropart. In [29], the microassembly is performed using a robotic station called by authors μ^3 due to the presence of three robotic manipulators as shown in Figure 1.21a. The robotic station μ^3 has 19-DOF stages arranged into three robotic manipulators (M_1, M_2 and M_3). It is used to achieve both serial and deterministic parallel micro/nano scale assembly outside and inside the SEM. M_1 and M_2 are two robotic manipulator arms with 7 degrees of freedom each where the central M_3 is a 5-DOF robot and it carries custom designed fixtures for microparts (the dies/substrate) and a custom designed hotplate for process ability such as interconnect solder reflow. The dimensions of the microparts are 800 µm × 1300 µm × 100 µm.

Automated microassembly has been achieved in the open loop. In order to perform the open loop automation, precise calibration of the robotic station has been performed in order to

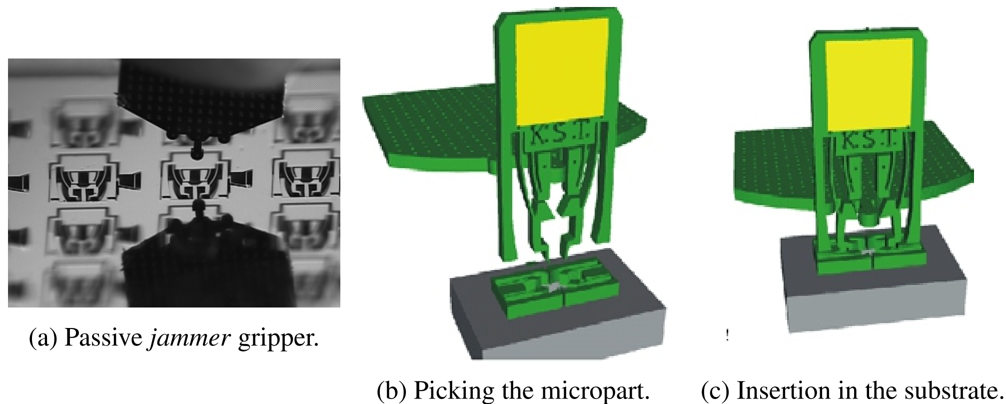

(a) Passive *jammer* gripper.

(b) Picking the micropart. (c) Insertion in the substrate.

FIGURE 1.20: The passive *jammer* gripper and some figures showing the manipulation and the insertion of the micropart into the substrate.

compensate the static errors of the robotic stations and to perform the precise positioning of the system. The calibration should be repeated when the conditions of the experiment change. The calibration refers to a set of procedures for locating the robot end-effectors in a global coordinate frame. Coordination within the μ^3 system is accomplished by expressing the local coordinate frames attached to robots M_1 and M_3 in a common frame, attached to the end-effector frame of robot M_2. In a typical calibration sequence, each manipulator is commanded to several locations and the actual 3D positions are calculated using a vision system. From these two sets of values (commanded position and actual position) a mapping can be derived by doing constrained least-squares fit on the data. The number of data points should be sufficient to bring the variance of the pose estimate below the robot repeatability.

In [29], series of 12 microparts have been assembled successively after calibrating the robotic station. Assembly yield was 100% (12 out of 12) in this case. Figure 1.21 shows the robotic station and the results of the successful assembly of these 12 microparts with a 100% yield.

Example 2 - Automated microassembly using active microgripper with vision feedback: An active microgripper has been used to perform automated microassembly of microparts using vision feedback in [161]. In this work, visual servoing has been used to automate 3D microassembly of microparts. An active Microrobotic Microprehensile On Chip (MMOC) gripper [118] (Figure 1.22-(b)) developed in the department AS2M of FEMTO-ST Institute is used for the handling of the microparts shown in Figure 1.22b. The robotic station SAMMI (Systèmes Automatisés de Micromanipulation et Micro-Assemblage) was used to perform the microassembly. SAMMI station is a 5-DOF robotic station (3 translational axis and 2 rotation axis). The microparts to handle or assemble consist of three dimensions silicon components (Figure 1.22)-(b).

The interest of the work done in [161] was to perform high precise micromanipulation and microassembly processes using vision feedback control. The vision system delivers images

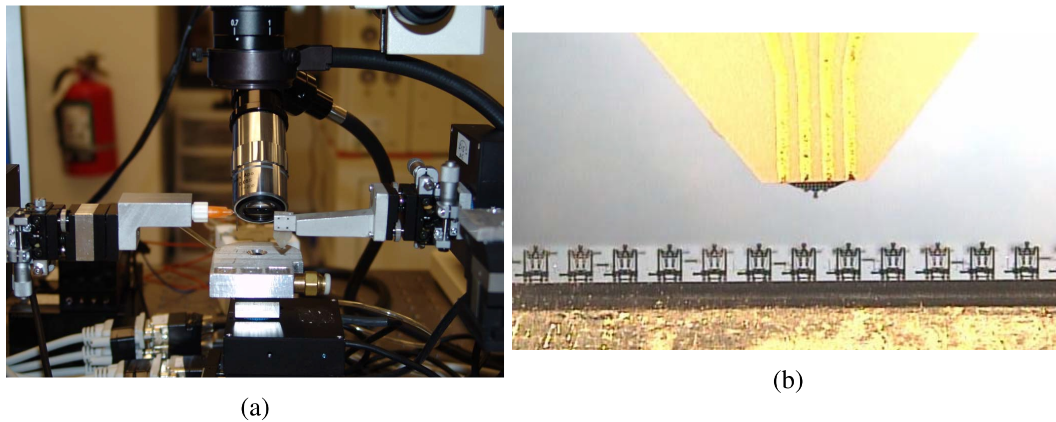

(a) (b)

FIGURE 1.21: (a) The robotic station of the system and (b) the results of the automated open loop microassembly of 12 microparts using a passive microgripper (*jammer*) and calibrating the robotic station.

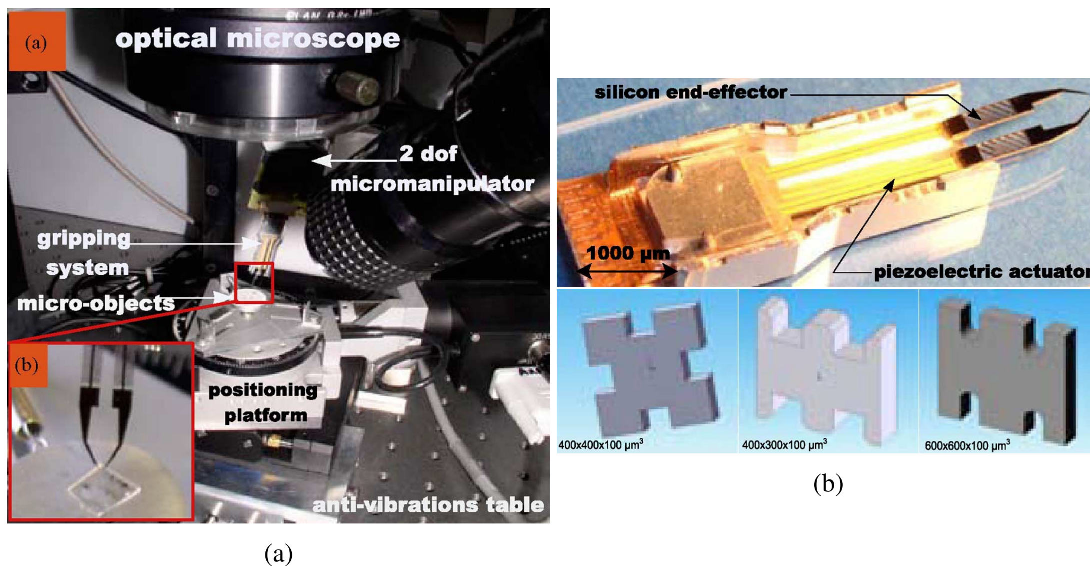

(a) (b)

FIGURE 1.22: (a) Microaasembly robotic station illustrating the global view of the station and the zooming view in the MMOC and (b) the complete view of the MMOC and the microparts used for the microassembly [161].

from which a lot of information can be extracted. The problem is that high-resolution (local view) and low-resolution (global view) information must be caught at the same time. A multiple scale imaging using a photon video microscope equipped with a tunable zoom has been used to perform visual servoing.

The desire to achieve automated complex microassemblies leads to its decomposition into a set of basic tasks like orientation, positioning, centering, gripping, transferring, inserting and releasing of the micro-object. Full-automatic pick-and-place cycles and assembly of silicon microparts have been achieved based on CAD model tracking of the component through vision. The tasks were performed with a positioning accuracy of 1.4 µm and an orientation accuracy of 0.5°. The steps of the automated microassembly and the result of 3D complex microassembly are presented in Figure 1.23

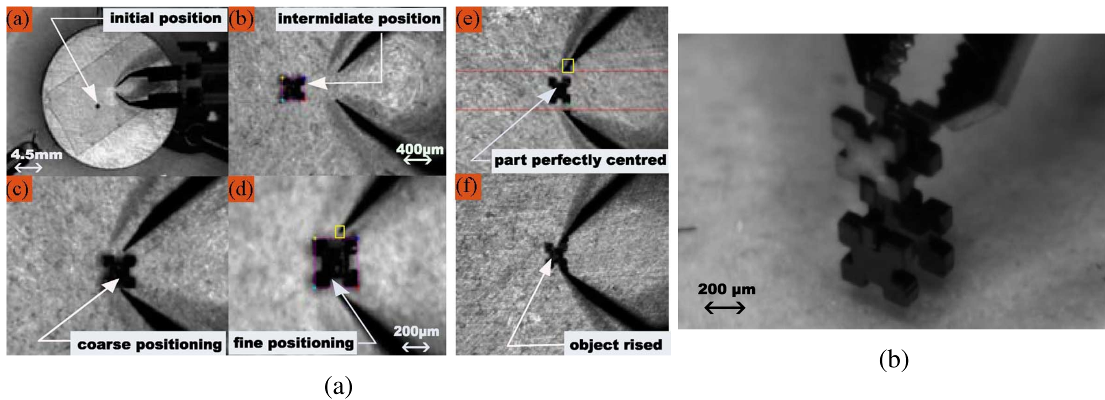

FIGURE 1.23: (a) Some shots during the different microassembly steps and (b) zooming picture of the complex 3-D structure assembled [161].

Example 3 - Automated multiprobe microassembly with vision feedback: An automated multiprobe microassembly using vision feedback has been presented in [178]. 3D structures are constructed by the assembly of planar microfabricated microparts. Instead of using grippers, multiple sharp-tipped probes are coordinated to manipulate parts by using vision feedback. Machine vision with multiple cameras is used to guide the motion. Grasp force control is also used in the microassembly using vision force sensing of the probe bending. The use of multi-probe enables the grasping, rotation, insertion and releasing of multiple shapes and dimensions microparts. Two probes are used to grasp the microparts and the third probe is used for out-of-plane rotation.

Since multiple cameras and probes are used, several calibration processes are required for the parameters identification in the system including experimental force calibration. Intrinsic parameters of each camera (*e.g.* focal length), extrinsic parameters of the cameras (position and orientation relative to some reference frame), kinematics of the die stage, and kinematics of the probe stages are notably considered. After the calibration of the cameras and the probes, the micropart is centered between the two probes and the grasping, rotation, insertion and releasing tasks are studied and performed automatically by vision-based motion and force control. The manipulated parts are as small as 200 µm × 100 µm × 25 µm up to approximately 1 mm × 1 mm × 25 µm. Figure 1.24 shows the robotic microassembly station used in this work and some

shots during the microassembly process showing the automated sequence of the microassembly including the centering, the grasping, the rotation , the alignment and the insertion of the part.

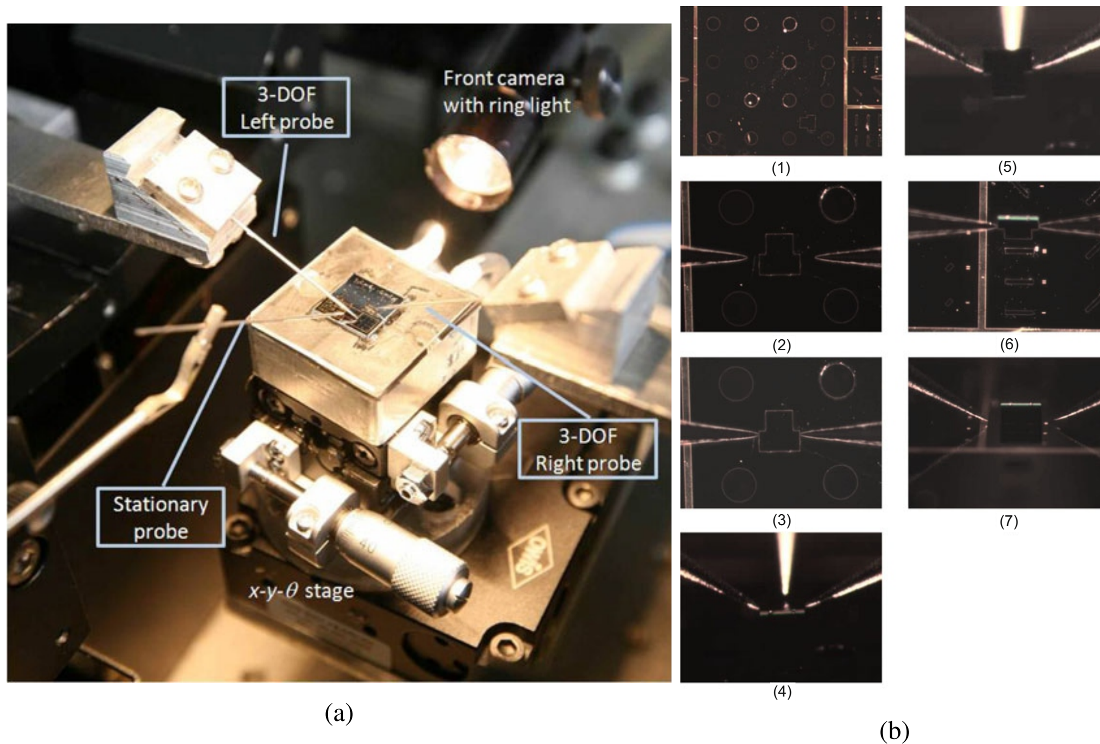

(a) (b)

FIGURE 1.24: (a) Closeup view of the robotic microassembly station, (b) (1) Initial part position, (2) Part rotated and probes moved close to part, (3) Probes gripping part after automated sequence, (4) Part at start of out of plane rotation, (5) Part after out of plane rotation, (6) Part and slot prealigned, (7) Part inserted [178].

Example 4 - Use of two AFM cantilevers with vision and force measurement for the micromanipulation: The use of AFM cantilevers for micro/nano-manipulation enables to take into consideration some microscale specificities. A work for the microassembly using the AFM cantilevers has been achieved in [186] in the ISIR (Institut des Systèmes Intelligents et de Robotique) institute. 3D automated micromanipulation microspheres with diameters from 3 μm to 4 μm using a nanotip gripper with multi-feedback is presented. The gripper is constructed from protrudent tips of two individually actuated atomic force microscope cantilevers; each cantilever is equipped with an optical feedback for force estimation. A manipulation protocol allows these two cantilevers to form a gripper to pick and place micro-objects without adhesive-force obstacles in air and with force feedback by optical measurement. Indeed, the grasping force is measured in real-time by measuring the displacement of the cantilever, using the optical measurement, to enable the handling, manipulation and the release of the microspheres. The force measurement is used for force feedback in order to control the interaction between the grip-

per and the microsphere. A robotic station including large coarse positioning systems and fine coarse positioning systems is used with an optical microscope as shown in Figure 1.25.

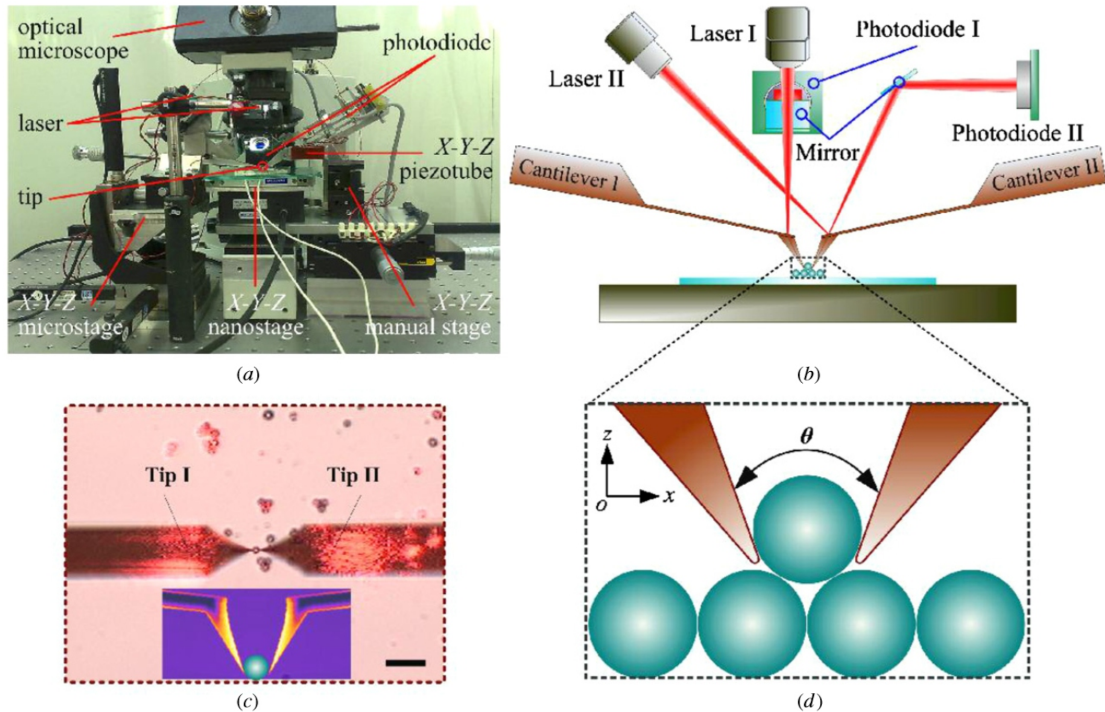

FIGURE 1.25: Structure and manipulation schemes of the 3D Micromanipulation System (3DMS) [186]. (a) A photo of the developed 3DMS. (b) System configuration of the 3DMS, which mainly consists of two sets of devices used in a commercially available AFM, including two cantilevers and the corresponding two sets of nanopositioning devices and optical levers. (c) A microscopic image captured during the pick-up operation of a microsphere using the gripper constructed by tip I and tip II. The bottom inset shows a side view of the pick-and-place scheme with a gripper. The scale bar represents 20 µm. (d) Close-up figure showing the scheme for grasping a microsphere with the nanotip gripper.

The optical measurement enables to locate the microspheres and to planify the trajectory by calculating the shortest path solution to achieve the task with high level of efficiency. In experiments, 20 microspheres with diameters from 3 µm to 4 µmwere manipulated and five 3D micropyramids with two layers were built as shown in Figure 1.26.

1.3.4 Choice of a robotic system for the microassembly

A summary of the existing microassembly techniques is presented in Figure 1.27. The choice of a microassembly technique depends on the application and the microscale specificities. A choice needs to be done for each of the presented classifications (sections 1.3.1, 1.3.2 and 1.3.3) of the microassembly. The choice starts from choosing how many dimensions are needed for

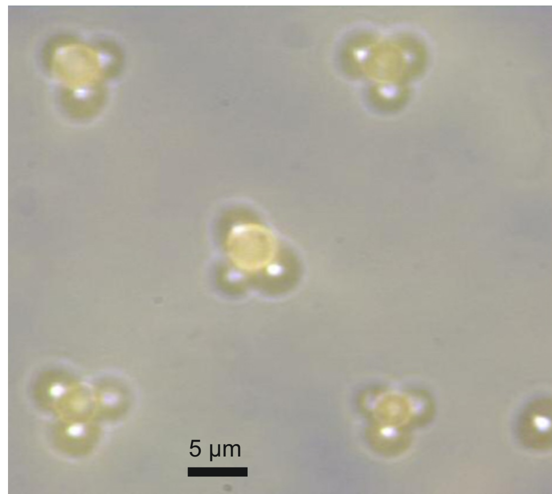

FIGURE 1.26: The 3D microassembly results under magnification of 100× [186].

the microassembly: 2D, 2D½ or 3D. In the needed application, a 3D microassembly is the objective. The dimensions, robot structure, types of end-effectors are elements to be chosen in order to make a choice on a robotic system for the microassembly.

The objective of our work is to perform the assembly of hybrid 3D MOEMS issued from several microfabrication batches processes. The project has been presented in section 1.1.3. The choice of robotic system will be done for each of the presented classifications as follows:

1. Type of end-effectors: the use of non-contact manipulation or self-assembly is interesting because it reduces the effect of contact forces and takes benefit of surface forces. However, its use is limited to 2D or 2D½ microassembly and the ability to perform complex 3D microsystems needs more investigations. The remaining option is the contact manipulation which can be performed by passive or active fingers microgripper. The use of passive finger microgripper has enabled good and high throughput microassembly in [29]. However, its use is limited to the manipulation of the same micropart design without having the possibility to use the same gripper for other microassembly products. Contrary to passive fingers, active fingers have the possibility of using the same microgripper for the manipulation of several types, sizes and dimensions of the microparts (*e.g.* the same microgripper has been used for the microassembly of the examples given in section 1.1.3 and section 1.3.1 for the microgripper using active fingers). Furthermore, the objective of project MIAAMI and MIOP presented in section 1.1.3 is to fabricate reconfigurable MOB (Micro-Optical-Bench). The active-based gripping system allows modification of the holder position on the baseplate with nanometre precision. Thus, modification of the components position on the baseplate can be possible by making the reconfiguration of the complex microsystem easy and reducing manufacturing costs. Consequently, an active gripping system will be used for the microassembly.

2. Throughput of fabrication: the parallel microassembly offers higher throughput and low unit cost due to batch fabrication. However, their use is also limited to 2D or 2D½ microassembly and the ability to perform complex 3D microsystems needs more investigations. Furthermore, as discussed in the parallel microassembly, the uncertainties in the microfabrication processes can reduce the success rate of microcomponents issued from each wafer and by combining the wafers, the success rate of the fabrication can be reduced significantly.

   Another approach to perform parallel microassembly is to build several robotic stations in order to perform several serial microassemblies in parallel. This approach has been used in [121] where 12 jammers have been used in parallel to perform 12 parallel microassembly of the same approach presented in Figure 1.21. Despite the high throughput of this technique, it presents high cost because 12 robotic stations need to be built.

3. The modes of microassembly: the use of manual microassembly is not adapted due to reasons in section 1.3.3. Both teleoperated and automated microassembly are capable of building complex 3D microsystems. However, the teleoperated microassembly requires good dexterity of the human operator and a lot of time to perform each assembly. In addition, in order to increase the precision of the teleoperated microassembly sensors must be integrated to quantify and reduce the errors to improve the precision. If sensors are integrated in the microassembly station, it is more appreciated to perform automated microassembly which reduces the operation time, increase the precision and needs much lower dexterity than teleoperated mode.

To summarize all of the above, automated robotic microassembly is the most adapted in terms of precision, accuracy repeatability and time of the microassembly because the automation of the microassembly tends to improve the performances of the robotic station due to the integration of position or/and force sensor and vision systems which enables the closed loop control of the robotic station. In addition, the use of active gripping offers more flexibility in the design and the assembly of microsystems.

1.4 Towards an automated robotic microassembly of MOEMS using hybrid force/position control

In section 1.3, microassembly techniques were presented and several works dealing with microassembly were presented. The choice of automated robotic microassembly is chosen in order to increase the precision of the microassembly and to reduce the time of each microassembly step. The automated microassembly is also chosen in order to fabricate complex 3D structures using separately fabricated planar microparts. The desired application is proposed by the project MIOP (Microsystems for instrumented optical chips) in FEMTO-ST institute. This project is presented in Section 1.1.3 and Figures 1.5, 1.6 and 1.7. In previous works [10], teleoperated microassembly has been performed and in order to achieve this microassembly, a lot of dexterity of the user is required and a lot of time is needed in order to perform the task. Furthermore, high risks of breaking the microparts and microgripper's end-effectors exist. The objective of

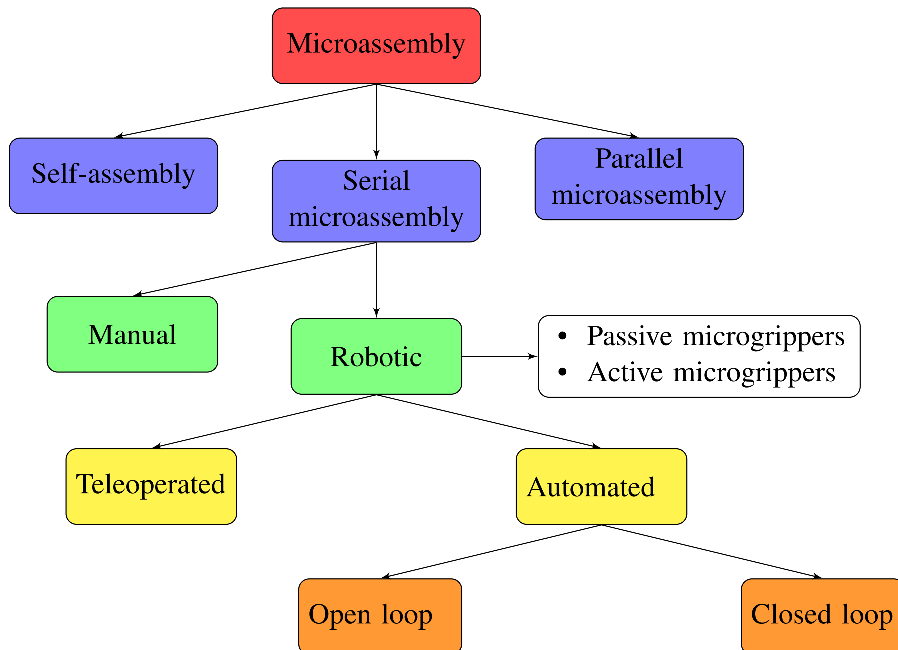

FIGURE 1.27: Summary of microassembly techniques.

the MIOP project is to fabricate RFS-MOB (using the same design of optical components and silicon substrates as presented in Figures 1.5, 1.6 and 1.7) using an easy, reliable and precise process. Thus, an automation of the microassembly process is chosen to increase the precision, to ensure the safety of the microparts and the microgripper, and to improve the dynamic behavior of the system in order to reduce the time duration of the microassembly.

To perform closed-loop automation, integration of sensors is important because it provides additional information to the user in a teleoperated microassembly and to control local forces for automated microassembly. Hence, extensive researches exist on the integration of force sensors into the microassembly robotic station. In the following, the need of integration of force sensors in the robotic station and the interest of using force control for the automation will be justified.

1.4.1 Interest of force control for the assembly of MOEMS

A lot of works exist on the integration of force sensors into the microassembly station. There are two main types of forces which need to be measured in the system:

- Gripping forces which are the forces applied by the gripper's end-effector on the micropart. The importance of their measurement is to guarantee the security of the microparts and the microgripper and to master the manipulation of the micropart by applying a desired force.

- Interaction forces which are the forces generated when a contact between a micropart and the substrate appears. These forces appear during several tasks such as guiding or insertion tasks.

The knowledge of each of the applied forces is an important issue in the microassembly steps in order to master the whole microassembly process and to achieve the task. In addition, at the microscale, due to the predominance of surface forces, measuring the force is an important issue which enables to deal with them and compensate their effects such as pull-off force which has an undesired adhesive effect on the microassembly. Furthermore, due to the very low inertia of the microsystems and the high dynamics, fine and rapid control is required to control the evolution of forces during pick and place steps of the microassembly in order not to loose the microcomponent. In literature, extended researches exist on the integration of force sensors into the robotic microassembly station. Two solutions exist: integration of the force sensor into the substrate [111] or integration of the sensor into the microgripper [12]. The integration of force sensors into the microgripper is more convenient because it offers the possibility of measuring the gripping forces and to estimate the interaction force. The exiting force sensors integrated into microgrippers will be detailed in the chapter 2.

The integration of force sensor into the microassembly station enables to control gripping and interaction forces. Indeed, force measurement and force control have many advantages when it used for the microassembly. They enable to:

- measure surface and contact forces which are predominant at the microscale and consequently to propose a strategy to deal with these forces,
- perform precise force/position modeling of the system and to study the interactions between the microgripper and the micropart,
- understand the gripping system behavior and to switch between free motion control and constrained motion control of the microgripper,
- control finely and rapidly gripping forces which enables to obtain stable and reliable grasping and to guarantee the safety of both the micropart and the microgripper by setting a desired force which is calculated in function of the application to secure the gripping task and the manipulation without loosing the micropart,
- detect if a contact appears between the micropart and the substrate or any perturbation contact,
- detect the side and the value of contact if the two fingers of the microgripper are sensitized.

Issues relevant to robot force control at the macroscale are well known due to extensive research conducted in the 80s and 90s. Several classic control schemes have been developed including explicit force control [173], admittance control [140], impedance control [64], and hybrid force/position control [129]. Recently, with the advance on the microassembly techniques, several researches have paid attention to the importance of force control at the microscale and have used force control for automated microassembly [142, 100, 186, 198, 178, 85]. Other works deal with the force control for the micromanipulation [191, 15, 84]. However, none

of the past works have performed a comparative study of the force control techniques in order to determine whether the microscale physics require to adapt or propose new force control schemes.

1.4.2 Automated microassembly of MOEMS using hybrid force/position control

In order to perform successful precise positioning for the microassembly, force control laws are not sufficient. Position sensors and position control is also needed in order to succeed the task. Thus several control technique have been proposed in order to combine both the force and position in the same control law taking benefit of both control laws including hybrid force/position control, impedance control, admittance control and stiffness control. The hybrid force/position control enables to select some robot axes to be controlled in position and the others are controlled in force. The impedance control, admittance control and stiffness control consider both the position and the force for the same axes by setting a desired relation between the position and the force. The relation can be dynamic as in impedance control and admittance control, or quasi-static as in stiffness control.

1.5 Conclusion

In this chapter, the MOEMS and their fabrication were presented as well as some of their applications covering both research and commercial interests. Works done at the research level clearly show the feasibility to assemble complex MOEMS products. The predominance of microscale specificities has also been noticed and induce many trade-off, specific strategies or performances limitations. Notably, very few works deal with automated assembly of complex tasks based on closed loop control whereas its great interest (to overcome NL behaviors, high influence of environmental conditions, very low inertia inducing difficulties to obtain stable and reliable grasping of components, etc). Several microassembly techniques exist to overcome the challenges and they were detailed and some examples and applications of several research teams using different microassembly techniques were given. The integration of force sensors into the microassembly station is of great interest because it provides a local feedback (at contacts) that cannot be predicted through models. Nevertheless, the question of integrating force sensors with sufficient performances is also a complex challenge. Researches dealing with force control at the microscale show the significance of controlling the forces which are predominant at this scale in order to perform dexterous manipulation of the micropart.

Using the state of the art study performed in this chapter around the microassembly techniques for the fabrication of microsystems, automated robotic serial microassembly technique using an active microgripper with force feedback has been chosen allowing the microassembly of MOEMS. Hybrid force/position control enables to position of the micropart in its desired position while controlling the interaction forces. The full automation of the microassembly using an active microgripper with force feedback and hybrid force/position control which will be the final objective of this PhD.

Chapter 2

Piezoresistive Force Sensor for Microscale Applications

In this chapter, the state of the art of microforce sensors integrated in microgrippers is presented showing the lack of powerful and high sensitive sensors integrated in microgrippers. A piezoresistive force sensing principle is adopted for its design according to required specifications. Then, a novel piezoresistive force sensor is presented in this chapter and its prototyping through clean room microfabrication is proposed. Finally, performances of the force sensor are quantified through several experimental set-ups and analyzed.

2.1 Introduction

Sensors are necessary in order to measure local information (especially at contact), to understand systems behaviors and to control them. This need is all the more important at the microscale because of the predominance of surface and contact forces and the high dynamics of microsystems and notably force measurement. Force measurement is used in many applications such as biology [103, 63], biomedical [106], microgrippers [2], microassembly [10], micromanipulation [133], etc. Integrating force sensors in microsystems may improve and facilitate the tasks by providing a force feedback which enables force control of the system [85, 84]. Measuring the force at the microscale not only requires to integrate the sensors on or inside the system itself but also to perform measurement the closest to the area of interest [24]. This avoids measuring perturbations, reduces the consequences of parameter variations of the system and reduces the noise which are predominant factors at the microscale [16].

Furthermore, the sensor should be able to measure forces present and predominant at the microscale such as surface forces, van der Waals forces, capillary forces, contact forces, manipulation forces, etc. These forces are in the range of hundreds of nN up to several hundreds of μN [19, 128, 85, 127].

However, few solutions exist to fabricate a force sensor in this measuring range and most of the works present force sensors which are difficult to be integrated. The lack of works is essen-

tially due to the design constraints, sensor's performances required (size, resolution, dynamics, microfabrication aspects, etc) and the need of multidisciplinary skills (design, simulation, microfabrication, electronics, characterization, etc).

Thus, the aim of this chapter is to propose a force sensor which can be integrated on each of the tip of the 2 fingers of the 4-DOF piezoelectric actuator presented in [31]. The force sensor should be able to measure and produce forces to manipulate objects at the microscale and in particularly the objects presented in Figure 2.1. The following specifications should be considered for the design of the force sensor:

- **Size of the force sensor:**
  The size of the force sensor should be small enough to be integrated into a microgripper but also to perform measurement the closest to the area of interest. The application, chosen as case of study, also induces some design constraints, notably the gap between the figers of the microgripper and the size of the tip to each microgrippers finger (that has to be inserted into very small appertures of the holder to achieve its manipulation.) Consequently, the dimensions of the force sensor are fixed to be smaller than 1000 µm $\times$ 100 µm $\times$ 20 µm.

- **Sensor's resolution and sensing range:**
  The sensor should be able to measure forces present at the microscale to succeed in taking them into account for both control and assembly purpose. As already discussed, these forces are in the range of hundreds of nN up to hundreds of μN which fixes the resolution of the force sensor to be in the range of hundreds of nN. Moreover, forces up to 1 mN have to be applied to the springs of the holder to enable its grasping (linked with the stiffness of holders spring that has been chosen to ensure a "good" mechanical stability of the holder onto the baseplate once assembled). These forces are in the same range of the forces met in [127, 85]. Consequently, the sensing range of the force sensor is fixed to between hundreds of nN and several mN.

- **Dynamics of the force sensor:**
  The bandwidth of the force sensor is important in order to measure and control both static and dynamic forces. This is important especially for microsystems which have small inertia and big accelerations. These big accelerations can lead to loose the micropart if the evolution of the force is not dynamically controlled. Thus, the bandwidth of the force sensor should be bigger than the bandwidth of the actuator to have measurement faster than actuation and consequently to have good force control performances. The bandwidth of the piezoelectric actuator to be used is 1 kHz. Consequently, the bandwidth of the force sensor is fixed to be bigger than 5 kHz (*i.e.* five times bigger than the dynamics of the actuator).

- **Microfabrication process:**
  The aim is to fabricate the force sensor with a low cost and simple microfabrication process in order to be able to integrate the force sensor in any microsystems without adding complex fabrication processes.

In order to propose a design and the microfabrication process of the force sensor, some force sensing techniques will be presented, in this chapter, showing the advantages and the drawbacks of each technique, then a design and a fabrication process are proposed. Finally, the calibration of the force sensor is performed.

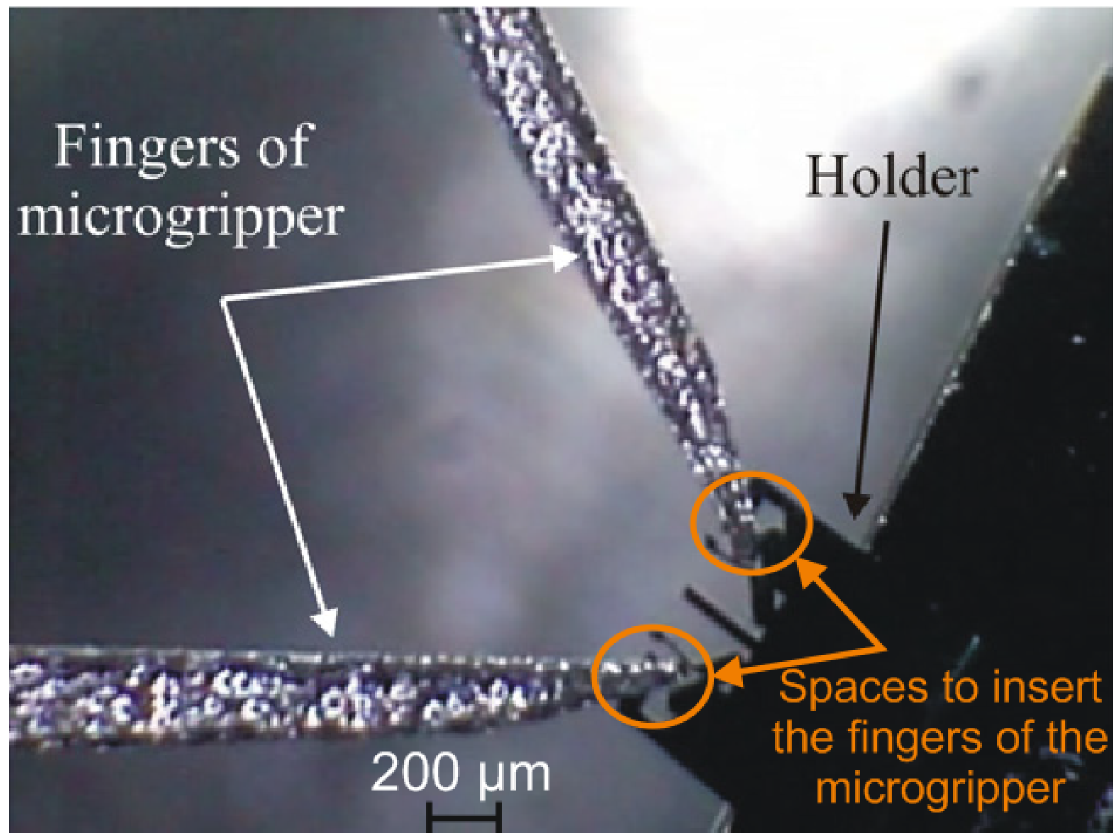

FIGURE 2.1: Manipulation of the holder (presented in chapter 1 section 1.1.3) from the flexible part and showing the small gap of the holder where the microgripper fingers should be inserted to perform manipulation of the holder.

2.2 Force sensors integrated in microgrippers

Several force sensing principles exist in literature: capacitive, thermal, piezoelectric and piezoresistive. Many of these sensing principles have been used to fabricate integrated force sensors into microgrippers in the past years. In this section, force sensing principles will be briefly presented and compared.

2.2.1 Non contact force measurement techniques

Several techniques exist for measuring the forces without any contact between the sensor and the object where the force measurement is required notably: vision feedback, optical sensors and observers.

- **Vision feedback**
  In this technique, a camera is used to measure the displacement of a compliant structure and the force is calculated by the relation $F = K\delta$, where K is the stiffness of the structure, δ is the measured displacement and F is estimated force. This technique requires a precise knowledge on the stiffness of the structure which is not so easy at the microscale due to the change of the stiffness caused by the environmental changes. This measuring technique is attractive since it overcomes a major challenge in microrobotics which is the limited space available for the actuation and measurement function. This solution is less cumbersome and less expensive. Thus, it is used for many microscale applications such as the automation of the assembly [178, 18] and sensing the gripping forces [136].
  However, performing dynamic force measurement using vision feedback is a challenge due to the lack of the high speed acquisition cameras and the need of adding a deformable structure int the system which reduces its dynamics. In addition, it is difficult to detect precisely, using pure vision feedback, the contact between the microgripper and the object to be manipulated.

- **Optical sensors**
  Similarly to the vision feedback, optical sensors measure the displacement of a compliant structure by measuring the variation in the intensity of an incident laser beam and then deduce the force knowing the stiffness of the structure. This technique enables precise dynamic position measurement. This method has been used in [186] to measure the displacement of atomic force microscope cantilever through optical measurement and has shown interesting results for measuring the forces with high dynamics. However, knowing the precise stiffness is also a challenge for this technique. In addition, the high cost and big size of laser sensors (such as laser sensors from Keyence and laser interferometer from SIOS Meβtechnik GmbH) increase the difficulty of their integration in the robotic station due to the limited space available in the zone of operation.

2.2.2 Thermal Force sensing technique

Thermal sensing technique is used for many applications including the sensing of displacement [203], force [119], acceleration [202] etc. It consists in measuring the temperature change in the sensor using three different principles: thermal bi-morph sensors, thermocouples and thermal resistive sensors. This sensing technique is used for many applications

The thermal sensors are used due to their small size, simple structure and low fabrication cost. Despite these facts, thermal force sensors are not widely used and particularly they are not integrated into microgrippers in many works. The main limitation of thermal sensors are notably their dynamic behavior and slow response. A work on the integration of a thermal force sensor with an electrostatic actuator is presented in [119] where one finger of the microgripper

is actuated via an electrostatic actuator and the other finger is a passive finger with force estimation based on thermal sensing. Figure 2.2 shows the microgripper developed in [119] where it can be shown that the thermal sensor is much smaller than comb drive used for electrostatic actuation. The sensor is composed of a sink plate and two electrically biased identical silicon beams. The simplified sensor model is shown in Figure 2.2-(b). At the rest position, a DC bias voltage is applied across the beams. While at rest, the heat fluxes out of the beam resistors are identical. Thus, the temperature and resistances of the two sensors are identical. Once the sensing arm experiences the gripping force, it moves and forces the sink plate to move toward right. The resulting difference in heat flux generates a difference between the resistances R_1 and R_2. This differential change in resistance results in a current variations between the two heaters. With a half Wheatstone bridge and an instrumentation amplifier, the current variations are then converted to an output voltage.

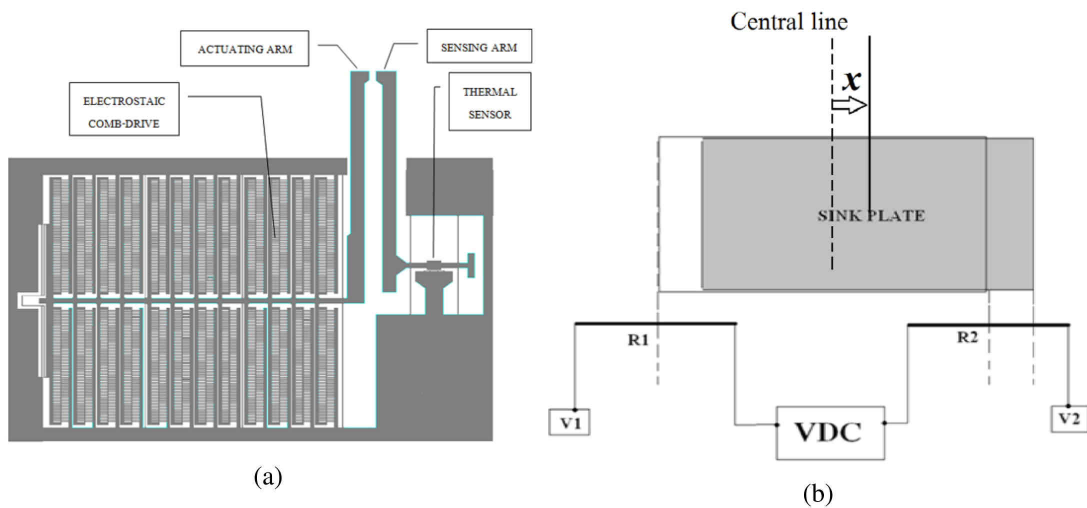

FIGURE 2.2: (a) The structure of a MEMS Micro-gripper presented in [119], (b) a simplified sensor model as presented in [119].

2.2.3 Electrostatic sensing

A capacitor is defined as two parallel conductor plates, that can hold opposite charges, separated by a dielectric as shown in Figure 2.3. In electrostatic force sensor, one of the two plates is fixed and the other is fixed on a compliant structure and thus move. Its behavior may be modeled by a mass-spring-damper system. In quasi-static approach, the second plate can move accordingly to a spring with a stiffness k:

$$F = k \cdot \Delta x \tag{2.1}$$

where F is the force applied to the mobile plate, k is the stiffness of the deformable system and Δx is the displacement at the point where the force is applied. The capacitance of the two

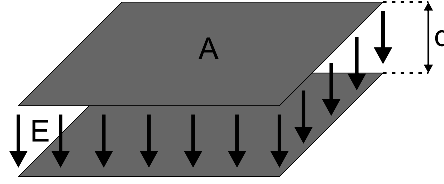

FIGURE 2.3: Parallel plate capacitor.

parallel plates can be calculated as:

$$C = n\varepsilon_0 \cdot \varepsilon_r \cdot \frac{A}{d} \tag{2.2}$$

where n is the number of capacitors, ε_0 is the vacuum permittivity ($\varepsilon_0 \approx 8.854 \times 10^{-12}$F.m^{-1}), ε_r is the relative permittivity of the material between the plates, A is the overlapping area of the plates and d is the thickness of the gap between the plates. Two parallel plates can move with respect to each other in two ways: normal displacement or parallel sliding displacement. The first displacement changes the gap between the plates while the second displacement changes the overlapping area and both of the displacements induce change in the capacitance. However, changing the size of the gap induces higher sensitivity for small displacements than changing the area of overlap [45].

A specific electronic circuit can be used in order to measure the capacitance variation (such as MS3110 or SWS1130). Using this circuit, and considering an electrostatic force sensor with plate dimensions are 400 µm in length, 50 µm in width and 5 µm as initial gap between the two plates, the capacitance variation can reach 3.54 pF for $n = 100$ capacitors. This value of capacitance change can be measured by the MS3110 circuit which can measure the capacitance variation between 0.25 and 10 pF.

To increase the linearity and to improve the sensitivity of the sensor, double (or more) differential capacitors can be used such as the capacitor shown in Figure 2.4. In this case, the mobile electrode lies between two fixed electrodes, so that at equilibrium $e_1 = e_2 = e$. The capacitances at the equilibrium are then $C_1 = C_2 = C_0 = \varepsilon_0 \cdot \varepsilon_r \cdot \frac{A}{e}$. Once the mobile electrode moves, the mobile electrode forms two capacitors, one with each of the two fixed electrodes:

$$\begin{aligned} C_1 &= \frac{\varepsilon_0\varepsilon_r A}{e - \Delta x} = \frac{\varepsilon_0\varepsilon_r A}{e} \cdot \frac{1}{1 - \frac{\Delta x}{e}} = C_0 \cdot \frac{1}{1 - \frac{\Delta x}{e}} \\ C_2 &= \frac{\varepsilon_0\varepsilon_r A}{e + \Delta x} = \frac{\varepsilon_0\varepsilon_r A}{e} \cdot \frac{1}{1 + \frac{\Delta x}{e}} = C_0 \cdot \frac{1}{1 + \frac{\Delta x}{e}} \end{aligned} \tag{2.3}$$

In practice, such devices consist of interdigitated combs with variable spacing, micromachined in silicon, which act as capacitors, or even double differential capacitors [48, 159, 158, 156]. The force acting on the mobile part of the comb produces a movement in the mobile arm, leading to a change in the capacitances.

This principle of force measurement may be used to integrate the force sensor into micro-grippers. Indeed, 1-D electrostatic force sensors have been integrated monolithically with an electrothermal actuator in [81, 157] and with an electrostatic actuator in [12, 90] in order to

fabricate a microgripper with integrated force sensors. However in these cases, one arm of the gripper is active and the other one is passive with force sensor.

The measurement ranges of such devices are of the order of milliNewton, with a high resolution. These devices are relatively large, but incorporate multiple capacitors (a single comb has an area of the order of $170 \times 500\ \mu m^2$ [48]) which can be used to measure two axes of force. Although conceptually simple, the implementation of this design requires sophisticated microfabrication resources.

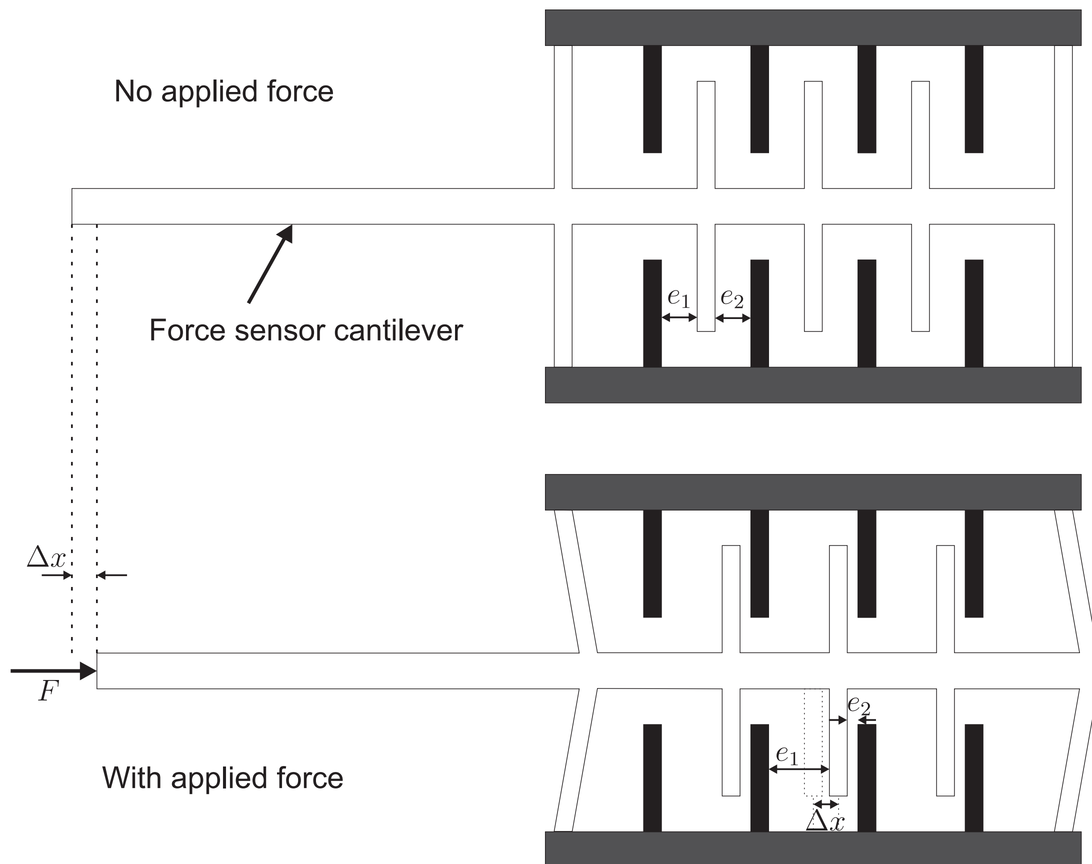

FIGURE 2.4: Differential capacitors used in electrostatic sensors.

Figure 2.5 shows some examples of microgrippers with integrated capacitive force sensors.

2.2.4 Piezoelectric sensing

The piezoelectric materials are used to fabricate actuators and sensors. The piezoelectric sensors use **direct effect of piezoelectricity** to generate an electric charge (or voltage) while the sensor is under a mechanical stress, where the piezoelectric actuators use the **indirect effect**

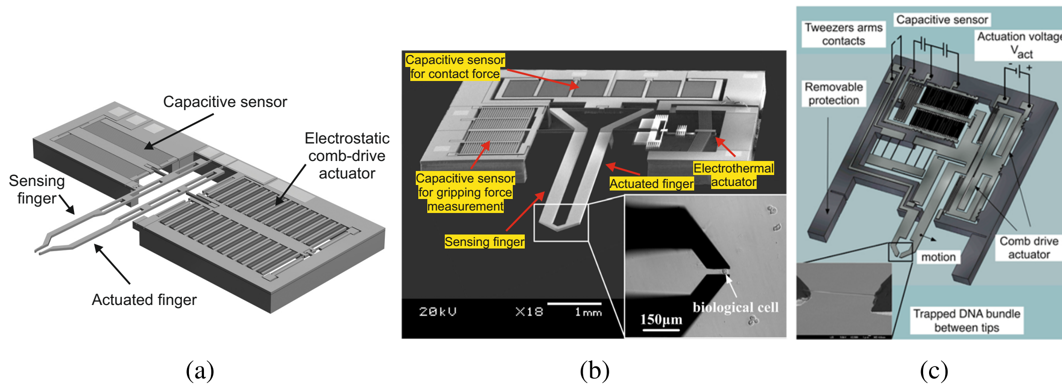

(a) (b) (c)

FIGURE 2.5: Examples of microgrippers with integrated capacitive force sensors: (a) Microgripper from FemtoTools [54] showing one capacitive sensing finger and one electrostatic comb-drive based actuated finger, (b) Microgripper presented in [81] showing two axis capacitive sensors and one electrothermal actuated finger, (c) Microgripper presented in [90] showing one electrostatic based sensing finger and one electrostatic based actuated finger.

of piezoelectricity to produce a mechanical deformation (or force) when an electric field is applied.

In a piezoelectric crystal, the direct effect of piezoelectricity can be described by the following general constitutive equation that relates electric displacement field (D) and the applied mechanical stress (T):

$$D = dT + \varepsilon E \tag{2.4}$$

where d is the piezoelectric coefficient matrix, ε is the electrical permittivity matrix and E is the electrical field. In most of the cases, no electric field is present (i.e., $E = 0$) and consequently the second term of the right hand side of Equation (2.4) can be eliminated.

The working principle is simple, where an applied force induces a stress to the force sensor and the stress generates a proportional voltage on the output of the force sensor according to Equation (2.4). However, in practice, the stress and the voltage relation is nonlinear. Thus, the relation between the stress and the electric charge is considered in order to measure the applied force and the charge is converted into voltage using charge amplifiers.

Piezoelectric force sensors are used to measure forces for some microscale applications like the micro-assembly in [143] and the scanning force microscopy [68]. In addition, they are integrated with actuators in [69, 89]. The long-term electric charge leakage across the material and the complex fabrication process are some drawbacks of this force sensing technique.

Piezoelectric sensors have a good dynamic behavior which is of high interest for many applications. However, their use in static mode is limited due to their relative poor DC response caused by the electric leakage across the material and the nonlinear behavior of materials. In addition, the fabrication of piezoelectric force sensors are relatively complex.

Another sensing technique which is compatible only with piezoelectric actuators is the piezoelectric self-sensing technique. Self-sensing consists of using at the same time an actuator as a sensor. This is particularly achievable for piezoelectric actuators thanks to the direct

and indirect piezoelectric effects. This simple and cost effective solution for existing piezoelectric actuators allows actuating a piezoelectric actuator while sensing its displacement (strain) and/or applied force (stress).

This technique has been used to measure the displacement and the force applied on a piezoelectric actuator in [7, 70] in order to integrate it into a piezoelectric microgripper.

The limitations of this sensing technique consist in the long term charge leaking, the temperature influence, the need of nonlinear compensation of the hysteresis and the creep and the need of an additional electronic circuit.

2.2.5 Piezoresistive sensors

The piezoresistive force sensing technique uses the piezoresistive effect induced by the resistance change according to the deformation of a compliant structure. The piezoresistive sensors are widely used in many applications due to their small scale, easy integration, convenient readout method and high measurement dynamics. They are widely used as sensing elements in pressure sensors [176], accelerometers [65], flow sensors [95], Atomic Force Microscopy (AFM) [167].

The resistance value, R, of a resistor is given by:

$$R = \rho \frac{L}{A} \tag{2.5}$$

where ρ is the bulk resistivity, L is the length of the resistor and A is the cross section area of the resistor. The resistance value depends on the bulk resistivity and the dimensions of the resistor. Consequently, there are two ways to change the resistance value of a resistor by applying strain. The first by changing the length or the cross section area of the resistor due to the applied strain. The second by changing the resistivity of some materials as a function of the applied strain. The magnitude of resistance change from the second principle is much greater than what is achievable from the first one. By definition, piezoresistors refer to resistors whose resistivity changes with applied strain [97].

The resistance change can be expressed by the logarithmic derivative of Equation (2.5) as follows:

$$\frac{\Delta R}{R} = \frac{\Delta L}{L} - \frac{\Delta A}{A} + \frac{\Delta \rho}{\rho} \tag{2.6}$$

where ΔL is the increased length, ΔA is the decreased area and $\Delta \rho$ is the change in resistivity. The piezoresistive effect can be expressed as follows:

$$\frac{\Delta \rho}{\rho} = C\frac{\Delta V}{V} = C\left(\frac{\Delta L}{L} + \frac{\Delta A}{A}\right) \tag{2.7}$$

where C is the Bridgman's constant and V is the volume. Replacing Equation (2.7) in Equation (2.6), the following can be deduced:

$$\frac{\Delta R}{R} = (1+C)\frac{\Delta L}{L} + (C-1)\frac{\Delta A}{A} \tag{2.8}$$

Due to Poisson's effect, the following can be deduced:

$$\frac{\Delta A}{A} = -2\nu\frac{\Delta L}{L} \tag{2.9}$$

where ν is the Poisson coefficient. Replacing Equation (2.9) in Equation (2.8), the resistance change can be expressed as follows:

$$\frac{\Delta R}{R} = G\cdot\varepsilon \qquad \text{where} \qquad G = 1 + C + 2\nu\,(1-C) \tag{2.10}$$

where $\varepsilon = \frac{\Delta L}{L}$ is the applied strain. The proportional constant G is called the **gauge factor** of the piezoresistor and it determines the sensitivity of the force sensor (*i.e.* the sensitivity increases with the gauge factor G).

There are several approaches for fabricating piezoresistive force sensors with high performances. Some piezoresistive force sensor using metal materials are presented in [183, 96], and others using silicon are presented in [180, 41, 110]. Metal gauges are mainly sensitive to changes in geometry (C is close to 1 leading to G near to 2 according to Equation (2.10)) [72] and silicon strain gauges have a large piezoresistive effect (C is big leading to $G > 100$) [163]. Thus, the latter are commonly used for the fabrication of microforce sensors.

Wheatstone bridge circuit and instrumentation amplifier are usually used to measure the resistance variation of the sensor by balancing the two legs of the bridge circuit and the force is measured by detecting the voltage difference between the two center points of each leg.

The piezoresistors could have very small dimensions such as in [180] where the fabricated beams are 5 µm long, 500 nm wide and 500 nm thick. Good dynamic behavior can be reached and resonant frequencies up to 100 kHz have been fabricated in [41]. High sensitivity and resolution up to pN can be reached using piezoresistive force sensors [41]. In addition, the fabrication process of the piezoresistive force sensor is relatively simple which enables a flexibility in the design to integrate the strain gauges inside the system. However, piezoresistive force sensors are mainly sensitive to environmental temperature changes.

In the past years, many piezoresistive force sensors have been integrated into microgrippers and AFM cantilevers. Most of the microgrippers with integrated piezoresistive force sensors compromise two-sensing-fingers microgripper. Force and positions piezoresistive sensors have been presented to be integrated in a microgripper in [181] with a force resolution of 1 µN and a sensing force range of 1 mN. Microgripping force measuring device based on SU-8 microcantilever sensor with very low stiffness of the sensor is presented in [197] where the sensing range is 405 µN. Piezoresistive force sensors have been integrated in electrothermal actuators in [110, 43] and in piezoelectric actuators in [175]. The main limitation of the integration of the piezoresistive force sensors in electrothermal actuator is the temperature dependance of the force sensor due to the temperature change during to the actuation of the actuator. Another limitation is the lack of precise models to study the performance of the electrothermal actuators which increases the complexity of control. In [175, 191], piezoelectric actuators with strain gauges force sensors are presented. Relative big strain gauges are used to measure forces (dimensions 11.6 mm $\times$ 8 mm in [175]) which enable the measurement of big forces (up to hundreds of mN) with resolution bigger than hundreds of µN.

Reference	Force Sensor	Actuation	Description
[119]	Thermal	Electrostatic	One finger actuated and the other is passive with force sensor
[12]	Capacitive	Electrostatic	One finger actuated and the other is passive with force sensor
[81]	Capacitive	Electrothermal	One finger actuated and the other is passive with force sensor
[175]	Piezoresistive	Piezoelectric	Two sensing and actuated fingers
[181]	Piezoresistive	Not presented	Two sensing fingers
This work	Piezoresistive	Piezoelectric	Two sensing and actuated fingers

TABLE 2.1: Comparison of different microgripper designs.

2.2.6 Choice of the force sensing principle

After presenting the sensor's specifications and detailing some of the force sensing techniques and their use in microgrippers, the characteristics of each force sensing technique are compared, in this section, in order to choose the sensing technique to be used to fabricate and integrate the force sensor into a microgripper.

First, Table 2.1 presents some of the existing microgrippers with integrated force sensors and a brief description of the operation technique of the microgrippers. In the existing works where thermal and capacitive sensors are integrated in the microgripper [119, 12, 81, 54, 157], one finger of the gripper is active and the other finger is passive with force sensor. While the works where piezoresistive force sensors are integrated in the microgripper [175, 191, 181] or using the piezoelectric self-sensing technique [70], both fingers are active and sensitized with force or/and position sensors. Thus, integrating piezoresistive force sensors enables to use two active fingers with sensitized force sensors. Indeed, in this work, the aim is to manipulate objects presented in Figure 2.1 where the contact between each finger of the microgripper and the holder's springs is independent from the other. Consequently, the forces applied by each finger on the spring of the holder is different from the other and need to be measured separately. Thus, using piezoresistive force sensors or piezoelectric self-sensing techniques is more adapted to this work.

Secondly, as presented in Section 2.2.3, in order to increase the sensitivity of the capacitive force sensors, many comb drives should be added which increase the size of the comb drive which could reach 3.6 mm $\times$ 2.1 mm $\times$ 0.5 mm [155]. However, the piezoresistive force sensors and the thermal force sensors have smaller size where the size of a piezoresistive force sensor can reach 5 μm $\times$ 500nm $\times$ 500nm [41]. The piezoelectric self-sensing technique needs no additional space for the sensor. Consequently, in terms of size of the sensor, piezoresistive sensor, thermal sensor and piezoresistive self-sensing are the most adapted to this works.

Thirdly, the sensing ranges of some existing force sensors are compared versus the sensor's resolutions in Figure 2.6 and Table 2.2. This Figure shows that the best resolutions and sensing ranges can be reached using capacitive and piezoresistive force sensors. In the specifications of the desired force sensor, the desired resolution is 100 nN and the force sensor should be able to measure forces up to several mN. Consequently, in terms of resolution and sensing range, the capacitive and the piezoresistive force sensors are the most adapted to this work.

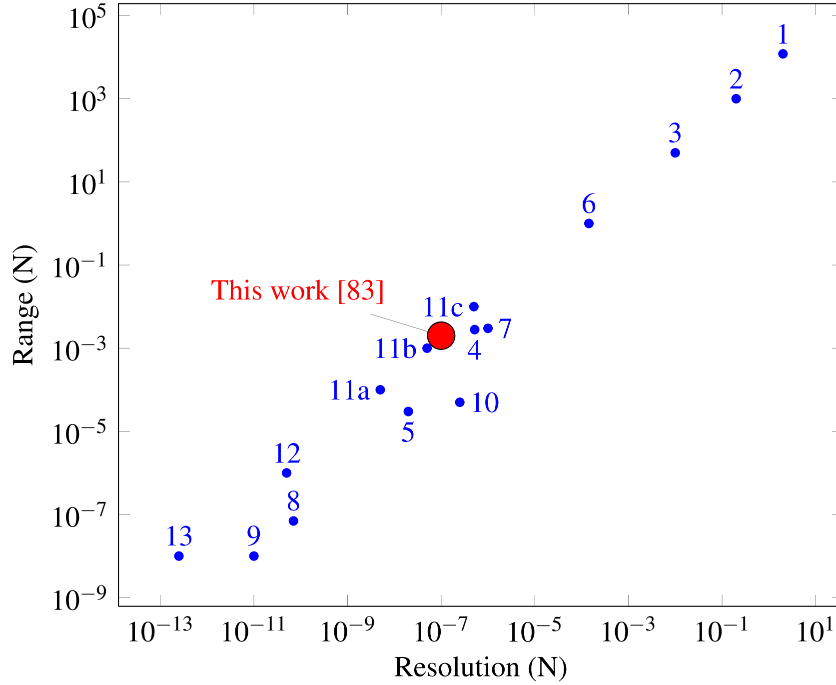

FIGURE 2.6: The range of some existing force sensors versus the resolution. The details of the force sensors are presented in the Table below.

Number	Reference	Description
1	[168]	Truck Weigh
2	[125]	Precision Force Gauge PCE-FG 1K
3	[124]	Precision Force Gauge PGE-FG-50
4	[12]	Capacitive Force Sensor
5	[81]	Capacitive Force Sensor
6	[175]	Piezoresistive Strain Gauges
7	[181]	Integrated Piezoresistive Force Sensor
8	[117]	Integrated Piezoresistive Force Sensor
9	[41]	Integrated Piezoresistive Force Sensor
10	[18]	Vision Based Force Sensor
11a	[54]	FemtoTools Ft-S100
11b		FemtoTools Ft-S1000
11c		FemtoTools Ft-S10000
12	[130]	Optical Measurement
13	[145]	Micropipet Based Force Tranducer

TABLE 2.2: Details of the force sensors presented in the above Figure.

Fourthly, the dynamics of the piezoelectric and piezoresistive force sensors are the best adapted to this work. Indeed, the frequency of the piezoresistive force sensor can reach 100 kHz [41] depending on the size of the force sensor. The capacitive force sensor has an acceptable dynamic behavior and the resonant frequency should be chosen carefully to have a quasi linear performance along the sensing range of the force sensor. The thermal force sensor has relatively slow response and dynamic behavior.

Fifthly, comparing the microfabrication processes to fabricate each type of the force sensor, the piezoelectric self-sensing technique needs no additional fabrication process. However, an effort to implement a supplementary relatively complex electronic circuit needs to be performed in order to be able to measure the force using the self-sensing technique. For the other type of sensing techniques, the piezoresistive force sensors enables the simplest fabrication processes.

Lastly, using all of the above analysis, two techniques are the most adapted to this work: the piezoresistive force sensing technique and the piezoelectric self-sensing technique. For the latter, it is mostly used to measure the displacement of actuator and few works exist on measuring the applied force on a piezoelectric actuator. In addition, the self-sensing technique presents relative poor DC response due to electric leakage across the material. It is influenced by temperature and needs nonlinear compensation of the hysteresis and the creep of the material in order to be applied. These facts increase the difficulty and the reliability of its use for precise force sensing. The advantages and the disadvantages of each of the force sensing technique are summarized in Table 2.3.

Consequently, the piezoresistive force sensing technique is adopted to fabricate the force sensor in the rest of the work. Piezoresistive force sensor with silicon strain gauges will be fabricated due to its high Gauge factor compared to metallic strain gauges.

2.3 Piezoresistive Force Sensor Theory and Design

After choosing the piezoresistive force sensing principle, a design to fabricate the force sensor is proposed in this section.

2.3.1 Working principle of the piezoresistive force sensor

As presented in Section 2.2.5, a piezoresistive force sensor exploits the resistance change according to the deformation of a compliant structure. The resistance change is then converted into voltage using a Wheatstone bridge circuit and an instrumentation amplifier. As shown in Equation (2.10), the resistance change $\left(\frac{\Delta R}{R}\right)$ changes with the applied stress (ε) according to the gauge factor of the material that the strain gauges are made with.

In the following, the study of the piezoresistive sensing technique is done for Silicon strain gauges due to their better sensitivity. For a 3-dimensional anisotropic crystal, the electric field is related to the current-density field by a 3-by-3 resistivity tensor. In piezo crystals, the nine components always reduce to six values arranged in a symmetric tensor [97]:

$$\begin{pmatrix} E_x \\ E_y \\ E_z \end{pmatrix} = \begin{pmatrix} \rho_1 & \rho_6 & \rho_5 \\ \rho_6 & \rho_2 & \rho_4 \\ \rho_5 & \rho_4 & \rho_3 \end{pmatrix} \begin{pmatrix} i_x \\ i_y \\ i_z \end{pmatrix} \tag{2.11}$$

Force sensing technique	Advantages	Disadvantages
Thermal sensing	• Small size • Simple structure • Low fabrication cost	• Slow response and dynamic behavior
Electrostatic Sensing	• Rapid response • High sensitivity achievable	• Big size for comb to provide sufficient capacitance • Complex fabrication process
Piezoelectric Sensing	• Good dynamic behavior • High resolution • Good linearity	• Relative poor DC response due to electric leakage across the material • Complex material growth and process flow • Piezoelectric material cannot sustain high temperature operations
Piezoelectric self-sensing	• Low cost • No integration needed • Same structure is used as actuator and sensor	• Long term charge leakage • Temperature influence • Need of nonlinear compensation of the hysteresis and the creep of the material • Need of a supplementary relatively complex electronic circuit
Piezoresistive Sensing	• Small size • High sensitivity achievable • High resonant frequency • Very good resolution can be reached • Flexibility (gauges can be integrated on many different structures) • Simple fabrication process	• Requires doping of silicon to achieve high performance piezoresistors • Only allowing front-facing surfaces • Sensitive to environmental temperature changes

TABLE 2.3: Comparison between the force sensing techniques.

Direction of strain	Direction of current	Configuration	Piezoresistive coefficient
<100>	<100>	Longitudinal	π_{11}
<100>	<010>	Transverse	π_{12}
<110>	<110>	Longitudinal	$(\pi_{11}+\pi_{12}+\pi_{44})/2$
<110>	$< 1\bar{1}0 >$	Transverse	$(\pi_{11}+\pi_{12}-\pi_{44})/2$
<111>	<111>	Longitudinal	$(\pi_{11}+2\pi_{12}+2\pi_{44})/2$

TABLE 2.4: Formula for transverse and longitudinal gauge factors for various commonly encountered resistor configurations.

In the case of Silicon, if the x, y and z axis are aligned to the <100> crystal axis of Silicon, ρ_1, ρ_2 and ρ_3 define the dependence of the electric field on the current along orthogonal directions; the other components are the cross terms.

The six resistivity components depend on the normal and shear stresses in the material. Under stress-free conditions and with Cartesian coordinates aligned with the material <100> axes, the normal resistivity components are equal, and the cross terms are zero. Thus, under these conditions, the resistivity tensor is isotropic:

$$\rho_{3-\text{by}-3} = \rho_0 \begin{pmatrix} 1 & 0 & 0 \\ 0 & 1 & 0 \\ 0 & 0 & 1 \end{pmatrix} \tag{2.12}$$

where ρ_0 is the isotropic resistivity of the unstressed crystal.

The relative changes in the resistivity can be written as a product of the structural stresses, $[T]$, and the piezoresistance tensor, $[\pi]$, as follows:

$$\frac{1}{\rho_0}\begin{pmatrix} \Delta\rho_1 \\ \Delta\rho_2 \\ \Delta\rho_3 \\ \Delta\rho_4 \\ \Delta\rho_5 \\ \Delta\rho_6 \end{pmatrix} = [\pi]\,[T] = \begin{pmatrix} \pi_{11} & \pi_{12} & \pi_{12} & 0 & 0 & 0 \\ \pi_{12} & \pi_{11} & \pi_{12} & 0 & 0 & 0 \\ \pi_{12} & \pi_{12} & \pi_{11} & 0 & 0 & 0 \\ 0 & 0 & 0 & \pi_{44} & 0 & 0 \\ 0 & 0 & 0 & 0 & \pi_{44} & 0 \\ 0 & 0 & 0 & 0 & 0 & \pi_{44} \end{pmatrix} \begin{pmatrix} \sigma_{xx} \\ \sigma_{yy} \\ \sigma_{zz} \\ \tau_{yz} \\ \tau_{xz} \\ \tau_{xy} \end{pmatrix} \tag{2.13}$$

where σ_{xx}, σ_{yy} and σ_{zz} are three normal stresses, τ_{yz}, τ_{xz} and τ_{xy} are three shear stresses; the π_{ij} are the component of the piezoresistance tensor or also the piezoresistive coefficients. According to this change in the resistivity of the piezoresistor, parameters, ρ_i, in Equation (2.11) change and consequently the current, which goes through the piezoresistor, changes if the electric field is constant by the application of a constant voltage. This current change is converted by a Wheatstone bridge to a voltage change which enables to measure the applied force.

The gauge factor of the piezoresistive force sensor can be calculated using the elements of the piezoresistance tensor and the directions of strain and current as shown in Table 2.4 [77]. The piezoresistive gauge factors attributed to each case in Table 2.4 are determined by multiplying the piezoresistive coefficient with the Young's modulus in the direction of the applied strain. For silicon and using the crystal orientation <110>. Using a p-type doped silicon with resistivity of

7.8 $\Omega \cdot cm$, the piezoresistive coefficient is calculated, using the values defined in [77, 97], by:

$$c_p = \frac{\pi_{11} + \pi_{12} + \pi_{44}}{2} = \frac{(6.6 - 1.1 + 138.1) \times 10^{-11}}{2} = 71.8 \times 10^{-11} \mathrm{Pa}^{-1}$$

The Young modulus of single-crystal silicon is 168 GPa in the <110>, the gauge factor, defined in Equation (2.10), in this orientation is:

$$G = c_p \times E = 71.8 \times 10^{-11} \mathrm{Pa}^{-1} \times 168 \times 10^{9} \mathrm{Pa} = 120.6 \tag{2.14}$$

This high value of gauge factor is the main reason for using silicon for the fabrication of piezoresistive sensors.

2.3.2 Piezoresistive Force Sensor Design

Many force sensors using silicon strain gauges have been developed in the past years including bulk piezoresistors [110] and the deposition of the piezoresistors on the force sensor's structure [181]. The advantage of using the bulk piezoresistive properties of silicon is that the same structure of the force sensor is used to measure the resistance change which simplifies the microfabrication process and enables to integrate the force sensor into many structures without adding complex microfabrication processes. Thus, in this work, a design taking advantage of both mechanical structural properties of the silicon as well as its bulk piezoresistive properties is proposed. In addition, in order to separate electrically the strain gauges, some cavities between the strain gauges are introduced. These cavities have a positive effect on the sensitivity of the force sensor due to the increase of strain generated by these cavities. Figure 2.7 shows the difference of the strain applied on a cantilever without cavities (Figure 2.7-(a)) and with cavities (Figure 2.7-(b)). According to [180], adding a cavity before the strain gauge increases the sensitivity of the sensor due to the amplification of strain in the gauge. Thus, as shown in Figure 2.8-(a), a structure, composed of three parallel beams where the two side beams are sensitive to stresses exerted by the application of a force F_y, is proposed. The strain in this case can be written as:

$$\varepsilon_c = \frac{dL}{L} = c \cdot \varepsilon \tag{2.15}$$

where ε_c is the strain inside the strain gauges after adding cavities (shown in Figure 2.7-b) and c is a constant which adds the effect of adding the cavities and ε is the strain without cavity. Using [180], c is bigger than 1 ($c > 1$) and its value will be determined by simulations in Section 2.4. Using Equations (2.10) and (2.15), the piezoresistive change in the strain gauge resistance after adding cavities is given by:

$$\frac{\Delta R}{R} = c \cdot G \cdot \frac{\Delta L}{L} = c \cdot G \cdot \varepsilon \tag{2.16}$$

Hence, the complete sensitivity of the force sensor is increased by a factor of c relatively to the force sensors with bulk or surface strain gauges.

Figure 2.8 shows the structure of the proposed force sensor and the Wheatstone bridge used to convert the resistance change into voltage. Without applying any force to the tip of the force sensor, the two gauge resistances are identical and equal to R_o. The application of a positive force F_y causes a contraction of the upper beam conducting to the decrease of its resistance

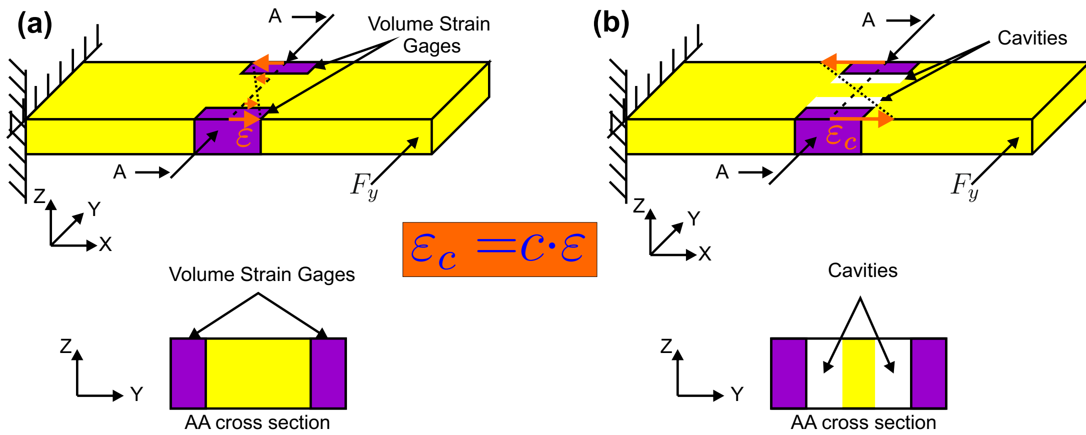

FIGURE 2.7: Strain distribution inside a cantilever with two bulk strain gauges where a force is applied at its tip: (a) no cavity and (b) with cavities.

$(R_o - dR)$, and an extension of the lower beam conducting to the increase of its resistance $(R_o + dR)$. After applying positive force F_y, the left and right gauges resistances become respectively $R_1 = R_o - dR$ and $R_2 = R_o + dR$. The central beam is a common electrode (point A in Figure 2.8 of the Wheatstone bridge) and allows for better symmetry of deformation of the sensitive beams.

Antagonistic resistances R_1 and R_2, which are sensitive to F_y, are mounted in a Wheatstone

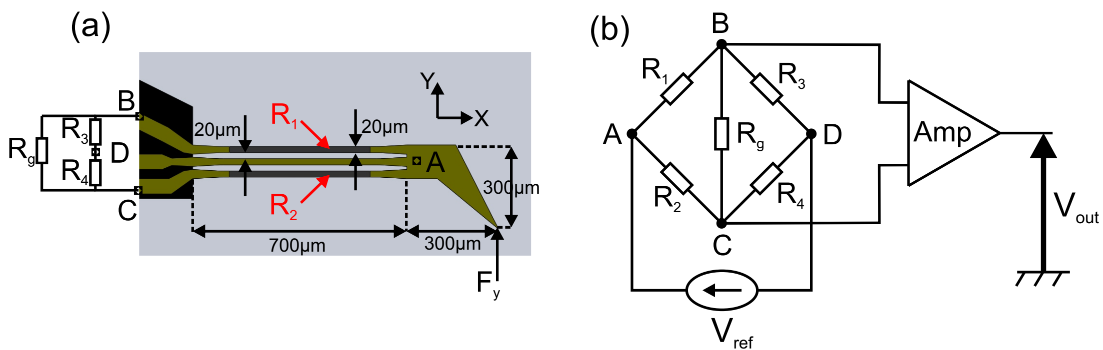

FIGURE 2.8: (a) Sensing beam structure and (b) its Wheatstone bridge.

bridge. The latter is connected to a differential amplifier, Amp, to obtain a voltage image, V_{out}, of the applied force F_y as shown in Figure 2.8-(b). V_{ref} is the voltage applied to the Wheatstone bridge.

Parameter	Value
Young Modulus	169 GPa
Poisson ratio	0.278
Electrical Resistivity	1000 $\Omega \cdot$m
π_{11}	6.6×10^{-11}Pa^{-1}
π_{12}	-1.1×10^{-11}Pa^{-1}
π_{44}	138.1×10^{-11}Pa^{-1}

TABLE 2.5: Silicon parameters used in the simulations using COMSOL MULTIPHYSICS.

2.4 Simulations studies of the force sensor

Simulations are performed to finalize the design of the sensor by determining its dimensions and testing its desired specifications. The simulations are performed using COMSOL MULTIPHYSICS. The parameters used in the simulations for the design of the piezoresistive force sensor are detailed in Table 2.5; these parameters being , issued from [97].

The force sensor main design given in Figure 2.8 is used. The dimension to be fixed are the length and the thickness of the complete sensor and the width of each beam. The following steps are used for the simulation:

1. The maximal size of the force sensor is fixed in the specifications to be less than 1000 μm $\times$ 100 μm $\times$ 20 μm.

2. The thickness is chosen according to specifications presented in section 2.1 to be less than 20 µm. Using default thicknesses of the SOI wafers, the thickness is chosen to be 12μm.

3. The resolution of the force sensor should be in the range of several hundreds of µN. For the piezoresistive force sensors, it is known that a strain of 1 $\mu\varepsilon$ [1] is easily detected by the sensor despite the noise signal. The force able to induce 1 $\mu\varepsilon$ of strain in the gauge of the force sensor is then the resolution of the system.

4. The maximal force which generates the maximal stress, supported by silicon, in the force sensor is determined in simulations. The sensing range is fixed to be 5 times smaller than the value of this maximal force.

5. The dimensions of the gauge are determined by fixing a range for the electric resistance. The range is fixed to be between 2 kΩ and 8 kΩ which is a trade-off between sensor sensitivity and heating effect. If the gauge resistance is small, a lot of current passes inside the gauge which increase the heating effect in the gauge influences the performances of the sensor. If the gauge resistance is big, the ratio $\frac{\Delta R}{R}$ becomes smaller and consequently the sensitivity of the force sensor becomes smaller.

After performing several simulations, the final dimensions of the force sensors are determined and theoretical performances of the force sensor are also calculated. The thickness of the

[1] the $\mu\varepsilon$ is defined when $\frac{\Delta L}{L} = 10^{-6} = 1\mu\varepsilon$

force sensor is fixed to 12 µm by choosing the thickness of the device layer of the wafer to be used for the microfabrication. The width is fixed to 100 µm. Then, the length of the sensor is changed to meet the desired specifications. Thus, the dimensions of the force sensor are fixed to be 700 µm in length, 100 µm in width and 12 µm in thickness. Each gauge of the sensor has 20 µm of width. The sensor's expected resolution is 500 nN, its complete sensing range is 2 mN and its stiffness is 125 N/m. The resistance for each of the silicon strain gauge without any applied stress, R_o, is 3 kΩ. The coefficient c presented in Equation (2.16) is tested in simulations and is equal to 1.25 ($c = 1.25$) which means that the sensitivity of the force sensor is increased 25% by adding the cavities to the design. The simulation results will be compared with the experimental results in section 2.6.

2.5 Microfabrication

In this section, a microfabrication process to fabricate the presented force sensor is proposed. The silicon is a widespread material used for the fabrication of many types of MEMS due to the standard microfabrication processes that can be used, its relatively low cost production and its mechanical and structural properties. SOI wafers, commonly used to master the thickness of each of silicon layers during the microfabrication processes, enable the fabrication of this kind of piezoresistive microforce sensor with adequate quality to obtain good sensor performances. Indeed, each silicon layer of the wafers can be separately etched: the handle layer (350 µm) for the base of the finger and the device layer (10 µm) for the gripping beam. Some dry and wet etching processes were considered, and finally DRIE (Deep Reactive Ion Etching), with BOSCH process was chosen for many reasons. The DRIE process is often used for many MEMS microfabrication process due its capability of deeply etching the silicon with a good anisotropy and to the speed of etching (around 6 µm/min) that the BOSCH process provides. In addition, the etching side has a particular roughness, called scalloping, as a result of the way of guaranteeing etching anisotropy. This roughness presents an interest in many applications like gripping because it reduces the gripping surface between silicon force sensor and manipulated micro-objects [62].
The microfabrication flowchart presented in Figure 2.9 was used to manufacture the microforce sensor. It can be summarized by the following steps:

1) SOI wafer is used to start the fabrication. The wafer is composed of a 10μm device layer of silicon, 1μm of silicon oxide layer and 350μm handle layer of silicon,

2) The wafer is thermally oxidized to create 1 μm thick SiO_2. The SiO_2 is, then, etched in a BHF solution (Buffered Hydrofluoric Acid) using photolithographically patterned photoresist,

3) This step is a critical step in the microfabrication process, it is used to establish electric contact between the silicon piezoresistive gauge and the external electrodes, which is called *ohmic contact*. It is formed by sputtering an aluminium layer on the silicon device layer and annealing it at a specific temperature in order to diffuse the aluminium atoms into the silicon. The diffusion of the aluminium atoms into the silicon determines the

contact resistance which should be the smallest possible to enable good performance of the sensor. Usually, high temperatures and long annealing time are used to diffuse the alumium atoms. However, this will decrease the sensitivity of the force sensor by decreasing the strain gauge resistance. Indeed, the choice of the parameters in the annealing process is a critical step of the microfabrication process used. Finally, the ohmic contact is performed by sputtering 200 nm of aluminium, annealing it at 600°C for 1h and etching the aluminium using photolithographically patterned photoresist,

4) Patterning of 800 nm of aluminium by lift-off to realize the electric connections on the device (figure 2.9.4),

5) The handle layer is etched using DRIE after sputtering 200 nm of aluminium to realize a mask for the DRIE on the handle layer,

6) The device layer is etched using DRIE process using masks of SiO_2 and aluminium,

7) The process is finished by a top side RIE etching of the SiO_2 to realize the sensor.

Figures 2.10a and 2.10b show some SEM pictures at the end of the microfabrication process. Figure 2.10a shows the complete force sensor view while Figure 2.10b-(a) and (b) shows respectively the side and the top view of the clamping part of the force sensor to the rigid part (handle layer). The two figures also show the ohmic contact part (3rd step in the microfabrication flowchart presented in figure 2.9). Figure 2.10b-(a) shows also the scalloping due to the back side DRIE etching (5th step in the microfabrication flow chart). Figure 2.10b-(c) and (d) show respectively the side and the top view of a sensitive silicon beam. In figure 2.10b-(c), the scalloping effect due to the front side DRIE is present (6th step of the microfabrication flowchart).

The dimensions obtained after the fabrication are measured using SEM pictures as in figure 2.10b. The sensor's length in the design is 700 µm while the measurements using SEM showed that the sensor's length is 702.8 µm with a fabrication error of 0.4%. The width of the sensor's gauges in the design is 20 µm while the measurements using SEM showed that it is 20.05 µm with a fabrication error of 0.25%. The thickness of the device layer of the SOI wafer used in fabrication is 10±1 µm. As shown in figure 2.9, 1 µm of SiO_2 is fixed on the device layer. In addition, 1 µm of SiO_2 is present on the internal layer of the SOI wafer. Adding the three layers, the theoretical thickness of the force sensor is 12±1 µm. After measurements, the thickness is measured to be 12.24 µm which means 2% of error in the thickness to the model due to the uncertainty of the device layer thickness by construction. These errors have a small impact on the predicted performances of the force sensor. Their impact being studied in section 2.6.

2.6 Experimental sensor Calibration

In this section, the sensor characteristics are investigated. First, an experimental setup used for the sensor calibration is proposed. Then, several tests are performed to determine the piezoresistive force sensor's stiffness, its sensitivity, its signal to noise ratio and its resolution.

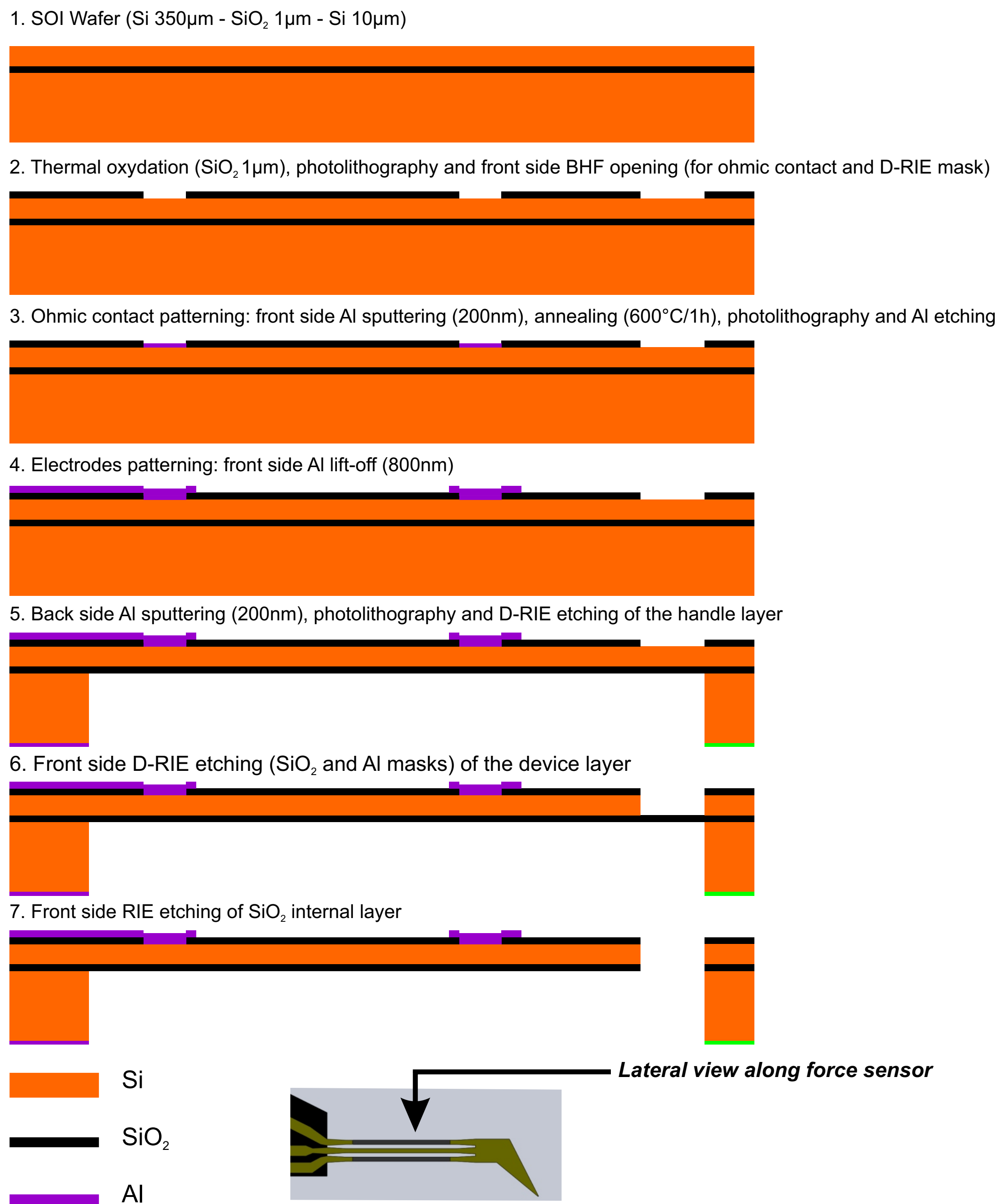

FIGURE 2.9: Microfabrication process flowchart.

2.6.1 Experimental Setup

An experimental setup is proposed to calibrate the piezoresistive microforce sensor (PiezoFS) (see Figure 2.11). The objective of this section is to determine the force sensor characteristics especially the stiffness, the sensitivity, the SNR (Signal to noise ratio) and the resolution of the

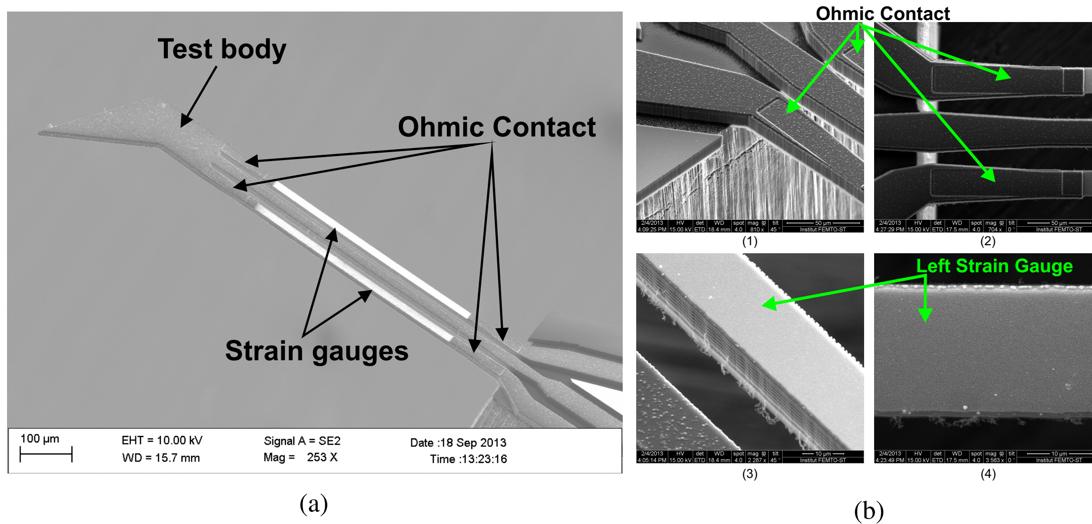

FIGURE 2.10: SEM pictures of the force sensor showing: (a) complete force sensor with the strain gauges ,the ohmic contact and the test body (b) closed view on the ohmic contacts part and the strain gauges of the three beams structure of the sensing part: (1)&(2) fixation of the three beam, (3)&(4) zoom on one beam. (1)&(3) are side photos while (2)&(4) are top view.

PiezoFS. Using a Wheatstone bridge, the resistance variation of the gauges of the PiezoFS are converted into voltage in order to perform the acquisition signal of the PiezoFS. An industrial and calibrated force sensor (CalibFS) is used to calibrate the PiezoFS. The CalibFS is a force sensor FT-S270 from FemtoTools with a measuring range of 2000 µm and a resolution of 50 nN. The CalibFS comprises a probe tip, of 3 mm in length and 50 µm in thickness, that moves along its main direction, Y (Figure 2.11), once a force is applied at its tip. The displacement is converted into a voltage thanks to a capacitive variation measured by a dedicated circuit. The complete CalibFS with electric connections and mechanical support has dimensions of 4 cm $\times$ 2.5 cm $\times$ 1.5 cm. The CalibFS is mounted on a microrobotic structure composed of a fine positioning stage and rotation stage. The fine positioning stage is a P-611.3 NanoCube with 100 µm range and 1 nm resolution allowing a relative displacement of the CalibFS relative to the PiezoFS to apply forces. The rotation stage is a SmarAct SR-3610-S with 1.1 $\mu°$ resolution is used to adjust the perpendicularity of contact between the PiezoFS and the CalibFS. These two motion devices are equipped with internal sensors and are closed loop controlled. The positioning stage and the voltage acquisition of the two force sensors are performed via a dSpace 1104 acquisition board with a sampling frequency of 20 kHz.
The calibration of the PiezoFS is done by moving the CalibFS, which is fixed to the fine positioning stage, into contact with the PiezoFS and then moved it in the opposite direction to separate contact along the Y direction. The output voltage of the PiezoFS, the force measurement of the CalibFS and the position measurement of the internal sensor of the fine positioning stage are simultaneously saved and considered to determine the PiezoFS characteristics.

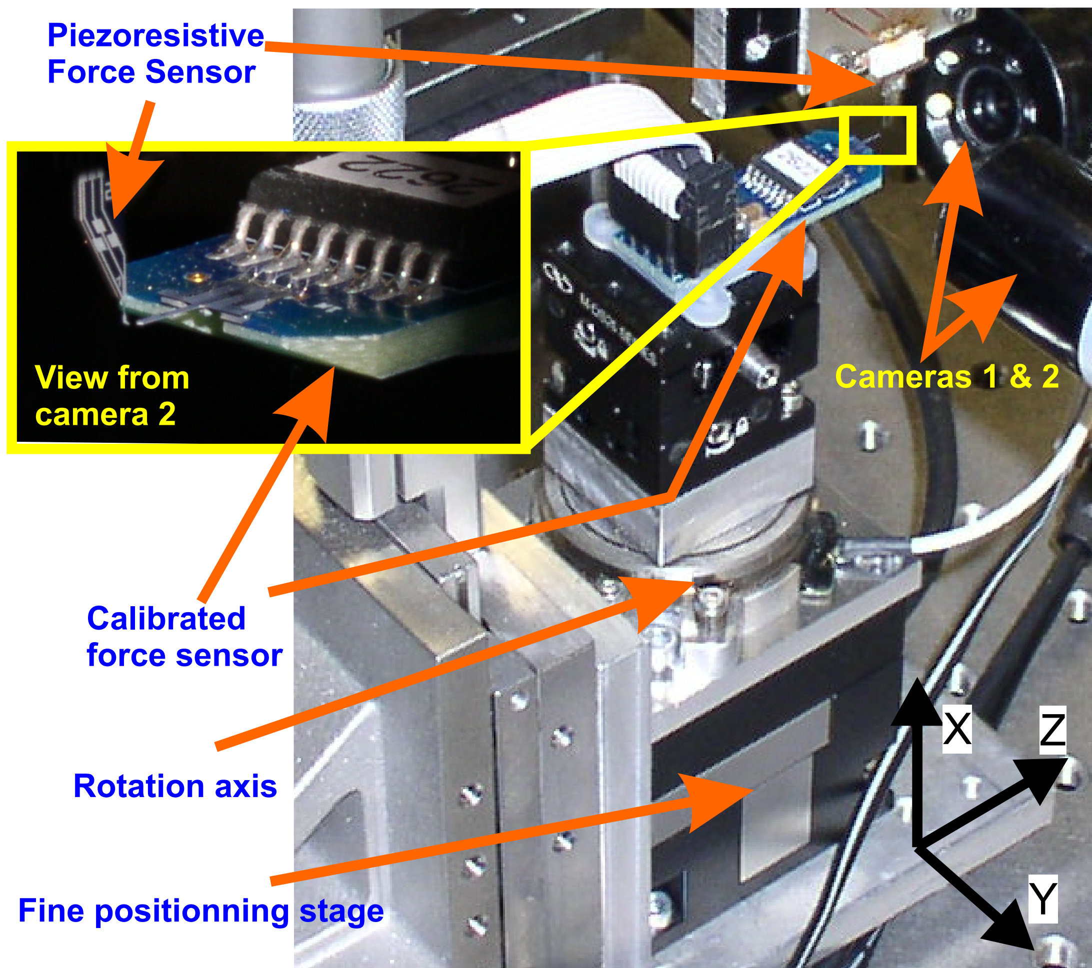

FIGURE 2.11: Experimental setup used for the characterization of the piezoresistive force sensor. A calibrated force sensor (CalibFS) is fixed on a robotic system consisting of a fine positioning stage and rotation stage. The piezoresistive force sensor (PiezoFS) is fixed. Two cameras are used to see the contact.

2.6.2 Mechanical Characterization

The first step of the characterization of the PiezoFS is the mechanical characterization which consists of measuring the stiffness of the PiezoFS. The stiffness measurement is done by moving forward the CalibFS to be in contact with the PiezoFS with a constant velocity and then moving it back. The force measurement is done using the CalibFS and the position measurement is done using the internal sensor of the fine positioning stage. In order to determine the displacement of the PiezoFS, the stiffness of the CalibFS is 1000N/m. The displacement of the PiezoFS is calculated by Equation (2.17):

$$\delta_{PiezoFS} = \delta_s - \frac{F_{CalibFS}}{K_{CalibFS}} \tag{2.17}$$

where $\delta_{PiezoFS}$ is the displacement of the PiezoFS after contact, δ_s is the currently measured position of the internal sensor of the fine positioning stage after contact and $F_{CalibFS}$ and $K_{CalibFS}$ are respectively the force measurement signal of CalibFS and its stiffness.
Figure 2.12 shows the force measurement of the CalibFS with respect to the displacement of the PiezoFS. After contact, the force increases linearly with respect to the displacement. The stiffness is calculated using Equation (2.18):

$$K_{PiezoFS} = \frac{F_{CalibFS}}{\delta_{PiezoFS}} \tag{2.18}$$

After doing several set of 10 measurements, the stiffness of the force sensor is determined to be 130N/m±1N/m while the theoretical stiffness is 125N/m which means 4% of error.

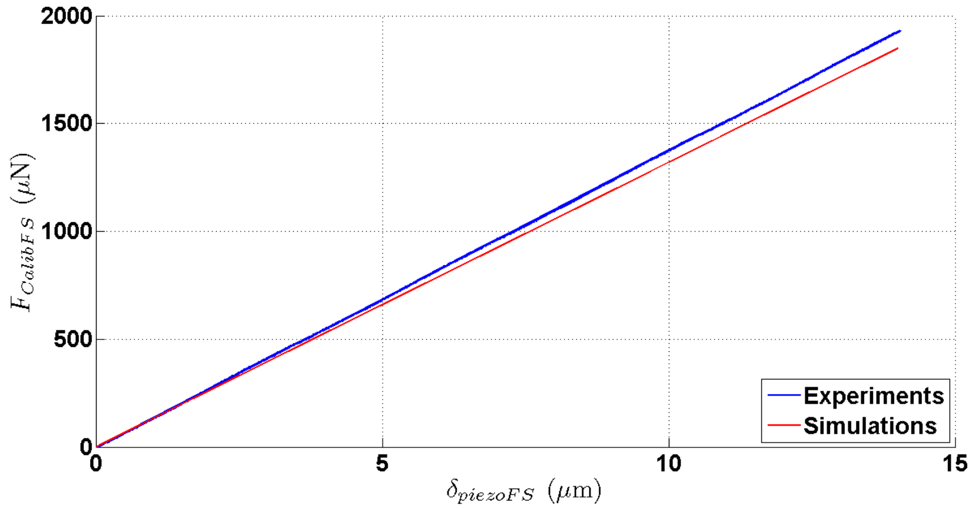

FIGURE 2.12: Force measurement of the CalibFS with respect to the position of the fine positioning stage in order to measure the stiffness of the force sensor.

2.6.3 Resistance variation and sensor's sensitivity relative to the applied stress

Without any applied stress on the force sensor, the gauge resistance is equal to $R_{1o} = 2.76$ kΩ for one resistance and $R_{2o} = 2.71$ kΩ for the other. The resistance variation of the silicon strain gauges is measured while applying a stress on the force sensor. The variation is given in Figure 2.13-(a). The two strain gauges resistances change in push-pull where their variation is linear and symmetric with a relative absolute value of their slope 0.09 Ω/μN for each resistance. The error on the linearity of the resistance variation is less than 0.3%.
Figure 2.13-(b) shows an example of the readout voltage, V_{out}, at the output of the Wheatstone Bridge circuit supplied with a referenced voltage $V_{ref} = 5$V and with a differential amplifier composed of a INA103 configured with an amplification factor $A = 100$. The voltage variation relative to the force is linear and the measurements are repeatable for several tenth set of measurements done. The average sensitivity of the readout voltage for 10 measurements is 197.5

µN/V for a referenced voltage of $V_{ref} = 5$V. The standard deviation of the 10 measurements with respect to the average is 0.73 µN/V. The error on the repeatability of the force sensor is less than 0.3%.

The noise amplitude at the voltage of the PiezoFS has almost the same level of that of the

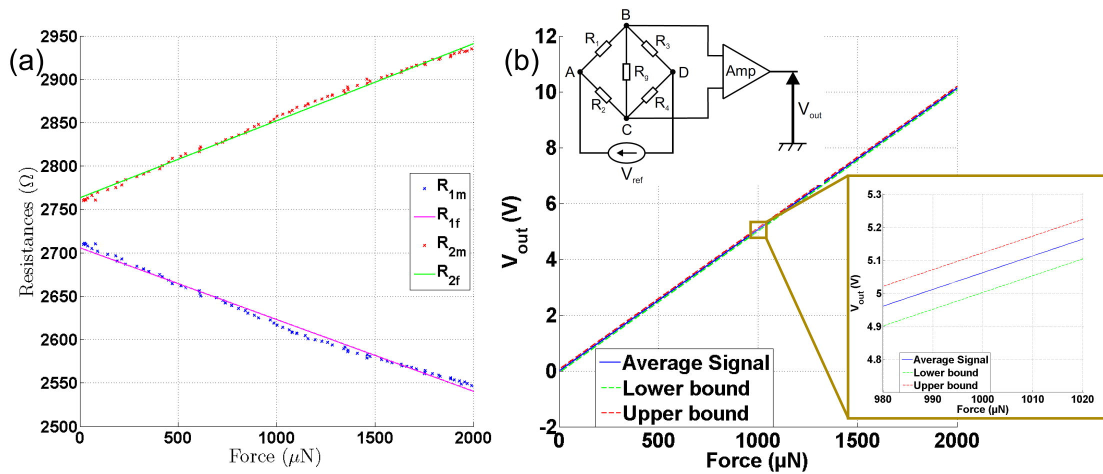

FIGURE 2.13: (a) The variation of the strain gauges resistances relative to an applied force on the tip of the force sensor. R_{1m} and R_{2m} are the measured values of resistances in experiments and R_{1f} and R_{2f} are the approximated linear variation of the resistances and (b) The variation of the readout voltage from the Wheatstone Bridge, V_{out}, for a referenced voltage of $V_{ref} = 5$V and amplification gain, $A = 100$, relative to an applied force.

CalibFS. The maximal peak to peak amplitude of noise without contact is around 40 mV. The noise amplitude is almost constant for any applied force on the two force sensors. However, the main advantage of the PiezoFS is that it presents much bigger signal to noise ratio (SNR) than the CalibFS. The SNR being dependent of the applied force on the force sensor, the SNR for the PiezoFS reaches 50 dB at a force of 2 mN where it is 37 dB for the CalibFS.

2.6.4 Resolution

The resolution is the smallest reliable force detected by the force sensor. It depends on the bandwidth of the electric circuit and on the filtering. There are many ways of considering the resolution. The first and the worst case is to consider the signal without any filtering on a specific time. In this case, the resolution is equal to the level of noise in the signal (i.e. 8 µN). The second case consists of considering the signal over an interval of time without filtering and then a small variation of force can be detected by the force signal as shown in Figure 2.14-(a). In Figure 2.14-(a), the noisy signal of the sensor is shown with respect to the time with the average signal and the upper and lower bounds of the signal which was determined using the filter presented in [86]. A force variation smaller than 1 µN (800 nN) is detected. The latter force (800 nN) is smaller than the amplitude of the noise as shown in the figure. The third case consists in filtering the signal given by the force sensor over an interval of time. By considering

some filtering of the data, a much smaller resolution could be detected by using some signal processing techniques or some advanced filters. The resolution reaches less than 500 nN with a first order low-pass filter with a cut-off frequency of 1 kHz and around 100 nN with a first order low-pass filter with a cut-off frequency of 10 Hz as shown in Figure 2.14-(b). The last and ideal case is the theoretical resolution that could obtained by detecting the smallest voltage detection of the data acquisition card. In the case of the study, the data acquisition card is a 16 bits Analog to Digital Converter (ADC) with an input of the card going from -10V to 10V, the lowest voltage that could be detected is given by the following $\frac{20}{2^{16}} \approx 0.3$ mV. Then using an appropriate filter the resolution of the force sensor could be improved. The corresponding theoretical limit of the resolution is 60 nN.

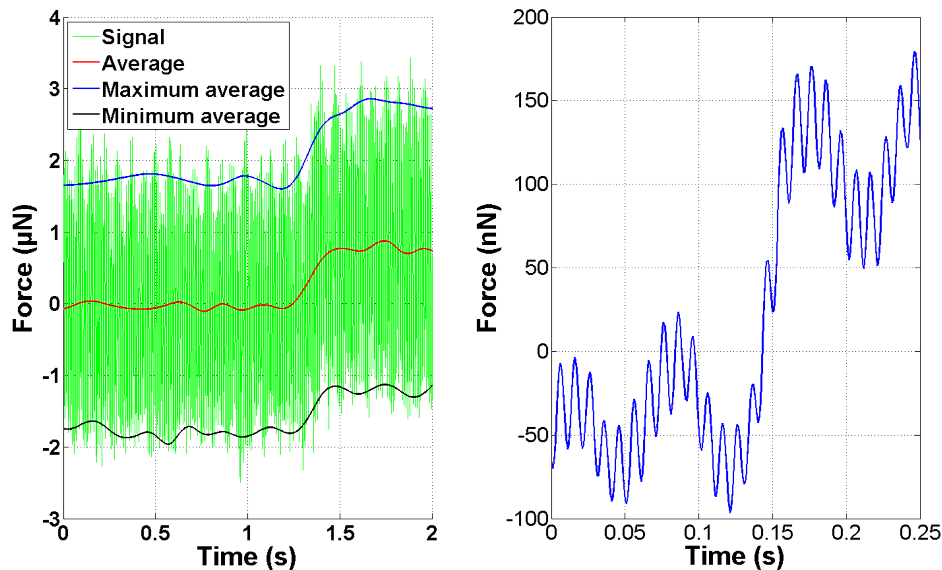

FIGURE 2.14: The force sensor signal measured while applying small displacement of the positioning stage in order to determine the resolution of the sensor: (a) resolution of 800 nN without filtering, (b) resolution of 100 nN with a low pass filter with a cut-off frequency of 10 Hz.

2.6.5 Dynamic Characterization

In order to determine the dynamic behavior of the sensor, a response of the force sensor is tested in free vibrations. Thus, a rigid object fixed on a microrobotic positioning stage enters in contact with the tip of the force sensor and apply a preload force of 150 µN for $t > 0$ and at time $t = 0$ the positioning stage is taken off to separate the contact. The free vibrations of the force sensor are registered using a sampling frequency of 20 kHz (which is the maximal sampling frequency of the dSpace1104 used). Some oscillations occur as shown in Figure 2.15 before the signal stabilizes to zero. The force sensor can be modeled as a second order system with damping. A Fast Fourier Transform (FFT) is applied to the acquisition signal in order to determine precisely the natural frequency of the force sensor. The result of the FFT is shown in Figure 2.15. The

natural frequency, f_0, of the system is then determined to be 8520 Hz. The force sensor can be modeled as a mass-spring-damper system which leads to its modeling as a second order transfer function with a natural frequency $f_0 = 8520$ Hz and a damping coefficient $\xi = 0.006$. The damping coefficient of the force sensor is determined by applying a nonlinear least square in order to fit the second order model of the free vibrations with the experimental data. The results of fitting are shown in Figure 2.16.

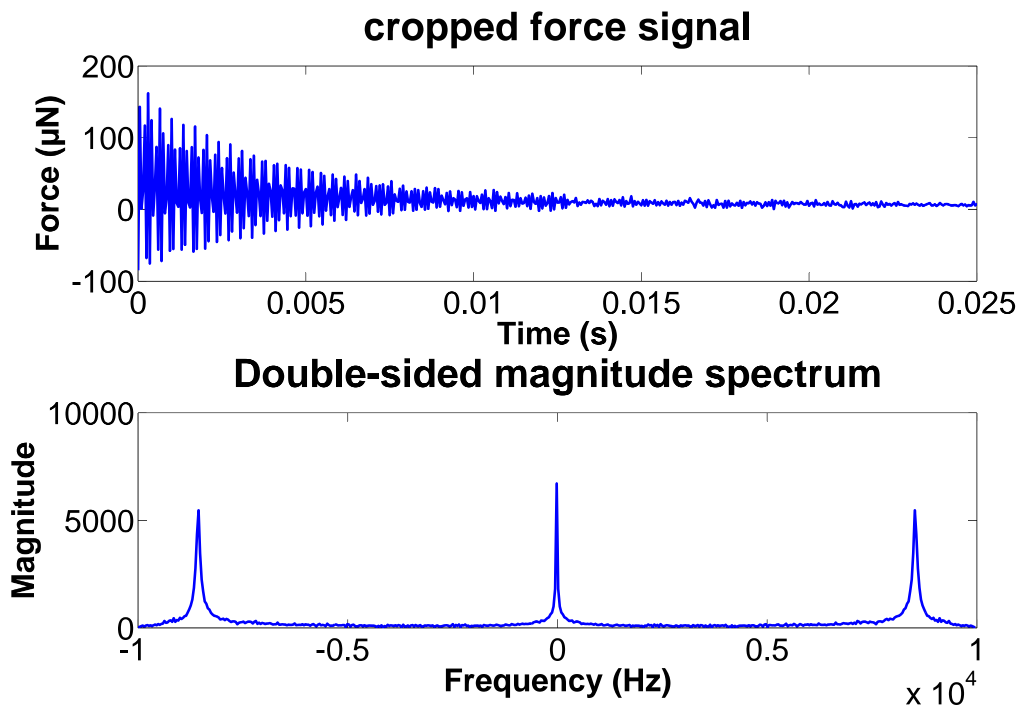

FIGURE 2.15: The time signal and the FFT signal of the signal measured by the force sensor when free vibrations are applied to the force sensor.

2.6.6 Discussions about experimental results

In this section, the experimental results are compared with the design parameters presented in section 2.3. The dimensions of the force sensor after the microfabrication have been presented in section 2.5. The length of the strain gauges is 700 µm, their width is measured to be 20.05 µm while in the design it is 20 µm and the thickness of the force sensor is measured to be 12.52 µm while in the design it is 12 µm.

The stiffness of the force sensor using the design parameters (i.e. 700 µm in length, 20 µm in width of the gauges and 12 µm in thickness) is 125 N/m. Inducing the experimental dimensions obtained after the microfabrication (i.e. 700 µm in length, 20.05 µm in width and 12.52 µm in thickness instead of 20 µm and 12 µm respectively) in simulations, the stiffness of

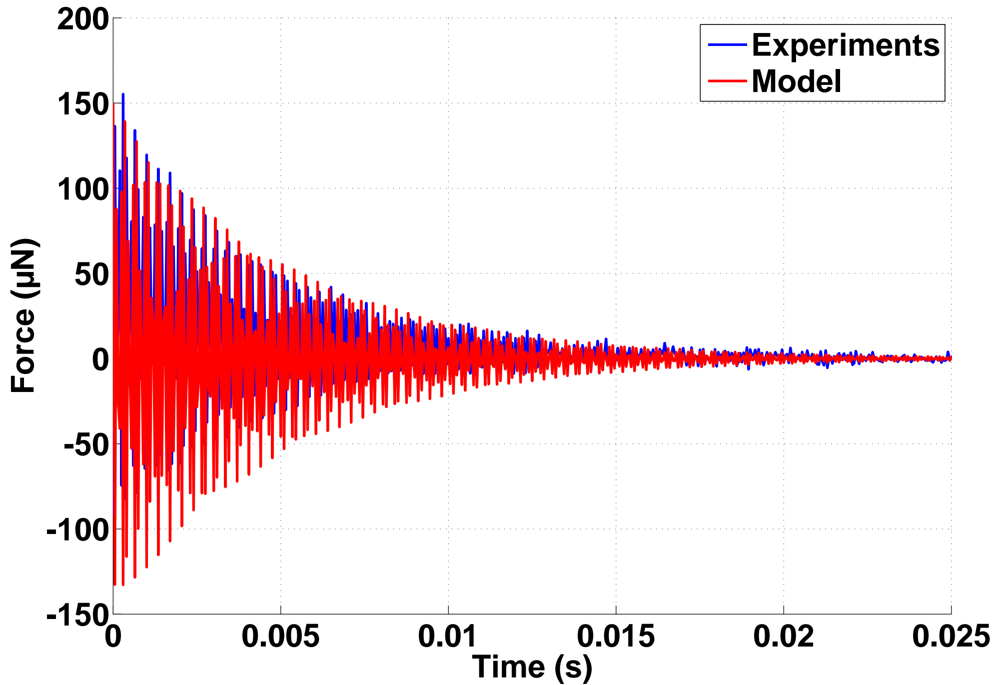

FIGURE 2.16: The time signal of the force sensor compared to the model after fitting the damping coefficient.

the force sensor is calculated to be 130.4 N/m. In experiments, the stiffness of the PiezoFS is 130N/m which means 0.31% of error after taking in consideration the dimensions errors in the microfabrication and 4% of error relative to the initial design.
The gauge resistances of the force sensor without any applied stress is set to be 3 kΩ in design. However, using the experimental results of the dimensions, the gauge resistance is calculated to be 2.75 kΩ. The experimental results show that the gauge resistances without any stress applied at the tip of the force sensor is 2.8 kΩ which means 1.8% of error relative to the resistance taking into consideration the dimensions errors of the microfabrication and 6.7% of error relative to the design gauge resistance. This step shows that the ohmic contact step (3rd step of the microfabrication process) is done in a good way and the aluminium has well diffused in the silicon.
Once a force is applied to the tip of the force sensor, the left and right resistance change in push-pull. In simulations, the variation of each gauge resistance is 0.1 Ω/μN in each direction. While in experiments, the variation of each gauge resistance is measured to be 0.09 Ω/μN which means 10% of error. However, taking into consideration the uncertainities of the microfabrication, the variation of the resistance in simulations was 0.95 Ω/μN which means 5.3%.
Furthermore, theoretical gauge factor is bigger than 100 [163] for silicon and has been estimated to be 120.6 in Equation (2.14) while in experiments it is estimated to be around 120 which means 0.5% of error.

		Initial Model	Experimental Results	Error (%)
Microfabrication	Length (μm)	700	702.8	0.4
	Beam width (μm)	20	20.05	0.25
	Thickness (μm)	12	12.24	2
Performances	Stiffness (N/m)	125	130	4
	gauge resistance (kΩ)	3	2.76	8
	ΔR (Ω/μN)	0.1	0.09	10

TABLE 2.6: Comparison between theoretical model and microfabrication results. The dimensions are measured using SEM and the other variables are measured through experiments. The error is between experimental results and the theoretical parameters with taking into consideration the dimensions error in the microfabrication process.

These experimental results show that the microfabrication process is reliable and the performances differences between the simulations and the microfabriaction are due to the small microfabrication errors. The differences between the model and the results are summarized in Table 2.6.

2.7 Conclusion

In this chapter, a design taking advantage of both mechanical and bulk piezoresistive properties of silicon has been studied, designed and prototyped. This force sensor is fabricated using silicon because it is widespread in MEMS, it presents a high gauge factor and it is fabricated using classical MEMS microfabrication processes. This piezoresistive force sensor has been fabricated using a relatively simple and cheap microfabrication process making it easy to integrate in most of MEMS devices and especially in the fingers of a microgripper. The sensor also presents high performances compared to the sensors presented in literature thanks to its sensitivity of 197μN/V, its resolution of 100nN, its sensing range of 2mN, its signal to noise ratio of 50dB at a force of 2mN and its stiffness of 130N/m. The signal of the force sensor is repeatable with an error less than 0.3%. It was shown that experimental results are very close to the theoretical results which shows that the process used guarantees the desired behavior of the sensor. The success rate of the force sensor was around 95% and regarding its small dimensions, many of these sensors could be fabricated on the same SOI wafer which enables to integrate them easily in many MEMS structures and offer measurement very close to the area of interest which is a very important issue at microscale.

The characteristics of this force sensor are compatible with many microscale applications such as biological, biomedical, microassembly, micromanipulation, etc. The main advantages of this force sensor are:

- it can easily be integrated into microsystems due its small size and especially inside a microgripper as it will be shown in chapter 3,
- its simple and basic based microfabrication steps allowing its integration in a wide range of MEMS devices by adapting the design to the specifications of the application,

- its high performances
- it enables the measurement of local information very efficiently.

Chapter 3

Fabrication and Dynamic Nonlinear Model of Two-Smart-Fingers Microgripper (TSFM)

In this chapter, the force sensor presented in chapter 2 is integrated into an active piezoelectric microgripper. The whole system is composed of two active fingers with sensorized end-effectors. A dynamic nonlinear force/position model of the complete gripper while manipulating a micropart is presented. Non-contact and contact scenarios are notably studied, modeled and finally validated experimentally.

3.1 Introduction

The integration of force sensors into an active microgripper has led to several studies in the past years including several types of actuators and force sensors [12, 81, 119, 175]. This study is motivated by the need of force sensing to understand what is happening at this scale, model the microsystems and especially control the interaction forces between the microgripper and the manipulated micropart in order to succeed the task. In this chapter, the force sensor developed in chapter 3 is integrated into a 4-DOF piezoelectric microgripper already developed in the AS2M department of FEMTO-ST institute [1, 31, 118].

This chapter will be organized as follows. First, the method of integration of the piezoresistive force sensor on each of the two fingers of the duo-bimorph piezoelectric actuator is described. Second, the model of the piezoelectric actuator studied and based on state of the art works. The considered model is dynamic, nonlinear and combining the direct and indirect effects of the piezoelectric materials into one voltage/force/displacement model. Third, after the integration of force sensors into the fingers of the microgripper, the model of the Two-Smart-Fingers Microgripper (TSFM) in free motion and in constrained motion (while the microgripper is manipulating an object) is developed. To develop the model, each finger (actuator + sensorized end-effector) is considered in interaction with a flexible environment. Finally, an identification

of the system parameters and experimental investigations for the TSFM model are done. The experimental validations are performed for two types of manipulated objects. Figure 3.1 shows a summary of the method followed in this chapter.

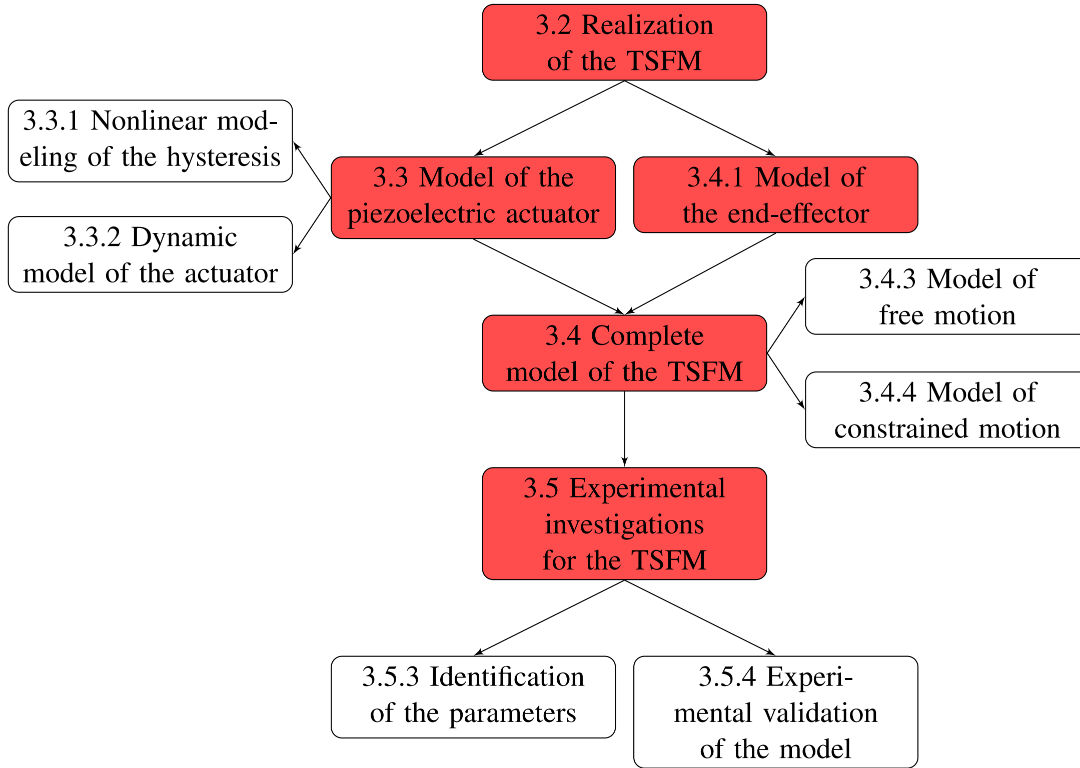

FIGURE 3.1: Organization of this chapter showing the steps to model the TSFM.

3.2 Realization of the Two-Smart-Fingers-Microgripper (TSFM)

The objective of this section is to realize a *Two-Smart-Fingers Microgripper* (TSFM) by integrating a sensorized end-effector, equipped with the piezoresistive force sensor presented in Chapter 2, onto each of the two tips of the piezoelectric actuator. The actuator used is the duo-bimorph piezoelectric actuator developed inside AS2M department [1, 30]. The whole system is called Two-Smart-Fingers-Microgripper where each finger is composed of an active piezoelectric actuator with sensorized end-effector. The realization of the TSFM is shown in Figure 3.2. In the design of the force sensor, the force sensor is fixed on a rigid 350 μm thick silicon layer which is used for three main reasons: 1) it is used as a lever system to amplify the displacement of the actuator, 2) it is used to help the fixing and the manipulation of the fragile force sensor, 3) it is used to put the electric connections of the force sensor. The rigid part and the force sensor form the sensorized end-effector. A scheme of the TSFM is presented in Figure 3.3. The two fingers are supposed to be identical.

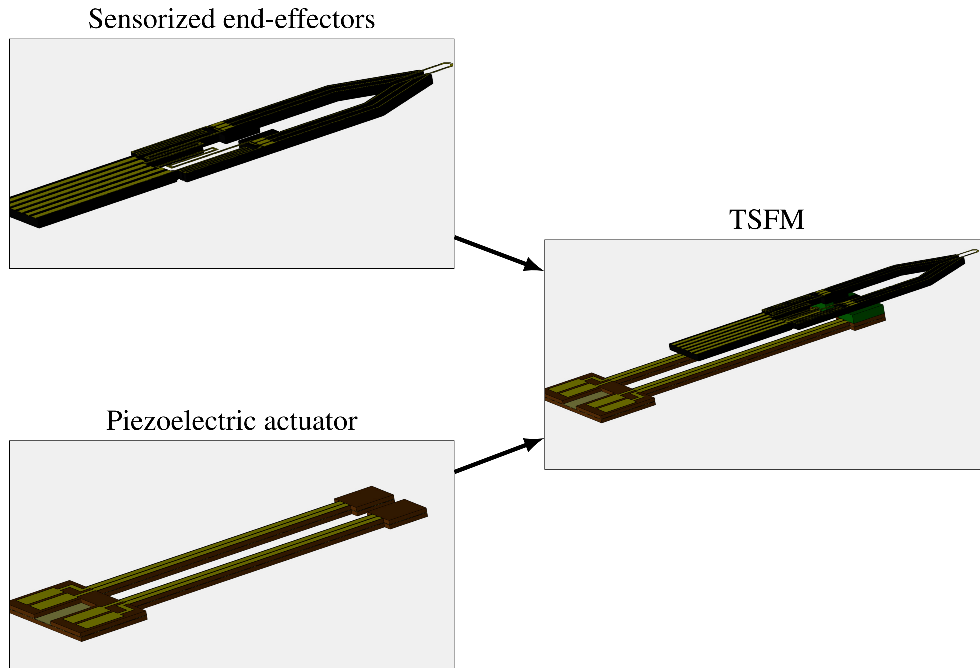

FIGURE 3.2: Integration of the sensorized end-effectors into a piezoelectric actuator to realize TSFM.

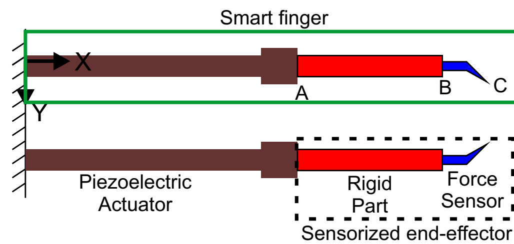

FIGURE 3.3: Complete scheme of the two-smart-fingers microgripper (TSFM).

Several steps and cautions have to be considered in order to realize the TSFM. First, the components are so fragile, so special care needs to be done in order not to break the components. Second, mechanical fixation between the actuator and a fix support on the one hand and between the end-effector and the actuator on the other hand. Third, electric connections need to be performed in order to be able to generate voltage to displace the force sensor and to retrieve the force sensor signal to an electronic circuit. Fourth, electronic circuit needs to be done to condition the signal of the force sensor. All these steps are difficult at the microscale and they require dexterity and precision to realize the TSFM. This task is done manually which increases the risks and the difficulty of the task. Indeed, the mechanical and electric assembly of actuators

and sensors at this scale with the ambition of having performant microgripper is challenging. The least error can generate the breaking of the components. For this reason, a method to reduce the risks of the manual assembly of the actuators and sensors and enabling to retrieve the signals of the force sensors and to command the actuator needs to defined.

The method consists of fabricating mechanical parts which enables the positioning of the these parts together to realize a packaged microgripper. The piezoelectric actuator is fixed mechanically and electrically on one of these parts and the sensorized end-effector is also fixed mechanically and electrically on another part. Then, the two parts are joined together using screws and holes which enable precise positioning and guiding of the two parts to form a final packaged TSFM. The procedure to realize the TSFM can be divided in five steps which are detailed in the following steps and are summarized in Figure 3.4:

1. Two mechanical hoods (hoods 1 and 2) are fabricated using aluminium with positioning zone and screws and an electric connector for the actuator is fixed on hood 1. Hood 1 is used to fix the actuator and hood 2 is used to fix the sensorized end-effectors. The positioning zone and screws enable to position and fix the two hoods finely precisely. The electric connector enables to fix the actuator mechanically and electrically to hood 1.

2. An electric connector is fixed on the hood 2 in order to fix the sensorized end-effector inside this connector while performing electrical connection of the force sensor signal. In addition, electric resistances are fixed on the tips of actuator. These resistances are used to heat and melt down the thermal glue to fix the sensorized end-effector to the actuator.

3. the piezoelectric actuator and the sensorized end-effectors are inserted and fixed inside the two connectors while enabling access to electric connections.

4. Solid thermal glue is fixed on each finger of the actuator and an electric voltage is applied to the heat the resistances and to melt down the thermal glue, then the hood 2 is fixed on the hood 1 using the positioning zone and screws until a contact happens between the sensorized end-effectors and the actuator's fingers.

5. The electrical voltage is turned off and the thermal glue solidify fixing the end-effectors to the actuator's fingers. TSFM is then realized by achieving mechanical fixation and electrical connections. Finally, the signals of the force sensors are connected to a convenient electric circuit to retrieve the force information.

The complete microgripper is shown in Figure 3.5 after its realization, showing the piezoelectric actuators, the sensorized end-effector and a zoom on the piezoresistive force sensors.

3.3 Model of an active piezoelectric microgripper

Piezoelectric actuators use the inverse piezoelectric effect of piezoelectric materials to generate forces and displacement where a stress is generated by applying electric charges to the actuator. Their use is due to their high resolution, high speed, low response time and their ability to produce large forces. They are widely used for the development of robotic platforms [42],

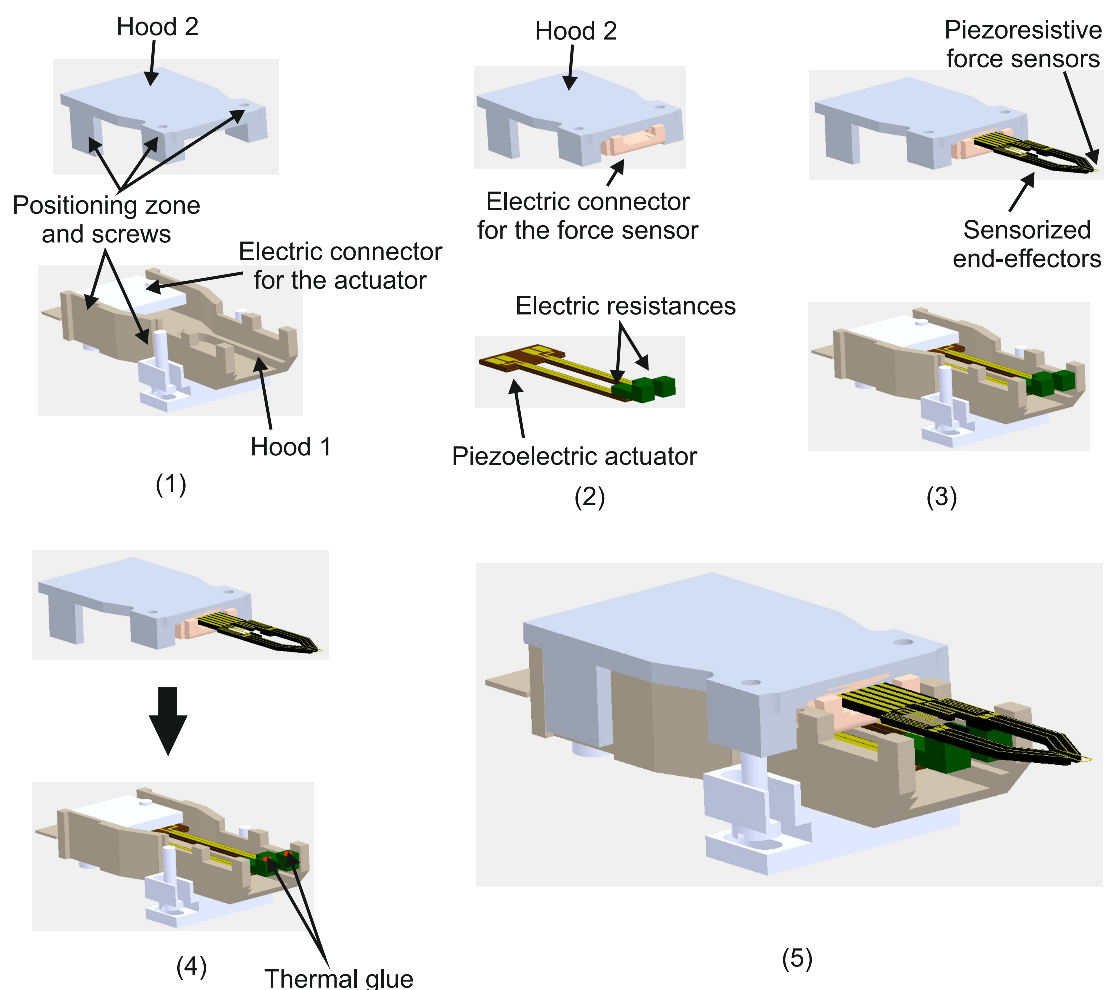

FIGURE 3.4: The procedure for the integration of the force sensor into the piezoelectric actuator showing five main steps which are detailed in section 3.2.

nanopositioning [195] and especially for the fabrication of microgrippers [175, 191, 31]. However, piezoelectric materials have nonlinear behavior that must be considered for the model and control in order to take benefit of the advantage of the piezoelectric actuators and their need for microassembly tasks. The nonlinearities are manifested by the hysteresis and the creep. A nonlinear model of the hysteresis is first studied in this section. The main objective of this section is to develop a dynamic nonlinear model of the piezoelectric actuator inspired from literature.

3.3.1 Nonlinearities in the piezoelectric actuators

The modeling and the control of the hysteresis and of the creep have raised many works, including linear approximation and linearization [22], algebraic or differential nonlinear modeling

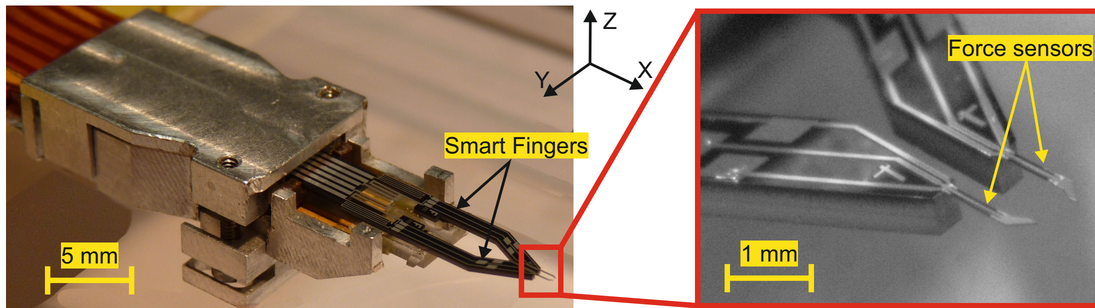

FIGURE 3.5: Two-smart-fingers microgripper (TSFM).

[3, 184], feedforward control [94, 131] and feedback control [134, 109, 132]. The effect of hysteresis is more significant because it affects both the dynamic and static part where the creep affects only static part and its effect is small compared to the effect of hysteresis. Furthermore, the static part may be easily compensated through closed loop control.

A typical curve of the hysteresis in the piezoelectric actuators is given in Figure 3.6 where internal loops and external loop hysteresis exist. In practice, the external loop hysteresis is the hysteresis loop which corresponds to the bigger amplitude voltage and the internal loops hysteresis correspond to an amplitude of voltage lower than the maximal voltage. In practice, especially while performing control of the system, the input signals are not sine waves signals and the applied voltage are usually lower than maximal voltage. Due to this fact, the hysteresis model should model both internal loops and external loop hysteresis in order to perform precise model of the system.

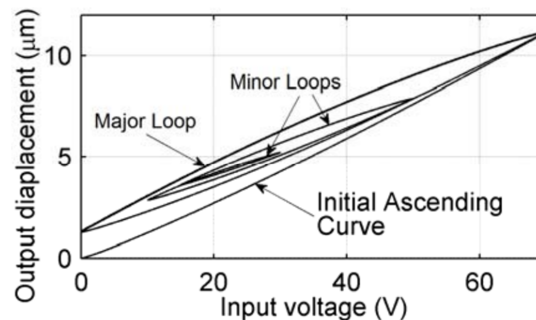

FIGURE 3.6: A typical curve showing the internal loop and external loop hysteresis for piezoelectric actuators.

The first models of the hysteresis, such as Polynomial models [60], were developed to take into consideration the external loop of the hysteresis and not the internal loops. Then, several hysteresis models have been developed in the past years in order to be able to model both external and inner loops of the hysteresis. These methods will be discussed in the following. It is known that the hysteresis in piezoelectric actuators is rate-dependent which means that the

hysteresis depends on the frequency of the system as well as on the past values of the applied voltage. It can be represented by an operator $\Gamma(U,s)$ where U is the applied voltage and $s = j \times 2\pi f$ is the Laplace operator which depends on the frequency f of the applied voltage signal. Some applications model the rate-independent hysteresis by working on a definite frequency for the system and others consider the rate-dependent hysteresis. The rate-dependent hysteresis models can be considered as extension of the rate-independent hysteresis models. Thus, most used rate-independent models of the hysteresis are detailed in the following and the final rate-dependent model of the hysteresis is deduced as an extension of the rate-independent hysteresis models by combining the hysteresis model to the dynamics of the actuator as it will be presented.

Rate-independent hysteresis model

The first approach of modeling the hysteresis is to model the static hysteresis or the hysteresis for a definite frequency. Such type of hysteresis is called *rate-independent* hysteresis. Preisach, Prandtl-Ishlinskii, Maxwell resistive capacitor and Bouc-Wen models are the most used hysteresis models in the literature.

- **Preisach hysteresis model**
  represents the hysteresis by the combined effect of infinite number of Preisach hysteresis operators $\delta_P(\alpha, \beta, u(t))$ as shown in Figure 3.7. Two parameters are used to characterize a Preisach hysteresis operator: the up switching value, α, and the down switching value, β, with $\alpha > \beta$. Each operator has two saturation values: 0 and 1, and its contribution to the model output is adjusted by $\mu_p = \mu_p(\alpha,\beta)$, referred to as the Preisach weighting function. The expression of Preisach (P) hysteresis model, involving N operators, is expressed in the discrete domain as follows:

  $$h_P(t) = \sum_{p=1}^{N} \mu_p \delta_p(\alpha,\beta,u(t)) \tag{3.1}$$

  where h_P is the output of the hysteresis and N is the number of the considered operators. As shown in Figure 3.7, the precision of the hysteresis loop increases when N increases at the cost of higher computation time. The ideal model is obtained when $N \to \infty$.

- **Prandtl-Ishlinskii hysteresis model**
  is represented by the combined effect of a finite number of plays or backlash operators as shown in Figure 3.8. The output, h_{PI}, of the Prandtl-Ishlinskii (PI) hysteresis model, involving N play operators, is defined as the sum of several backlashes each one having a threshold r_i and a weighting w_i as follows:

  $$h_{PI}(t) = \sum_{i=1}^{N} w_i \gamma_i(r_i,u(t)) \tag{3.2}$$

- **Maxwell resistive capacitor**
  represents the hysteresis by the combined effect of finite number of elasto-slide elements

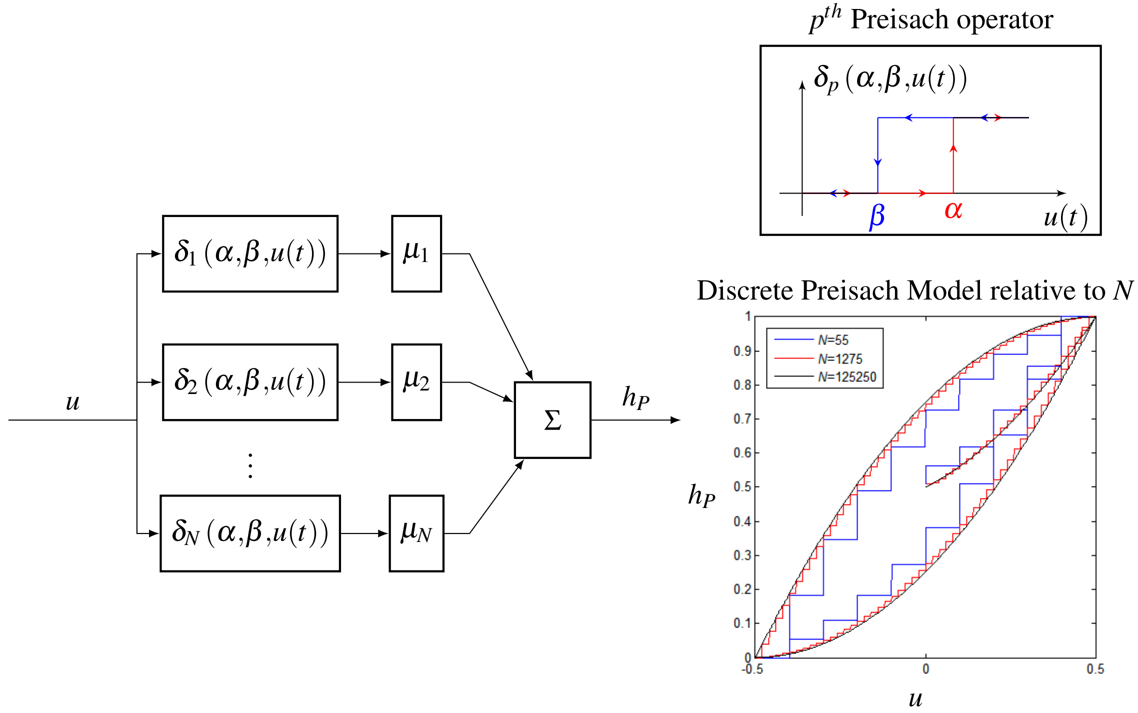

FIGURE 3.7: A block diagram showing the Preisach operators and the output of the hysteresis model, h_P, as sum of all the Preisach operators with weight functions.

or operators as shown in Figure 3.9. Each elasto-slide operator is composed of a mass connected to a spring of stiffness k and sliding on surface with a Coulomb friction $c = \mu \cdot N$, where μ is the friction coefficient and N is the normal force between the mass and the surface. The spring is connected from one end to the mass and is free from the other end. The free end of the spring can be used as input for the elasto-slide operator. Resulting from this model of the operator, a hysteresis relationship exists between the input displacement of the free end of the spring , $u(t)$, and the resulting force of the spring $F(u(t))$ as shown in Figure 3.9. Involving N operators, the resulting Maxwell resistive capacitor (MRC) hysteresis model is expressed as the total force experienced at the free end of the springs $h_{MRC}(t)$ as follows:

$$h_{MRC}(t) = F_{\text{total}} = \sum_{i=1}^{N} F_i(u(t)) \tag{3.3}$$

where $F_i(u(t))$ is the force in the ith spring of the operator induced by $u(t)$.

- **Bouc-Wen hysteresis model**
  consists of a nonlinear first order differential equation mathematical model to describe the hysteresis of the system. The Bouc-Wen model has been modified in [99] to fit to the

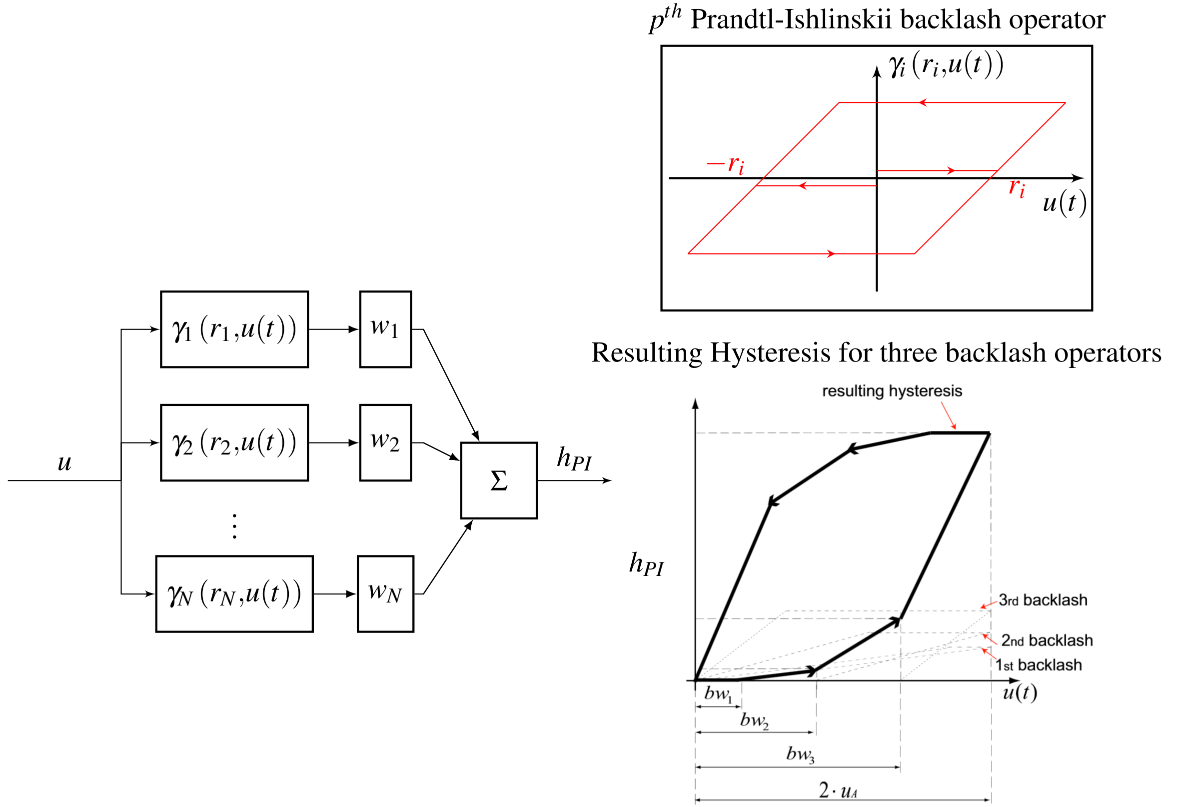

FIGURE 3.8: A block diagram showing the Prandt-Ishlinskii operators and the output of the hysteresis model, h_{PI}, as sum of all the Prandt-Ishlinskii operators with weight functions.

hysteresis of the piezoelectric actuator. It can be represented by the following equation:

$$\dot{h}_{BW}(t) = \lambda \dot{u}(t) - \beta |\dot{u}(t)| h_{BW}(t) - \gamma \dot{u}(t) |h_{BW}(t)| \quad (3.4)$$

where h_{BW} is the operator of the Bouc-Wen hysteresis, λ is a parameter which determines the amplitude of the hysteresis and β and γ are parameters which determine the shape of the hysteresis.

Rate-dependent hysteresis model

Rate-independent hysteresis models have been already presented and are only capable of representing the hysteresis behavior of a piezoelectric actuator in a narrow frequencies bands. In practice, the hysteresis of the piezoelectric actuator is highly dependent to the frequency of the system. Thus, in wide band frequencies applications as our application, the presented models need to fit to the rate-dependent hysteresis of the piezoelectric actuator. Two approaches exist to fit the models to rate-dependent hysteresis. The first approach is to combine rate-independent hysteresis model with the dynamic model of the system. The second approach is to modify

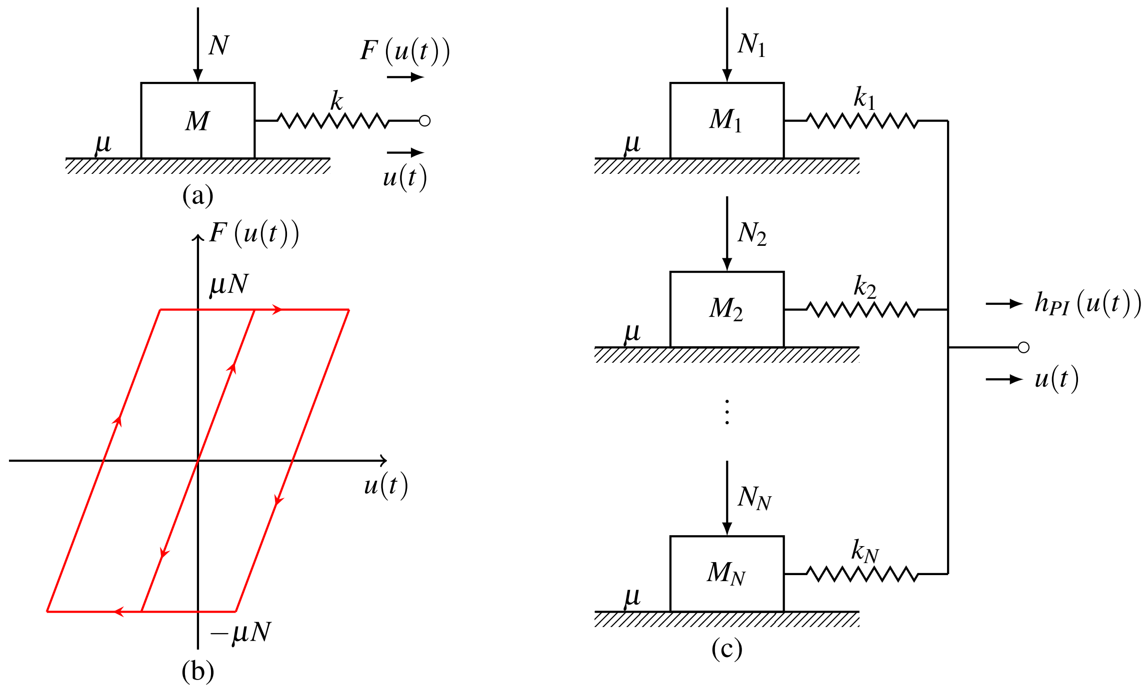

FIGURE 3.9: (a) An elasto-slide element, (b) its input-output relationship and (c) the physical interpretation of the Maxwell-resistive-capacitor hysteresis model.

the rate-independent hysteresis model into rate-dependent hysteresis models. In literature, both Preisach and Prandt-Ishlinskii hysteresis models have been modified into rate-dependent hysteresis models while the other models have been combined with the dynamic model of the system.

Choice of a hysteresis model

The Preisach and Prandt-Ishlinskii hysteresis models are the most used and the most precise models to model the piezoelectric actuator hysteresis. Due to their precision, they are used to perform feedforward control of the piezoelectric actuators. The use of Bouc-Wen model is less accurate for the modeling of the hysteresis. However, the model of the Bouc-Wen is simple and the identification of the Bouc-Wen model's parameters is also simple. In addition, the Bouc-Wen model can easily be extended to multi-input multi-output (MIMO) systems where the extension of the other models are mostly used for single-input single-output systems (SISO).

In this work, the choice has been made to combine the Bouc-Wen hysteresis model with the dynamic model of the system in order to model the hysteresis of the piezoelectric actuator. Indeed, the Bouc-Wen model is sufficient to model the hysteresis, its model is simple and its identification process is also simple. Moreover, using Bouc-Wen model, the same approach can be used to extend our work to multi-DOF piezoelectric actuators.

3.3.2 Dynamic nonlinear model of a 2-DOF duo-bimorph piezoelectric actuator

Extensive researches have been made in the past years on the piezoelectric actuators including their fabrication, models and control. Several models have been developed for the piezoelectric actuators. The main differences between the models are the method to model the nonlinearities and the dynamics of the system. Some linear and static models have been developed in [150]. Others consider the nonlinearities of the actuator in several methods as presented in section 3.3.1. Others consider the dynamics as a linear second or higher order transfer function [99]. Some researchers have also developed discrete-models for the piezoelectric actuator [17]. In this section, a dynamic nonlinear model of the piezoelectric actuator is developed. The nonlinearity is modeled by the Bouc-Wen hysteresis model with a dynamic linear part which represents the dynamics of the actuator. Although the linear part of the actuator can be described by a higher order transfer function, a second order transfer function is sufficient to represent the dynamics and its use is popular in many applications [99, 134, 192].

In our application, the duo-bimorph piezoelectric actuator [30, 1] developed in AS2M department of FEMTO-ST is used. It is a 2-DOF actuator and can move in both directions y and z. A static and linear model of the duo-bimorph piezoelectric actuator has been developed in [118]. Figure 3.10 shows a scheme of the duo-bimorph piezoelectric actuator showing the two layers of piezoelectric material, an elastic layer between them and the electrodes where a voltage is applied. An extension of the 1-DOF piezoelectric actuator model developed in [150, 9] have been developed in [30, 118] to take into account the 2-DOF displacement. To develop the model of the 2-DOF actuator, two main assumptions are considered:

- No coupling between the axis y and z is considered. This assumption has been made in [118] to simplify the model. Moreover, in our application, 1-DOF model is needed and consequently this assumption simplifies the development of the model.
- The actuator is composed of three layers (2 piezoelectric material layers and 1 elastic layer). No sliding between the layers of actuators is considered. This assumption is a classical assumptions for the modeling of piezoelectric actuator.

The validity of these assumptions will be investigated in the experimental validation step.

The model at the tip of the duo-bimorph actuator, without taking into consideration the coupling between the y and z axis, can be written as follows:

$$\begin{pmatrix} \alpha_y \\ \delta_y \\ V_y \\ Q_y \\ \alpha_z \\ \delta_z \\ V_z \\ Q_z \end{pmatrix} = \begin{pmatrix} a_{11} & a_{12} & a_{13} & a_{14} & 0 & 0 & 0 & 0 \\ a_{21} & a_{22} & a_{23} & a_{24} & 0 & 0 & 0 & 0 \\ a_{31} & a_{32} & a_{33} & a_{34} & 0 & 0 & 0 & 0 \\ a_{41} & a_{42} & a_{43} & a_{44} & 0 & 0 & 0 & 0 \\ 0 & 0 & 0 & 0 & a_{55} & a_{56} & a_{57} & a_{58} \\ 0 & 0 & 0 & 0 & a_{65} & a_{66} & a_{67} & a_{68} \\ 0 & 0 & 0 & 0 & a_{75} & a_{76} & a_{77} & a_{78} \\ 0 & 0 & 0 & 0 & a_{85} & a_{86} & a_{87} & a_{88} \end{pmatrix} \begin{pmatrix} M_z \\ F_y \\ p_y \\ U_y \\ M_y \\ F_z \\ p_z \\ U_z \end{pmatrix} \tag{3.5}$$

where M_y and M_z are the bending moments along y and z axes respectively, F_y and F_z are the applied forces along y and z axes respectively, p_y and p_z are the pressure loads along y and z

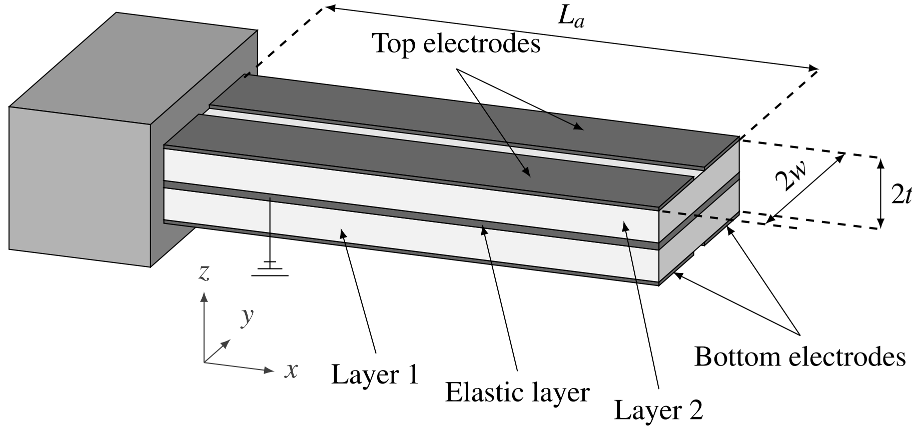

FIGURE 3.10: A scheme of a 2-D duo-bimorph piezoelectric actuator showing the two layers of piezoelectric materials, the elastic layer which is connected to the ground and the electrodes.

axes respectively, U_y and U_z are the electrical voltages along y and z axes respectively, α_y and α_z are the bending angles along y and z axes respectively. δ_y and δ_z are the deflections along y and z axes respectively, V_y and V_z are the volume displacements along y and z axes respectively and Q_y and Q_z are the charges along y and z axes respectively. The parameters a_{ij} of the system are calculated using the same approach used in [150].

In a micromanipulation or microassembly task, the gripping forces are along the Y axis. Thus, in our study, we will develop the model along the Y axis without considering the model along the Z axis. The model of the piezoelectric actuator can be reduced in this case to the 1-DOF case studied in [150, 9]. A scheme of a 1-DOF bimorph piezoelectric actuator is shown in Figure 3.11 where a voltage U, a force F, a moment M and a pressure load p are applied on the actuator. t_1 and t_2 are thicknesses of layers 1 and 2 respectively, w is the width of the two layers and l is the length of the two layers. Among the widely existing models, one classical, commonly used, static, linear model of the actuator is presented in [150, 9] as follows:

$$\begin{pmatrix} \alpha(x) \\ \delta(x) \\ V(x) \\ Q(x) \end{pmatrix} = \begin{pmatrix} m_{11}(x) & m_{12}(x) & m_{13}(x) & m_{14}(x) \\ m_{21}(x) & m_{22}(x) & m_{23}(x) & m_{24}(x) \\ m_{31}(x) & m_{32}(x) & m_{33}(x) & m_{34}(x) \\ m_{41}(x) & m_{42}(x) & m_{43}(x) & m_{44}(x) \end{pmatrix} \begin{pmatrix} M(x) \\ F(x) \\ p \\ U \end{pmatrix} \tag{3.6}$$

where $M(x)$ is the bending moment, $F(x)$ is the applied force, p is the pressure load, U is the electrical voltage, $\alpha(x)$ is the bending angle along the Y axis and around the Z axis, $\delta(x)$ is the deflection along the Y axis, V is the volume displacement and Q is the charge as shown in Figures 3.11 and 3.12. The parameters m_{ij} are the parameters of the coupling matrix. $\alpha(x)$, $\delta(x)$, $V(x)$, $Q(x)$, $M(x)$ and $F(x)$ and the parameters $m_{ij}(x)$ depend on the position on the actuator along the X axis where the each value needs to be calculated (e.g. at the tip of the actuator $x = L_a$). In the following, the problem will be considered at the tip of the actuator and consequently $x = L_a$.

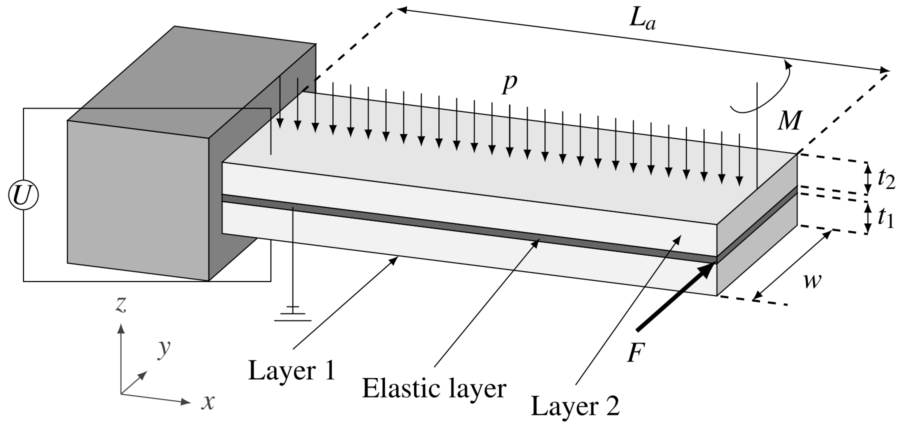

FIGURE 3.11: A scheme of a 1-D bimorph piezoelectric actuator where a voltage U, a force F, a moment M and a pressure load p are applied.

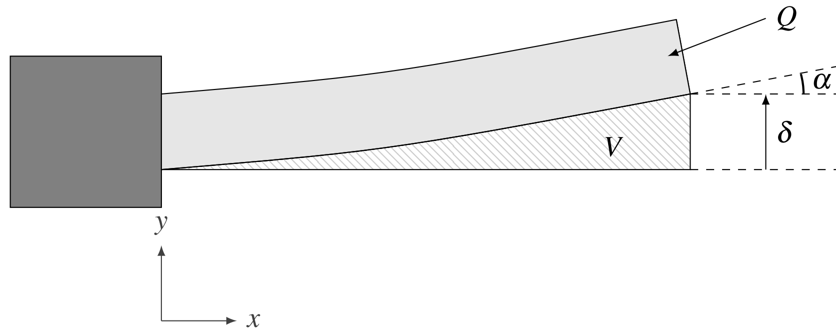

FIGURE 3.12: A top view of Figure 3.11 showing the displacement of the bimorph piezoelectric actuator and showing the output variables: the bending angle α, the deflection δ, the volume displacement V and the charge Q.

In a micromanipulation or microassembly task, the deflections and the bending angles are the most important to perform the precise positioning where the inputs of the system can be the forces, moments and the voltage. The pressure loads can be ignored because it is rarely encountered in a microassembly or micromanipulation task. Consequently, the model defined in Equation (3.6) can be simplified as follows:

$$\begin{pmatrix} \alpha_A \\ y_A \end{pmatrix} = \begin{pmatrix} m_{11} & m_{12} & m_{14} \\ m_{21} & m_{22} & m_{24} \end{pmatrix} \begin{pmatrix} M_A \\ F_A \\ U \end{pmatrix} \tag{3.7}$$

where the parameters $\alpha_A = \alpha(x = L_a)$, $y_A = \delta(x = L_a)$, $M_A = M(x = L_a)$, $F_A = F(x = L_a)$ and $m_{ij} = m_{ij}(x = L_a)$ are respectively the bending angle along the Y axis, the displacement along

the Y axis, the bending moment at the actuator tip around Z axis, the applied force at the actuator tip along the Y axis and the parameters at the tip of the actuator.

This static model (defined in Equation (3.7)) can be extended to develop a dynamic model by adding the dynamic part of the actuator which can be modeled as a linear transfer function, $D(s)$, with a static gain equal to 1, where s is the Laplace operator. Although the linear part of the system can be described by a higher order transfer function, a second order transfer function is sufficient to represent the dynamics of the actuator and its use is popular in many applications [99, 134, 192]. Adding the transfer function to the static model defined in Equation (3.7), the following dynamic model can be developed:

$$\begin{pmatrix} \alpha_A \\ y_A \end{pmatrix} = D(s) \cdot \begin{pmatrix} -\frac{3}{L_a^2} s_p & -\frac{3}{2L_a} s_p & \frac{2}{L_a} d_p \\ -\frac{3}{2L_a} s_p & -s_p & d_p \end{pmatrix} \cdot \begin{pmatrix} M_A \\ F_A \\ U \end{pmatrix} \tag{3.8}$$

where d_p is the piezoelectric coefficients along the Y axis, s_p is the elastic constant along the Y axis and L_a is the length of the actuator. The values of the parameters of the matrix defined in Equation (3.8) are calculated using the parameters m_{ij} defined in [150, 9, 1] for $x = L_a$.

The nonlinearties of the piezoelectric actuator are mainly manifested by the hysteresis (with neglecting the effect of creep as already discussed in section 3.3.1). As discussed in the section 3.3.1, the nonlinearities are rate-dependent and can be modeled by a nonlinear operator $\Gamma(U,s)$ as follows:

$$\Gamma(U,s) = H(U,s) \tag{3.9}$$

where $H(U,s)$ is the hysteresis of the piezoelectric actuator. In section 3.3.1, the choice has been made to combine the Bouc-Wen hysteresis model with the the dynamic model of the system to model the rate-dependent hysteresis of the piezoelectric actuator. This consists of modeling the dynamical hysteresis of the piezoelectric actuator, $H(U,s)$, by a static hysteresis $H_s(U)$, followed by a linear dynamic part, $D(s)$, which represents the dynamics of the piezoelectric actuator, as shown in Figure 3.13. In Figure 3.13, U is the voltage applied to the piezoelectric

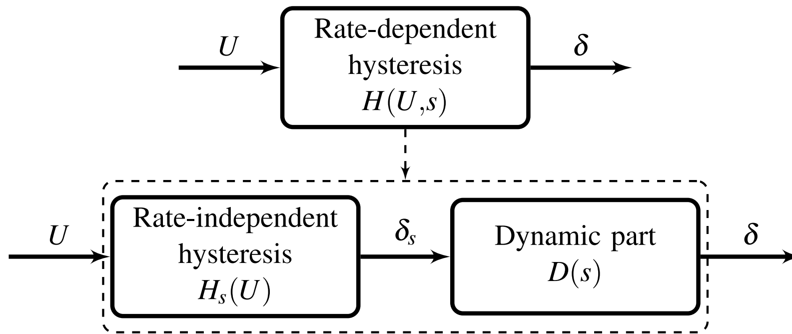

FIGURE 3.13: Dynamic hysteresis could be decomposed in a static part followed by a dynamical part.

actuator, δ is the output of the hysteresis bloc, δ_s is the static output of the Bouc-Wen static hysteresis model, $H(U,s)$ is the rate-dependent hysteresis which depends on the voltage, U,

and the frequency which is written as the Laplace operator, $s = j2\pi f$, and $H_s(U)$ is the static hysteresis determined by the Bouc-Wen model (see Equation (3.4)).

The dynamical hysteresis of the piezoelectric actuator is determined using the following steps, [131]:

1. The dynamic part of the piezoelectric actuator, $D(s)$, is identified. The dynamical part could be considered independent of the amplitude of the input voltage U. It is determined by applying several steps of different amplitudes and then the dynamical response could be approximated by a second order transfer function as is commonly used with a unit static gain (*i.e.* $D(0) = 1$).

2. We apply a sine voltage with a low frequency (0.1 Hz) and identify the Bouc-Wen parameters to minimize the error between the experimental result of the displacement of the actuator and the Bouc-Wen model for the displacement of the actuator. Using this method we determine $H_s(U)$.

3. The dynamical hysteresis of the piezoelectric actuator is determined, using the two previous steps, by the relation $H(U,s) = H_s(U) \cdot D(s)$.

The nonlinearities depend on the voltage of the piezoelectric actuator and not on the forces and moments. Including the Bouc-Wen hysteresis model of the piezoelectric actuator in Equation (3.8), the following model can be deduced:

$$\begin{pmatrix} \alpha_A \\ y_A \end{pmatrix} = D(s) \cdot \begin{pmatrix} -\frac{3}{L_a^2} s_p & -\frac{3}{2L_a} s_p & \frac{2}{L_a} d_p \\ -\frac{3}{2L_a} s_p & -s_p & d_p \end{pmatrix} \cdot \begin{pmatrix} M_A \\ F_A \\ U \end{pmatrix} - D(s) \cdot \begin{pmatrix} \frac{2}{L_a} H_s(U) \\ H_s(U) \end{pmatrix} \tag{3.10}$$

where $H_s(U)$ represents the static hysteresis using the Bouc-Wen model along the Y axis. Equation (3.10) can also be written by separating the static part and the dynamic part as follows:

$$\begin{pmatrix} \alpha_A \\ y_A \end{pmatrix} = D(s) \cdot \left[\begin{pmatrix} -\frac{3}{L_a^2} s_p & -\frac{3}{2L_a} s_p & \frac{2}{L_a} d_p \\ -\frac{3}{2L_a} s_p & -s_p & d_p \end{pmatrix} \begin{pmatrix} M_A \\ F_A \\ U \end{pmatrix} - \begin{pmatrix} \frac{2}{L_a} H_s(U) \\ H_s(U) \end{pmatrix} \right] \tag{3.11}$$

Using Equations (3.4) and (3.11), the final model of the duo-bimorph actuator, which will be used in the rest of this manuscript, including the Bouc-Wen model for the hysteresis and the dynamic part, can be written in the following equation which is convenient with the models presented in literature:

$$\begin{cases} y_A(s) = \left[d_p U - H_s(U) - s_p F_A - \dfrac{3}{2L_a} s_p M_A \right] \cdot D(s) \\ \alpha_A(s) = \left[\dfrac{2}{L_a} \left(d_p U - H_s(U) \right) - \dfrac{3}{2L_a} s_p F_A - \dfrac{3}{L_a^2} s_p M_A \right] \cdot D(s) \\ \dot{H}_s(U) = \lambda \dot{U} - \beta \left| \dot{U} \right| H_s(U) - \gamma \dot{U} \left| H_s(U) \right| \\ D(s) = \dfrac{1}{as^2 + bs + 1} \end{cases} \tag{3.12}$$

where the third line of Equation (3.12) is a rewritten of the Equation of Bouc-Wen hysteresis model which has been defined in Equation (3.4) where h_{BW} is replaced by H_s. All the parameters of the actuator's model defined in Equation (3.12) are summarized as follows:

- y_A is the displacement of the piezoelectric actuator's tip A along the Y axis,
- α_A is the bending angle of the actuator's tip along the Y axis and around the Z axis,
- d_p is the piezoelectric constant and s_p is the elastic constant,
- L_a is the length of the actuator,
- F_A is an external force applied at the actuator's tip along the Y axis,
- M_A is an external torque applied at the actuator's tip around the Z axis,
- U is the applied voltage to the piezoelectric actuator,
- $H_s(U)$ is an internal variable to represent the rate-independent Bouc-Wen hysteresis model,
- λ is a parameter which determines the amplitude of the hysteresis,
- β and γ are parameters which determine the shape of the hysteresis,
- $D(s)$ is a transfer function to represent the dynamics of the actuator,
- a and b are constants to determine the dynamics of the actuator.

3.4 Model of the Two-Smart-Fingers Microgripper (TSFM)

The model of a piezoelectric actuator has been developed in Section 3.3. However, the integration of the force sensor into the piezoelectric actuator has to be considered in the complete system modeling. A scheme of the Two-Smart-Fingers Microgripper (TSFM) is presented in Figure 3.14. The points A, B and C are respectively the tips of the actuator, the rigid part and the force sensor.

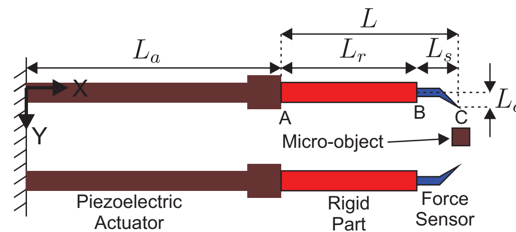

FIGURE 3.14: Complete scheme of the two-smart-fingers microgripper (TSFM).

Two steps will be considered during the modeling of the system:

- free motion step where the two fingers of the TSFM move without contact,

- constrained motion step where there is a contact between each finger and the manipulated micropart.

Two types of objects are also considered in the modeling: rigid and flexible.

3.4.1 Model of the sensorized end-effector

The end-effector is composed of two parts: a rigid part made of 350 µm thick silicon layer and the force sensor which has 10 µm of thickness. The rigid part tip of the end-effector is the point B (see Figure 3.14) and the force sensor tip is the point C (see Figure 3.14).

The rigid part can be considered as a lever system with a length of L_r. It is used for three main reasons:

1. the end-effector can be manipulated, after its fabrication and before the integration inside the TSFM, using this rigid part, otherwise the force sensor can easily be broken,
2. the electric connections of the force sensor are made on this rigid part,
3. the effect of adding a rigid part, which acts as a lever system, increases the displacement of the whole finger ($y_B > y_A$).

The force sensor is flexible and can be modeled as a beam with length L_s with a mass-spring-damper system with mass m_s, damping d_s and stiffness k_s. L_s is the length of the force sensor.

The end-effector equivalent system is represented in Figure 3.15.

3.4.2 Micromanipulation sequence and related modeling

As the microgripper enters in interaction with different types of objects, a generic scenario is considered for the model of the system where one smart finger enters in contact with a flexible environment. The environment represents the system which the smart finger enters in contact. In our case, it can be flexible or rigid microparts. The flexible environment can be modeled as a mass-spring-damper system. A typical micromanipulation scenario is presented in Figure 3.16 showing the free motion of the two fingers of the TSFM and the constrained motion. First, the two fingers and the micropart are in their initial positions with no motion. The micropart is not exactly at the middle of the two fingers. Thus, a contact may happen between one finger and the micropart before the other finger. Second, the two fingers are in the free motion without any contact between the fingers and the micropart. Third, a contact appears between one of the fingers and the micropart while the other finger stills in the free motion. Fourth, both of the fingers have contact with micropart and both of them are in the constrained motion. and contact steps for the manipulation of a micropart. When the fourth case reached, each of the fingers of the TSFM is supposed to have contact with a flexible environment where the environment is the micropart and the second finger. The same model applies for both flexible micropart and rigid micropart. However, the only difference between the two types of microparts are the mechanical parameters (*i.e.* mass, damping and stiffness). Moreover, in the case of rigid micropart, we can consider that the stiffness of the flexible environment resulting of the micropart and the second

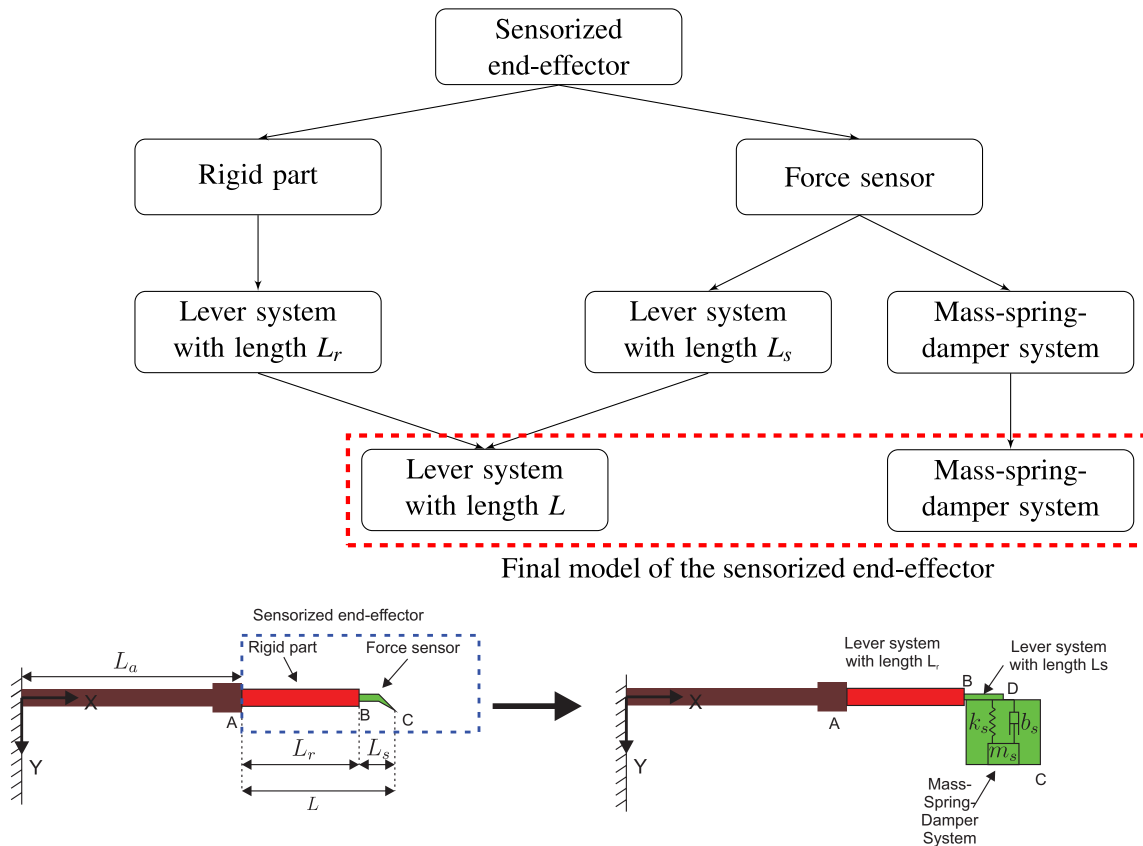

FIGURE 3.15: Equivalent scheme of the sensorized end-effector.

finger is variable in order to compensate the effects of the active part of the actuator. A generic equivalent scheme of the manipulation is given in Figure 3.17.

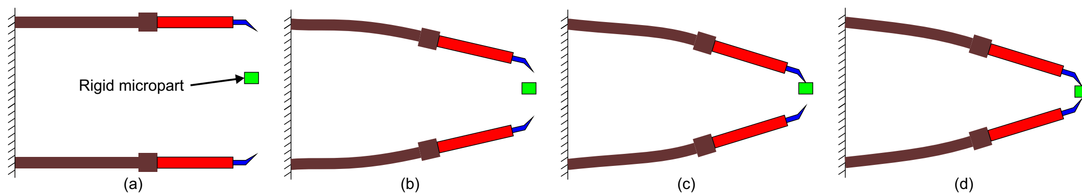

FIGURE 3.16: Four cases for the manipulation of a rigid micropart: (a) the micropart is placed between the fingers of the microgripper, (b) a voltage is applied to move the two fingers, (c) a contact appears between one of the fingers and the micropart and (d) a contact between the two fingers and the micropart appears.

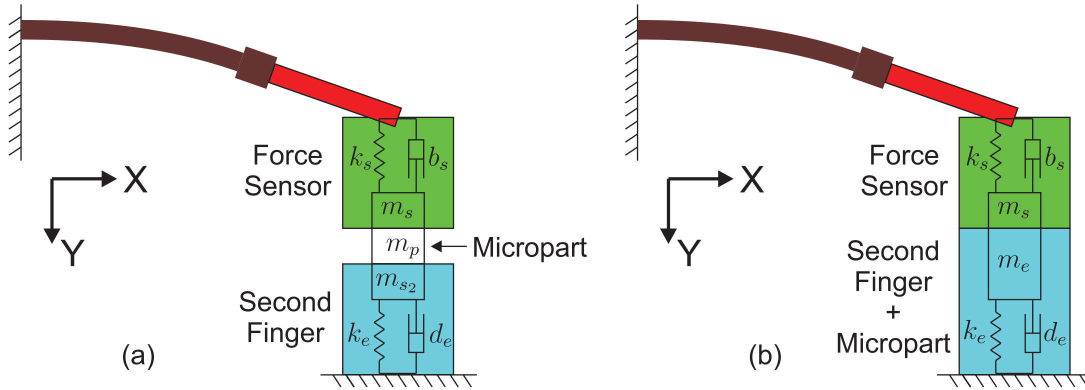

FIGURE 3.17: The equivalent scheme of microgripper manipulating a rigid micropart: (a) the mass of finger (m_{s_2}) is separated of the mass of the micropart (m_p) and (b) the mass of the finger is combined with the mass of the micropart ($m_e = m_{s_2} + m_p$).

Finally, one model needs to be developed for the two types of the microparts because the final equivalent scheme is the same where a smart finger has a contact with a flexible environment which can be modeled as a mass-spring-damper system with mass m_e, damping d_e and stiffness k_e. Note that in the case of the manipulation of a rigid micropart k_e is the stiffness of one finger, d_e is the damping of one finger and $m_e = m_{s_2} + m_p$ is the sum of the mass of the second smart finger and the mass of the micropart; where in the case of the manipulation of the flexible micropart, m_e, d_e and k_e are respectively the mass, damping and stiffness of the flexible micropart.

3.4.3 Model of the free motion of the TSFM

In this section, the model of each finger of the gripper is considered in the free motion case where a voltage is applied on the actuator and no contact happens during the motion of the finger between the microgripper and the micropart (no force is applied). The dynamic scheme of the system is shown in Figure 3.18. In this Figure, three cases are considered and for each case there are two equivalent schemes: the left schemes represent the scheme of the system in three different cases while the rights schemes represent the scheme of the system after replacing the force sensor in a lever system and mass-spring-damper system. D is the tip of the lever system of the force sensor. Figure 3.18 shows three different scenarios for the system:

(a) no voltage is applied at the actuator,

(b) a voltage is applied and the actuator position is considered in a case where the spring of the force sensor (k_s) is in its equilibrium position without any deformation *i.e.* $L_e = L_o cos\alpha_A$,

(c) a voltage is applied and the actuator position is considered in a case where the spring of the force sensor (k_s) has deformed and is not in its equilibrium position *i.e.* $L_e \neq L_o cos\alpha_A$,

In the following small deformations are considered and then $cos\alpha_A \approx 1$ and $sin\alpha_A \approx \alpha_A$.

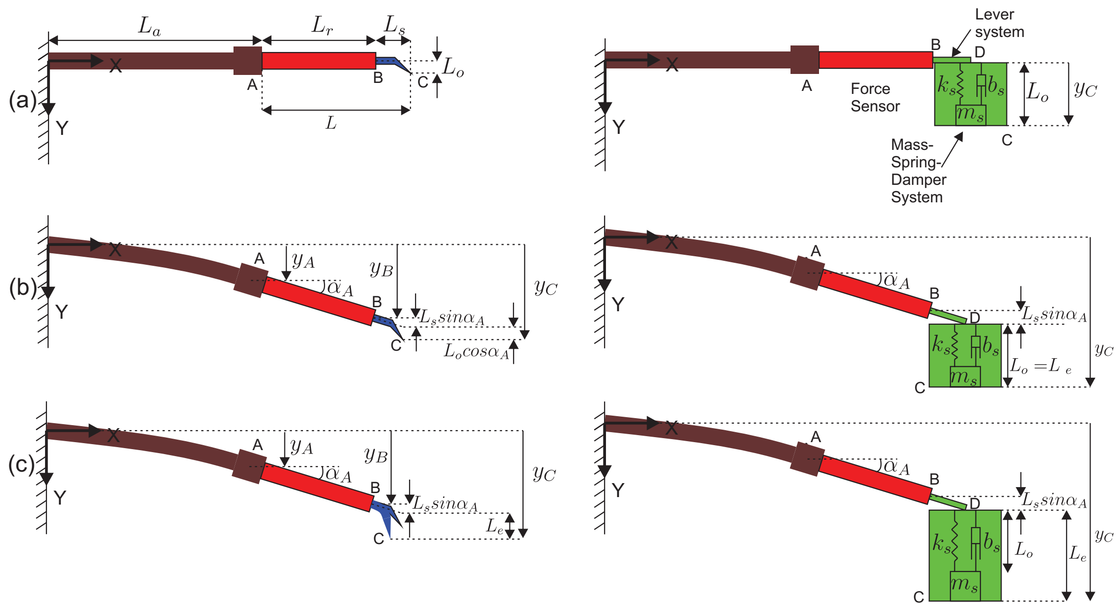

FIGURE 3.18: Equivalent scheme of the free motion of one smart finger: (a) without any applied voltage ($U = 0$), (b) voltage is applied (quasi-static behavior), (c) voltage is applied (dynamic behavior). For each of the three cases, at left the scheme of the gripper and at right the scheme of gripper after replacing the force sensor by a lever system connected to a mass-spring-damper system.

The steps to determine the model of the system are summarized in Figure 3.19. First, the model of the piezoelectric actuator is presented alone, then the model at the tip B of the lever system of the rigid part is considered, then the model at the tip D of the lever system of the force sensor is considered, finally the model of the system at the force sensor's tip C is considered.

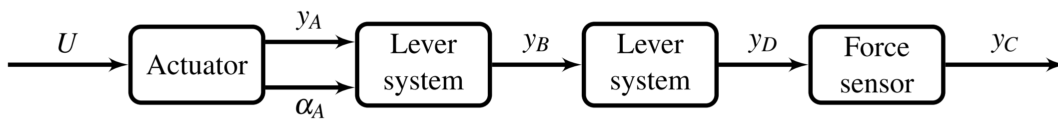

FIGURE 3.19: Bloc diagram to show the method to determine the free motion model of the TSFM.

The model of the piezoelectric actuator given in Equation (3.12) is rewritten in the following in the case of free motion without any applied force or moment:

$$\begin{cases} y_A(s) = (d_pU - H_s(U))\,D(s) \\ \alpha_A(s) = \dfrac{2}{L_a}(d_pU - H_s(U))\,D(s) \\ \dot{H}_s(U) = \lambda\dot{U} - \beta|\dot{U}|H_s(U) - \gamma\dot{U}|H_s(U)| \\ D(s) = \dfrac{1}{as^2+bs+1} \end{cases} \tag{3.13}$$

The displacement at the tip B is given by the following:

$$y_B = y_A + L_r sin\alpha_A \approx y_A + L_r\alpha_A \tag{3.14}$$

where L_r is the length of the rigid part. Using Equations (3.13) and (3.14), y_B can also be written as:

$$y_B = \left(1+\frac{2L_r}{L_a}\right)(d_pU - H_s(U))\,D(s) \tag{3.15}$$

As the force sensor is modeled as a lever system with a mass-spring-damper system at its tip, the displacement at the lever system tip is given as follows:

$$y_D = y_B + L_s\alpha_A = y_A + (L_r+L_s)\,\alpha_A = y_A + L\alpha_A = \left(1+\frac{2L}{L_a}\right)(d_pU - H_s(U))\,D(s) \tag{3.16}$$

where $L = L_r + L_s$. As no force is applied at the tip C of the force sensor, the following could be written:

$$m_s\ddot{y}_C(t) + b_s\Delta\dot{L} + k_s\Delta L = 0 \tag{3.17}$$

where ΔL is the deformation of the force sensor and is given as follows considering small deformation ($L_o cos\alpha_A \approx L_o$):

$$\Delta L = L_e - L_o \tag{3.18}$$

where L_e is the equivalent current length of the force sensor and L_o is the length of the lever of the force sensor on the Y axis at equilibrium. Using Figure 3.20, L_e can be given as follows:

$$L_e = y_C - y_D \tag{3.19}$$

Replacing Equation (3.18) in Equation (3.17), the following can be deduced:

$$m_s\ddot{y}_C + b_s\left(\dot{y}_C - \dot{y}_D - \dot{L}_o\right) + k_s\left(y_C - y_D - L_o\right) = 0 \tag{3.20}$$

Then, using the Laplace transform of Equation (3.20):

$$Y_C = \frac{b_s s + k_s}{m_s s^2 + b_s s + k_s}\left(Y_D + L_o\right) \tag{3.21}$$

Replacing Equation (3.16) in Equation (3.21), the displacement of point C in free motion can be deduced by:

$$Y_C = \frac{b_s s + k_s}{m_s s^2 + b_s s + k_s}\left[\left(1+\frac{2L}{L_a}\right)(d_pU - H_s)\,D(s) + L_o\right] \tag{3.22}$$

3.4.4 Model of the constrained motion of the TSFM

In this section, the microgripper finger moves until entering in contact with the micropart. The considered scenario is that one of the fingers of the microgripper enters in contact with the micropart and brings the micropart towards contact with the second finger in order to manipulate the micropart. The force measured by the force sensor increases once a contact appears ($F_s \neq 0$). Figure 3.20 shows four different cases for the system:

(a) no motion of the finger and no applied voltage,

(b) free motion of the actuator without any contact (the same case as in section 3.4.3),

(c) just at transition between free and constrained motion of the finger ($F_s = 0$),

(d) constrained motion which happens after the contact ($F_s \neq 0$).

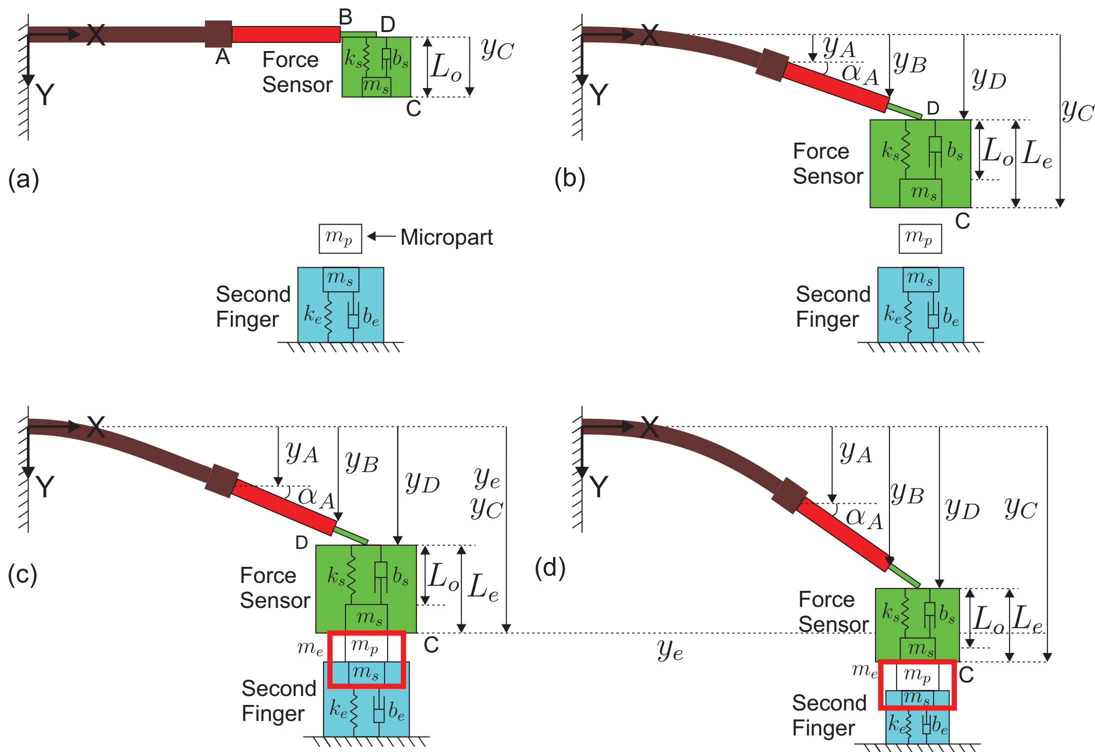

FIGURE 3.20: Equivalent dynamic scheme of the constrained motion of one of the TSFM fingers in four cases: (a) no motion without contact and without any applied voltage ($F_s = 0$ and $U = 0$) (b) free motion with an applied voltage to the finger ($F_s = 0$ and $U \neq 0$ the same case considered in Figure 3.18-(c)), (c) just at the transition between free motion and constrained motion ($F_s = 0$) and (d) constrained motion after contact ($F_s \neq 0$).

Notice that the deflection of the actuator is always considered to be in a simple deflection mode as shown in Figure 3.20-(d). This assumption is done because the actuator is 10 time stiffer than

the force sensor which means that the deflection due to contact force will be mainly at the force sensor.

The method to determine the model of the system, when a contact between the microgripper and micropart exists, is summarized in Figure 3.21. First, the model of the piezoelectric actuator is presented alone taking into consideration the voltage applied on the actuator, the force and the moment, then the model of the displacement of tip B of the lever system of the rigid part is considered, then the model of the displacement at the tip D of the lever system of the force sensor is considered, finally the model of both displacement, y_C, and gripping force F_g is applied at the force sensor's tip C is considered. A gripping force, F_g, is applied by the force sensor on the micropart while F_s is the measured force by the force sensor which is the force applied by the micropart on the force sensor. An applied force, $F_s = -F_g$ on the force sensor induces reaction force and a moment on the actuator's tip A as follows:

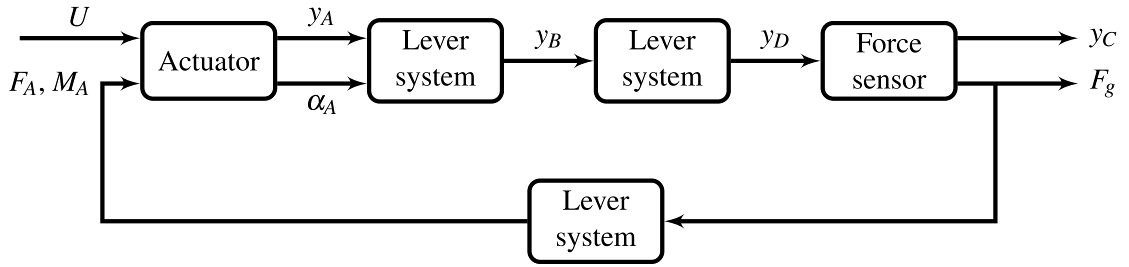

FIGURE 3.21: Bloc diagram to show the method to determine the constrained motion model of the TSFM. Notice that y_A and α_A are coupled but their separation is done to clarify the parameters needed for the model.

$$\begin{cases} F_A = -F_s + m_s\ddot{y}_C = F_g + m_s\ddot{y}_C \\ M_A = -LF_s = LF_g \end{cases} \tag{3.23}$$

where $F_g = -F_s$ is the gripping force applied by the force sensor on the micropart and F_s is the force measured by the force sensor.

The piezoelectric actuator model with the presence of an applied force, F_A, and a torque, M_A, on the actuator's tip A is given, according to Equation (3.12), as follows:

$$\begin{cases} y_A(s) = \left[d_pU - H_s(U) - s_pF_A - \frac{3}{2L_a}s_pM_A\right]\cdot D(s) \\ \alpha_A(s) = \left[\frac{2}{L_a}\left(d_pU - H_s(U)\right) - \frac{3}{2L_a}s_pF_A - \frac{3}{L_a^2}s_pM_A\right]\cdot D(s) \\ \dot{H}_s(U) = \lambda\dot{U} - \beta\left|\dot{U}\right|H_s(U) - \gamma\dot{U}\left|H_s(U)\right| \\ D(s) = \frac{1}{as^2+bs+1} \end{cases} \tag{3.24}$$

In the case considered in this document, the force is applied at the tip of the force sensor C. Replacing Equation (3.23) in Equation (3.24), the following can be deduced:

$$\begin{cases} Y_A(s) = \left[d_pU - H_s(U) - \left(1+\dfrac{3L}{2L_a}\right)s_pF_g - m_ss_ps^2Y_C\right]D(s) \\ \alpha_A(s) = \left[\dfrac{2}{L_a}\left(d_pU - H_s(U)\right) - \left(\dfrac{3}{2L_a}+\dfrac{3L}{L_a^2}\right)s_pF_g - \dfrac{3}{2L_a}m_ss_ps^2Y_C\right]D(s) \end{cases} \tag{3.25}$$

The position of the point D, y_D, is calculated as follows:

$$y_D = y_B + L_s\alpha_A = y_A + (L_r + L_s)\,\alpha_A = y_A + L\alpha_A \tag{3.26}$$

where $L = L_r + L_s$. Replacing Equation (3.25) in Equation (3.26), the following can be deduced:

$$Y_D = \left[\left(1+\frac{2L}{L_a}\right)\left(d_pU - H_s(U)\right) - \left(1+\frac{3L}{L_a}+\frac{3L^2}{L_a^2}\right)s_pF_g - \left(1+\frac{3L}{2L_a}\right)m_ss_ps^2Y_C\right]D(s) \tag{3.27}$$

In this case as a force is applied at the tip of the force sensor which is modeled as a mass-spring-damper system, the applied force at the tip of the force sensor can be given as follows:

$$F_s = m_s\ddot{y}_C(t) + b_s\dot{\Delta L} + k_s\Delta L \tag{3.28}$$

where $\Delta L = L_e - L_o = y_C - y_D - L_o$ is the same as in the non contact case Equation (3.18). Then, replacing ΔL in Equation (3.28), the following can be deduced:

$$F_s = m_s\ddot{y}_C + b_s\left(\dot{y}_C - \dot{y}_D - \dot{L}_o\right) + k_s\left(y_C - y_D - L_o\right) \tag{3.29}$$

In the other hand, using Equation (3.29), the following can be deduced:

$$Y_C = \frac{b_ss + k_s}{m_ss^2 + b_ss + k_s}\left(Y_D + L_o\right) - \frac{1}{m_ss^2 + b_ss + k_s}F_g \tag{3.30}$$

Replacing Equation (3.27) in Equation (3.30), the displacement Y_C can be given as follows:

$$Y_C = G_u(s)\left(d_pU - H_s(U) - G_fF_g\right) \tag{3.31}$$

where:

$$\begin{cases} G_u(s) = \dfrac{\left(1+\frac{2L}{L_a}\right)(b_ss+k_s)}{(as^2+bs+1)(m_ss^2+b_ss+k_s) + \left(1+\frac{3L}{2L_a}\right)(b_ss+k_s)\,m_ss_ps^2} \\ G_f(s) = \dfrac{as^2 + \left[b + \left(1+\frac{3L}{L_a}+\frac{3L^2}{L_a^2}\right)s_pb_s\right]s + 1 + \left(1+\frac{3L}{L_a}+\frac{3L^2}{L_a^2}\right)s_pk_s}{\left(1+\frac{2L}{L_a}\right)(b_ss+k_s)} \\ \dot{H}_s(U) = \lambda\dot{U} - \beta\left|\dot{U}\right|H_s(U) - \gamma\dot{U}\left|H_s(U)\right| \end{cases} \tag{3.32}$$

When a contact is established between the two fingers and the micropart, each finger could be considered in contact with a mass-spring-damper environment. The model of the environment is given by:

$$F_g = \begin{cases} 0 & \text{if} \quad y_C < y_e \\ m_e\ddot{y}_C + b_e\dot{y}_C + k_e\,(y_C - y_e) & \text{if} \quad y_C \geq y_e \end{cases} \tag{3.33}$$

Using Equation (3.31) and Equation (3.33), the following can be deduced:

$$F_g = \begin{cases} 0 & \text{if} \quad y_C < y_e \\ H_u(s)\,[d_pU - H_s(U)] - H_e(s)Y_e & \text{if} \quad y_C \geq y_e \end{cases} \tag{3.34}$$

where $H_s(U)$ is an operator to show the static Bouc-Wen hysteresis model; $H_u(s)$ and $H_e(s)$ are two 4th order transfer functions combining the dynamics of the actuator, force sensor and flexible environment. Their big expressions are given in the Appendix A.

The final model of the TSFM can be represented as a bloc diagram in Figure 3.22 where the voltage, U, applied to the actuator is a single input to the TSFM and the outputs are the displacement, y_C, of the force sensor's tip C and the measured gripping force, F_g. Notice that, the location, y_e, of the component to be manipulated relative to the TSFM's fingers when the contact object-fingers is established (i.e. just before applying a force on the object) is a parameter which influences the model as shown in the same Figure. However, y_e is not a controlled input.

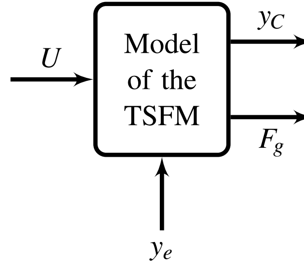

FIGURE 3.22: Bloc diagram showing the final model of the TSFM.

The models defined in Equation (3.31) and Equation (3.34) are developed in order to determine the control law in the next chapter. In experiments, it is difficult to measure the displacement of the force sensor's tip C because its thickness is 10 µm where the minimal possible measured thickness using the existing displacement laser sensors is bigger than 20 µm. Thus, the model of the displacement of the tip C defined in Equation (3.31) will be used to estimate the position of the force sensor's tip C in the manipulation. In order to validate the model, the model of the force defined in Equation (3.34) will be tested experimentally in the following section.

3.5 Experimental investigations

The objective of this section is to compare the model of the TSFM (Equations (3.31) and (3.34)) with experiments. In this section, experiments are performed to see if the model developed in

the previous section fits to the experiments after identification of the TSFM parameters. The identification of the parameters of the TSFM include the identification of the parameters of the two actuators and two force sensors.

3.5.1 Experimental setup

Several scenarios are tested in this section. Thus, different experimental setups are used. However, all experimental setups used include a TSFM, two laser Keyence sensors to measure the displacements of the fingers, a FemtoTools force sensor to measure the stiffness of the actuators and to characterize the piezoresistive force sensors, Nanocube positioning stage to move the FemtoTools force sensor towards the actuators or piezoresistive force sensor in order to determine the stiffness of the actuator or the characteristics of the piezoresistive force sensors. The experimental setup used for each identification step will be presented when presenting the steps.

3.5.2 Identification of the parameters of the piezoresistive force sensors

In order to identify the parameters of the TSFM, we will start with the identification of the parameters of the two piezoresistive force sensors. The parameters of the piezoresistive force sensors are identified experimentally. These parameters consist of the mechanical parameters the two sensors m_s, d_s and k_s and their sensitivities. The parameters of the two force sensors are identified before fixing the force sensors on the actuators tip due to the difficulty of estimating the parameters of the force sensors after its fixation and especially the dynamic parameters. The same procedure used in chapter 2 section 2.6 is used to identify the parameters of the two force sensors. Thus the procedure will not be repeated in this section. The value of the identified parameters for the two sensors and of the actuators are summarized in Table 3.1 which will be given at the end of section 3.5.3 after detailing the identification of the actuator's parameters.

3.5.3 Identification of the actuator parameters

After the identification of the parameters of the two piezoresistive force sensors, the parameters of the two piezoelectric actuators are identified in this section. The identification of the parameters are performed after the integration of the piezoresistive force sensors in order to take into consideration the effect of adding the force sensor to the actuator which can change the dynamic response of the actuator due to the change of the mass. The procedure is detailed for one actuator and then the parameters of the two actuators are going to be summarized in Table 3.1. The identification process concerns the identification of the parameters d_p, s_p, λ, β, γ, a and b shown in Equation (3.12). The first five parameters can be identified in static mode while the others are identified dynamically.

Identification of the static parameters of the free motion d_p, λ, β and γ

In this case, a voltage is applied to the piezoelectric actuator and the displacement of the TSFM tip B (see Figure 3.14) is measured using Keyence Laser sensor without any contact between the actuator and the micropart. The experimental setup used is shown in Figure 3.23-(a). To identify these parameters, a sine wave with a frequency of 0.1 Hz and an amplitude of 100 V is applied to

the actuator. The frequency 0.1 Hz is chosen in order to ignore the dynamic part of the actuator, $D(s)$, and to identify the static parameters. The amplitude of the sine wave 100 V is chosen to identify the parameters for the external loop of the hysteresis and then the model is validated for the internal loops. The displacement is measured at the tip B and not at the tip A due to the too small workspace at this point. Equation (3.15) can be used to perform the identification. Then, the parameters of the actuator, d_p, λ, β and γ, defined in Equation (3.12) can be identified using the nonlinear least square method in order to fit the experimental results of the displacement at the tip B with the model defined in Equation (3.15) for the hysteresis external loop. The model is then tested for the internal loops. A comparison between the model and the experiments after the parameter estimation is shown in Figure 3.23-(b) for three different amplitudes of the sine waves (30V, 60V and 100V). Figure 3.23-(b) shows that the Bouc Wen hysteresis model used

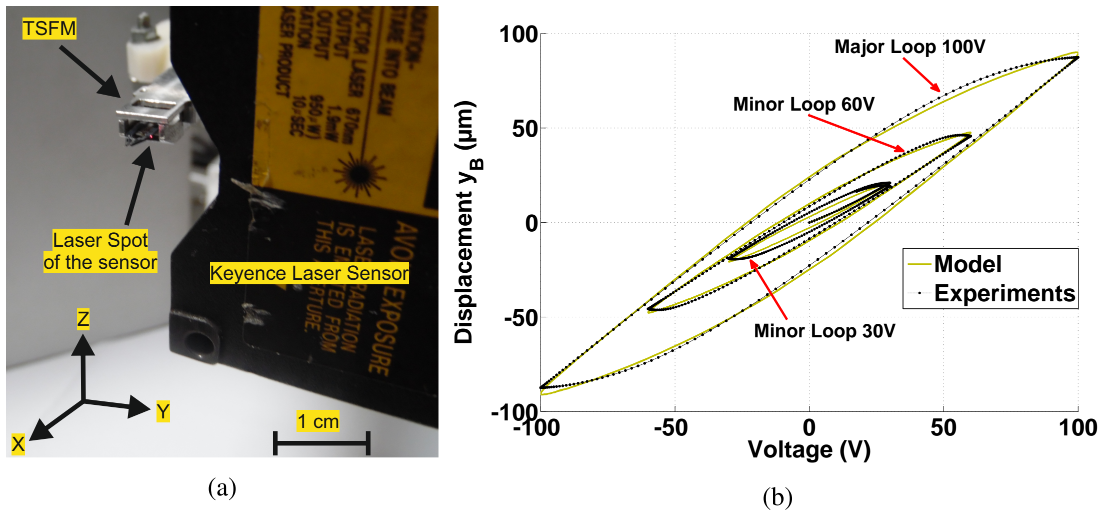

FIGURE 3.23: (a) Experimental setup used for the identification of the static parameters of the actuators; (b) Comparison between the Bouc-Wen static hysteresis model and experimental results for many sine voltages with three different amplitudes 30V, 60V and 100V at a frequency 0.1 Hz.

to model the hysteresis of the piezoelectric actuator is able to model both internal and external loops of the hysteresis. The maximal relative error is reached for the smaller internal loop with amplitude of the sine wave 30 V and the lower relative errors are for the external loop. This was expected because the parameters d_p, λ, β and γ are calculated to fit the external loop. The maximal error is less than 20% for the internal loop of 30 V and less than 10% for the external loop.

Identification of the dynamic part $D(s)$ and the constants a and b of the actuator

In this case, a step voltage is applied to the actuator and the displacement of the smart finger's tip B is measured using a Keyence sensor. The same experimental setup presented in Figure

3.23-(a) is used to identify the dynamical part of the actuator. The dynamical response, $D(s)$, is identified using a normalized second order transfer function with a static gain of 1 (see Equation (3.12)). The parameters to be identified are a and b. The normalized step responses of the model of the displacement of Y_B given in Equation (3.15) and the experimental measurements are compared in Figure 3.24 after the estimation of the parameters a and b. Figure 3.24 shows

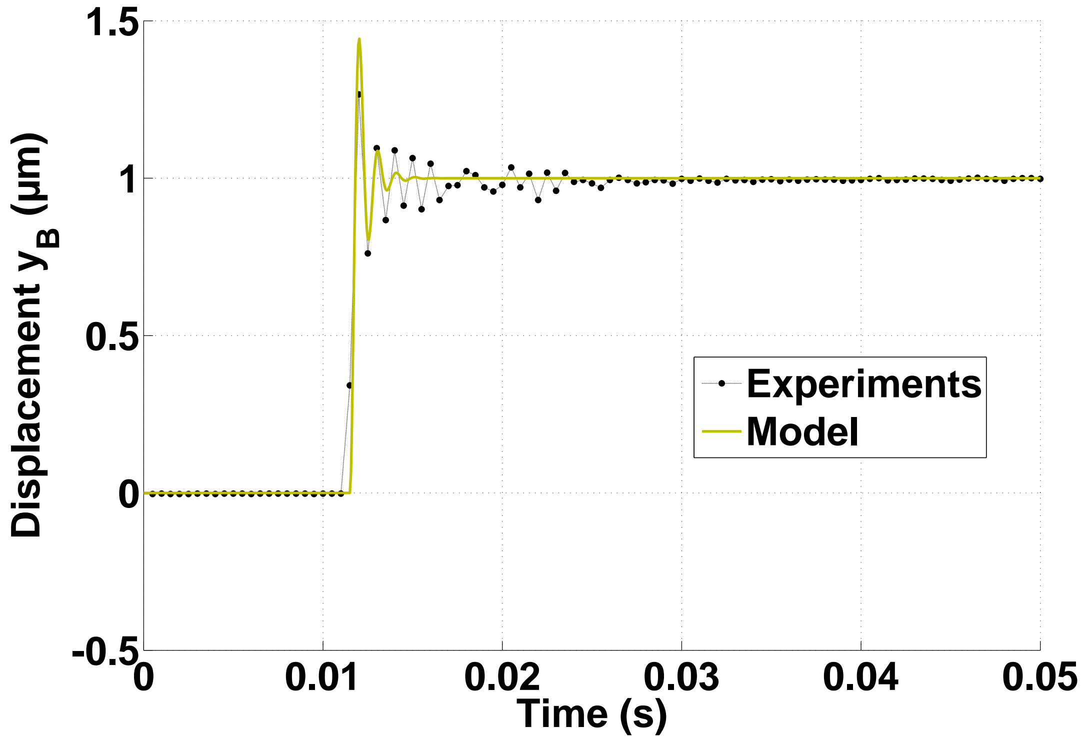

FIGURE 3.24: Comparison between the normalized step responses of the model of the displacement of Y_B given in Equation (3.15) and the experimental measurements of Y_B.

that the choice of a second order transfer function to model the first mode of the dynamics of the actuator is sufficient despite the presence of some errors between the model and the experiments. These errors can be reduced by using a higher order transfer function to represent the higher modes dynamics of the actuator. However, the relative error is smaller than 10% which is an acceptable error. The higher order modes of the actuator are exited with very small energies which justifies the possibility of neglecting their effects. In the following, second order transfer function will be used to model the dynamics of the piezoelectric actuator.

Moreover, it has been shown in experiments that the parameters a and b of the second transfer function are quasi-independent of the amplitude of the voltage because several step responses with different amplitudes have been applied to the actuator. The maximal variation of parameters is 5%. This fact validates the choice of separating the dynamical part of the actuator from the hysteresis made in section 3.4 with small errors.

Identification of the elastic parameter s_p of the actuator

In this case, a force sensor from FemtoTools is mounted on a Nanocube micropositioning stage to come into contact with the piezoelectric actuator's tip B. The displacement of the micropositioning stage is measured using an internal sensor which enables the estimation of the displacement of the actuator's tip B by knowing the stiffness of the force sensor. Due to the small operation zone, the force is applied at the tip B because it is difficult to apply the force on the tip A directly. Then using the Equation (3.27), ignoring the voltage, the hysteresis and the dynamical part and replacing y_D by y_B and L by L_r because the force is applied at the tip B in this case, the following can be deduced:

$$Y_B = -\left(1 + \frac{3L_r}{L_a} + \frac{3L_r^2}{L_a^2}\right) s_p F_g \tag{3.35}$$

Thus, according to Equation (3.35), the elastic constant s_p can be estimated using the measurements of the force applied on the tip B, F_g by the force sensor and the displacement of the tip B, y_B. Figure 3.25-(a) shows a comparison between the measured force and the force obtained using Equation (3.35) after replacing the identified value of s_p. In Figure 3.25-(a), the Nanocube positioning stage moves the FemtoTools force sensor into contact with the tip B of smart finger, once a contact appears the force starts to increase until a maximal force around 5000 µN. Then, the positioning stage moves the force sensor back until the measured force returns to zero. However, the contact is not broken when the measured force is zero and a pull-off force appears when the contact is broken for a negative displacement as shown in Figure 3.25-(a). In this case, the pull-off force has reached around 400 µN.

After identifying the constant s_p, the model of the displacement of Y_B given in Equation (3.35) is compared with the measured displacement in Figure 3.25-(b). The results shows the effectiveness of the identification.

Validation of the dynamical model of the hysteresis of the actuator

In this case, four sine waves with four frequencies are applied on the actuator's tip A while measuring the displacement of the tip A of the actuator. The experimental measurements are compared with the model of the actuator after identification of the parameters. The results of the comparison are shown in Figure 3.26 which shows that the model is able to measure the dynamic hysteresis of the actuator.

3.5.4 Experimental investigations of the model of the TSFM

In this section, the model of the TSFM defined in Equations (3.31) and (3.34) is tested experimentally. In experiments, it is difficult to measure the displacement of the end-effector's tip C because its thickness is 10 µm where the minimum thickness which can measured by the Keyence laser sensor or laser interferometer is of the order of 20 µm. For that the model of the force given in Equation (3.34) will be only tested in experiments while the model of the displacement y_C will be shown without comparison with experiments. The model will be tested for the manipulation of a flexible micropart. The two models being similar and the parameters being close the model of the flexible micropart is only tested in this section.

			Parameter	Symbol	Identified Value
TSFM	Left finger	Left actuator	Piezoelectric coefficient (µm/V)	d_p^l	0.77
			Elastic constant (m/N)	s_p^l	9.1×10^{-4}
			Hysteresis parameters	λ^l	0.43
				β^l	10.8×10^{-2}
				γ^l	7.5×10^{-3}
			Dynamic parameters	a^l	2.5×10^{-8}
				b^l	8×10^{-5}
		Left sensor	Mass (Kg)	m_s^l	1.8×10^{-6}
			Damping (N·s/m)	d_s^l	7×10^{-4}
			Stiffness (N/m)	k_s^l	128
			Sensitivity (V/ µN)	s^l	6×10^{-3}
	Right finger	Right actuator	Piezoelectric coefficient (µm/V)	d_p^r	0.78
			Elastic constant (m/N)	s_p^r	8.5×10^{-4}
			Hysteresis parameters	λ^r	0.39
				β^r	11.1×10^{-2}
				γ^r	3.5×10^{-3}
			Dynamic parameters	a^r	2.5×10^{-8}
				b^r	8×10^{-5}
		Right sensor	Mass (Kg)	m_s^r	1.79×10^{-6}
			Damping (N·s/m)	d_s^r	6.98×10^{-4}
			Stiffness (N/m)	k_s^r	130.8
			Sensitivity (V/ µN)	s^r	5.1×10^{-3}

TABLE 3.1: Identified parameters of the TSFM including the parameters of the two piezoelectric actuators and the two piezoresistive force sensors. The powers l and r correspond to the left and right fingers respectively.

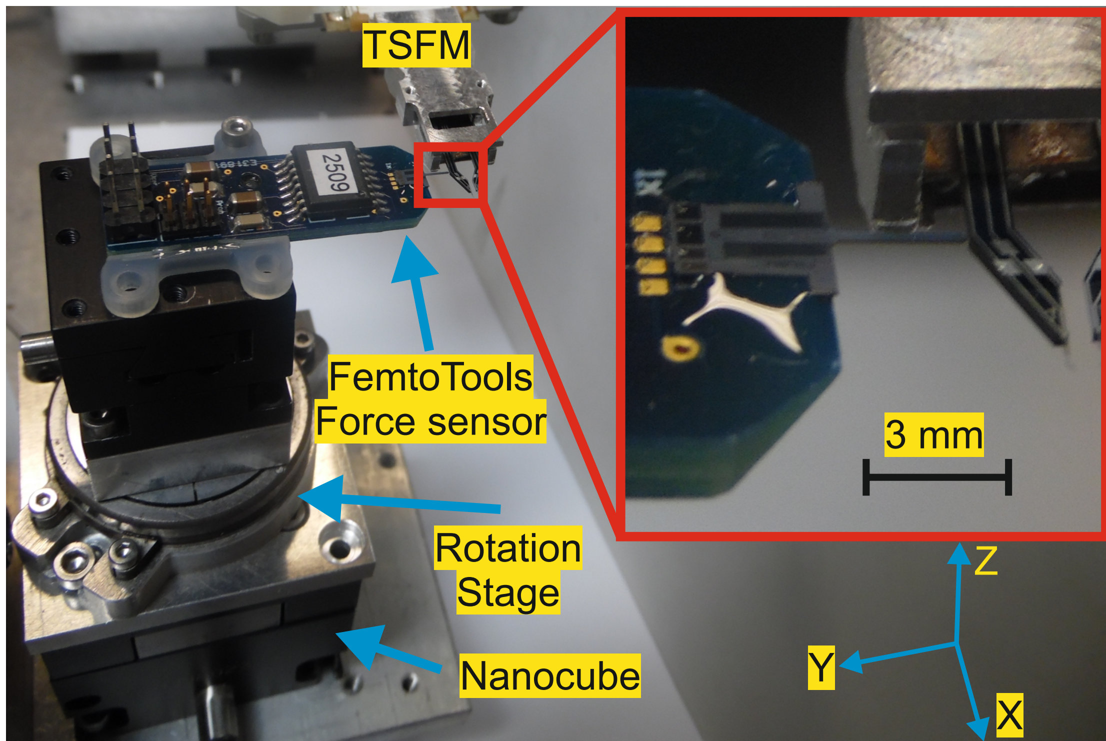

(a)

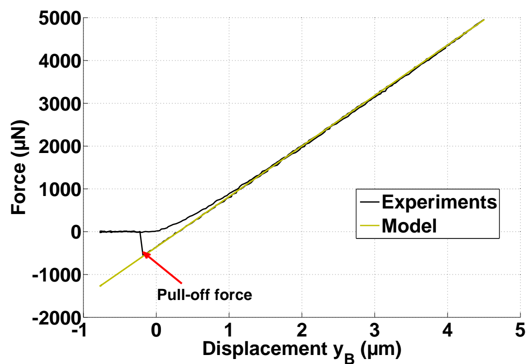

(b)

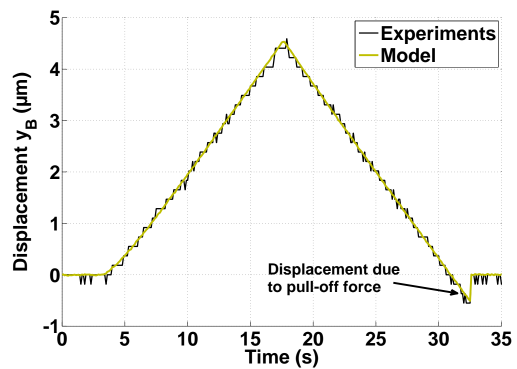

(c)

FIGURE 3.25: Experimental setuo and results of the identification of the actuator's elastic constant s_p: (a) experimental setup used including TSFM, FemtoTools force sensor, nanocub and rotation stage, (b) comparison between the measurement and the model of the force relative to the displacement leading to the identification of s_p, (c) comparison between the model and the experimental results of the displacement of the tip B y_B when a force is applied at the tip B after identifying s_p.

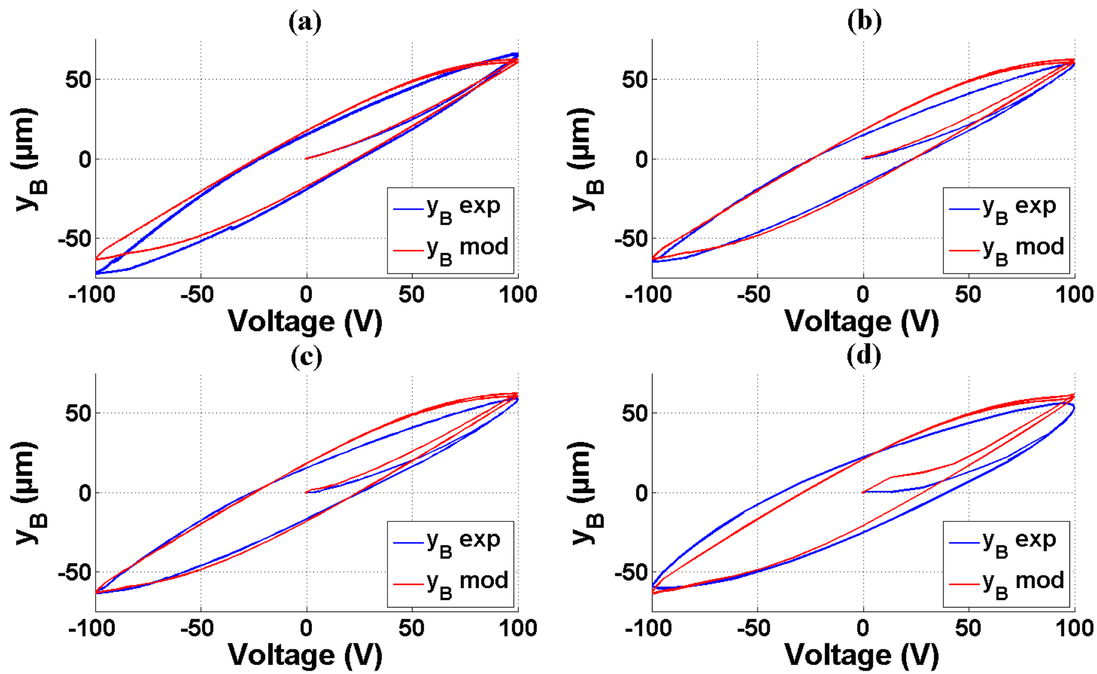

FIGURE 3.26: Comparison between the displacement model of the tip B y_B given in Equation (3.15) and experimental results for many sine voltages with an amplitude of 100V and with different frequencies where no force is applied: (a) 10Hz, (b) 50Hz, (c) 100Hz and (d) 500Hz.

Manipulation of a flexible micropart

In this part, the flexible micropart is hold using a vacuum gripper as shown in Figure 3.27. The TSFM is initially placed close to the springs of the flexible part. A sine wave is applied to move the TSFM fingers. First, no contact exists between the fingers and micropart where the force is null and the fingers are in a free motion. Then, a contact happens and the model of the force defined in Equation (3.34) is used. The free motion model and the constrained motion are shown in Figure 3.28 where the slope of the displacement changes after contact. The force is null in the free motion. In constrained motion, the errors between the model and the force is also less than 20% which are bigger than the errors in the case of pure displacement. This fact was expected because the errors in the model are combined with the errors on the estimation of the stiffnesses of the force sensor and of the flexible micropart on the one hand and the error on the estimation micropart's location y_e (see Equation (3.33)) on the other hand which increase the errors on the force model and made it bigger than the position model. The presence of errors in the model due to the errors of estimation justifies the need of online parameter estimation of the environment's stiffness in the control.

The main objective of modeling the system is to use the model for the control. Force model has shown its significance and its capability of modeling the system with small errors. The

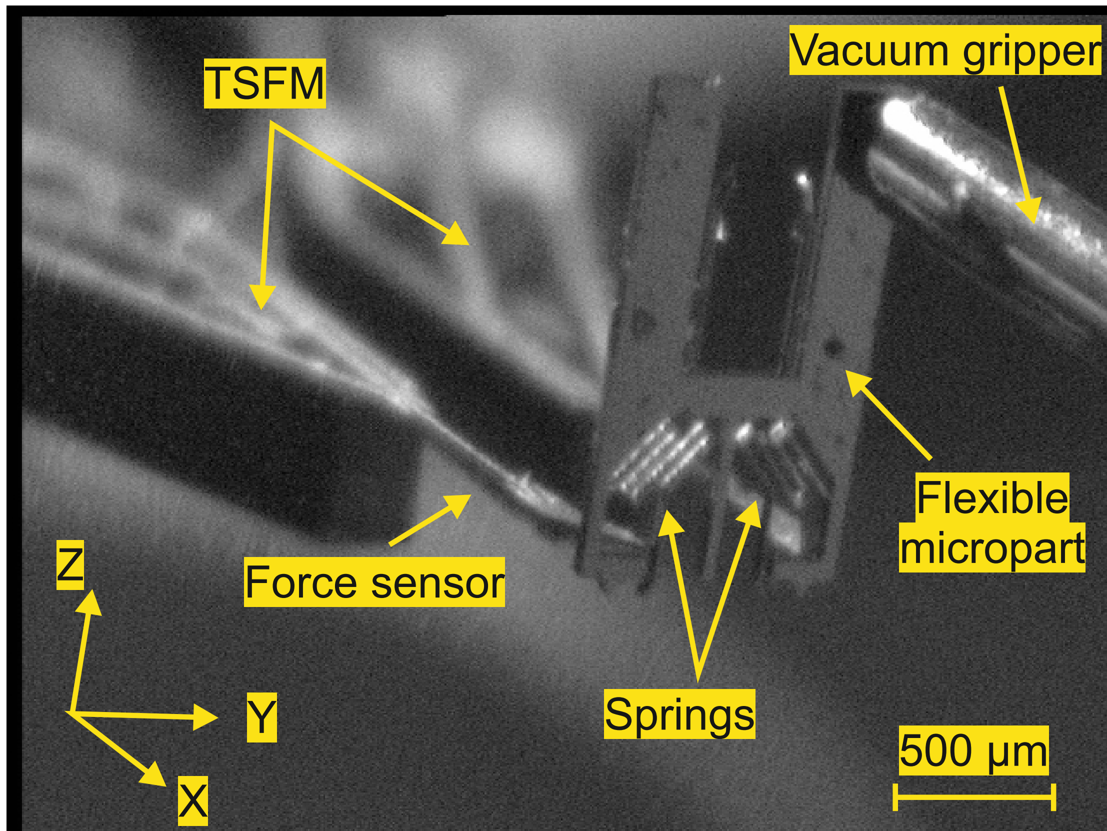

FIGURE 3.27: Experimental setup showing the TSFM end-effectors, the flexible micropart and a vacuum gripper to hold the flexible micropart.

validation of the force model can be extended to forecast the effectiveness of the model at the end-effector's tip C, y_C.

3.6 Conclusion

In this chapter, the piezoresistive force sensor is integrated into a 4-DOF piezoelectric actuator to realize a Two-Smart-Fingers-Microgripper (TSFM). A voltage/force/displacement dynamic nonlinear model for the TSFM is developed taking into account the rate-dependent hysteresis of the piezoelectric actuator. The model has been developed for a single axis with neglecting the effect of coupling between the axis of the piezoelectric actuator. The rate-dependent hysteresis has been modeled as by a static hysteresis using Bouc-Wen hysteresis model followed by a linear transfer function to represent the dynamics of the actuator. The force sensor has been modeled as mass-spring-damper system. The parameters of the TSFM are identified offline in order to test the model of the system in experiments. The model of the force applied on the TSFM fingers has been tested in experiments and the errors between the model and the measurement

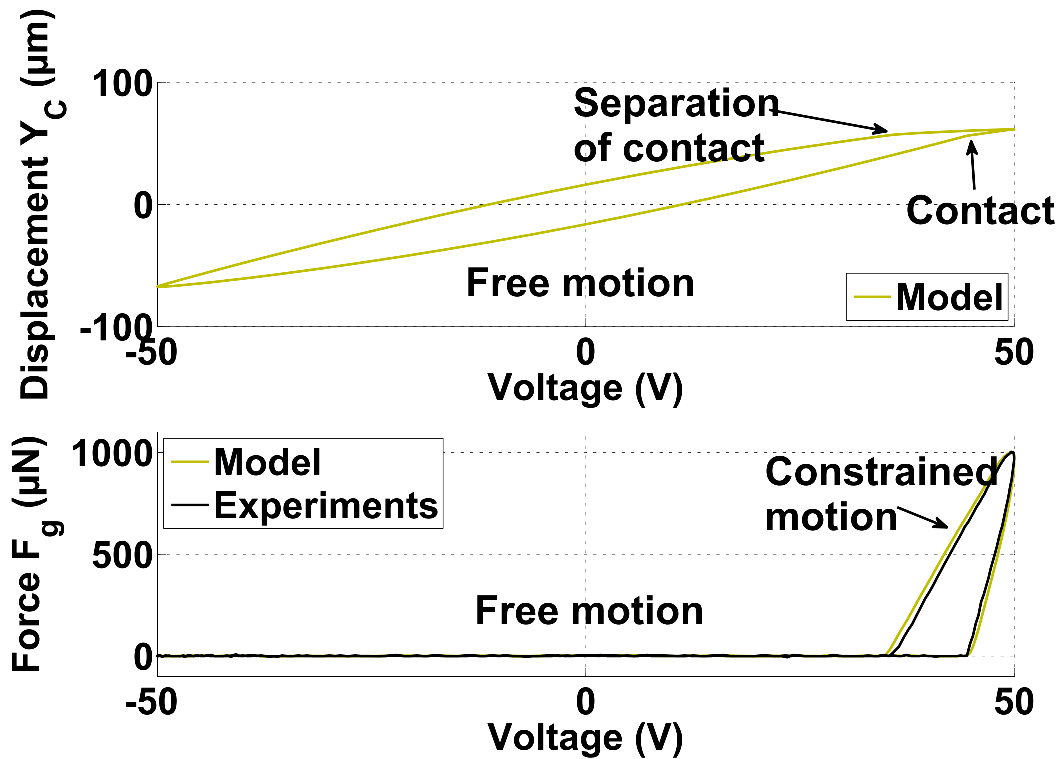

FIGURE 3.28: Comparison between the model of the force given in Equation (3.34) and the experimental measurements. The model of the displacement given in Equation (3.31) is also shown.

are less than 20% in the worst case. The worst case is when errors exist on the estimation of the stiffnesses of the micropart and the location of the micropart relative to the end-effector. The experimental results validate all the assumptions used to develop the model of the TSFM. The developed model will be used in the following to determine a control for the TSFM and the robotic platform.

Parameters estimation playing an important role onto the model, the use of a robust controller with online parameter estimation may be of great interest to obtain high performances (in terms of control of the system then in terms of microassembly).

Chapter 4

Dynamic Force Control for the automation of the grasp and release steps at the microscale

In this chapter, the automation of grasp and release of microcomponents is investigated. Existing force control techniques are detailed and their use at the microscale is discussed. Experiments are performed to compare the results of several force control techniques for a representative microscale case study. An impedance control technique is finally chosen taking into consideration microscale specificities notably pull-off force and high dynamics of microscale objects.

4.1 Introduction

Robotic microassembly offers a promising solution to fabricate complex 3D microsystems issued from several microcomponents fabricated from separate processes. Robotic microassembly can be done in teleoperated or automated modes. The automated microassembly enables more precise, repeatable and lower operation time microassembly process. In chapter 3, a two smart fingers microgripper has been presented and its model has been studied. In order to perform the automation of the microassembly, a control of the robotic station needs to be done. Thus, in this chapter, several approaches for the automation are detailed and the automation using force control is chosen. Several force control techniques are compared theoretically and experimentally. The objective of this chapter is to propose a force control approach to successfully automate some microassembly tasks. In this chapter grasp and release tasks of microcomponents are tested while in chapter 5 automated guiding task will be tested.

4.2 Automation at the microscale

The automation of the microassembly have raised many works due to its importance on the performances of the microassembly. These works include, open-loop based automation and closed-loop based automation. In the closed loop automation, position or/and force control techniques are used as summarized in Figure 4.1. From a control point of view, both open-loop

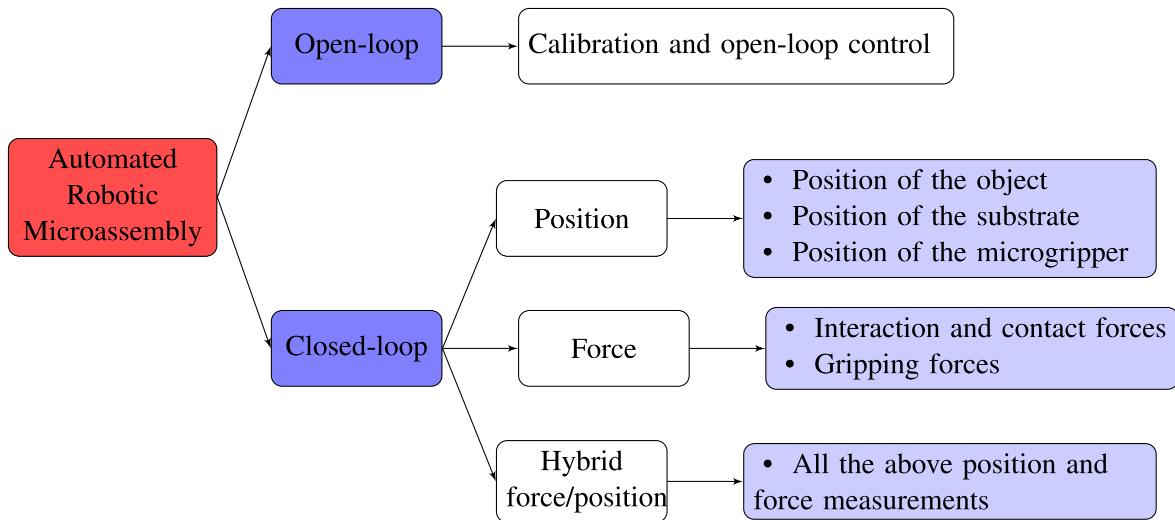

FIGURE 4.1: The different approaches for the automation of the microassembly tasks.

and closed-loop control approaches can be performed. However, in practice, the choice of the control strategy highly depends on the desired application and the existing materials. In this section, open-loop and closed-loop techniques are presented and compared.

4.2.1 Open-loop based automation

The open-loop based automation consists of calibrating the robotic station in order to compensate the static and dynamic errors, nonlinearities, temperature drift, etc using feedforward and sensorless control. The main advantage of the feedforward control technique is that it is sensorless which simplifies the robotic station design and reduces the cost of building the robotic station. This issue is interesting at the microscale due to the difficulty of integrating sensors into the robotic station due to their big size which increase the complexity of the design of the robotic station where its workspace is small.

The use of feedforward control can lead to improve output-tracking performance in many applications such Scanning Probe Microscope [25]. The feedforward control method does not share the low-gain margin problem of the feedback approach. Therefore, it is able to increase the bandwidth of the system while achieving good performances for the system. In [25], subnanometer-scale positioning precision with an increased bandwidth have been performed

using feedforward control. In addition, feedforward control improves performance without incurring the stability problems associated with feedback design.

Open-loop based automation has been used for many microassembly tasks including [123, 122] and for the control of piezoelectric actuators [132, 131]. However, to perform open-loop based automation with good performances, precise modeling of the system is required. The precise modeling of the system is a difficult task especially at the microscale due to high dependance of the system on the environment conditions (temperature, humidity, etc), the high nonlinear behavior of the system such as presented in chapter 3 section 3.3 and the lack of suitable sensors which enables precise modeling. These facts increase the difficulty of precise modeling and consequently the success of the desired task. Indeed, the feedforward control cannot account for modeling errors [199] and parameters variation due to environment changes (temperature, humidity, etc).

Open-loop based automation can be done if the same exact task is repeated within constant environment which is not usually the case when it comes to micromanipulation and microassembly where several component sizes, shapes and mechanical characteristics (mass, stiffness, damping, etc) can be faced. Considering an example of an open-loop controlled piezoelectric actuator used in two scenarios: the first scenario is free-motion of the actuator where the actuator moves without any contact and the other scenario is a constrained motion where a contact exists between the actuator and an environment. Precise modeling and open-loop based control can be performed to control the free-motion of the actuator. If the same open-loop control calculated for the free-motion is applied to the same actuator in a constrained-motion scenario, the open-loop control already calculated will not be valid because the model of the actuator changes completely and thus the open-loop cannot control the actuator in the second scenario. Moreover, open-loop based automation is also very sensible in presence of disturbances of the system and model uncertainties due to microfabrication errors.

4.2.2 Closed-loop based automation

In the closed-loop based automation, vision feedback or position and force sensors need to be used in the system to provide the feedback information for the closed-loop control. This control technique is the most used at the microscale due to its reliability. Indeed, this control method enables to compensate modeling errors, environment variations, different scenarios of a task, undesired perturbations by the use of an appropriate control technique. Hence, the choice and the design of the closed-loop control technique is critical to succeed the task. However, sensors and/or cameras are needed to perform closed-loop control which increases the cost and the complexity of the robotic station due to the difficulty of integrating sensors into the microrobotic station. Considering the same example given in the case of the open-loop control for the control of a piezoelectric actuator. The control still operates in the closed-loop in both cases because using closed-loop control and the sensor measurements, an appropriate control law will be able to track the desired behavior with and without contact.

The use of feedback control changes the performances of the closed-loop system and it may affect the stability of the system. In addition, feedback control can significantly reduce the bandwidth of the closed-loop system. To overcome these limitations, the feedback control needs to be chosen appropriately to reduce these effects. Moreover, for some applications, such

Open-loop based automation	Closed-loop based automation
• sensorless control • low cost and small size system integration • possibility of high bandwidth control • cannot account for modeling errors, parameter variation and unknown disturbances	• need of sensors to perform control • high cost and big size system integration • can reduce the bandwidth of the system • possibility of accounting for modeling errors, parameter variation and unknown disturbances

TABLE 4.1: Comparison between open-loop based and closed-loop based automation at the microscale.

as nanopositioning of piezoelectric actuators and piezoelectric micropositioners, some authors have proposed to use feedback control in conjunction with feedforward control to improve the bandwidth of the controller due to the closed-loop and to reduce uncertainty-caused errors due to feedforward control [38, 39]. Note that the use of feedforward inputs can improve the tracking performance compared with the use of feedback alone, even in the presence of plant uncertainties [38]. Such feedforward usually improves the feedback controller.

Table 4.1 presents the main differences between open-loop based automation and closed-loop based automation for microscale purpose. It is for the robustness and the possibility of accounting the modeling errors and parameter variations in the system that closed-loop based automation is used. Indeed, this fact is important in order to perform repeatable and precise tasks at the microscale. Among the closed-loop based automation techniques (vision-based, position, force and hybrid force/position), force control presents a significant importance at the microscale. Indeed, force control enables:

- to control the gripping forces by setting a desired force reference which guarantee the safety of both the micropart and the microgripper,
- to achieve a stable grasp of microparts without loosing the micropart due to high dynamics and small inertia of microsystems,
- to detect if an undesired contact appears between the micropart and the substrate,
- to detect the side of contact between the micropart and the substrate,
- to separate the undesired contact,
- to increase the dexterity of the microassembly tasks,
- to limit the effect of surface forces which are predominant at the microscale by controlling and limiting preload forces applied on the micropart.

These characteristics cannot be provided with other technique than force control. However, the use of position measurement cannot provide information about the force applied on an object

which can generate the breaking or the loose of the microcomponents. For example, the force sensors from FemtoTools [54] can be broken if a displacement bigger than 2 μm is applied at their tips which means that for a small displacement the force sensor can be easily broken if the control of the contact force is not considered even if position is controlled by a nanopositioning stage. In addition, the use of position measurement is necessary in order to perform precise positioning of the microparts in the microassembly process. Consequently, combining force and position control is promising in order to achieve automated, safe and stable microassembly tasks. Thus, the closed-loop based automation approach using hybrid force/position control is chosen to be used for the automation of the microassembly. In the hybrid force/position control, position control is performed for some axes and force control for others. The position control being easier to be performed because most of the positioning stages have their own internal controller which facilitates the task of the position control. The force control remains the challenge to be performed. Thus, in this chapter, the study will be firstly focused on the force control and the hybrid force/position control approach will be detailed in chapter 5.

4.3 Scaling issues in robot force control

Issues relevant to robot force control at the macroscale are well known due to extensive research conducted in the 80s and 90s. Several classic control schemes have been developed including explicit force control and indirect force control. Recently, with the development of microrobotics, researchers start to use force control to perform more precise and stable tasks at the microscale in many applications such as microassembly and micromanipulation, microcell injection, etc. In this section, the force control techniques used at the both scales will be studied and compared theoretically and experimentally. At the end of this section, a choice of a force control technique for microscale purpose will be done at the microscale.

Before detailing the existing force control techniques, the experimental setup for which the force control techniques are compared is presented. The force control will be tested in an automated grasp and release tasks of a flexible microcomponent. The micropart used in this chapter are the MOEMS presented in section 1.1.3 which was named *holder*. The holder has two flexible parts (springs) as shown in Figure 4.2 which will be considered *flexible environment*. To perform the experiments, the holder is initially handled by vaccum gripper which is shown in Figure 4.2. Two-Smart-Fingers-Microgripper (TSFM) comes to handle the holder from its flexible parts as shown in Figure 4.2. In the experiments, first no contact exist between the TSFM and the holder's springs then a reference force is applied to the system and the controller objective is to let the TSFM fingers move to grasp the holder from its springs by controlling the free and constrained motions. The grasping force should track the reference force. Once the reference force is tracked the release of the holder is also tested.

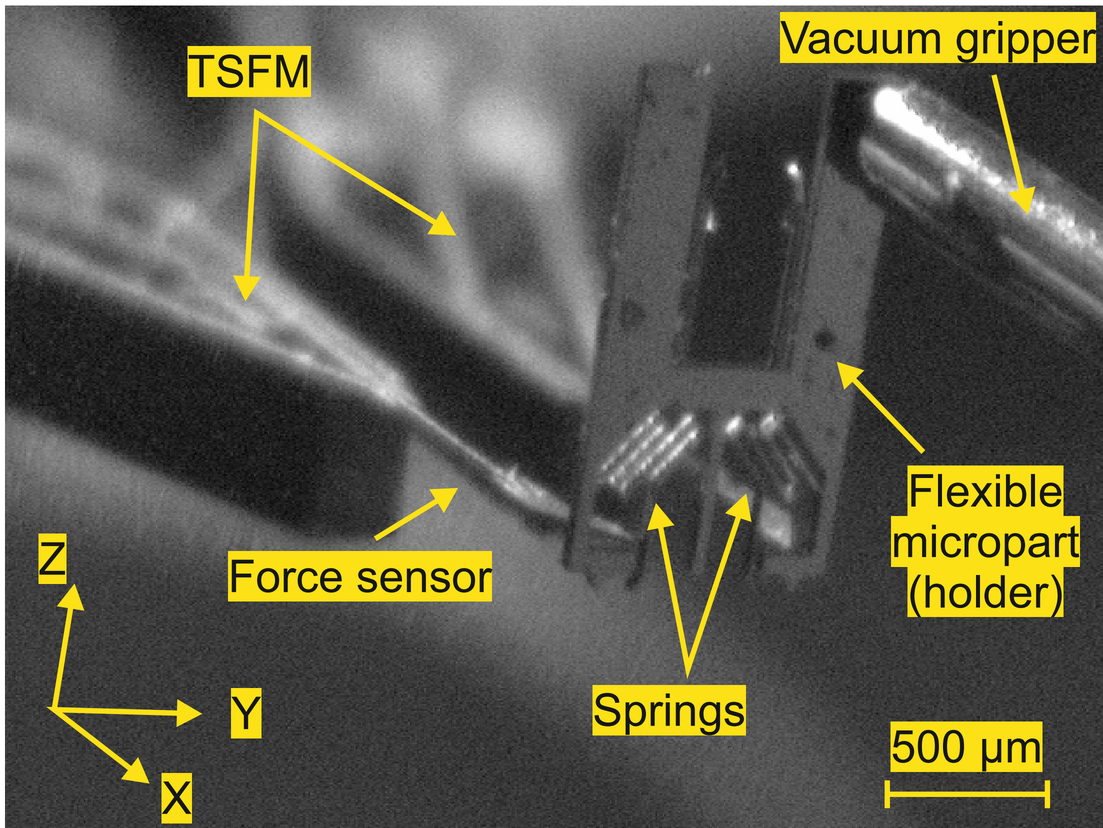

FIGURE 4.2: The figure showing the experimental setup showing the TSFM end-effectors, the flexible micropart and the vacuum gripper.

4.3.1 Explicit force control

Explicit force control involves the direct force reference and measurement of force values, with the goal of having the output following the input as closely as possible. Explicit force control usually employs some forms of PID control, as well as various simple forms of filtering.

Explicit force control involves the measurement of force directly in the feedback control law which is directly provided to the system plant which is in our case the TSFM in interaction with a flexible environment. Feedforward and feedback signal can be combined in the control law. A general control diagram of the force-based explicit force control is shown in Figure 4.3 where f_r is the reference force, f_g is the measured contact force, $e_f = f_r - f_g$ is force error and u is the command. The system plant represents the interaction between the robot end-effector and the environment.

The feedback controller is usually a subset of PID control (*i.e.* P, I, PD, PI, etc). In [173], several classes of force-based explicit force controllers have been used including proportional control (P), integral control (I) proportional integral control (PI) and proportional derivative control (PD). Integral control provides a zero steady-state force error for a constant reference

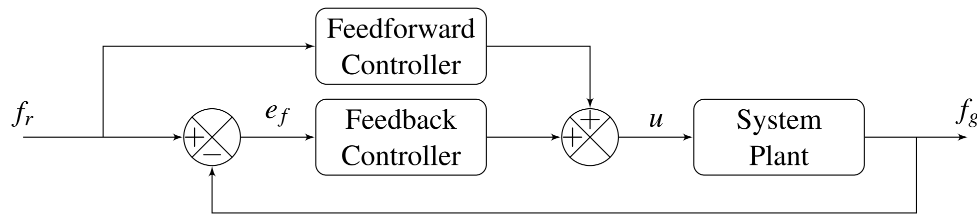

FIGURE 4.3: Force-based explicit force control diagram.

force for the system. The introduction of integral action to the controller adds a pole near the origin which has been viewed in [49] as destabilizing for the system. However, this fact has been viewed as an important characteristic in [173] because the integral action in this case acts as a low pass filter which reduces the chance of resonance oscillations and signal noise occurring in the system. However, integral control limits the bandwidth of the closed-loop system, can cause phase lag and may destabilize the system especially with the presence of nonlinearities (*e.g.* hysteresis, saturation). Proportional derivative control is usually combined with a feedforward signal in order to reduce the steady-state force error. It acts as band pass filter increasing closed-loop bandwidth but amplifying noise and oscillations at the resonant frequency. Furthermore, force feedback signal is very noisy and taking the derivative of the signal without filtering is not advisable and the use of filter to reduce the noise will reduce the closed-loop bandwidth. Consequently, the use of PI controller is the most adapted, between the subsets of the PID controller, for force control.

Robust force control has also been investigated in several works including the design concept of sliding mode control which is widely used in the framework of robust force control [154, 174, 200]. The objective of robust force control is to achieve the desired behavior of the closed-loop system and to guarantee the stability of the force control in the presence of modeling errors and system parameter variations in robot and environment.

Explicit force control at the microscale

Explicit force control is the most used force control technique at the microscale. It is used due to the simplicity of the control scheme and of its implementation. Indeed, only the force measurement or force estimation is needed to perform the explicit force control. Both PID force control and robust force control have been used for microscale applications. Some force control applications used at the microscale are presented in the following and a discussion about these force techniques will be done.

In [47], the authors have proposed a procedure based on the frequency response of the manipulation system in order to perform stable grasping while analyzing the dynamics of the grasping motion. First, a piezo-actuated gripper was identified by means of a small step impulse excitation, filtering and Fast Fourier Transform (FFT) of the output signals in the case without contact with an object. The frequency response of the system was obtained based on principal component analysis techniques, and the corresponding transfer function was obtained. The same process was repeated for the case of grasping a sample object (i.e., the grasping condi-

tion). A controller was then synthesized based on the frequency response of the system without grasping and during grasping of an object. This design procedure was applied for manipulating optical fibers with 190 μm diameter using a microgripper. A proportional integral controller was designed to compensate the undesirable change of phase at about 1 kHz. The experiment results demonstrated the effectiveness of controlling the grasping of fibers with a force of 3 mN.

In [101] and [100] PI explicit force controller has been used to control two experiments one involving pick-up operation and the other an insertion. The controller was able to track the desired force references 150 mN in the first experiment and 400 mN for the second within 20 seconds.

In [178], integral control has been used to control the grasping force. It was shown that the controller is able to track the grasping force reference with fluctuations around the set point.

In [81], a PID controller is used to control the grasping force of biological cells. The controller was able to track several force references of 60 nN, 100 nN, 120 nN, 180 nN and 240 nN within a setting time of 200 ms with some fluctuations, which are quantified only around the force reference 100nN, with a peak-to-peak value of 20 nN which means around $\pm 10\%$.

In [120], integral control is used to control the grasping force of a microgripper composed of an actuated electrostatic finger and a sensitive finger with thermal sensor. The controller values where quantified relative to voltage where the controller was able to track the desired force voltage reference with a setting time around 1 s and different overshoot values depending on the input reference where the values of the overshoot were smaller than 15%. In the signal, fluctuations also exist around the reference value and the amplitude of fluctuations is around 5%.

In [135], robust H_∞ is used to control the gripping force applied by a thermo-piezoelectric actuator to manipulate a micropart. The principle of the microgripper is based on the combination of the thermal actuation (for the coarse positioning) and the piezoelectric actuation (for the fine positioning). One finger of the microgripper is controlled in position and the other is controlled in force. The force controller was able to track the desired force in several hundreds of ms with small overshoot and a small steady state force error.

In [15], optimal and robust control have been used to control the gripping force applied by a microgripper to grasp calibrated micro-glass balls of 80 µm diameter. Although, the microgripper has an internal force sensor, the gripping force has been estimated using Kalman filter in order to reduce 97% of the force sensor signal noise. An LQG (Linear Quadratic Gaussian) has been used to control the force reference, the force controller was able to track a desired force of 10 µN in a setting time less than 10 ms and almost without overshoot. The effectiveness of the Kalman filter has been proven using a high performance laser interferometer sensor which measures the displacement of the force sensor tip and estimates the force using the value of the stiffness. The microgripper's model being nonlinear, a linear model has been extracted from the nonlinear model around a nominal actuation voltage (60 V in the paper) in order to apply the LQG control. The effectiveness of the controller remain limited to a neighborhood around the nominal voltage and the performances of the controller are not guaranteed outside the neighborhood which limits the use of this approach to control forces if the nominal actuation voltage is not known.

The main advantage of explicit force control is the simplicity of both controllers and implementation. In addition, explicit force control enables to track a reference force directly through

the control. Explicit force control is sufficient for many applications such as that presented above. The most used technique in the explicit force control is the PI control. Indeed, the derivative control is usually avoided due to the noisy signal of the force sensors. Most of the considered applications apply forces in the range going from several mN up to several hundreds of mN or the range going from several tenth of nN up to several µN. In our work, we are mainly interested by forces going from several tenth of µN up to 1 mN. In this range, contact and surface forces are predominant and their effects are more important than for mN forces. In addition, at the microscale, in order to improve the performances of the explicit force control, advanced control technique needs to be used [135, 15]. The main limitation of the explicit force control technique is the dynamic performances of the controller. In the PID control and robust control, controlling the dynamic of the contact is not straightforward. Indeed, PI and robust controllers slow down the system in order to guarantee the stability and the tracking for the system despite the change of environment or also the parameter uncertainties. In order to control the dynamics, the only way is to test and tune the gains of the controller in order to obtain an acceptable dynamic behavior which is not an easy task in applications where the environment is not known.

Experimental results of the explicit force control

The explicit force control technique is tested in the automated grasp and release tasks of the micropart (holder) using the experimental setup shown in Figure 4.2. PI control is used due to its easy implementation, its wide use and good performances as presented at both microscale and macroscale. The gains of PID are calculated through "Good Gain" tuning method [61] and then they are refined in experiments to try to increase the performances. This tuning method is chosen because, contrary to Ziegler-Nichols or trial-and-error methods, it does not require the system to go to oscillations in order to determine the gains. Several values of gains of the PI control are tested and compared. The results are shown in Figure 4.4. The specifications for the control are set to have a settling time lower than 100 ms with overshoot lower than 10%. For the grasp task, a force reference of 1 mN is set to the controller and the aim of the controller is to follow the desired reference. The results show that the settling time changes from 530 ms (Figure 4.4-(d)) to 1 s (Figure 4.4-(b). The lower rising time is 70 ms but it presents highest overshoot up to 20% and lowest settling time of 1s in Figure 4.4-(b) where the lower settling time is 530 ms in Figure 4.4-(d). The performances of the controller relative to the gains are compared in Table 4.2. Due to overshoot present in Figure 4.4-(b), the proportional and integral gains can not be increased more to prevent increasing the amplitude of oscillations in the system.

For the release task, a zero force reference is set to the controller. The settling time is almost the same as for the case of the grasping except Figure 4.4-(b) where the settling time is 730 ms. This difference is that in the release task no overshoot has occurred and the force remained to zero. For the release task at the microscale, if the measured force is null, this does not imply that the contact is separated. Indeed, due to contact and surface forces, notably pull-off force, the contact remains and the micropart still sticked to the TSFM fingers although the force is null. Using explicit force control, it is difficult to separate the contact automatically using the

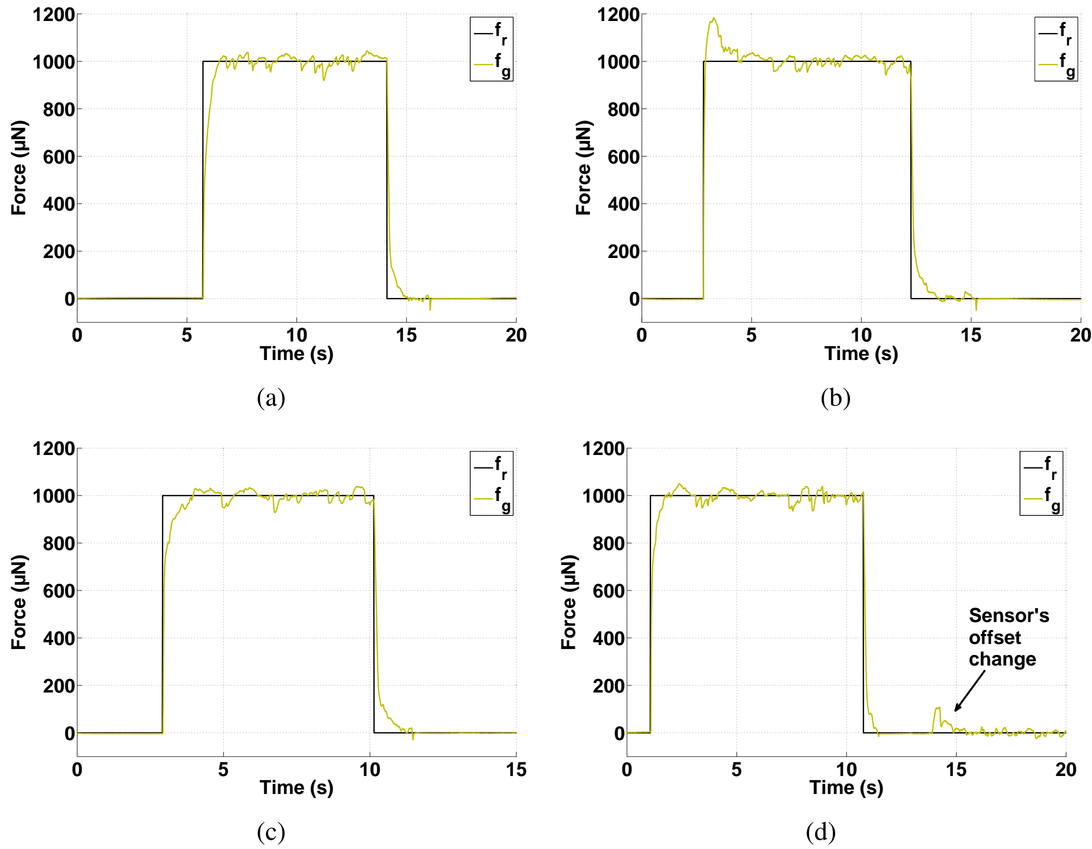

FIGURE 4.4: Experimental results of the explicit force control using PI controller for four different values of proportional and integral gains K_p and K_i: (a) $K_p = 0.3$ and $K_i = 0.6$, (b) $K_p = 0.4$ and $K_i = 1$, (c) $K_p = 0.2$ and $K_i = 0.5$, (d) $K_p = 0.3$ and $K_i = 0.7$.

control law. The separation can be done by the user by changing the voltage applied to the TSFM fingers in order to open these fingers and separate the contact.

The control is able to cancel the steady state force error and to track the desired force. Some oscillations exist around the reference force in the four cases. These oscillations can be reduced by adding a derivative action. However, due to high noise of the force sensor, the derivative action is unadvised. These results are coherent with the presented performances of the explicit force control schemes at the microscale. In addition, one issue with most of existing force sensors is the variation of the force sensor offset with no applied force. This issue is common with piezoresistive and capacitive force sensors when these sensors are not used in a controlled environment. Due to this issue, the offset may change and the force measurement may change than zero even if no contact exist and the control will react to the cancel the error and a contact may happen even if force reference is zero. This is what happens in Figure 4.4-(d) at time $t = 14$ s where the offset of the force sensor has changed and consequently the force changes and a contact happens even if the force reference is null. The latter shows that the only force

Figure	Proportional gain K_p	Integral gain K_i	Settling time (ms)	Overshoot (%)
4.4-(a)	0.3	0.6	570	2
4.4-(b)	0.4	1	1000	20
4.4-(c)	0.2	0.5	790	3
4.4-(d)	0.3	0.7	530	5

TABLE 4.2: Comparison between the PI controller performances relative to different gains.

control scheme cannot control the position of the system when the measured contact force is null.

4.3.2 Indirect force control

Indirect force control achieves force control via motion control without explicit force feedback loop. Two of the most known indirect force control are impedance control and admittance control. Special cases of impedance and admittance control are stiffness control and compliant control, respectively, where only the static relationship between the end-effector position deviation from the desired motion and the contact force is considered. Notice that in the robot control literature, the terms impedance control and admittance control are often used to refer to the same control scheme; the same happens for stiffness and compliance control.

The aim of both admittance and impedance control is to set a desired dynamic behavior to the system by setting a desired impedance or admittance. The mechanical admittance, A, of the system is the inverse of the mechanical impedance, Z, and can be defined as follows:

$$A = Z^{-1} = \frac{X}{F} \tag{4.1}$$

where $X = (x,y,z)$ is the position[1] of the end-effector and $F = (F_x, F_y, F_z)$ is the force applied by the end-effector on the environment which is in our case the manipulated object. In the case of Figure 4.2, the environment is the flexible part (springs) of the holder. In the following, the position of the end-effector and the force applied by the end-effector on the environment will be considered along the y axis.

Notice that, Equation (4.1) several possible relations can be considered in the framework of admittance and impedance control. Some authors use directly the position, X, and the force, F, where others replace one or both of the variables by position or force errors. Consequently, the dynamic relation can be written along several ways defined in the following equation:

$$\begin{cases} \text{I} : M_d\ddot{y} + D_d\dot{y} + K_d y = -f_g \\ \text{II} : M_d(\ddot{y} - \ddot{y}_r) + D_d(\dot{y} - \dot{y}_r) + K_d(y - y_r) = -f_g \\ \text{III} : M_d(\ddot{y} - \ddot{y}_r) + D_d(\dot{y} - \dot{y}_r) + K_d(y - y_r) = f_r - f_g \end{cases} \tag{4.2}$$

[1] In mechanics, the mechanical admittance/impedance is defined as the ratio $A = Z^{-1} = \frac{\dot{X}}{F}$ where in robotics, it is defined as in Equation (4.1) in order to consider the stiffness of the environment in the control.

where M_d, D_d and K_d represent the desired mass, damping and stiffness respectively, y_r and y are respectively the position reference and the current position along Y axis, f_r and f_g are respectively the reference and the current gripping forces. The mechanical impedance, Z, can be written as:

$$Z = M_d \times s^2 + D_d \times s + K_d \tag{4.3}$$

Admittance control

Admittance control has an outer force control loop that provides position commands to an inner position loop controller as shown in Figure 4.5 where f_r and f_g are respectively the desired and measured forces, y_r and y are the desired and measured positions, ε_y and e_f are respectively the position and force errors and u is the command. The inner position control loop is usually as subset of PID (P, PI, PD, PID, etc). The force reference is transformed into a reference position through an admittance filter, A. The admittance filter relates the force error, $e_f = f_r - f_g$, to the

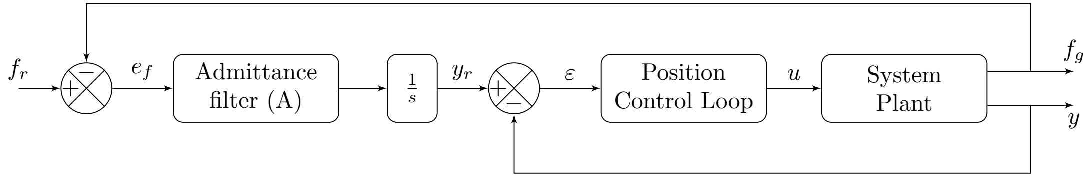

FIGURE 4.5: Admittance control diagram.

end-effector velocity, $A = \frac{\dot{y}_r}{f_r - f_g}$, as proposed in [36, 139]. For a known environmental stiffness, an admittance A can be constructed to achieve a desired force reference with small or zero error, low overshoot and rapid rise time. The position reference can be calculated from the force error by:

$$y_r = \int A\,(f_g - f_r)\,\mathrm{d}t \tag{4.4}$$

In some works, admittance control has been classified in the explicit force control category and has been called inner position loop based explicit force control [173] due to the presence of an outer force control loop. Although an outer force control loop exists, an admittance is used to convert the force error into a position reference which means that force is not controlled directly and the force control depends on the choice of the admittance.

Impedance control

The impedance control has been proposed by Hogan [64] to control the dynamics of the contact between a robot and its environment. It is widely used at the macroscale. Several control techniques have been proposed including the position-based impedance control where a diagram is shown in Figure 4.6 which is the most used control diagram. It consists of designing the control that will establish a dynamic relationship given in Equation (4.2). However in any practical implementation, y is the measured position of the environment which is an output of the system and it can not be controlled directly. Thus, a desired trajectory, y_d, needs to be specified, and the role of the inner position control loop is to track the position y to the desired

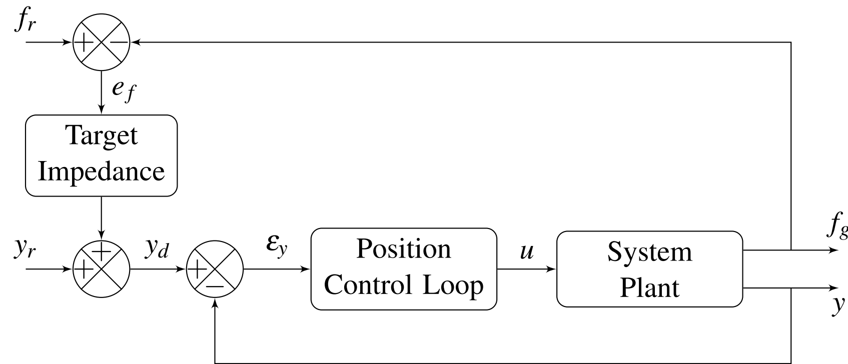

FIGURE 4.6: Position-based impedance control diagram as proposed by [64].

trajectory y_d which is the input of the inner position control loop as shown in Figure 4.6. A position tracking error exists between y and y_d due to the dynamics of the robot. The desired trajectory can be calculated by replacing y in Equation (4.2)-III by y_d:

$$M_d\left(\ddot{y}_d-\ddot{y}_r\right)+D_d\left(\dot{y}_d-\dot{y}_r\right)+K_d\left(y_d-y_r\right)=f_r-f_g \tag{4.5}$$

Although the dynamic relation is controlled in the impedance control framework, one weak point of the impedance control is the lack of the direct force control capability by specifying a desired force contrary to the explicit force control which enables to control the force directly. Many researchers have paid attention to this fact and tried to solve the direct force control capability. In the following the force tracking capability is discussed in order to perform force tracking in impedance control.

Force tracking in indirect force control

The indirect force control enables to control the dynamics of interaction between a robot end-effector and a flexible environment. One lack of indirect force control is the direct force control capability. This issue is similar for both admittance and impedance control. Indeed, the difference between impedance and admittance control is the causality consideration. Causal analysis provides insight into the important question whether it is better to regulate impedance or admittance. For most robotics applications, the environment primarily consists of movable objects, most simply represented by their inertia and surfaces or other mechanical structures that kinematically constrain their motion. The interaction dynamics in both cases may be represented as an admittance. An unrestrained inertia determines acceleration in response to applied force, yielding a proper admittance transfer function. A kinematic constraint imposes zero motion in one or more directions regardless of applied force; it does not admit representation as an impedance. Inertias prefer admittance causality; kinematic constraints require it. Because the environment has the properties best represented as an admittance, the ideal robot behavior is an impedance, which can be thought of as a dynamic generalization of a spring, returning force in response to applied displacement. Initially assuming that arbitrary port impedance could be achieved, Hogan argued for this approach [64].

As the ideal robot behavior is an impedance, impedance control is the most used control technique in literature. In this section, the force tracking problem will be studied for impedance control.

To study the force tracking in impedance control, the robot is considered to have contact with a flexible environment which can be modeled as a mass-spring-damper system which is a general case considered in many works [78] (see section 3.4). The force, f_g, applied on the environment can be written, in function of the position of both robot and environment y when a contact exists, as follows:

$$f_g = m_e \ddot{y} + d_e \dot{y} + k_e (y - y_e) \tag{4.6}$$

where y_e is the location of the environment at equilibrium when no force is applied on the environment and m_e, d_e and k_e are respectively the mass, damping and stiffness of the environment. The position tracking error of the robot is called $\varepsilon_y = y_d - y$. Replacing Equation (4.6) in Equation (4.5), the latter equation can be rewritten as follows:

$$Y_d - Y_r = Y + \varepsilon_y - Y_r = \frac{F_r - F_g}{Z} \tag{4.7}$$

where $Z = M_d s^2 + D_d s + K_d$ is the impedance filter, Y_d, Y_r, Y, F_r and F_g are respectively the Laplace transforms of y_d, y_r, y, f_r and f_g. Using the Laplace transform of Equation (4.6), the position Y can be given as follows:

$$Y = \frac{F_g}{Z_e} + \frac{k_e Y_e}{Z_e} = \frac{F_r - e_f}{Z_e} + \frac{k_e Y_e}{Z_e} \tag{4.8}$$

where $Z_e = m_e s^2 + d_e s + k_e$ and $e_f = F_r - F_m$ is the force error. Replacing Equation (4.8) in Equation (4.7), the following can be deduced:

$$\frac{F_r - e_f}{Z_e} + \frac{k_e Y_e}{Z_e} + \varepsilon_y - Y_r = \frac{e_f}{Z} \tag{4.9}$$

Then, we have:

$$e_f = \frac{Z Z_e}{Z + Z_e} \left(\frac{F_r}{Z_e} + \frac{k_e Y_e}{Z_e} + \varepsilon_y - Y_r \right) \tag{4.10}$$

In the steady state mode, $Z_e \to k_e$ and $Z \to K_d$. The steady state force error can be written as:

$$e_f^{ss} = K_{eq} \left(\frac{f_r}{k_e} + y_e - \varepsilon_y - y_r \right) \tag{4.11}$$

where e_f^{ss} is the steady state force error and $K_{eq} = \frac{K_d k_e}{K_d + k_e}$. Equation (4.11) shows that if an inner position control loop is used in such a way to have a zero steady state position error (*i.e.* $\varepsilon_y \to 0$), the steady state force error can be canceled (*i.e.* $e_f^{ss} \to 0$) if the position reference, y_r, is chosen as follows:

$$y_r = \frac{f_r}{k_e} + y_e \tag{4.12}$$

which means that the precise location of the environment and the exact value of the environment stiffness k_e should be known in order to generate a reference position trajectory y_r which enables

the force tracking. However, in practice, the values of y_e and k_e are not known perfectly and, as a result, the desired force, f_r, will not be exactly exerted on the environment (a force error will exist on the exerted force). Let $(\Delta y_e, \Delta k_e)$ be the uncertainties on the environment's location and stiffness respectively, that is:

$$\begin{cases} y_e = \hat{y}_e + \Delta y_e \\ k_e = \hat{k}_e + \Delta k_e \end{cases} \tag{4.13}$$

where $\hat{y}_e$ and $\hat{k}_e$ are respectively the estimated values of y_e and k_e. Then, using the estimated values $\hat{y}_e$ and $\hat{k}_e$ in Equation (4.12) to generate a reference position $y_r = \hat{y}_e + \frac{f_r}{\hat{k}_e}$, the steady state force error given in Equation (4.11) can be written as in Equation (4.14) which shows that if the uncertainties $(\Delta y_e, \Delta k_e)$ are big then the steady state force error is also big.

$$e_f^{ss} = \frac{K_d}{K_d + \hat{k}_e + \Delta k_e}\left[\hat{k}_e \Delta y_e - \frac{\Delta k_e}{\hat{k}_e} f_r + (\Delta y_e)(\Delta k_e)\right] \tag{4.14}$$

The complete classic position-based impedance control diagram with force tracking and parameter estimation is presented in Figure 4.7 where the red dashed box is the same impedance control diagram shown in Figure 4.6 and the part outside the box is the modified scheme in order to perform force tracking.

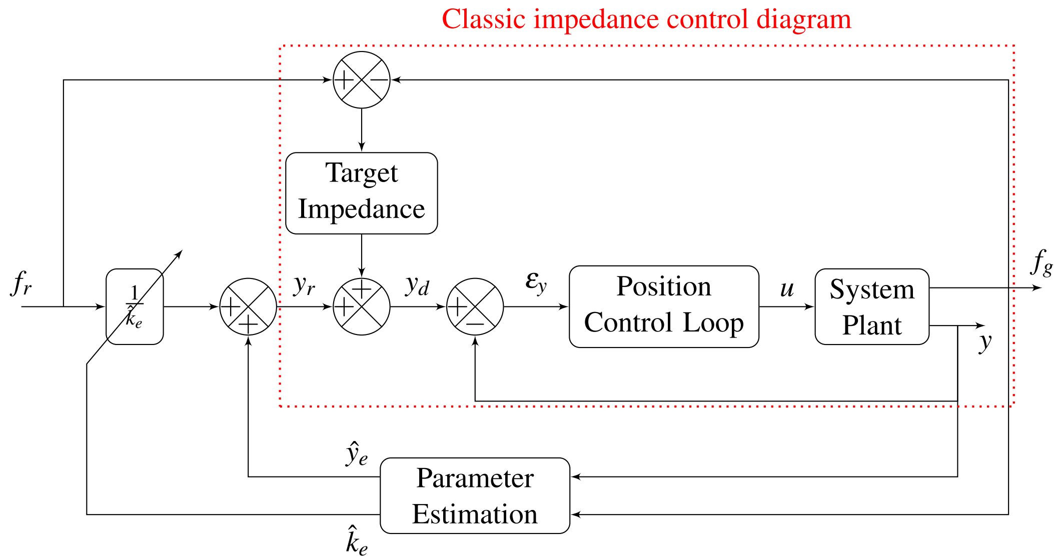

FIGURE 4.7: Force tracking position-based impedance control diagram where the part of the diagram inside the box is the same as the diagram shown in Figure 4.6.

An estimation of the environment parameters is required in order to perform force tracking in impedance control. Many researchers have paid attention to this fact and tried to solve the direct force control capability by using direct and indirect adaptive impedance control [141, 147, 108, 193], recursive least square [98] or offline signal processing [50]. The latter can be

used to estimate the parameters of the environment offline and then use the estimated values in the control loop which is difficult to be done especially in a system where the environment parameters are variable such as microscale systems.

Indirect force control at the microscale

Indirect force control has also been used for several microscale applications due to the ability to control the dynamics of the contact between the end-effector and an environment in a straightforward manner by setting a desired dynamic relation between the force exerted on the environment and the displacement. In this section, the works dealing with indirect force control schemes at the microscale are presented.

In [188, 187], an impedance control with force tracking is used to control the penetration force during robotic cell injection. The force control used includes two control loops. The inner loop is an impedance control used to specify the interaction between the needle and the cell. The outer loop is a force tracking non-linear controller using a feedback linearization technique. The cell model is identified online with a least-squares parameter estimator. In experiments, the controller has been tested to track ramp force reference and second order polynomial force reference. Therefore, the controller has been used in the framework of pure force control without a study of the dynamic interaction between the microrobot end-effector (called needle) and the biological cell. The dynamic performances of the controller are not studied. However, the estimation of the parameters converge in 250 ms which means that the desired behavior can be reached after the estimation of the parameters converges to the final values. The tracking performance of the controller has been evaluated by calculating the relative root mean square error (RRMSE) between the reference force f_r and the measured actual force f_g over the trial time T which is given by RRMSE $= \sqrt{\frac{1}{T}\sum_{t=0}^{T}\frac{(f_g(t)-f_r(t))^2}{f_r^2}}$. The maximal RRMSE was 0.4371.

In [191], two schemes of impedance control are tested and compared. The two controllers are position-based sliding mode impedance control (PBSMIC) scheme and a discrete-time sliding mode impedance force control (DSMIFC) scheme. For the first controller, an outer loop controller generates a desired trajectory for the system and the inner loop controller is sliding-mode controller calculated through the use of PI (Proportional Integral) sliding surface. For the other controller, a sliding-mode controller is used to control directly the impedance error and a PI sliding surface is used to track the desired impedance relationship. The impedance control formulation presented in Equation (4.2) is changed by adding a gain K_f as follows:

$$M_d\,(\ddot{y}-\ddot{y}_r)+D_d\,(\dot{y}-\dot{y}_r)+K_d\,(y-y_r)=K_f\,(f_r-f_g)$$

The gain K_f is added in order to reduce the force reference error. The two control schemes are tested experimentally to follow sine waves references. The controller performances were studied in terms of position and force tracking of force control and the relative root mean square error (RRMSE) has been identified relative to K_f. The tuning of the gains depends on the application and needs to perform tests in order to find the best gains. The maximal RRMSE force error was 10% for small values of K_f (near zero) and the RRMSE decreases when K_f increases. The minimal RRMSE was 7.5% for $K_f = 5000$. When $K_f > 6000$, the controller produces oscillations in the system. The best balance between position and force tracking is

achieved for $K_f = 4000$ where both force and position RRMSE are around 8%. This control scheme has not considered additional work to perform the force tracking, the force has been controlled by adapting a gain K_f which is not able to cancel the force error alone. Furthermore, the add of the gain K_f induces some difficulty to the user to perform the control in order to determine the gain which minimizes the force error which means that the gain should be tuned experimentally depending on the application.

In [67], vision based impedance control is used. Vision system enables to perform an inner loop position control which is controlled by a PID controller. Position-based impedance control is used without developing a force tracking method and the force tracking is performed by tuning the impedance control parameters to minimize the force error. In experiments, the controller succeeded to track the desired force with small force error less than 5% and with a settling time bigger than 400 ms.

The impedance control is used at the microscale for several applications due to its robustness, facility of integration and its ability to control the dynamic of interaction between the microrobot and the environment control. However, the lack of direct force capability stills an issue in the application of this technique and especially at the microscale where the environment is often unknown. Another issue of impedance control at the microscale is the lack of suitable sensors. For example, adaptive control methods used at the macroscale to perfrom force tracking in impedance control require the measure of the velocity of the robot end-effector which is not available at the microscale.

Experimental results for the indirect force control

The force tracking position-based impedance control technique is tested in the automated grasp and release tasks of the micropart (holder) using the experimental setup presented in Figure 4.2. In this method, the position of the end-effector is estimated through model defined in section 3.4) using the measurements of force f_g and the applied voltage U. Indeed, it is difficult to measure the position of the end-effector due to its small thickness (10 µm). PID control is used as an inner loop position control. The tested control scheme is the one presented in Figure 4.7. In order to perform force tracking in impedance control, the parameters of the environment, more precisely the location and the stiffness of the environment, should be known. In practice, it is difficult to known the stiffness and the location of the environment and it can easily change during the same experiment. Two approaches are tested for this control law in this section:

- an offline parameter estimation technique is used to estimate the location and the stiffness of the environment, then the impedance control scheme (Figure 4.7) is used to control the system while the parameters $\hat{y}_e$ and $\hat{k}_e$ are constants and have the values of the offline estimation;
- an online parameter estimation technique is used to estimate the location and the stiffness of the environment while controlling the system.

Then, the two approaches are compared in terms of performances of the controller and their feasibility.

The specifications used for the impedance control are the same than the specifications used for explicit force control (settling time lower than 100 ms with overshoot lower than 10%). The

desired impedance is chosen to be as second order transfer function without oscillations. The desired impedance parameters are: $M_d = 1$, $D_d = 200$ and $K_d = 10000$ which result that the impedance is: $Z(s) = s^2 + 200s + 10000$.

In the first approach, the impedance control technique is used after the offline parameter estimation. When no force reference is set to the controller ($f_r = 0$), the position reference y_r is equal to the offline estimated location of the environment y_e which is around 18.5 µm as shown in Figure 4.8 which shows the experimental results corresponding to the impedance control scheme with offline parameter estimation. Then, at time $t = 0.7$ s, a force reference of 1 mN

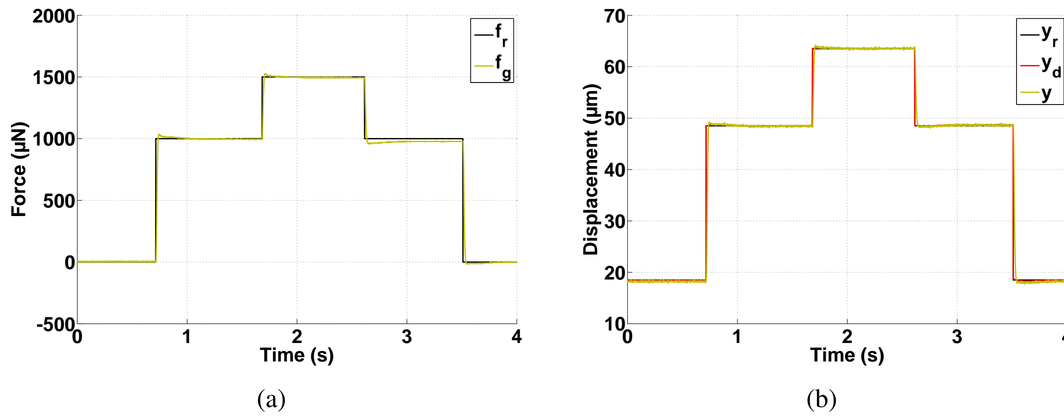

FIGURE 4.8: Experimental results for the position-based impedance control with offline environment parameter estimation: (a) force response compared to the reference force, (b) position response compared to y_r and y_d.

is set to the controller ($f_r = 1$ mN) and the controller is able to track the reference force with small steady state force error of 4 µN within a settling time of 20 ms and an overshoot of 3.7%. The small steady state force error is due to errors on the estimated environment parameters. Then, at time $t = 1.7$ s, a force reference of 1.5 mN is set to the controller and the controller is able to track the reference force within the same settling time and overshoot but with a steady state force error of 7 µN. Then, at time $t = 2.6$ s, a force reference of 1 mN is set again to the controller and the steady state force error increases to reach 23 µN. This increase of the value of the steady state force error can be caused by a mechanical change of the contact between the TSFM fingers and the springs of the holder where a sliding along the Z axis may happen between the TSFM fingers and the spring of the holder leading to a change in the stiffness k_e and even possible change of y_e. It may also be caused by some errors in the estimation of the end-effector's position which can not be accounted using this control law. Finally, at time $t = 3.5$ s, a zero force reference ($f_r = 0$) is set again to the controller and the force returns to zero within same dynamic performances. When the measured force is null, this does not imply that the micropart is released due to pull-off forces.

The controller is able to grasp the micropart with good performances. However, in our case, the stiffness and the location of the environment may change from one experiment to another but also may change during the same experiment as shown in Figure 4.8-(a) for a time duration

2.6 s $< t <$3.5 s. Indeed, the location of the environment depends on the initial position of the microgripper finger relatively to the spring. Its value can change easily between two experiments (the change can easily reach several tens of µm) but can change during the same experiment. For the stiffness, it depends on the location of the contact along the Z axis between the TSFM fingers and the springs of the holder along the Z axis and consequently it can be changed easily between two different experiments but also during the same experiment if the TSFM fingers slides along the Z axis. Consequently, an estimation of the environment parameters need to be performed.

In the second approach, the impedance control technique is used with online parameter estimation. The control scheme presented in Figure 4.7 is used with an online parameter estimation technique. It will be presented in details in section 4.4.2 and it consists of measuring the stiffness and the location of the environment (holder's spring) using the measurements of the applied force and using the estimation of the position of the end-effector's tip. The estimated location, $\hat{y}_e$, can be estimated once a non zero force is measured by the force sensor while the estimated stiffness can be estimated using $\hat{k}_e = \frac{f_e}{y - \hat{y}_e}$ (for more details see section 4.4.2). The estimation is reinitialized for each change in force reference except the return of the force reference to zero. Figure 4.9 shows the experimental results of the position-based impedance control scheme with online parameter estimation. First, the initial estimation of the location of the environment is set to $\hat{y}_e^o = 30$ µm. The reference position is given, according to Equation (4.12), by $y_r = \frac{f_r}{\hat{k}_e^o} + \hat{y}_e^o$ where $\hat{y}_e^o$ and $\hat{k}_e^o$ are the initial guess of environment's location and stiffness respectively. It is also set to 30 µm as no reference force is applied. The controller aim to track the position y to the reference position and contact 1 happens. Once contact 1 happens, the new estimation of the environment location is calculated, $\hat{y}_e$. Then, a reference force of 1 mN is set the controller. Contact 2 happens in this case and the controller is able to track the reference force with no steady state force error within a settling time of 148 ms and an overshoot of 20% while estimating the environment stiffness online. The new overshoot value is caused by the environment stiffness estimation which affects the dynamics of the controlled system. The grasp of the micropart being successful, the release is tested by applying a negative force reference at time $t = 0.62$. The reason for which, a negative force reference is set to the system is to cancel the effect of pull-off forces which is shown in Figure 4.9-(a). The contact in this case is separated and the release is successful.

Comparing the results of the impedance control with online parameter estimation to the with offline parameter estimation, it is clear that the dynamic response of the case with offline parameter estimation is better. Indeed, in the case of online estimation, the dynamics of the parameter estimation technique influences the dynamics of the impedance controller and consequently the desired impedance of the system will not be satisfied with the online parameter estimation technique. However, the online estimation is required to cancel the steady-state force error especially in the presence of an unknown or variable environment such in our case. Then, solutions need to be developed to use the impedance control with online parameter estimation while considering the dynamic relation.

Indeed, when the force returns to zero in Figures 4.8 and 4.9, this does not mean that the contact between the microgripper and the micropart is broken. The contact will persist and then if the microgripper needs to get away of the micropart at the end of the process, the micropart

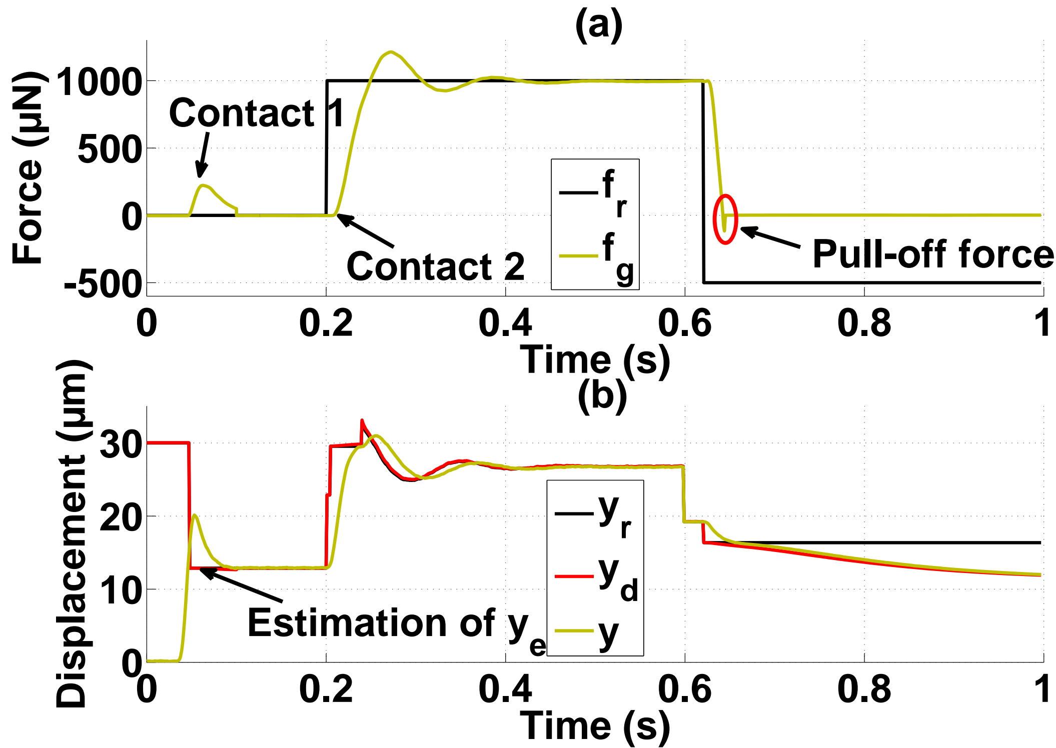

FIGURE 4.9: Experimental results for the position-based impedance control with online estimation of the environment parameters: (a) force response compared to the reference force, (b) position response compared to y_r and y_d.

can be lost because a pull-off force exists which maintains the contact. The solution using the position-based impedance control is to apply a negative force reference which is lower than the pull-off force. For example, if the pull-off force is known to be less than 50 μN, then a force reference of -60 μN is sufficient to break the contact between the micropart and the microgripper. The reason of this is that the control scheme is position-based and consequently the reference force is converted into position reference thanks to Equation (4.12) and the controller operates to track the position to the position reference. Consequently, using this strategy the release of the micropart can be achieved successfully.

4.3.3 Choice of the force control technique

The explicit force control enables the direct control of the interaction force while the indirect force control enables the control of the force indirectly. The indirect force control control enables to control the dynamics of the contact between the robot and the micropart contrary to the explicit force control which enables to control only the direct force applied on the micropart. The most known indirect force control scheme is the impedance control which is sufficient to

Explicit force control	Impedance control
• controls explicitly the force	• possibility of performing force tracking but indirectly
• difficulty of controlling the dynamic of the contact	• enables the control of the dynamics of the contact
• may reduce the bandwidth of the system	

TABLE 4.3: Comparison between explicit force control and impedance control schemes.

control the dynamics of the contact. However, one drawback of the impedance control technique is the lack of direct force capability which is important for many applications and especially at the microscale. This fact has been investigated in several works and solutions have been proposed to perform force tracking in impedance control. Table 4.3 presents a summary of the characteristics and differences between explicit force control and impedance control techniques.

The force tracking impedance control scheme presents an advantage, when it is compared to explicit force control, for the ability of controlling both the dynamics of the contact and the force applied on the environment. Due to this fact, a force tracking impedance control scheme enables more options to be controlled in the system. Furthermore, controlling the dynamics at the microscale is of great interest because the dynamics of microsystems are higher and the microsystems are more flexible which means if the transient behavior in the control is not controlled, the applied force can change in the transient part in an undesired behavior which can lead to breaking the micropart or the end-effectors or loosing the micropart. One challenge of the force tracking impedance control with parameter estimation is to guarantee the desired dynamics without being influenced by the dynamics of convergence of the parameter estimation technique. Force tracking impedance control technique will be chosen in the following to control the TSFM.

4.4 Proposed control technique

In section 4.3, the force tracking impedance control technique has been chosen as a force control technique to be used to control the TSFM. In this section, the sliding mode based control is used to perform the force tracking impedance control technique. First the sliding mode-based impedance control is discussed. Then, the force tracking problem is investigated. Finally, the experimental results of the proposed control are presented.

4.4.1 Sliding mode impedance control (SMIC)

Position-based impedance control is the most used impedance control technique and it is used in [141, 75, 74, 189, 188, 187, 67]. In order to perform force tracking in impedance control, an estimation of the environment parameters needs to be done. However, it is difficult to guarantee that the dynamics of the contact between the end-effector and the environment track the desired

impedance due to the robot dynamics and the parameter estimation dynamics. Several techniques for the parameter estimation have been presented as will be discussed in section 4.4.2. The settling time of parameter estimation technique should be faster than the controller in order not to destabilize the system. In order to guarantee the desired impedance of the system despite the robot dynamics and the parameter estimation dynamics, a solution needs to be proposed.

Noticing this fact, in the work of [102], the authors proposed to adopt a sliding mode-based approach to formulate a robust impedance controller. This approach is interesting in the fact that the control law forces the system to slide along a sliding surface which is defined as a function of the desired impedance. In addition, sliding mode control is well known for its robustness property [149]. When the system is in the sliding mode, the state trajectory remains on or near a surface (called the sliding surface) in the state space, regardless of model uncertainties and disturbances. The robustness of sliding mode control is achieved by switching the control law such that the state trajectory, in the region around the surface, always tends toward this surface. In the implementation, the desired dynamics (impedance) of the system is the equation of a sliding surface. When the system variables correspond to the sliding surface, the desired impedance is implemented. Furthermore, the sliding mode control has shown its effectiveness for controlling nonlinear systems and is used to control piezoelectric actuator in many microscale applications [190, 191].

Recall from Equation (4.2) that the impedance control formulation is given as follows:

$$M_d\left(\ddot{y}-\ddot{y}_r\right)+D_d\left(\dot{y}-\dot{y}_r\right)+K_d\left(y-y_r\right)=f_r-f_g \tag{4.15}$$

where M_d, D_d and K_d are respectively the desired mass, damper and stiffness to set the desired dynamics of the contact and f_g is the gripping force.

The impedance error or what is also called the measure of impedance error is given in the following:

$$e_i=M_d\left(\ddot{y}_r-\ddot{y}\right)+D_d\left(\dot{y}_r-\dot{y}\right)+K_d\left(y_r-y\right)+e_f \tag{4.16}$$

where e_i is the impedance error and $e_f=f_r-f_g$ is the force error between the desired and the applied force. e_i and e_f have the unit of force.

In order to make the system to follow the desired impedance within a finite time, the impedance measure error is adopted as the sliding function to realize a sliding mode-based control in [102] where in [190, 191] the authors propose to use a PI type of sliding function based on the impedance error. The use of the impedance measure error as a sliding function is more straightforward to cancel the impedance measure error and consequently guarantee that the system follows the desired dynamic relation.

Using the impedance measure error, a sliding surface can be defined as follows:

$$\sigma=\left(\dot{y}_r-\dot{y}\right)+\frac{D_d}{M_d}\left(y_r-y\right)+\frac{K_d}{M_d}\int\left(y_r-y\right)dt+\frac{1}{M_d}\int\left(f_r-f_g\right)dt \tag{4.17}$$

When the system reaches the sliding surface and is in sliding mode, $\sigma=0$ and $\dot{\sigma}=0$. In this case, using Equation (4.16), the impedance measure error can be written as a function of the sliding surface as follows:

$$e_i=M_d\dot{\sigma}=0 \tag{4.18}$$

The above discussion indicates that the task of designing an impedance controller is equivalent to designing a sliding mode controller that guarantees that the state trajectory reaches the sliding surface and remains on it thereafter. The norm of σ is used to represent the deviation of the system state from the sliding surface. This deviation reflects the impedance control error and is called the measure of impedance error.

An ideal sliding mode controller can ensure that if the trajectory of the robot at $t = 0$ is not on the sliding surface (that is, $\sigma(y_0) \neq 0$) it will reach the surface within a finite time ($\sigma(y(t_r)) = 0; t_r < \infty$) and will remain on it thereafter ($\sigma(y(t_r)) = 0; t_r < t < \infty$). Such a performance can be realized by using a switching element without any time delay [171]. In the following we first consider the implementation of a desired impedance using a switching compensator.

The control law using a switching compensator for the implementation of the targeted impedance is given as follows:

$$U = U_{eq} - K \cdot sgn(\sigma) \tag{4.19}$$

where U_{eq} is the equivalent control is the solution of $\dot{\sigma} = 0$, and is calculated with the dynamic model given in Equation (3.31) and *sgn* is the sign function. Using Equations (4.16) and (4.18), $\dot{\sigma} = 0$ implies:

$$M_d\ddot{y} + B_d\dot{y} + K_d y = M_d\ddot{y}_r + B_d\dot{y}_r + K_d y_r + f_g - f_r \tag{4.20}$$

In the Laplace domain, Equation (4.20) can be written in the Laplace domain as follows:

$$Y = Y_r + \frac{F_g - F_r}{Z(s)} \tag{4.21}$$

where Z is the desired impedance defined in Equation (4.3) and Y and Y_r are respectively the Laplace transform of y and y_r. Replacing Y in Equation (4.21) by the value of Y_C calculated from the model defined in Equation (3.31), the following can be deduced:

$$G_u(s)\left(d_p U_{eq} - H_s\right) - G_f(s) F_g = Y_r + \frac{F_g - F_r}{Z(s)} \tag{4.22}$$

The latter equation can be written as follows:

$$U_{eq}(s) = \frac{1}{d_p \cdot G_u(s)} Y_r - \frac{1}{d_p \cdot Z(s) \cdot G_u(s)} F_r + \frac{1 + Z(s) \cdot G_f(s)}{d_p \cdot Z(s) \cdot G_u(s)} F_g + \frac{1}{d_p} H_s \tag{4.23}$$

After calculating the equivalent control which is the solution of $\dot{\sigma} = 0$, the control law can be deduced by replacing U_{eq} (Equation (4.23)) in Equation (4.19). In many applications, the sign function causes chattering in the system which is undesirable in practice. One approach to reduce chattering is to modify the switching control law Equation (4.19) in a small region around the sliding surface, such that the modified control law is continuous in this region. Several variations of this approach have been reviewed by [172]. An effective approach is to use a proportional impedance error function with saturation. Using this approach, the controller becomes:

$$u = u_{eq} - Ksat\left(\frac{\sigma}{\varepsilon}\right) \tag{4.24}$$

where ε is a boundary which is a threshold chosen to reduce the chattering and the saturation function is given as follows:

$$sat\left(\frac{\sigma}{\varepsilon}\right) = \begin{cases} sgn\left(\frac{\sigma}{\varepsilon}\right) & \text{if} \quad |\sigma| > \varepsilon \\ \frac{\sigma}{\varepsilon} & \text{if} \quad |\sigma| \leq \varepsilon \end{cases} \tag{4.25}$$

When the state trajectory is outside the boundary layer ($||\sigma|| > \varepsilon$), the control law defined in Equation (4.24) is equivalent to the control law given in Equation (4.19). Therefore, the trajectory will be attracted to this layer. Within the boundary layer, the dynamics of the system is the approximation of the desired dynamics as defined by the equation of the sliding surface.

4.4.2 Force tracking in impedance control

As presented in section 4.3.2, in order to perform force tracking in impedance control, the environment parameters need to be estimated. Many researchers have paid attention to this fact and tried to solve the direct force control capability by using direct and indirect adaptive impedance control [141, 147, 108, 193], recursive least square [98] or offline signal processing [50]. The latter can be used to estimate the parameters of the environment offline and then use the estimated values in the control loop which is difficult to be done especially in a system where the environment parameters are variable such as microscale systems. The recursive least square method used in [98] is difficult to implement and it estimates the environment mass, damping and stiffness within the framework of pure impedance control without tracking a desired force signal because the environment location is not estimated. Most of the developed works use adaptive impedance control to estimate the parameters of the environment. However, the implementation of the parameter estimation in the indirect adaptive controller requires data on the current position and velocity of the end-effector and the interaction force. In practice, especially at the microscale, accurate measurement of absolute velocity at the robot tip is difficult to achieve and induce a challenge in the application of the method. Furthermore, to use the algorithm, the user must specify the gain matrix of the adaptation law which increases the complexity of the method.

In this work, a method to estimate the environment parameters is presented. The method is based on the force measurement of the force sensor and the end-effector's position estimation. The location of the environment, y_e, is located as the value for which the force measurement becomes bigger than a threshold which is defined relative to the amplitude of the noise of the force sensor. For the estimation of the stiffness, the method is based on the ratio of the force acting on the environment to the deformation of the environment. The proposed method is easy to be implemented, it does not need to specify adaptive gains and it requires only data on the location of the end-effector and the interaction forces.

The first step is to determine the location of the environment y_e. The idea is to apply the impedance control law presented in the previous section using assumptions $\hat{y}_e^0$ and $\hat{k}_e^0$ of y_e and k_e. Once the control law is applied, a transition between non contact and contact happens. During this transition, an on line acquisition of the force and position measurements is achieved and when a contact is detected the location of the environment, $\hat{y}_e$, is determined by the past

value of the position measurement. Due to the noisy force signal measurement (amplitude of noise $\pm 5\mu$N in our case), a dead zone is defined (5μN) and a contact is taken into consideration if the force measurement is bigger than the dead zone.

Once the environment location is estimated, the environment stiffness is estimated using the static part of Equation (4.6):

$$\hat{k}_e = \frac{f_g}{y - \hat{y}_e} \quad \text{if } y > \hat{y}_e \tag{4.26}$$

Note that ignoring the dynamical part of Equation (4.6) could modify the desired dynamic of the system but it will not affect the steady state part. Using Equation (4.12), we can write:

$$y_r = \hat{y}_e + \frac{f_r}{\hat{k}_e} = \hat{y}_e + \frac{f_r}{f_g}(y - \hat{y}_e) \Leftrightarrow y_r - \hat{y}_e = \frac{f_r}{f_g}(y - \hat{y}_e) \tag{4.27}$$

Equation (4.27) shows that if y tracks y_r, then f_g will track f_r.

Using the proposed online parameter estimation technique, the estimated parameter can change to new values if the micropart slides between the fingers of the microgripper or in presence of disturbances caused by the force sensor signal.

The complete impedance control scheme proposed in this work with parameter estimation is given in Figure 4.10.

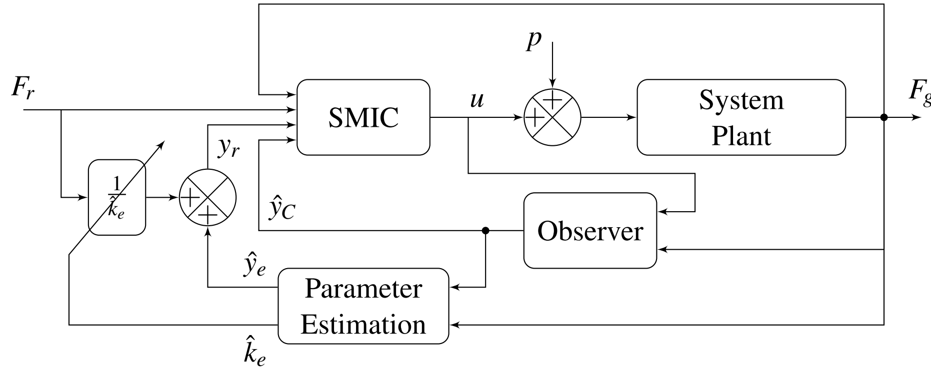

FIGURE 4.10: Diagram of the sliding-mode impedance control with force tracking.

4.4.3 Force tracking despite estimation errors

Using Equations (4.6) and (4.26), the steady state force applied on the environment, f_g^{ss}, could be written in the two forms of Equation (4.28):

$$f_g^{ss} = \hat{k}_e(y^{ss} - \hat{y}_e) = k_e(y^{ss} - y_e) \tag{4.28}$$

where y^{ss} is the position of the environment in steady state. Replacing Equation (4.13) in Equation (4.28):

$$\hat{k}_e y^{ss} - \hat{k}_e \hat{y}_e = (\hat{k}_e + \Delta k_e)(y^{ss} - \hat{y}_e - \Delta y_e) \tag{4.29}$$

After developing Equation (4.29), the following can be derived:

$$\Delta k_e = \frac{\hat{k}_e \Delta y_e}{y^{ss} - \hat{y}_e - \Delta y_e} \tag{4.30}$$

Using Equation (4.28), $y^{ss} - \hat{y}_e = \frac{f_e^{ss}}{\hat{k}_e}$, and replacing the latter in Equation (4.30), the following can be derived:

$$\Delta k_e = \frac{\hat{k}_e^2 \Delta y_e}{f_g^{ss} - \hat{k}_e \Delta y_e} \tag{4.31}$$

Thus, the error in the estimation of the stiffness of the environment, Δk_e, increases if the error of the estimation of the position, Δy_e, increases as Equation (4.31) shows. If the estimation of the position of the environment is small then the estimation of the stiffness is small.
Replacing Equation (4.31) in Equation (4.14), the following can be derived:

$$e_f^{ss} = \frac{-K_d \hat{k}_e \Delta y_e}{K_d f_e^{ss} + \hat{k}_e f_g^{ss} - K_d \hat{k}_e \Delta y_e} e_f^{ss} \tag{4.32}$$

Equation (4.32) is true if and only if:

$$\begin{cases} e_f^{ss} = 0 \\ \text{or:} \\ \dfrac{-K_d \hat{k}_e \Delta y_e}{K_d f_g^{ss} + \hat{k}_e f_g^{ss} - K_d \hat{k}_e \Delta y_e} = 1 \end{cases} \tag{4.33}$$

Equation (4.33) is equivalent to:

$$\begin{cases} e_f^{ss} = 0 \\ \text{or:} \\ f_g^{ss} = 0 \end{cases} \tag{4.34}$$

Equation (4.34) shows that using the presented parameter estimation technique, once a contact force is detected ($f_g \neq 0$), the steady state force error is always zero and the force tracking is guaranteed even if big estimation errors exist on y_e and k_e because the errors are compensated.

4.4.4 Strategy to deal with pull-off force

In this section, a simple strategy is proposed to deal with pull-off forces. This method is the same used in Figure 4.9-(a).

At the microscale, contact and surface forces have an adhesive effect which is mainly manifested by pull-off force. A release task in microassembly consists of releasing the task when the micropart is positioned in its final position and when the micropart is in contact with the microassembly substrate. Once a contact between the micropart and the substrate exists, the release of the micropart can be performed. In the microassembly context, if a release task need to be performed to a micropart handled between the fingers of a microgripper, usually a force reference of zero is set to the controller. However, if the measured force is null, this does not

mean that the micropart has been separated from the microgripper's fingers. As a result, the micropart can be lost if the microgripper moves.

To solve this problem and using the impedance control formulation, applying a negative force reference to the system enables to convert it to a position reference. The negative reference should be smaller than the maximal pull-off force, *e.g.* if the maximal pull-off force of the system is identified to be 100 µN, then the force reference should be smaller than 100 µN ($f_r < -100$ µN). The resulting position reference is calculated according to Equation (4.12). As a result of the change in the position reference, the position of the system changes breaking the contact between the micropart and the microgripper fingers.

4.4.5 Experimental results for the proposed control technique

The sliding mode impedance control with force tracking scheme presented in Figure 4.10 is tested in the automated grasp and release tasks of the micropart (holder) using the experimental setup presented in Figure 4.2. The environment parameters are not known at the beginning of the experiment and initial values are given without any knowledge on the their real values. The control scheme is applied and the experimental results showing the response of the system are given in Figure 4.11. First, the controller is turned off and initial estimations, $\hat{y}_e^o$ and $\hat{k}_e^o$, of parameters y_e and k_e are set to the controller. Then, the controller is turned ON at time $t = 50$ ms with no force reference, the TSFM fingers start to move to let the position tracks the position reference y_r which is equal to $\hat{y}_e^o$ because no force reference exists. Because $\hat{y}_e^o$ is bigger than the real value of y_e, the TSFM fingers enter in contact 1 with the micropart. When contact 1 is appears, a new estimation of the environment location $\hat{y}_e$ is calculated and the position reference y_r changes to the new estimated value $\hat{y}_e$ ($y_r = \hat{y}_e$). Then at time $t = 0.37$ s, a force reference is set to the controller and contact 2 happens enabling the estimation of $\hat{k}_e$. The controller is able to cancel the reach the steady state within a settling time of 20 ms and a small overshoot of 3.7% despite the online estimation of the stiffness of the micropart springs. The steady state force error is null showing the significance of the parameter estimation technique and the SMIC. The grasping task is then achieved with success.

The release task is then tested. For that, the strategy to deal with pull-off forces defined in section 4.4.4 is used. Thus, negative force reference is set to the system allowing the controller to break the contact between the TSFM and the micropart and succeeding the release task within a settling time of 19 ms.

Comparing the experimental results of Figures 4.4, 4.9 and 4.11, the last figure shows the best dynamic performances in terms of settling time and overshoot of the system. The SMIC scheme can also deal with pull-off force to successfully achieve release task.

4.5 Conclusion

This chapter has focused on the automation of the grasp and release of a flexible micropart using force control. A study on the existing force control techniques has been presented. Theoretical and experimental studies have been performed in order to compare the performances of each of the existing force control techniques taking into consideration the microscale specificities and

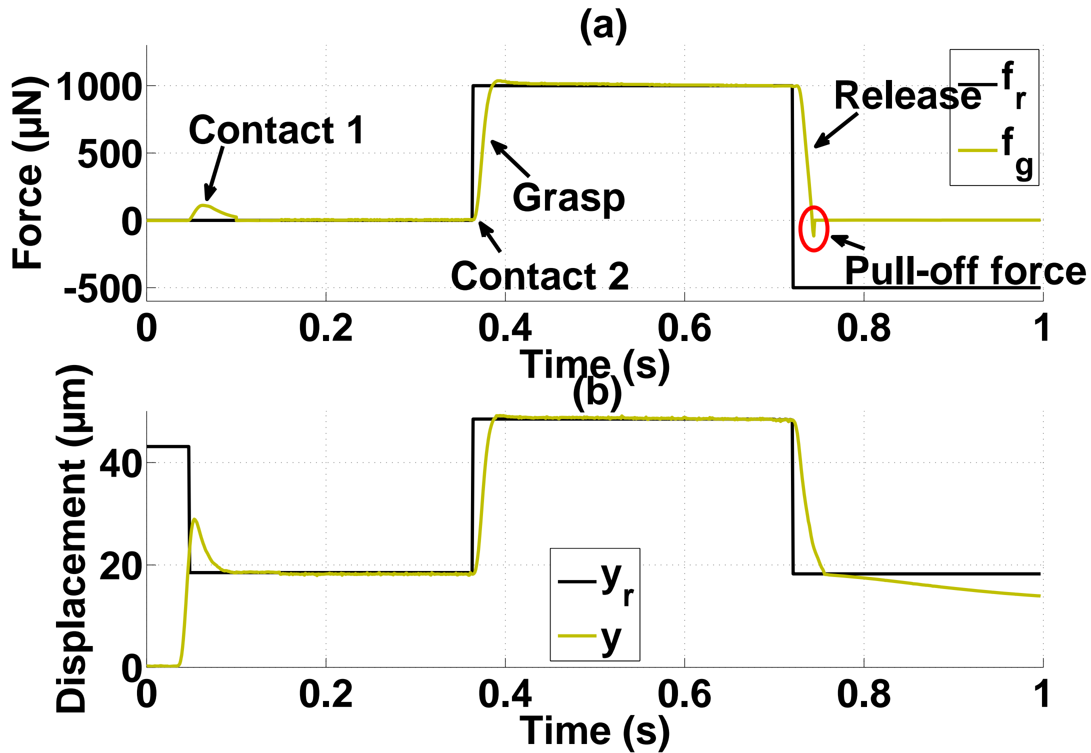

FIGURE 4.11: Experimental results for the Sliding Mode Impedance Control (SMIC) with online estimation of the environment parameters: (a) force response compared to the reference force, (b) position response compared to y_r.

to choose a force control technique which fits the best for these tasks. It was shown that using PI explicit force control, the grasp and release if the micropart has been performed within settling time going from 530 ms to 1 s depending on the gains of the PI controller. Some oscillations have also appeared around the desired grasping force in the steady state zone with an amplitude less than 5%. These dynamic behavior are consistent with the present works in literature using PI explicit force control at the microscale. Moreover, using the explicit force control, it is difficult to automatically release the micropart due to pull-off forces. The impedance control has shown good dynamic performances if an offline parameter estimation is done which not an easy task especially at the microscale where the environment may change during the same experiment. The impedance control with online parameter estimation has been able to track the desired force within a settling time of 148 ms and an overshoot of 20%. The dynamic behavior has been influenced by the dynamics of the online parameter estimation technique.

Using these results, it was shown that impedance control is the most promising approach to perform dynamic force control by setting a desired dynamic relation. However, in order to follow the desired dynamic relation with online parameter estimation, Sliding Mode based Impedance Control (SMIC) scheme is proposed to force the system to slide along a sliding sur-

face which is chosen in this case as a function of the desired impedance relation. The proposed control scheme enables to take into consideration microscale specificities notably pull-off force and high dynamics of the microscale objects. A strategy to deal with pull-off force using this control technique has been proposed. The online parameter estimation technique enables to estimate online the location and the stiffness of the environment, which is a flexible micropart in our case, and to use them in the control law in order to perform force tracking. The SMIC used has presented good dynamic behavior by tracking the reference within 20 ms and an overshoot of 3.7%. The SMIC enabled to automate the grasp and the release of a flexible micropart with very good and promising dynamic performances and despite the presence of pull-off forces. In next chapter, the proposed control technique will be used to achieve a full automated microassembly scenario.

Chapter 5

Hybrid Force/Position Control for a Full Automated Microassembly

In this chapter, a closed-loop automation using hybrid force/position control is done for some microassembly tasks. The main microassembly tasks are grasp and release of the micropart and guiding tasks. In the hybrid force/position control, the impedance control developed in chapter 4 is used in addition to a position control loop. It is used to control the dynamics of the contact for grasping, releasing and guiding tasks. The stability of the grasp during manipulation is studied and a guiding strategy is defined taking into consideration microscale specificities. The automated tasks are tested for rigid and flexible microparts.

5.1 Introduction

Automated robotic microassembly is often used to improve the precision, repeatability and operation time of microassembly process. To perform precise microassembly, several and consecutive tasks need to be performed including grasping, manipulation, moving, peg in a hole, guiding, etc. The automation of some of these tasks increase the success rate and the precision of the microassembly. In our work, we will focus on the automation of three main tasks of the microassembly: grasping, releasing and guiding. Special care needs to be performed for these three tasks because of microscale specificities (srface forces, low inertia, high acceleration)

5.2 Microassembly strategy

A microassembly strategy has been developed in previous works [10] to assemble the MOEMS defined in the MIAAMI project (presented chapter 1 section 1.1.3). The microassembly steps are presented in Figure 5.1 and can be summarized as follows:

1. picking up the holder from the snap connector and positioning of the micropart closely to the final position,

2. inserting the holder into the baseplate,
3. guiding of the holder inside the V-grooves and fine positioning of the micropart at its final position,
4. releasing of snap connector which enables to fix the micropart on the substrate,
5. moving back the microgripper.

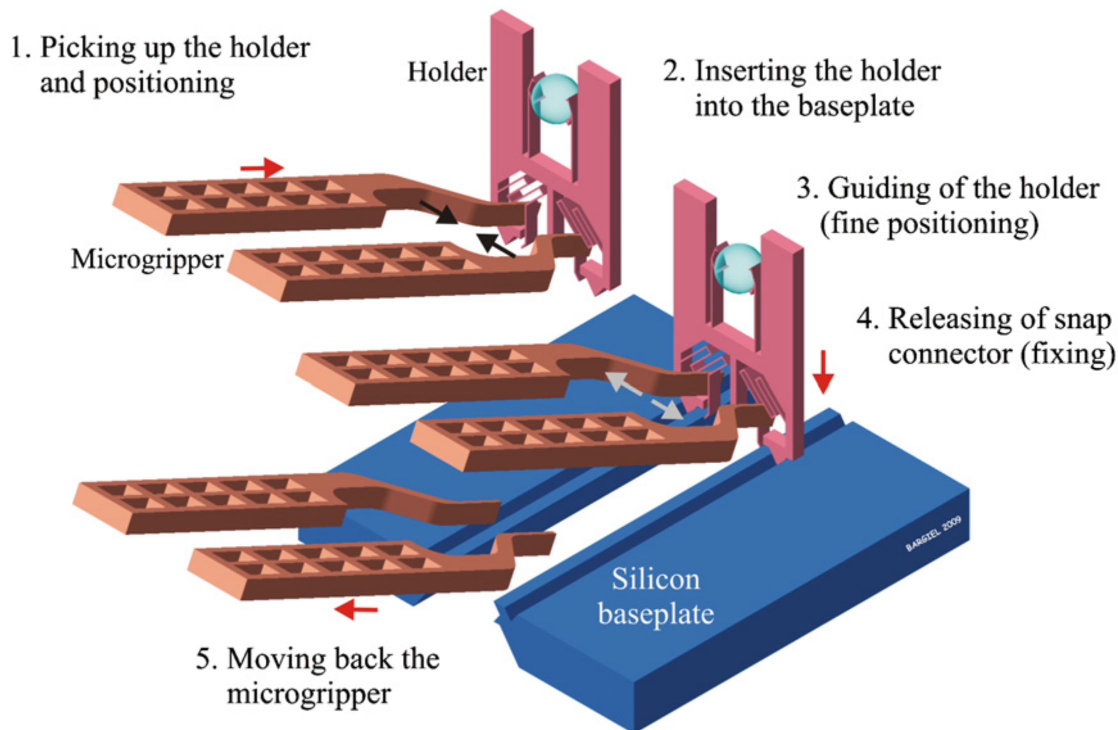

FIGURE 5.1: General concept of holder assembly based on the use of a robotic active microgripper as presented in [10].

Among these five steps, we will focus in our work on steps 1, 3 and 4 which are the most complex to control for the reasons which will be presented in the following.

5.2.1 Automated grasping and release of the micropart

The grasping and release of the micropart are critical in any microassembly or micromanipulation processes. Indeed, the grasping of the micropart is the first step of the microassembly process which means that a successful grasping enables to continue the process but failure grasping induces risks of breaking or loosing the micropart and consequently the microassembly process can not be continued. In the grasping process, the grasping should be performed to apply sufficient forces on the micropart without damaging the micropart or the microgripper due to big forces. The most adapted for the grasping step is the force control because it enables to control

the force applied on the micropart by setting a force reference and the control objective is to track the applied force to a desired force.

The release of the micropart is the last step of the microassembly and a failure in the release of the micropart generates the loosing or breaking of the micropart at the end of the microassembly process after successfully achieving three steps. The release should be performed when the micropart is positioned in its final position and it is done by separating the contact between the microgripper fingers and the micropart. It can be performed by controlling the force applied on the micropart because the information on the force can give an idea of the situation of the contact (contact, no contact, pull-off forces). Notice that at the microscale, if the measure of the gripping force is null, it does not imply that the contact is separated due to the presence of pull-off forces. In order to separate the contact, the pull-off forces need to be considered. Otherwise, if the contact still exists, loosing or breaking the micropart may happen when the microgripper is moved back to finish the microassembly process.

Consequently, automation of the grasp and release processes is required in order to avoid the presented issues and to increase the success rate of the microassembly. Force control is the most adapted for these two processes. In chapter 4, a sliding mode impedance control with force tracking control scheme has been used to automate the grasp and release of microcomponents. In addition, a strategy to deal with pull-off force in the release task has been presented. This strategy consists of applying a negative force reference to the control scheme as presented in section 4.4.4. The developed control scheme has shown its effectiveness for the automation of these two tasks while dealing with pull-off forces. Thus, in the following of this chapter, the focus will be on the guiding task.

5.2.2 Automated guiding and grasp stability

In our case, the automated guiding task (see Figure 5.1) requires the control of both the gripping force applied by the two fingers of the microgripper on the micropart and the contact force between the micropart and the rail. This task is of great interest because it enables to position the micropart in its desired position (along X axis) while controlling any contact force (along Y axis) which can appear during the guiding between the micropart and the substrate. The control of this interaction enables to ensure the stability of the grasp in order not to loose or break the micropart and to succeed the task. For the considered micropart scale, interaction forces (gripping force, contact force, pull-off force) have to be taken into account and few tens of µN forces have to be controlled. In the following, the grasp stability conditions of the micropart are studied and a guiding strategy is proposed.

5.2.3 Grasp stability

The study of the grasp stability is considered. While guiding the micropart in the rail (see Figure 5.2) a contact may appear along X, Y or Z at a distance ℓ (see Figure 5.3). When a contact appears, the grasp is perturbed due to the contact force. As a result, the micropart may slip through the fingers, rotate, be lost or broken. We separately consider each component of the contact force F: F_x, F_y, and F_z and we determine the gripping force to apply according to the contact force for ensuring the stability of the grasp. In Figure 5.2, y_p is a positioning stage along

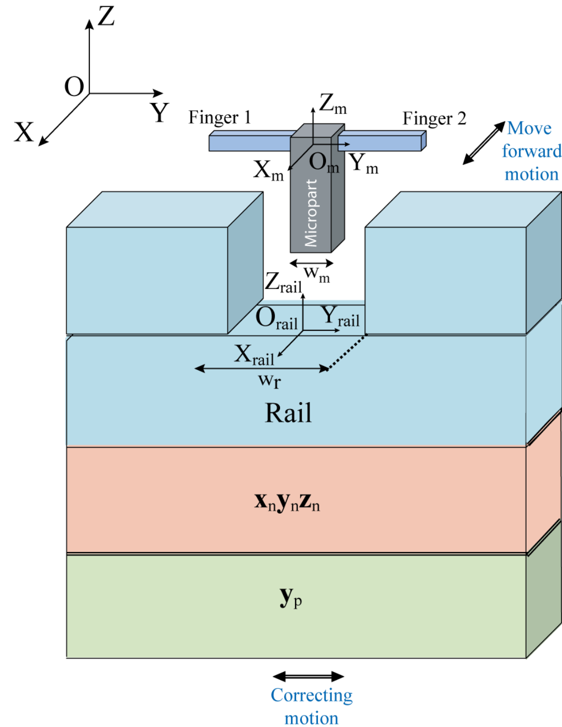

FIGURE 5.2: Guiding task based on two-sensing-fingers microgripper with coordinate frames: $O_{rail}X_{rail}Y_{rail}Z_{rail}$ and $O_mX_mY_mZ_m$.

Y axis to apply disturbances to the system to test the control technique while $x_ny_nz_n$ represents an XYZ NanoCube positioning stage which will enable the positioning of the system along X and Z axes and correction of the contact force along Y axis. $O_{rail}X_{rail}Y_{rail}Z_{rail}$ represents the coordinate frame if the rail and $O_mX_mY_mZ_m$ represents the coordinate frame of the micropart.

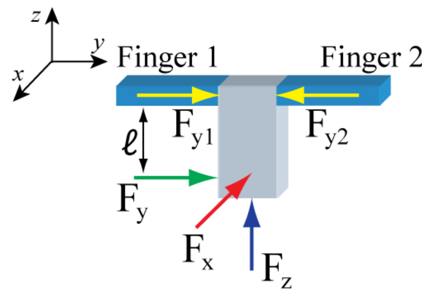

FIGURE 5.3: Perturbated grasp with each component of the contact force: F_x, F_y, and F_z.

Stability according to a F_z perturbation

Based on the Coulomb friction, the sliding does not happen if the tangential forces applied by the fingers are important enough to overcome F_z. The condition is $2\mu F_{yi} \geq Fz$ with $F_{y1} = F_{y2} = F_{yi}$ where μ is the friction coefficient and F_{yi} is the preload gripping force applied along Y by finger i. The friction coefficient depends of the roughness of the contact surface and the type of the materials. In practice, it is difficult to determine the friction coefficient of the Silicon. For this reason, we limit the study for the stability along the Z axis by applying preload gripping forces hard enough to reduce the effect of the perturbation.

Stability according to a F_x perturbation

F_x induces a torque that may cause the rotation of the micropart. To prevent rotation, the admissible force F_x can be approximated. The surface in contact (between fingers and micropart) is rectangular with 100 μm of length and 10 μm of thickness. Moreover, the contact is supposed to be perfect. The limit force which can cause the rotation can be calculated using previous works [85]. The objective is to determine the limit which can generate the rotation of the part. This limit is determined to be 30 µm. This limit signifies that the control should be so fast in order to overcome the effect of the perturbation without exceeding the limit force in order to guarantee a stable grasp.

Stability according to a F_y perturbation

The force F_y induces the displacement (linear displacement + deflection + rotation) of the micropart between the two fingers but the micropart is maintained. The maximum admissible force F_y corresponds to the breaking of the fingers due to the generated torque. It will be a great interest to study the evolution of the gripping forces F_{y1} and F_{y2} in function of the contact lateral force F_y, in order to determine a limit contact force to ensure that the gripping forces are in the safe range in order not to break the microgripper fingers. A scheme showing the simplified model of the system when a micropart is grasped between the fingers of the microgripper is presented in Figure 5.4 where it is shown the two fingers of the gripper with the two force sensors.

Previous studies showed the evolution of the gripping force evolution in the presence of lateral contact force for a rigid micropart. It was shown that the evolution of the gripping forces follows two steps, according to the contact between the microgripper fingers and the rigid micropart: planar contact and edge/vertex contact [127, 85]. The planar contact is characterized by the linear displacement of the micropart and the edge/vertex contact by combined linear translational displacement of the micropart along Y for small F_y force and rotation around X for higher F_y. For that, a system of 5 non linear equations based on the contact force F_y enables to determine the evolution of gripping force. This model has been established for a rigid micropart and experimentally validated. Based on that knowledge, Figure 5.5 displays the experimental behavior for a rigid micropart between the two fingers of the microgripper. These curves show that the gripping forces (F_{y1} and F_{y2}) on the two fingers are not equal when the lateral contact force, F_y, is applied. The finger on the opposite side of the contact applies the biggest force to the micropart. Consequently, the side of the contact can be distinguished thanks to a two-sensing-fingers microgripper.

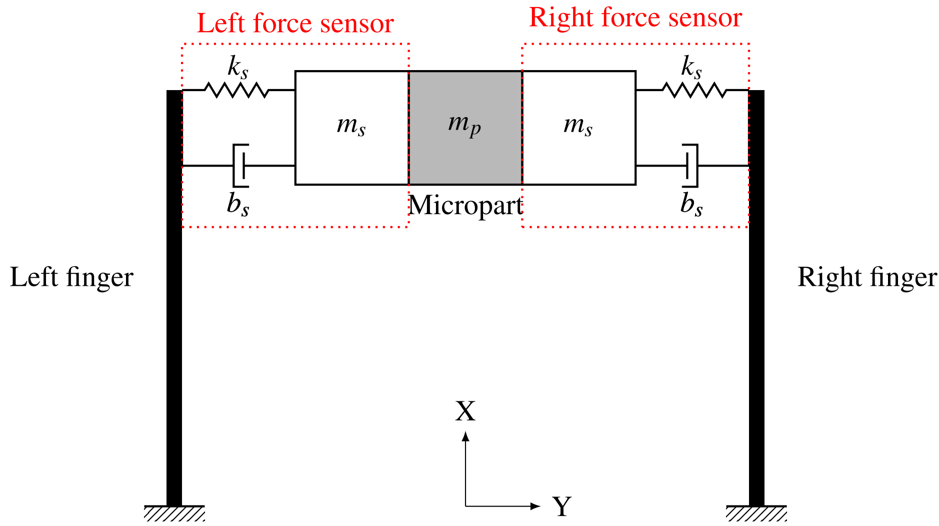

FIGURE 5.4: A scheme showing the simplified model of the system when a micropart is grasped between the fingers of the microgripper.

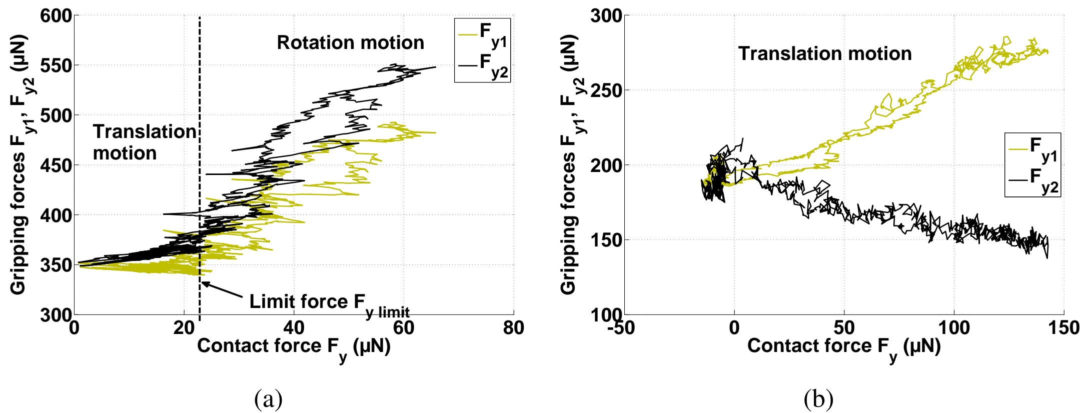

FIGURE 5.5: Experimental results of gripping forces evolution F_{y1} and F_{y2} according to an applied contact forceF_y for: (a) a rigid micropart and (b) a flexible micropart

Figure 5.5 shows that the evolution of the gripping forces for both rigid and flexible microparts. Rigid micropart has a translation motion and rotation motion as shown in Figure 5.5-(a). The contact between the rigid micropart and the microgripper fingers switches to the edge/vertex contact when F_y exceeds 20 µN. Once switching to the edge/vertex contact happens, both gripping forces increase rapidly in function of the contact force F_y. Thus, the limit of stability along the Y axis is the breaking of the microgripper which corresponds to the contact force F_y which generates gripping forces bigger than 2 mN. This force is reached for a contact force up to 500 µN, which is a very big contact force when it is compared to the values found

in [127, 85] (contact force was around 80 μN). This fact shows that the microgripper perform more stable grasp due to its flexibility compared to the microgripper used in [127, 85].

However, for the flexible micropart after applying 150 μN of lateral contact force, the rotation of the flexible micropart does not appear as shown in Figure 5.5-(b) which shows that the rotation becomes for a lateral contact force higher than 150 μN which induces better grasp stability because the micropart stays in the translational move for a big contact force.

5.2.4 Guiding strategy

To achieve automated guiding tasks, it is necessary to establish a strategy. Two important parameters have been considered: the stability of the grasp (section 5.2.3) and the microscale specificities (section 1.2) especially the pull-off force. These two aspects will be considered in the guiding strategy.

The handled micropart motion is composed of an unconstrained displacement along X with a fixed velocity and a constrained displacement along Y. Tp perform the guiding task, three possible strategies can be considered to achieve the guiding task despite the sticking effect of pull-off force which appears for every contact:

- Stop the motion along X and correct the trajectory along Y in order to break the contact. After that, the manipulator can be moved forward freely along X again.
- Move forward along X and correction along Y are performed simultaneously. In that case, the gripping force must comply the condition of stability in presence of a perturbation forces already presented. This strategy is often used for the automated guiding tasks in macroscale.
- Stop the motion along X and correct the trajectory along Y for ensuring the stability in presence of perturbation forces without breaking the contact.

First strategy may induce the presence of pull-off force and a remaining contact even for Fy = 0 μN. It will be difficult to locate the contact break because the pull-off force is not constant, it indeed depends on many parameters [128]. Second and third strategies could be applied. Third strategy is more secure than the second strategy because the motion is stopped and the correction is performed along the Y axis before continuing the motion along X axis. This strategy requires more time because the motion is stopped for correction. To apply the second strategy, high dynamics control is needed along the Y axis in order to compensate the effect of contact and the correction dynamics must have dynamics close to the moving stage in order to guarantee that the condition of stability along the X axis is satisfied.

Consequently, the second strategy called *sliding strategy* will be used in this work and the effort will be on performing high dynamic force control to compensate the effect of contact force and to go with the higher speed to position the micropart in its desired position without caring a lot of the effect of contact force. The term *sliding strategy* is used because once a contact happens, the controller will not break the contact but it will act to control the contact force to zero while sliding the micropart along X axis.

Notice that the same approach used in section 4.4.4 can be used to break the contact relative to pull-off force. However, due to the small width of the rail in the case of the flexible micropart,

the micropart risks to have contact with the second side of the rail and then to continue switching between the two sides of the rail. For this reason, a sliding strategy is chosen although the contact is maintained, the force is controlled to zero.

In order to perform the guiding strategy, two approaches exist:

- The correction is performed using the microgripper fingers which means that if the contact happens from the right side, both fingers must simultaneously go to the left side in order to separate the contact and vice versa.
- The correction is performed using a positioning stage mounted under the substrate.

The first approach enables to use the same control law presented in chapter 4 used for the grasp and release tasks to perform the guiding because the objective is to set the gripping forces to a desired force and a contact force will change the gripping forces which means that the controller will consider this change in each of the gripping forces as a perturbation and reacts to cancel the perturbation and indeed to return the contact force to null. The interest of this strategy comes from the fact that gripping forces will remain controlled to the desired force along the whole experiment.

The second approach is easier technically because the range of the displacement of the positioning stage is bigger than the range of displacement of each finger which means that the the correction using the positioning axis has more range of displacement for correction and as a result more safe zone of correction. Moreover, the use of positioning stage as an axis of correction facilitates the control due to the need of controlling only one axis which is not the case for the first approach where the two fingers need to be controlled simultaneously and their interaction is not mastered. However, to perform the second approach, the control of gripping forces should be turned off during the guiding task in order not to have two controllers which are operating at the same time to perform the same task.

For the above mentioned reasons, the second approach is chosen to perform the guiding task and the control of gripping forces is switched off to perform the automated grasp.

5.2.5 Lateral contact force estimation

In this section, while guiding the micropart inside a rail, a contact appears between the micropart and the rail generating a lateral contact force, F_y. The scheme of the contact is shown in Figure 5.6-(b). Using the Newton's second law fundamental dynamic equation

$$F_{y_1} + F_y - F_{y_2} = m_p \times a = m_p \times \ddot{y}_{C_1} \tag{5.1}$$

where C_1 is shown in Figure 5.6-(a), F_{y_1} and F_{y_2} are the gripping forces applied by the two fingers on the micropart, F_y is the contact force, m_p is the mass of the micropart and a is the acceleration of the micropart along the y axis. The acceleration a is considered to be the same of the acceleration of the point C_1 on the finger. The position of the point C_1 was given in Equation (3.31) and is re-written as follows:

$$Y_{C_1} = G_u(s)\left(d_pU - H_s - G_fF_{y_1}\right) \tag{5.2}$$

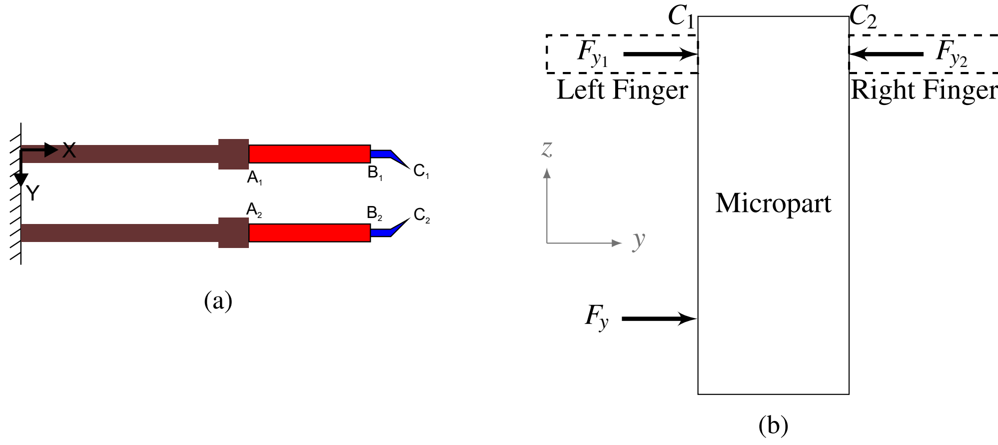

FIGURE 5.6: (a) TSFM initial scheme showing tips A, B and C of the two fingers, (b) a scheme showing the micropart between the fingers of the microgripper and a perturbation force F_y applied on the micropart, F_{y_1} and F_{y_2} being the gripping forces applied on the micropart.

where $G_u(s)$ and $G_f(s)$ are two 4th order transfer function, U is the applied voltage, F_{y_1} is the applied force and H_s is the hysteresis model.

Using Equation (5.2) and the Laplace transform of Equation (5.1), the model of the contact force F_y can be deduced using the following equation:

$$F_y = (F_{g_2} - F_{g_1}) + m_p s^2 \left[c \times G_u(s) - G_f F_{g_1}\right] \tag{5.3}$$

where $c = (d_p U - H_s)$ is constant in this case because in the guiding task, the control of the control of the microgripper is turned off and consequently the applied voltage remains constant (*i.e.* U and H_s can be considered constants in Equation (5.2). The final equation enables to estimate the unknown contact force using the two measured gripping forces. In quasi-static mode, Equation (5.3) becomes $F_y = F_{y_2} - F_{y_1}$.

Validation of the lateral contact force estimation

In order to validate the model for the lateral contact force estimation, a piezoresistive force sensor (presented in chapter 2), mounted on a robotic micropositioning stage, comes to apply a well-known contact lateral force on a micropart handled between the two fingers of the microgripper and the measured force is compared to the estimated force using the model of Equation (5.3). Figure 5.7a shows the micropart between the fingers of the microgripper and the piezoresistive force sensor used to apply contact forces on the micropart. The model presented in Equation (5.3), shows that the contact force can be measured using the two measured gripping forces. Figure 5.7b shows a comparison between the measured contact force and the estimated contact force. The input of the estimation block is the measured gripping forces F_{g_1} and F_{g_2} and Equation (5.3) is used for the estimation. The results also show that the estimation block presents a good dynamic estimation of the contact force.

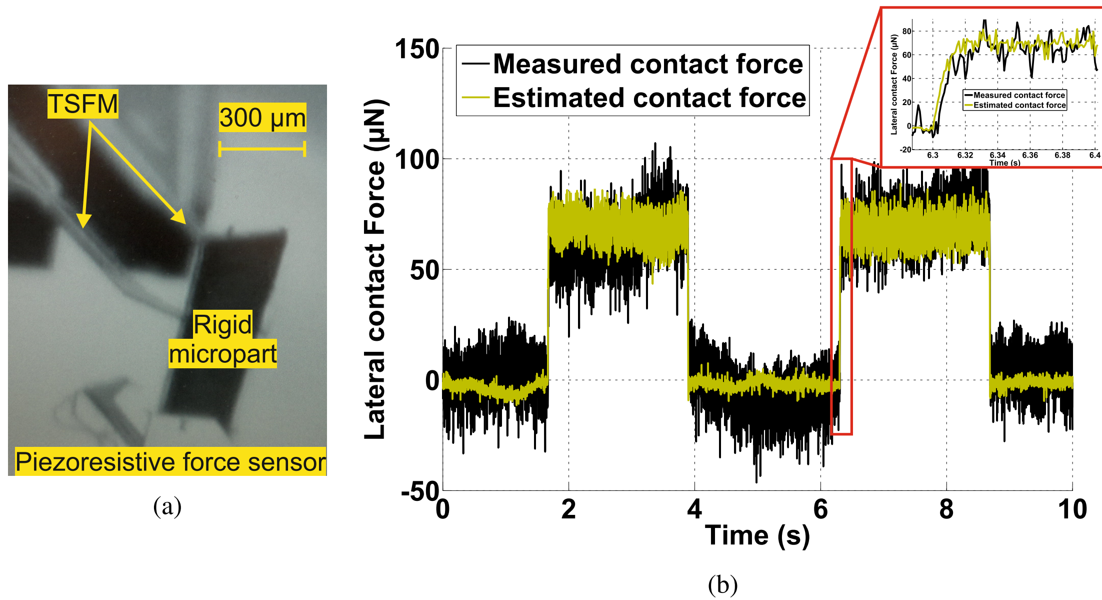

FIGURE 5.7: (a) Experimental setup for the contact lateral force estimation and (b) experimental results comparing the estimated contact force to the measured contact force.

5.3 Control for the automation of the microassembly

The strategies for the grasp, release and guiding have been defined in section 5.2 in order to ensure the stability of the grasp and the success of the microassembly process. The defined strategy requires to control the gripping force, the contact forces and the position of the micropart in order to perform precise positioning of the micropart. In this section, a control strategy is defined to perform the microassembly.

5.3.1 Hybrid force/position control

The hybrid force/position control has been introduced by Raibert and Craig in [129] and an improved formulation has been proposed in [53] to overcome the instability issues introduced by the inverse of manipulator Jacobian matrix which was identified as causing the kinematic instability of the hybrid force/position control scheme. It is among the most used control techniques for the microassembly where constrained and unconstrained spaces exist and where the force and position need to be controlled in different spaces.

The hybrid force/position formulation requires to combine two controls: some axis are controlled in position and others are controlled in force. An orthogonality between the constrained and unconstrained spaces is required to perform the hybrid force/position control. For any given task the position constraints are separated from the force constraints by a selection matrix **S**. **S** is a 6×6 matrix with the elements being either a 1 for position control or 0 for no position control. The 6×6 matrix corresponds to the six components of the joint torques control

$\Gamma = [F_x\ F_y\ F_z\ C_x\ C_y\ C_z]^T$. The force constraints are defined by the matrix **I-S** which is also a 6×6 matrix with the elements being either a 1 for force control or 0 for no force control. Figure 5.8 shows the bloc diagram of hybrid force/position control defined in [53]. J is the Jacobian matrix. The desired position is X_d and the desired force or torque is F_d. The elementary dis-

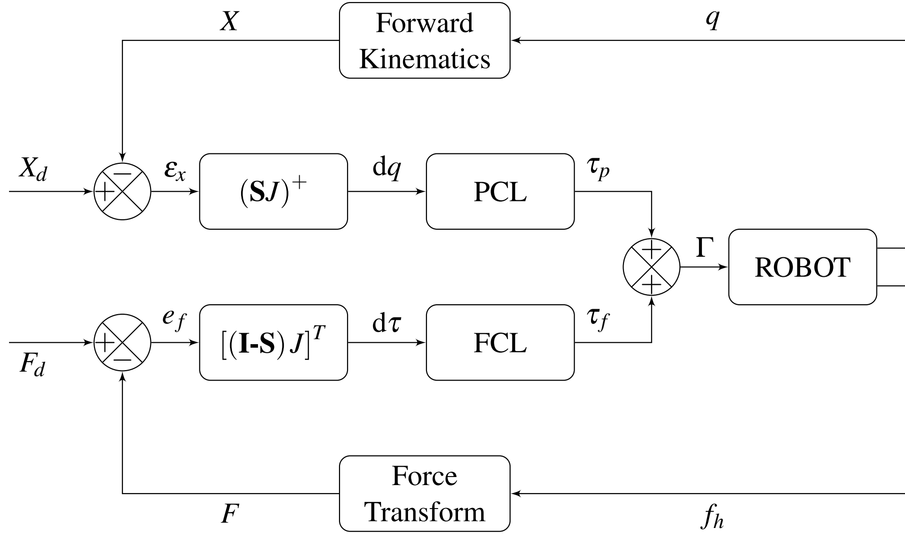

FIGURE 5.8: Hybrid force/position control diagram as defined in [53].

placement is given by $\mathrm{d}q = (SJ)^{+}\varepsilon_x$ with $(SJ)^{+}$ is the pseudo-inverse. The elementary torque variation is given by $\mathrm{d}\tau = [(I-S)J]^T (F_d - F)$. The PCL (Position Control Law) generates the torque control using the elementary displacement $\mathrm{d}q$. For robot manipulators, it is generally a PID control [79]. At the microscale, because the position control is performed using a micropositioning stage which has its own internal control structure, a PID control is also sufficient to track the desired position. The FCL (Force Control Law) has a lot of possible forms as discussed in chapter 4. The following remarks need to be considered for the implementation of the hybrid force/position control [79]:

1. for the implementation of hybrid force/position control, a lot of computations need to be performed online since several coordinate changes are made. Recently, with the advance and presence of powerful control and processing systems, high sampling frequencies can be reached which increases the performances of the control;

2. when a position disturbance is applied to the robot in a force controlled direction, it is not compensated by the force control unless the robot is in contact in this direction;

3. with the hybrid force/position control, the environment must be well known to prevent robot from having contact in a position controlled direction or from having displacement in a force controlled direction;

4. most tasks require an online change from one mode to another, which theoretically is realized by modifying the elements involved in the matrix S. The commutation mode

may also require modifications of controller gains which is more difficult if the position and force control laws comprise integral or derivative terms.

In the following, PCL and FCL are detailed and the final control diagram is proposed in order to perform the automation of grasping, guiding and release of the micropart.

Position control loop

For robot manipulators, it is generally a PID control [79]. At the microscale, most of the commercial positioning stages have their own inner closed-loop controllers which compensate the nonlinearities and perturbations of positioning stages. This fact facilitates the position control task of the positioning stage due to the good performance of the inner controller. The user can use the inner position control of the positioning stage or can also use PID control which is sufficient in this case.

Force control loop for grasping or lateral contact force control

At the macroscale, the robots can be categorized according to whether the inner servo loop is based on torque, velocity, or position. For the robots with inner servo loop based on position, indirect force control schemes, presented in chapter 4 are often considered. At the microscale and especially for the microassembly, the positioning stages use actuators (DC motors, piezoelectric actuators, etc) which are controlled in position. This fact justifies the use of indirect force control as FCL.

A force control law has been developed to control the TSFM fingers in order to automate the grasp and the release of microparts. It is based on Sliding Mode Impedance Control (SMIC) with online parameter estimation. For the guiding task, a strategy has been defined in section 5.2.4 and it consists of performing the force control through controlling a positioning stage. Thus, the same approach used in chapter 4 can be used to control the lateral contact force in this case. The objective of this part being to control the contact force to zero, no force tracking to non-zero force reference is needed. Consequently, no stiffness estimation technique is needed. The only parameter in the location of the micropart relative to the rail. Then, the use of position-based impedance control scheme shown in chapter 4 is sufficient. The diagram of force control law is shown in Figure 5.9.

In Figure 5.9, y_n is the measured position of the positioning stage, f_{y1} and f_{y_2} are the two measured gripping forces, $\hat{f}_y$ is the estimated lateral contact force, y_r is the reference position, f_{cd} is the desired contact force and k is a gain. The desired contact force, f_{cd} and the gain k could not be used but they are added as an additional option to deal with pull-off force in the guiding task using the strategy defined in section 4.4.4 where a negative force can applied. However, the chosen guiding strategy, defined in section 5.2.4, is a sliding strategy which does not need to separate the contact, the strategy consists of controlling the lateral contact force to zero and moving along X axis to position the micropart. In our case, f_{cd} is set to zero $f_{cd} = 0$.

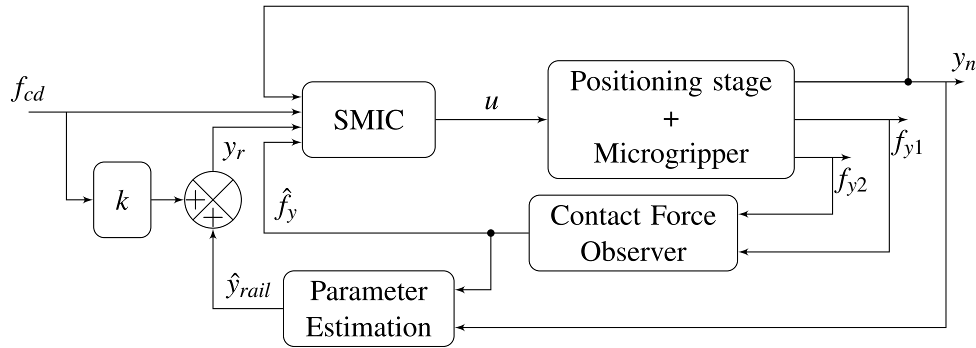

FIGURE 5.9: Force Control Law (FCL) used for the guiding task.

5.3.2 Final control diagram combining both position and force diagrams

Hybrid force/position control is used for the automation of three microassembly tasks. The microassembly strategy presented in section 5.2 is taken into account in the control scheme. For the grasp and release of the micropart, force control of the microgripper fingers is only needed without position control similarly to the work of chapter 4. For the guiding task, hybrid force/position control for the positioning stage is needed. Indeed, the FCL is the one defined in Figure 5.9. The complete control diagram is presented in Figure 5.10.

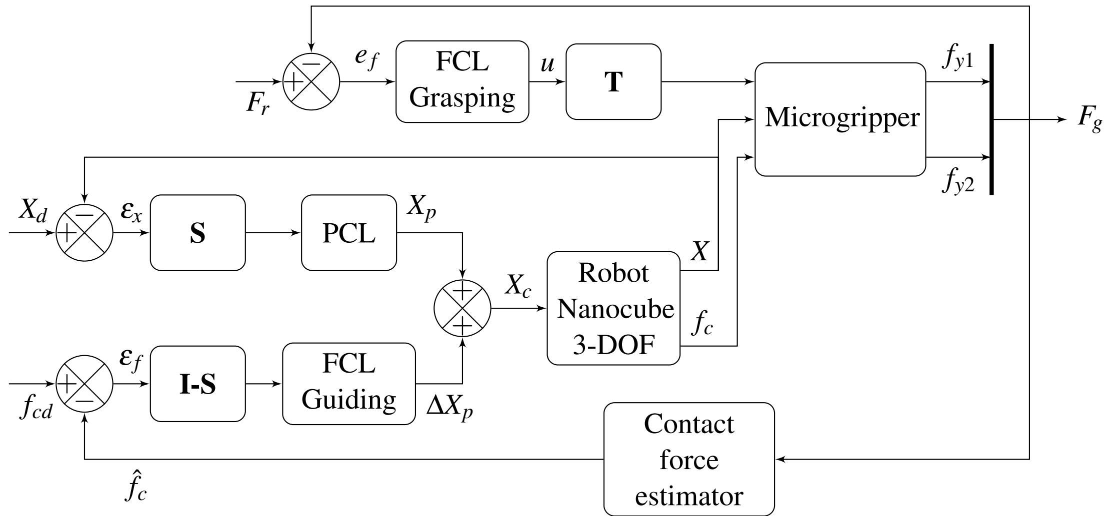

FIGURE 5.10: Hybrid force/position control diagram used for the automation of three microassembly tasks where $F_g = (f_{g_1}, f_{g_2})$ and $F_r = (f_{r_1}, f_{r_2})$.

The bloc **T** is a switch for the task specification. It enables to switch between the grasp and the release of the components tasks and the guiding task. It has two possible values 0 for

the guiding task and 1 for grasp and release tasks. In the grasp and release tasks, the microgripper fingers are controlled while in the guiding task the positioning stage is controlled. PCL corresponds to the position control law which is the internal controller of the positioning stage. FCL Grasping is the force control law presented in chapter 4 - section 4.4 which is the sliding mode impedance control used for the grasp and release of the microcomponent. FCL Guiding is the force control law for the guiding task which has been already presented in Figure 5.9. $X_d = (x_d, y_d, z_d)$ is a vector for the desired positions along the three axis X, Y and Z. f_{cd} is the desired contact force which is generally null because no contact between the micropart and the substrate is envisaged while the guiding task. f_c and $\hat{f}_c$ are respectively the contact force and its estimation using Equation (5.3). f_{y_1} and f_{y_2} are the two measured gripping forces and $F_g = (f_{y_1}, f_{y_2})$. F_r is a vector of the reference forces for the two gripping forces. ε_x and ε_f are respectively the position error and the error between the desired contact force and the estimated force while e_f is the force error between the reference gripping force and the applied gripping force. X_p is the output of the PCL. The output of the FCL Guiding, ΔX_p, is a added to X_p in order to determine X_c which is the position command of the robot positioning stage. $X_c = X_p + \Delta X_p$. X is the measured position of the positioning stage using the internal sensors.

In the control loop, X and Z axis are controlled in position and Y axis is controlled in force. Consequently, the selection matrix **S** can be written as follows:

$$\mathbf{S} = \begin{pmatrix} 1 & 0 & 0 \\ 0 & 0 & 0 \\ 0 & 0 & 1 \end{pmatrix} \tag{5.4}$$

In addition, the vectors X_d, X_p, ΔX_p and X_c can be written as follows:

$$X_d = \begin{pmatrix} x_d \\ 0 \\ z_d \end{pmatrix}, \; X_p = \begin{pmatrix} x_c \\ 0 \\ z_c \end{pmatrix}, \; \Delta X_p = \begin{pmatrix} 0 \\ y_c \\ 0 \end{pmatrix} \text{ and } X_c = \begin{pmatrix} x_c \\ y_c \\ z_c \end{pmatrix} \tag{5.5}$$

where x_c, y_c and z_c are the commands along the X, Y and Z axes respectively.

5.4 Experimental investigations

In this section, the microassembly strategy defined in section 5.2 and the control scheme presented in section 5.3 are investigated experimentally in grasping, releasing and guiding tasks for rigid and flexible microparts. The robotic microassembly station is presented and the performances of the tasks are investigated.

5.4.1 Experimental setup used for the automated microassembly

The experimental investigations of the microassembly tasks are performed using the robotic station shown in Figure 5.11. The experimental setup is composed of large range motorized stages, fine positioning stages, rotation stages, a vacuum gripper and the Two-Smart-Fingers-Microgripper (TSFM). The three large range motorized stages are M-112.1DG from PI (Physik Instrumente) to perform large range X, Y and Z displacement up to 15 mm. The fine positioning

stage is a P-611.3 NanoCube with 100 μm range and 1 nm in resolution with internal position sensors. Two rotation stages from SmarAct SR-3610-S with 1.1 μ° in resolution are used to adjust the alignment between the gripper and the micropart from one hand between the rails and the axis of the NanoCube from the other hand. The positioning and rotation stages are sensorized and closed loop controlled. The substrate is fixed on the fine positioning stage with a rotation

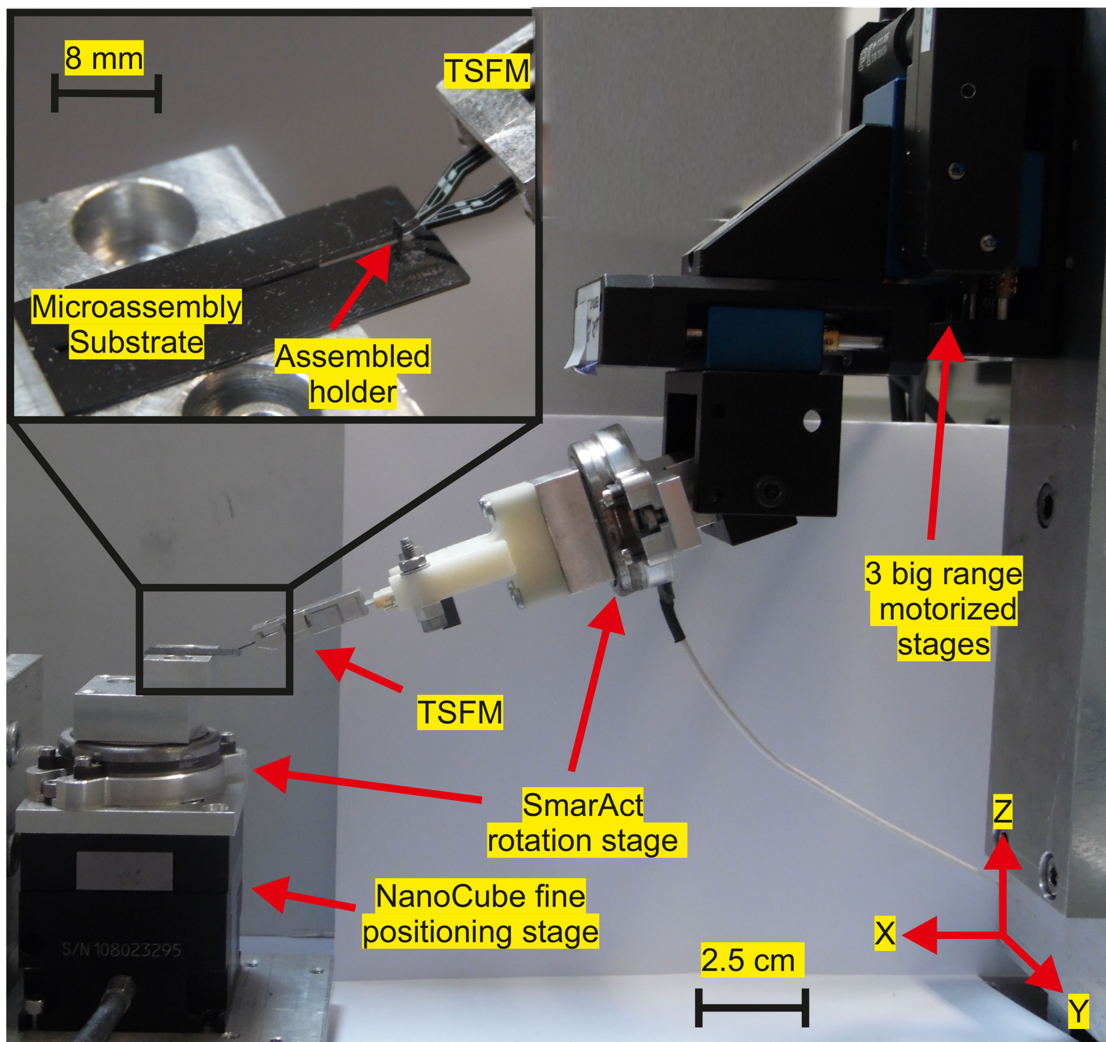

FIGURE 5.11: Robotic microassembly station used to investigate the experimental results of the automation of the microassembly tasks using the microassembly strategy defined in section 5.2 and the hybrid force/position control developed in section 5.3.

stage to perform $X_nY_nZ_n\theta_n$ positioning of the system. The TSFM is fixed on a rotation axis which is also fixed on three axes large range motorized stages to perfrom $X_mY_mZ_m\theta_m$ positioning of the system. The microgripper has 4-DOF. The whole robotic station has 12-DOF.

5.4.2 Automated microassembly of a rigid micropart

A micropart of size 340 µm × 50 µm × 2 mm is handled, guided inside a rail and released. First, automated grasp and release tasks of the micropart are tested, then an automated guiding task is performed to position the micropart in the desired position while controlling the lateral contact force.

Automated grasp and release of the rigid micropart

In this section, the micropart is initially positioned inside a hole. The robotic station moves the microgripper towards the micropart to handle it. Once the micropart is between the fingers of the microgripper, the **T** task specification switch (Figure 5.10) is set to 1 in order to perform the automated grasp. A force reference f_r is set for the two gripping forces. The sliding mode impedance control presented in chapter 4 is used to perform the control. The results are shown in Figure 5.12. The results are quite similar to the which presented in chapter 4 for the handling of a flexible micropart. The grasp of the micropart is performed successfully within a settling time of 20 ms with 4% of overshoot. The dynamics performances of the controller are very close to the which presented in Figure 4.11. The release task is also tested in the same experiment and its results are presented in Figure 5.12 where the micropart is released within 20 ms. A negative force reference is set to the controller in the release task in order to deal with pull-off force as presented in section 4.4.4. However, in this part, the pull-off force is so small.

After successfully automating grasp and release tasks, a guiding task will be tested in the following.

Automated guiding task with misalignment between the rail axis and the guiding axis

Once the micropart is handled, the micropart is guided inside a rail. To experiment the automated guiding task including a misalignment between the rail axis and the move forward axis, we introduce a ramp of moving forward along the X axis with a constant velocity of 25 µm/s. During this phase the **T** task specification switch is set to zero to disable force control of the microgripper finger as discussed in the guiding strategy (section 5.2.4). Hybrid force/position control scheme shown in Figure 5.10 where the force control law is performed by moving the rail which is fixed on the NanoCube. Results are shown in Figure 5.13 where the coordinates frames and positioning stages are detailed in Figure 5.2. It is observed that when the contact occurs, the estimated contact force gradually increases. The controller starts the correction to maintain the estimated contact force to zero. We can also observe that during the guiding task, gripping forces are maintained in around their initial values avoiding the risks of breaking or loosing the microparts. The increase of the preload is estimated to be less than 5% during the guiding task. The desired position along X axis is reached without micropart sliding thus the task is successfully achieved and the micropart reaches its final position within 4 s. Several speeds of motion along X axis are tested until the maximal velocity of the NanoCube axis which is estimated to be 5 mm/s. For all the velocities, the guiding task has been achieved successfully.

To estimate the angle, γ, between the rail axis and the move forward axis, measurements of both the displacement along the X axis D_x and the displacement along the Y axis $D_y = Y_m - Y_{\text{rail}}$

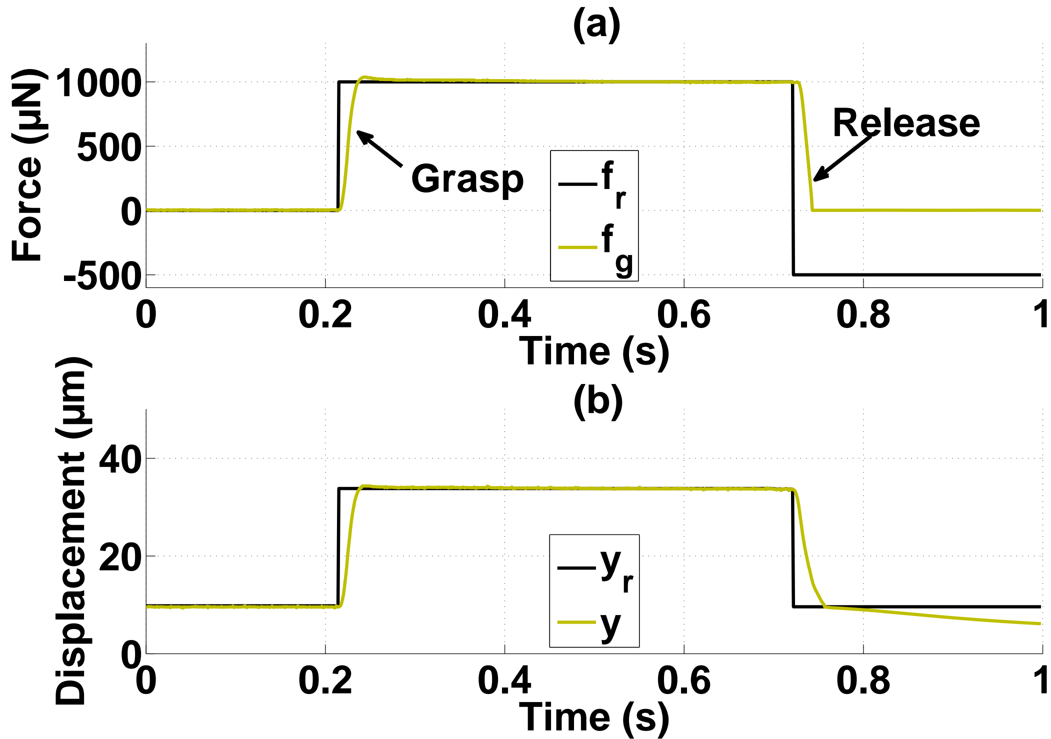

FIGURE 5.12: Experimental results for the automated grasp and release of a rigid micropart using Sliding Mode Impedance Control (SMIC) with online estimation of the environment parameters: (a) force response compared to the reference force, (b) position response compared to y_r.

are used. D_x and D_y are the displacement of the NanoCube along X and Y axis respectively. The angle γ of misalignment is estimated to be 30.2° by using $\gamma = \arctan\left(\frac{\Delta y}{\Delta x}\right)$.

Automated guiding task with dynamic perturbation by the rail

As shown in Figure 5.13, the hybrid force/position control is able to track the desired position while controlling the contact force to zero. The controller reacts so fast to the contact and consequently the influence of the contact force is not clear due to the reaction of the controller. In order to test the performances of the controller, dynamic perturbations are applied on the micropart and the rail enters in contact with the micropart. The micropart rotates between the fingers of the microgripper. The controller is turned off when the dynamic perturbations are applied. The gripping forces decrease due to the contact as shown in Figure 5.14. Then, the controller is set ON and the controller is able to cancel the force error within a time of 50 ms which is approximately the settling time of the NanoCube. These results show the robustness of the guiding task relative to perturbations.

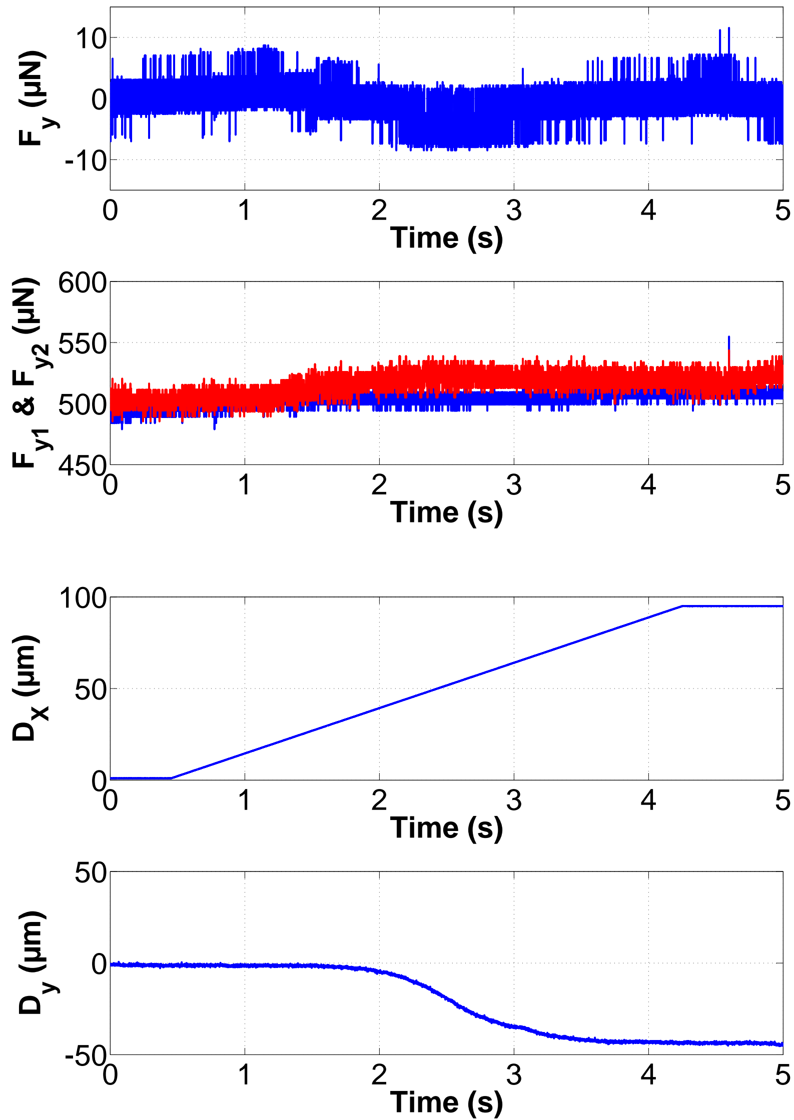

FIGURE 5.13: Experimental results for the automated guiding of a rigid micropart inside a rail showing the estimation of the lateral contact force, $\hat{f}_y$, and the gripping forces, the Nanocube displacement along the X axis, D_x, and the NanoCube displacement along the axis of correction Y, D_y.

An image of the automated guiding inside a rail is shown in Figure 5.15 where the TSFM microgripper is handling a rigid micropart and the guiding is performed along one sided rail.

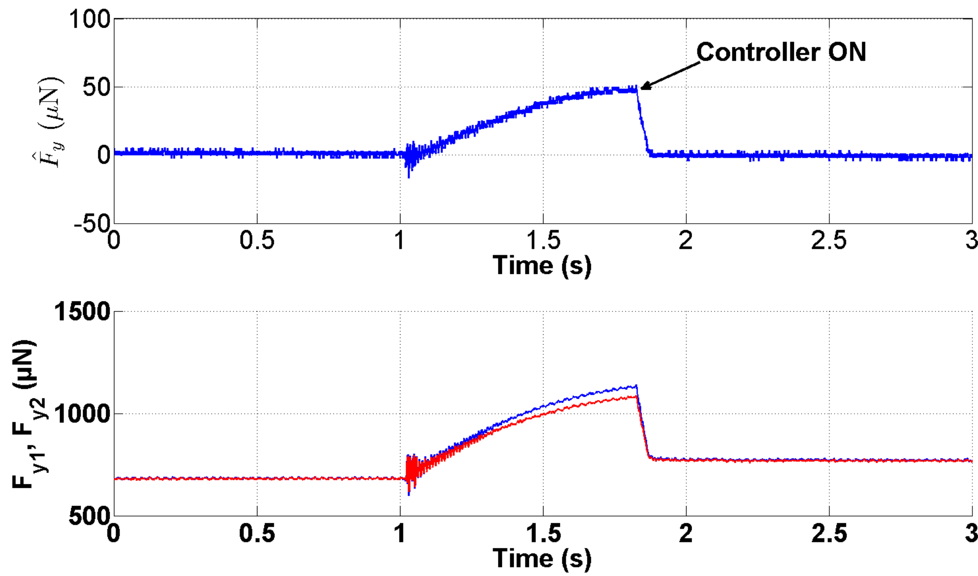

FIGURE 5.14: Experimental results for the automated guiding of a rigid micropart inside a rail showing the estimation of the contact force $\hat{f}_y$ and the gripping forces.

5.4.3 Automated microassembly of a flexible micropart

In this section, the microassembly of a flexible micropart is studied. The micropart is the MOEMS presented in Figure 1.6. The same procedure applied for the rigid micropart is applied to investigate the microassembly of the flexible micropart.

Automated grasp and release of the flexible micropart

In this section, the flexible micropart is initially handled using a vacuum gripper. The robotic station moves the microgripper towards the vacuum gripper to handle it. Once the micropart is between the fingers of the microgripper, the **T** task specification switch (Figure 5.10) is set to 1 in order to perform the automated grasp. A force reference f_r is set for the two gripping forces. The sliding mode impedance control presented in chapter 4 is used to perform the control. The results of the grasp have been already presented in chapter 4 Figure 4.11. The grasp and the release are performed with a settling time of 20 ms and overshoot of 3.7% for the grasp.

Automated guiding task with misalignment between the substrate axis and the guiding axis

The same approach presented for the rigid micropart is adopted for the flexible micropart. The performances are quite similar to the case of the rigid micropart where the change in the gripping force is less than 5% and the control is able to separate the contact and the desired position along

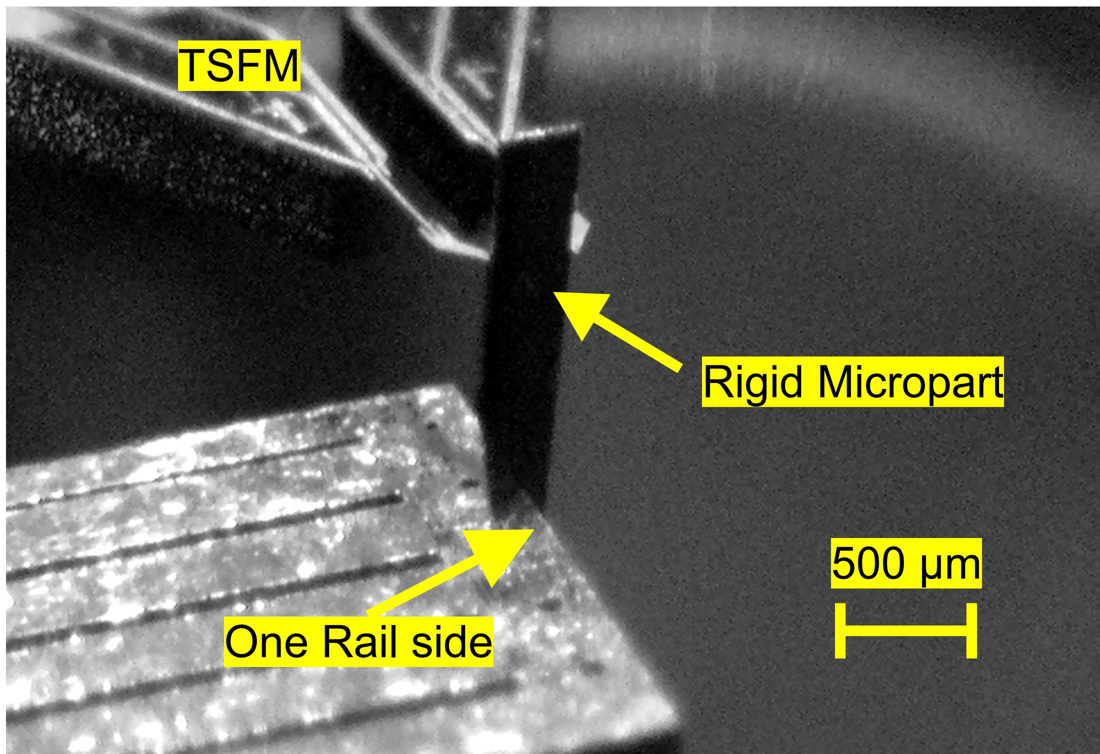

FIGURE 5.15: An image showing the rigid micropart handled between the two fingers of the microgripper and while the guiding task along of one sided rail.

X axis is reached without micropart sliding thus the task is successfully achieved. Due to the similarity of the results with Figure 5.13, the results are not shown in this part.

Automated guiding task with dynamic perturbation by the rail

The robustness of the guiding task control is tested by introducing a perturbation during the task. A contact force is applied and the controller is turned ON at time $t = 2.7$ s to test the effectiveness of the control technique. As a result of the contact force, the micropart does not rotate between the two fingers of the microgripper and the micropart remains in the translation mode where one of the gripping forces increases and the other decreases as shown in Figure 5.16. The controller is able to cancel the force error within a time of 50 ms which is approximately the settling time of the NanoCube. An image of the flexible micropart during guiding task is shown in Figure 5.17-(a) and an image of the assembled flexible micropart (holder) is shown in Figure 5.17-(b), showing the success of the automated microassembly.

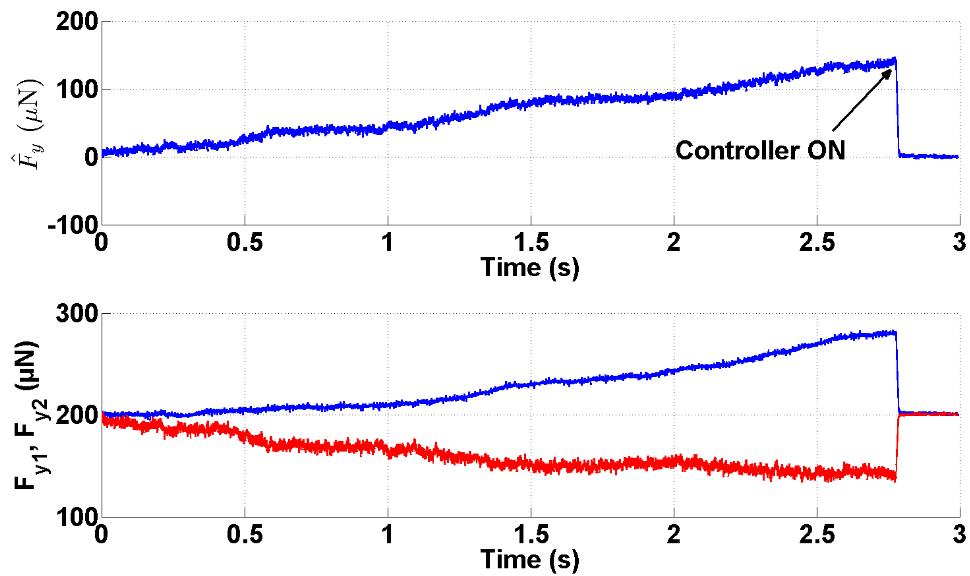

FIGURE 5.16: Experimental results for the automated guiding of a rigid micropart inside a rail showing the estimation of the contact force $\hat{f}_y$ and the gripping forces.

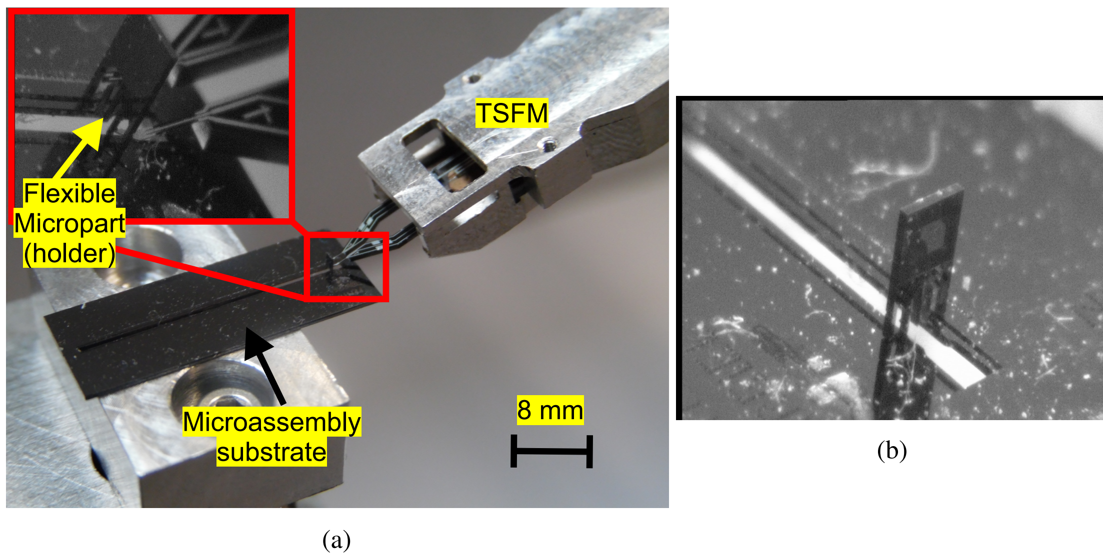

(a)

(b)

FIGURE 5.17: (a) Image showing the micropart in the guiding task, (b) an image of the assembled holder.

5.5 Conclusion

In this chapter, an automation of three common microassembly tasks (grasp, guiding and release) has been proposed using hybrid force/position control. A microassembly strategy has been proposed taking into consideration microscale specificities. An automated grasp is performed to handle and release the micropart. Mechanical stability conditions of the grasp of the micropart along X, Y and Z axis have been studied and the guiding tasks is performed by controlling the position to get the micropart towards its final destination while controlling the contact force to zero. The contact force is estimated using the two measured gripping forces. The performance of the microassembly tasks and the controller are studied in experiments. Automated grasp and release tasks of the microassembly have been achieved within a response time of 20 ms.

For the guiding task, the controller has succeeded to slide the micropart along the rail while controlling the contact force between the micropart and the platform of the microassembly to zero and to position the micropart in its final desired position with sliding speed up to 5 mm/s. The guiding strategy has been also tested with the application of dynamic perturbations by the microassembly substrate to the micropart and the controller has been able to cancel the contact force within 50 ms which is almost the response time of the positioning stage used for the control.

At the end of this chapter, fully automated microassembly of flexible and rigid microparts has been performed. For the assembly of the flexible microparts, the resulting component after the assembly is a 3D out-of-plane hybrid MOEMS. The experimental results shown that the effectiveness of the microassembly strategy and the control technique used for automation of the microassembly.

Conclusion and Future Works

This PhD thesis has addressed the need of automated high precision and dexterous robotic microassembly to fabricate complex out-of-plane three-dimensional (3D) hybrid reconfigurable MOEMS issued from different microfabrication approaches. Robotic microassembly has raised several challenges such as the need of microrobots with high performances, taking into account physical phenomenon that are predominant at the microscale and specific technological limitations. The physics of the microscale is mainly manifested by the predominance of surface forces, the high dynamics of the systems, the small inertia and the fragility of the microsystems.

This PhD work has proposed to investigate these specificities by integrating high dynamics force sensors into an active microgripper used in a robotic microassembly station enabling to model the system behavior and to achieve automated microassembly through hybrid force/position control. Each of the two fingers of the microgripper is composed of a piezoelectric actuator with an integrated piezoresistive force sensor. This microgripper enables to perform the microassembly of several types of microcomponents while measuring predominant surfaces and contact forces present at the microscale. The ability of measuring these forces enables more dexterity of the microassembly tasks and to take them into account in the control and microassembly strategy.

A dynamic nonlinear model of the microgripper has notably been proposed to understand the microgripper behavior and to develop a control law well adapted to the system. Then, a hybrid force/position control approach has been used to automate microassembly which enables to control some axes are controlled in position and others in force. For the force controlled axes, a new nonlinear force control scheme based on force tracking sliding mode impedance control is proposed with parameter estimation. Using the proposed hybrid force/position control scheme, full automation of the microassembly is performed, notably for the grasping and releasing of a flexible component and guiding it in a rail.

In this chapter, the contribution of this work will be detailed by chapters and several future works will be presented.

Contributions of the work

This work has proposed solutions to perform robotic microassembly which can deal with the microscale specificities by the use of an active microgripper with sensorized end-effector. In addition, a microassembly strategy has been proposed to deal with the microscale specificities and notably the high dynamics of microsystems and the presence of pull-off forces which has lead to increase the dexterity of the microassembly by limiting the effects of pull-off forces, to guarantee the stability of the grasp of the microcomponents and to reduce the time duration of a microassembly process.

In the following, the contributions of our work are detailed by each chapter.

In chapter 2, a new piezoresistive force sensor's design taking advantage of both mechanical and bulk piezoresistive properties of silicon has been studied, designed and prototyped. This force sensor has been fabricated using silicon because its use is widespread in MEMS, it presents a high gauge factor and it is fabricated using classical MEMS microfabrication processes. The design and fabrication technique enable to integrate the force sensor in a wide choice of MEMS devices because it does not need additional processes and the same silicon structure used for the fabrication of the device can be used as a force sensor. In our work, the interest has been to integrate the force sensor into an active microgripper to provide force feedback for the microgripper which has lead to design the force sensor using the specifications of micromanipulation and microassembly tasks. The sensor also presents high performances compared to the sensors presented in literature thanks to its sensitivity of 197 uN/V, its resolution of 100 nN, its sensing range of 2 mN, its signal to noise ratio of 50 dB at a force of 2 mN, its stiffness of 130 N/m and its dynamic force sensing where its natural frequency is around 8.5 kHz. The signal of the force sensor is repeatable with an error less than 0.3%.

Chapter 3 has focused on the integration of the piezoresistive force sensor into the microassembly station to perform the automation of the microassembly. The choice has been made to integrate the force sensor into an active piezoelectric microgripper to realize globally an active piezoelectric actuator with sensorized end-effectors. This complete microgripper has been called in the work Two-Smart-Fingers-Microgripper (TSFM). The TSFM enables to measure not only both of the gripping forces applied on the micropart but also the contact force between the micropart and the platform of the microassembly when a contact appears. A dynamic non-linear force/position model of the TSFM has been developed taking into account the dynamic hysteresis of the piezoelectric actuator. The model has been developed for the free motion (non contact between the fingers and the micropart) and constrained motion (while manipulating an the micropart). The parameters of the TSFM have been estimated experimentally and the model has been validated in experiments for the manipulation of rigid and flexible objects. The errors between the model and the experimental results have been lower than 10% in the case of the free motion and less than 20% in the case of constrained motion with flexible micropart. The bigger error in the case of constrained motion with flexible micropart is notably due to the errors in the estimation of the parameters of the flexible micropart and more precisely the errors in the estimation of the stiffness of the flexible environment and the initial location of the micropart between the two fingers of the TSFM. This fact justifies the need to perform robust control to deal with such model errors and to use an online parameter estimation technique of the stiffness and the location of the micropart to have suitable performances of the controller.

Chapter 4 has focused on the automation of the grasp and release of a flexible micropart using force control. A study on the existing force control techniques has been presented. Theoretical and experimental studies have been performed in order to compare the performances of each of the existing force control techniques taking into consideration the microscale specificities and to choose a force control technique which fits the best for these tasks. PI explicit force control has been first tested for the grasp and release tasks leading to a success of the automation of only the grasp within a settling time going from 530 ms up to 1 s with oscillations of 5% around the force reference. Then, impedance control with force tracking and online parameter estimation scheme has been tested showing that the online estimation technique perturbs the dynamic response of the controller. For this, a solution has been proposed to use Sliding Mode based Impedance Control (SMIC) scheme is proposed to force the system to slide along a sliding surface which is chosen in this case as a function of the desired impedance relation. The proposed control scheme enables to take into consideration microscale specificities notably pull-off force and high dynamics of the microscale objects. A strategy to deal with pull-off force and to separate the contact between microgripper fingers and the micropart using this control technique has been proposed. The online parameter estimation technique enables to estimate online the location and the stiffness of the environment, which is a flexible micropart in our case, and to use them in the control law in order to perform force tracking. The SMIC used has presented good dynamic behavior by tracking the reference within 20 ms and an overshoot of 3.7%. The SMIC enabled to automate the grasp and the release of a flexible micropart with very good and promising dynamic performances and despite the presence of pull-off forces.

In chapter 5, hybrid force/position control has been proposed to perform full closed-loop based automation of the microassembly. The considered microassembly tasks were grasping, releasing and guiding tasks for the microcomponent. Firstly, the stability of the grasp during the manipulation of the micropart is studied. Secondly, a microassembly strategy has been defined taking into consideration microscale specificities. Thirdly, a method to estimate dynamically the contact force between the micropart and the platform of the microassembly using the measurement of both of the gripping forces has been proposed and validated experimentally. Fourthly, hybrid force/position control formulation has been presented. In the hybrid force/position control formulation, some axes are controlled in position and others are controlled in force. For the force controlled axes, a force control technique based on Sliding Mode Impedance Control (SMIC) has been used. Finally, the automation of the microassembly using the proposed strategy and control technique has been tested for rigid and flexible micropart. For the two types of microparts, the automated tasks have been achieved with success. An automation of the grasp and release tasks of the micropart has been done with success within a settling time of 20 ms and an overshoot less than 4% in the case of grasp task and despite the presence of pull-off forces for the release task. For the guiding task, the controller has succeeded to slide the micropart along the rail while controlling the contact force between the micropart and the platform of the microassembly to zero and to position the micropart in its final desired position with sliding speed up to 5 mm/s. The guiding strategy has been also tested with the application of dynamic perturbations by the microassembly substrate to the micropart and the controller has been able to cancel the contact force within 50 ms which is almost the response time of the positioning stage used for the control.

At the end of this PhD, fully automated microassembly has been performed with success by the use of a microgripper with sensorized end-effector and hybrid force/position control. The developed solution enables more dexterity in the automation of the microassembly thanks to the local force measurement which enables to detect any contact between the microassembly platform and the micropart and consequently to ensure the safety of the grasp. 3D out-of-plane hybrid MOEMS have been automatically assembled with success showing the effectiveness of the developed microassembly strategy and control. In the following some future works are presented.

Future works

This work has proposed solutions to perform robotic microassembly which can deal with microscale specificities by the use of an active microgripper with sensorized end-effector. Moreover, a microassembly strategy has been proposed to deal with the microscale specificities and notably the high dynamics of microsystems and the presence of pull-off forces which lead to increase the dexterity of the microassembly by limiting the effects of pull-off forces, to guarantee the stability of the microcomponents and the microgripper and to reduce the time duration of a microassembly process.

These results enable several perspectives: first short term possible perspectives are presented and then some long term perspectives are discussed.

Short term perspectives

These works highlight several direct and short terms perspectives among them, the two following main topics:

- towards multi-DOF actuation and sensing and generalized integration of sensors,
- automation of the microassembly combining multi-DOF control, vision feedback and force control.

Towards multi-DOF force measurement and generalized integration of sensors

During this PhD, one-dimensional (1D) force measurement has been performed along the Y axis. Using this one-dimensional force measurement, the automation of microassembly tasks such as grasping, guiding and releasing of the micropart has been achieved successfully by the use of hybrid force/position control. However, in order to enable more precision and to achieve more automated microassembly tasks requiring multi-DOF actuation and force measurement (such as insertion, pushing, rotating, etc), developing multi-DOF microgrippers with multi-DOF force measurement would enable to measure and control the force along several axes and to achieve the tasks through multi-DOF force control to the system. The multi-DOF force measurement enables to understand and model the interaction between the microcomponents in a microassembly station which increases the dexterity of all the microassembly tasks.

Despite their need and their importance, no works exist on multi-DOF microgrippers with integrated multi-DOF force sensor in literature. It is due to the complexity of the task and the

need to search innovative solutions to design multi-DOF sensors with multi-DOF actuation in the same small operating zone. Some works have been done on MEMS based multi-DOF force sensors leading to the fabrication of 3-axis force sensor [112] and even 6-axis force and torque sensor [11]. These solutions can not be directly adapted to be used inside microgrippers and a lot of works need to be done to reach multi-DOF microgrippers with multi-DOF force sensors. The existing solutions can be developed to be used inside the microassembly robotic platform leading to measure directly multi-DOF contact forces. Combining such solution with the use of microgripper with force sensing can lead to perform multi-DOF microassembly tasks in the 6D space and consequently, to achieve wide choice and so complex tasks.

More generally, the designed force sensor could be used to integrate such force sensor in many MEMS structures. The same design can also be used for position sensing inside MEMS devices. This possibility can be a promising approach for MEMS devices operating in the open-loop due to the all problems that can be faced for microsystems such as nonlinearities, dependency on the environmental conditions, the repeatability, the precision, etc. Integrating such sensors inside MEMS devices enables to perform closed-loop control of MEMS devices which can increase significantly the performances of these devices. Furthermore, their integration may require adding one or two standard processes to the fabrication process of these MEMS devices. It may also not require any additional process depending on the defined microfabrication process.

Automation of the microassembly combining multi-DOF control, vision feedback and force control

In our work, an automation of the microassembly has been performed using one force controlled axis an other position controlled axis. In order to perform more complex multi-DOF microassembly tasks, vision feedback can provide information of global position and orientation along several axes of the micropart relative to the platform. Consequently, combining global information of the position using vision and local information using force sensor along several axes, would enable to perform precise relative positioning of two components and to master the local aspect such as surface and contact forces, small inertia and high dynamics. Force feedback enables to define an adapted strategy to perform the automation.

In addition, feedforward control can also be combined to force control and vision feedback. The interest of feedforward would be to compensate the nonlinearities of the actuators which simplifies the feedback control and enable higher dynamics feedback control. Consequently, combining feedforward control, force control and vision feedback control can be interesting to perform precise control with high dynamics.

Long term perspectives

The proposed long term perspectives can be summarized by the following two main topics:

- mechatronics approach for physical modeling of the system,
- towards high dynamic micromanipulation and microassembly,

Mechatronics approach for physical modeling of the system

During this PhD, a part of the works considered understanding some microscale specificities and then modeling the behavior of the system. A microassembly strategy to deal with microscale specificities has been proposed based on that knowledge. Some limitations exist on the modeling of forces such as pull-off forces at which have predominant effect at the microscale. The non presence of models increase the task and needs to define specific strategies to deal with these forces. Using a generalized physical model, a lot of research needs to be done to develop a reliable model of these forces and consequently to facilitate the control of such systems and consequently the task. An approach using Hamiltonian or Lagrangian approaches to model macrosystems can be considered as a base to do this work. In addition, as the MOEMS combines multiple functions (mechanical, electrical and optical), modeling of these multiphysics systems using port-Hamiltonian approach is an interesting topic which enables to model not only the mechanical behavior of the system but also to take into consideration the electrical, optical, thermal, thermodynamical and other multiphysics behavior in the system thanks to an energy based model. Few works exist at the microscale dealing with these approaches. The interest of such approach is that it may provide an optimal and energy based control approach, which is well known for these types of systems, to reduce the energy consumption of the system.

Towards high dynamic and dexterous micromanipulation and microassembly

Extending the approach presented in this PhD to multi-DOF smart microgripper with enough dynamics and multi-DOF robotic station, wide range of microassembly tasks including grasping, rotating, pushing, guiding, inserting, releasing, following a trajectory and others can be achieved with very high dynamics, precision, high stability and low operation time. One solution consists to develop very small microgrippers with much more dexterity in order to manipulate micro-components with high speed along 4, 5 or 6-D complex motions. Using this approach, we avoid the use of big, heavy and slow robots with very low dynamics. Using such approach, complex microassembly tasks can be achieved with high precision, repeatability and high yield due to the very small process time.

Furthermore, we can think of combining robotic microassembly approach with non-contact manipulation to increase the dynamics of the microassembly and reduce process time. Non-contact manipulation can be used, for example, for large displacement with high speeds and the final microassembly can be done using robotic microassembly which enables to apply big forces without a need of big displacements.

Finally, microassembly is a very promising research topic in the coming years. It is needed to fabricate complex 3D out-of-plane MOEMS. These devices becoming a part of our everyday life where they are used for mobiles, GPS, laptops, surgery, medical and several indispensable fields. Several researches exist nowadays on the microassembly. The main research topics are related to increase the precision, repeatability, dexterity, dynamics, process speed and yield of the microassembly. Our main contribution is on performing dexterous microassembly with high dynamics thanks to a microgripper with sensorized end-effector. The presented perspectives are

some examples of works which would improve one or more microassembly research topics in the coming years.

Bibliography

[1] AGNUS, J. *Contribution à la micromanipulation: Etudes, Réalisation, Caractérisation et Commande d'une Micropince Piezoélectrique*. PhD thesis, Université de Franche-Comté, 2003.

[2] AGNUS, J., CHAILLET, N., CLÉVY, C., DEMBÉLÉ, S., GAUTHIER, M., HADDAB, Y., LAURENT, G., LUTZ, P., PIAT, N., RABENOROSOA, K., RAKOTONDRABE, M., AND TAMADAZTE, B. Robotic microassembly and micromanipulation at femto-st. *Journal of Molecular Biology Research (JMBR) 8*, 2 (April 2013), 91–106.

[3] AL-JANAIDEH, M., RAKHEJA, S., AND SU, C. An analytical generalized prandtl-ishlinskii model inversion for hysteresis compensation in micropositioning control. *IEEE/ASME Transactions on Mechatronics 16*, 4 (Aug. 2011), 734–744.

[4] ALJASEM, K., FROEHLY, L., SEIFERT, A., AND ZAPPE, H. Scanning and tunable micro-optics for endoscopic optical coherence tomography. *Journal of Microelectromechanical Systems 20*, 6 (Dec. 2011), 1462–1472.

[5] ALJASEM, K., WERBER, A., SEIFERT, A., AND ZAPPE, H. Fiber optic tunable probe for endoscopic optical coherence tomography. *Journal of Optics A: Pure and Applied Optics 10*, 4 (April 2008), 044012.

[6] ANDERSEN, K., CARLSON, K., PETERSEN, D., MØLHAVE, K., EICHHORN, V., FATIKOW, S., AND BØGGIL, P. Electrothermal microgrippers for pick-and-place operations. *Microelectronic Engineering 85*, 5-6 (May-June 2008), 1128–1130.

[7] BADEL, A., QIU, J., AND NAKANO, T. Self-sensing force control of a piezoelectric actuator. *IEEE Transactions on Ultrasonics, Ferroelectrics and Frequency Control 55*, 12 (Dec. 2008), 2571–2581.

[8] BAHADUR, I., MILLS, J., AND SUN, Y. Design of a mems-based resonant force sensor for compliant, passive microgripping. *IEEE International Conference Mechatronics and Automation 1* (29 July-1 Aug. 2005), 77,82.

[9] BALLAS, R. *Piezoelectric Multilayer Beam Bending Actuators: Static and Dynamic Behavior and Aspects of Sensor Integration*. Springer, 2007.

[10] BARGIEL, S., RABENOROSOA, K., CLÉVY, C., GORECKI, C., AND LUTZ, P. Towards micro-assembly of hybrid moems components on a reconfigurable silicon free-space micro-optical bench. *Journal of Micromechanics and Microengineering 20*, 4 (April 2010), 045012.

[11] BEYELER, F., MUNTWYLER, S., AND NELSON, B. A six-axis mems force-torque sensor with micro-newton and nano-newtonmeter resolution. *Journal of Microelectromechanical Systems 18*, 2 (April 2009), 433–441.

[12] BEYELER, F., NEILD, A., OBERTI, S., D.J. BELL, Y. S., DUAL, J., AND NELSON, B. Monolithically fabricated microgripper with integrated force sensor for manipulating microobjects and biological cells aligned in an ultrasonic field. *Journal of Microelectromechanical Systems 16*, 1 (Feb. 2007), 7–15.

[13] BOHRINGER, K., COHN, K. G. M., HOWE, R., AND PISANO, A. Parallel microassembly with electrostatic force fields. *IEEE International Conference on Robotics and Automation 2* (16-20 May 1998), 1204–1211.

[14] BOUDAOUD, M., HADDAB, Y., AND GORREC, Y. L. Modelling of a mems-based microgripper: application to dexterous micromanipulation. *IEEE/RSJ International Conference on Intelligent Robots and Systems (IROS)* (18-22 Oct. 2010), 5634–5639.

[15] BOUDAOUD, M., HADDAB, Y., AND GORREC, Y. L. Modeling and optimal force control of a nonlinear electrostatic microgripper. *IEEE/ASME Transactions on Mechatronics 18*, 3 (June 2013), 1130–1139.

[16] BOUDAOUD, M., HADDAB, Y., GORREC, Y. L., AND LUTZ, P. Noise characterization in millimeter sized micromanipulation systems. *International journal of Mechatronics 21* (2011), 1087–1097.

[17] CAO, Y., CHENG, L., CHEN, X., AND PENG, J. Y. An inversion-based model predictive control with an integral-of-error state variable for piezoelectric actuators. *IEEE/ASME Transactions on Mechatronics 18*, 3 (2013), 895904.

[18] CAPPELLERI, D., PIAZZA, G., AND KUMAR, V. A two dimensional vision-based force sensor for microrobotic applications. *Sensors & Actuators: A Physical 171*, 2 (Nov. 2011), 340–351.

[19] CHAILLET, N., AND RÉGNIER, S. *Microrobotics for Micromanipulation*. Wiley-ISTE, 2010.

[20] CHANG, B., VIRTA, A., AND ZHOU, Q. Hybrid microassembly for massively parallel assembly of microchips with water mist. *International Conference on Manipulation, Manufacturing and Measurement on the Nanoscale (3M-NANO)* (Aug. 2012), 38–43.

[21] CHIU, Y., CHEN, C.-H., CHIOU, J.-C., FANG, W., AND SHIEH., H.-P. D. Mems-based miniature optical pickup. *IEEE Transactions on Magnetics 41*, 2 (Feb. 2005), 967–970.

[22] CHONAN, S., JIANG, Z., AND YAMAMOTO, T. Nonlinear hysteresis compensation of piezoelectric ceramic actuators. *Journal of Intelligent Material Systems and Structures 7*, 2 (March 1996), 150–156.

[23] CLÉVY, C., LUNGU, I., RABENOROSOA, K., AND LUTZ, P. Positioning accuracy characterization of assembled microscale components for micro-optical benches. *Assembly Automation 34*, 1 (Jan. 2014), 68–77.

[24] CLÉVY, C., RAKOTONDRABE, M., AND CHAILLET, N. *Signal Measurement and Estimation Techniques for Micro and Nanotechnology*. Springer, 2011.

[25] CROFT, D., AND DEVASIA, S. Vibration compensation for high speed scanning tunneling microscopy. *Review of Scientific Instruments 70*, 12 (Dec. 1999), 46004605.

[26] DAS, A., MURTHY, R., POPA, D., AND STEPHANOU, H. A multiscale assembly and packaging system for manufacturing of complex micro-nano devices. *IEEE Transactions on Automation Science and Engineering 9*, 1 (Jan. 2012), 160–170.

[27] DAS, A., SIN, J., POPA, D., AND STEPHANOU, H. Design and manufacturing of a fourier transform microspectrometer. *IEEE Conference on Nanotechnology* (Aug. 2008), 837–840.

[28] DAS, A., SIN, J., POPA, D., AND STEPHANOU, H. E. On the precision alignment and hybrid assembly aspects in manufacturing of a microspectrometer. *IEEE Conference on Automation Science and Engineering* (Aug. 2008), 959–966.

[29] DAS, A. N., ZHANG, P., LEE, W. H., STEPHANOU, H., AND POPA, D. μ^3: Multiscale, deterministic micro-nano assembly system for construction of on-wafer microrobots. *IEEE International Conference on Robotics and Automation* (Roma, Italia, 10-14 April 2007), 461–466.

[30] DE LIT, P., AGNUS, J., AND CHAILLET, N. The constitutive equations of a piezoelectric duo-bimorph. *Proceedings of the IEEE International Symposium on Assembly and Task Planning* (Besanon, France, 10-11 Jul. 2003), 16.

[31] DE LIT, P., AGNUS, J., CLÉVY, C., AND CHAILLET, N. A four-degree-of-freedom microprehensile microrobot on chip. *Assembly and Automation 24*, 1 (2004), 33–42.

[32] DECHEV, N., CLEGHORN, W., AND MILLS, J. Microassembly of 3-d microstructures using a compliant, passive microgripper. *Journal of Microelectromechanical Systems 13*, 2 (April 2004), 176–189.

[33] DECHEV, N., MILLS, J., AND CLEGHORN, W. Mechanical fastener designs for use in the microassembly of 3d microstructures. *Proceeding of ASME International Mechanical Engineering Congress and Exposition* (Anaheim, California, USA, November 13 19 2004), 19–21.

[34] DECHEV, N., REN, L., LIU, W., CLEGHORN, W., AND MILLS, J. Development of a 6 degree of freedom robotic micromanipulator for use in 3d mems microassembly. *IEEE International Conference on Robotics and Automation* (15-19 May 2006), 281–288.

[35] DEEDS, M., AND SANDBORN, P. Moems chip-level optical fiber interconnect. *Advanced Packaging, IEEE Transactions on 28*, 4 (Nov. 2005), 612,618.

[36] DÉGOULANGE, E., AND DAUCHEZ, P. External force control of an industrial puma 560 robot. *Journal of Robotic Systems 11*, 6 (1994), 523–540.

[37] DERJAGUIN, B., MULLER, V., AND TOPOROV, Y. Effect of contact deformations on the adhesion of particles. *Journal of Colloid and Interface Science 53* (1975), 314326.

[38] DEVASIA, S. Should model-based inverse inputs be used as feedforward under plant uncertainty? *IEEE Transactions on Automatic Control 47*, 11 (Nov. 2002), 18651871.

[39] DEVASIA, S., ELEFTHERIOU, E., AND MOHEIMANI, R. A survey of control issues in nanopositioning. *IEEE Trans. on Control Systems Technology 15*, 15 (2007), 802–823.

[40] D.J. BISHOP, C. G., AND AUSTIN, G. The lucent lambdarouter: Mems technology of the future here today. *IEEE Communications Magazine 40*, 3 (2002), 7579.

[41] DOLL, J., AND PRUITT, B. High-bandwidth piezoresistive force probes with integrated thermal actuation. *Journal of Micromechanics and Microengineering 22*, 9 (September 2012), 095012.

[42] DONG, W., SUN, L., AND DU, Z. Design of a precision compliant parallel positioner driven by dual piezoelectric actuators. *Sensors and Actuators A: Physical 135*, 1 (March 2007), 250–256.

[43] DUC, T., LAU, G., CREEMER, J., AND SARRO, P. Electrothermal microgripper with large jaw displacement and integrated force sensors. *Journal of Microelectromechanical Systems 17*, 6 (Dec. 2008), 1546,1555.

[44] DUDLEY, D., DUNCAN, W., AND SLAUGHTER, J. Emerging digital micromirror device (dmd) applications. *Proceedings SPIE 4985, MOEMS Display and Imaging Systems 4985* (Jan. 2003), 14–25.

[45] DURAND, S. Capteur de déplacement. *Technique de l'ingénieur R1800* (2002), 1–20.

[46] EBEFORS, T., ULFSTEDT-MATTSSON, J., KAELVESTEN, E., AND STEMME, G. 3d micromachined devices based on polyimide joint technology. *Proc. SPIE 3892, Device and Process Technologies for MEMS and Microelectronics 3892* (Oct. 1999).

[47] EISINBERG, A., A.MENCIASSI, CAMPOLO, D., CARROZZA, M. C., AND P.DARIO. Pi force control of a microgripper for assembling biomedical microdevices. *IEE Proceedings Circuits Devices Systems 148*, 6 (Dec. 2001), 348–352.

[48] ENIKOV, E., AND NELSON, B. Three-dimensional microfabrication for a multi-degree-of-freedom capacitive force sensor using fibre-chip coupling. *Journal of Micromechanics and Microengineering 10* (2000).

[49] EPPINGER, S., AND SEERING, W. Understanding bandwidth limitations in robot force control. *IEEE International Conference on Robotics and Automation 4* (Mars 1987), 904–909.

[50] ERICKSON, D., WEBER, M., AND SHARF, I. Contact stiffness and damping estimation for robotic systems. *The International Journal of Robotics Research 22*, 1 (Jan. 2003), 41–57.

[51] ESPINOSA, A., RABENOROSOA, K., CLÉVY, C., KOMATI, B., LUTZ, P., ZHANG, X., SAMUELSON, S., AND XIE, H. Piston motion performance analysis of a 3dof electrothermal mems scanner for medical applications. *International Journal of Optomechatronics 8*, 3 (June 2014), 179–194.

[52] FIALA, J., BINGGER, P., RUH, D., FOERSTER, K., HEILMANN, C., BEYERSDORF, F., ZAPPE, H., AND SEIFERT, A. An implantable optical blood pressure sensor based on pulse transit time. *Biomed Microdevices 15*, 1 (Feb. 2013), 73–81.

[53] FISHER, W. D., AND MUJTABA, M. S. Hybrid position/force control: a correct formulation. *The International journal of robotics research 11*, 4 (1992), 299–311.

[54] FT-S MICROFORCE SENSING PROBE. http://www.femtotools.com/index.php?id=products-s.

[55] FUJIMOTO, J. Optical coherence tomography for ultrahigh resolution in vivo imaging. *Nature Biotechnology 21*, 11 (2003), 1361–1367.

[56] FUKUSHIMA, T., KIKUCHI, H., YAMADA, Y., KONNO, T., LIANG, J., SASAKI, K., INAMURA, K., TANAKA, T., AND KOYANAGI, M. New three-dimensional integration technology based on reconfigured wafer-on-wafer bonding technique. *IEEE International Electron Devices Meeting (IEDM)* (Dec. 2007), 985–988.

[57] GAUTHIER, M., AND RÉGNIER, S. *Robotic Microassembly*. Wiley, 2010.

[58] GILCHRIST, K., MCNABB, R., IZATT, J., AND GREGO, S. Piezoelectric scanning mirrors for endoscopic optical coherence tomography. *Journal of Micromechanics and Microengineering 19*, 9 (Sept. 2009), 095012.

[59] GORECKI, C., BARGIEL, S., ALBERO, J., PASSILLY, N., KUJAWINSKA, M., AND ZEITNER, U. Micromachined array-type mirau interferometer for mems metrology. *Proc. SPIE 8494, Interferometry XVI: Applications* (September 13 2012).

[60] HARPER, P. Kinematic theory of piezoelectric hysteresis. *Journal of Applied Physics 52*, 11 (Nov. 1981), 6851–6855.

[61] HAUGEN, F. The good gain method for simple experimental tuning of pi controllers. *Modeling, Identification and Control 33*, 4 (2012), 141–152.

[62] HÉRIBAN, D., AND GAUTHIER, M. Robotic micro-assembly of microparts using a piezogripper. In *Proc. of the 2008 IEEE/RSJ International Conference on Intelligent Robots and Systems* (Nice, France, 2008), pp. 4042 – 4047.

[63] HIMMELHAUS, M., AND FRANCOIS, A. In-vitro sensing of biomechanical forces in live cells by a whispering gallery mode biosensor. *Biosensors and Bioelectronics 25* (Oct. 2009), 418427.

[64] HOGAN, N. Impedance control - an approach to manipulation. i - theory. ii - implementation. iii - applications. *ASME Transactions Journal of Dynamic Systems and Measurement Control B 107* (1985), 1 24.

[65] HSIEH, H., CHANG, H., HU, C., CHENG, C., AND FANG, W. A novel stress isolation guard-ring design for the improvement of a three-axis piezoresistive accelerometer. *Journal of Micromechanics and Microengineering 21* (2011).

[66] HUANG, D., SWANSON, E., LIN, C., SCHUMAN, J., STINSON, W., CHANG, W., HEE, M., FLOTTE, T., GREGORY, K., AND PULIAFITO, C. Optical coherence tomography. *Science 254*, 5035 (Nov. 1991), 1178–1181.

[67] HUANG, H., SUN, D., MILLS, J., LI, W., AND CHENG, S. H. Visual-based impedance control of out-of-plane cell injection systems. *IEEE Transactions on Automation Science and Engineering 6*, 3 (July 2009), 565–571.

[68] ITOH, T., AND SUGA, T. Piezoelectric force sensor for scanning force microscopy. *Sensors and Actuators A: Physical 43*, 1-3 (May 1994), 305310.

[69] ITOH, T., AND SUGA, T. Self-excited force-sensing microcantilevers with piezoelectric thin films for dynamic scanning force microscopy. *Sensors and Actuators A: Physical 54*, 1-3 (June 1996), 477–481.

[70] IVAN, I. A., RAKOTONDRABE, M., LUTZ, P., AND CHAILLET, N. Current integration force and displacement self-sensing method for cantilevered piezoelectric actuators. *Review of Scientific Instruments 80*, 12 (2009), 126103.

[71] JACKLE, S., GLADKOVA, N., FELDCHTEIN, F., TERENTIEVA, A., BRAND, B., GELIKONOV, G., GELIKONOV, V., SERGEEV, A., FRITSCHER-RAVENS, A., FREUND, J., SEITZ, U., SCHRÖDER, S., AND SOEHENDRA, N. In vivo endoscopic optical coherence tomography of esophagitis, barrett's esophagus, and adenocarcinoma of the esophagus. *Endoscopy 32*, 10 (2000), 750755.

[72] JEN, S., YU, C., LIU, C., AND LEE, G. Piezoresistance and electrical resistivity of pd, au, and cu films. *Thin Solid Films 434* (2003), 316–322.

[73] JOHNSON, K. *Contact mechanics*. Cambridge University Press, 1987.

[74] JUNG, S., HSIA, T., AND BONITZ, R. Force tracking impedance control of robot manipulators under unknown environment. *IEEE Transactions on Control Systems Technology 12*, 3 (May 2004), 474–483.

[75] JUNG, S., YIM, S. B., AND HSIA, T. Experimental studies of neural network impedance force control for robot manipulators. *IEEE International Conference on Robotics and Automation 4* (2001), 3453–3458.

[76] JUNG, W., MCCORMICK, D., ZHANG, J., WANG, L., TIEN, N., AND CHEN, Z. Three-dimensional endoscopic optical coherence tomography by use of a two-axis microelectromechanical scanning mirror. *Applied Physics Letters 88*, 16 (2006), Article ID 163901, 3 pages.

[77] KANDA, Y. Piezoresistance effect of silicon. *Sensors and Actuators A: Physical 28*, 2 (July 1991), 83–91.

[78] KAZEROONI, H., SHERIDAN, T., AND HOUPT, P. Robust compliant motion for manipulators, parts i and ii. *IEEE Journal of Robotics and Automation 2*, 2 (June 1986), 83–105.

[79] KHALIL, W., AND DOMBRE, E. *Modélisation, identification et commande des robots*. Hermes, 1999.

[80] KHARBOUTLY, M. *Modelling, realization and control a dielectrophoresis-based micromanipulation system*. PhD thesis, Université de Franche-Comté, 2011.

[81] KIM, K., LIU, X., ZHANG, Y., AND SUN, Y. Nanonewton force-controlled manipulation of biological cells using a monolithic mems microgripper with two-axis force feedback. *Journal of Micromechanics and Microengineering 18*, 5 (May 2008), 055013.

[82] KIM, K., PARK, B., MAGULURI, G., LEE, T., ROGOMENTICH, F., BANCU, M., BOUMA, B., DE BOER, J., AND BERNSTEIN, J. Two-axis magnetically-driven mems scanning catheter for endoscopic high-speed optical coherence tomography. *Optics Express 15*, 26 (2007), 1813018140.

[83] KOMATI, B., AGNUS, J., CLÉVY, C., AND LUTZ, P. Prototyping of a highly performant and integrated piezoresistive force sensor for microscale applications. *Journal of Micromechanics and Microengineering 24*, 3 (March 2014), 035018.

[84] KOMATI, B., PAC, M., RANATUNGA, I., CLÉVY, C., POPA, D., AND LUTZ, P. Explicit force control v.s. impedance control for micromanipulation. *ASME International Design Engineering Technical Conferences & Computers and Information in Engineering Conference (IDETC)* (Portland, USA, August 4-7 2013), V001T09A018.

[85] KOMATI, B., RABENOROSOA, K., CLÉVY, C., AND LUTZ, P. Automated guiding task of a flexible micropart using a two-sensing-finger microgripper. *IEEE Transactions on Automation, Science and Engineering 10*, 3 (July 2013), 515–524.

[86] KOMATY, A., BOUDRAA, A., AUGIER, B., AND DARE-EMZIVAT, D. Emd-based filtering using similarity measure between probability density functions of imfs. *IEEE Transactions on Instrumentation and Measurement 63, no.1* (Jan. 2014), 27–34.

[87] KOYANAGI, M., FUKUSHIMA, T., AND TANAKA, T. Three-dimensional integration technology using through-si via based on reconfigured wafer-to-wafer bonding. *IEEE Custom Integrated Circuits Conference (CICC)* (Sept. 2010), 1–4.

[88] KRATOCHVIL, B., DONG, L., AND NELSON, B. Real-time rigid-body visual tracking in a scanning electron microscope. *The International Journal of Robotics Research 28* (2009), 498511.

[89] KURSUA, O., KRUUSINGB, A., PUDASB, M., AND RAHKONEN, T. Piezoelectric bimorph charge mode force sensor. *Sensors and Actuators A: Physical 153*, 1 (June 2009), 4249.

[90] LAFITTE, N., HADDAB, Y., GORREC, Y. L., GUILLOU, H., KUMEMURA, M., JALABERT, L., FUJITA, H., AND COLLARD, D. Closed-loop control of silicon nanotweezers for improvement of sensitivity to mechanical stiffness measurement and bio-sensing on dna molecules. *IEEE/RSJ International Conference on Intelligent Robots and Systems* (Nov. 2013), 1022–1027.

[91] LAI, K., HUI, A., AND LI, W. Non-contact batch micro-assembly by centrifugal force. *IEEE International Conference on Micro Electro Mechanical Systems* (24-24 Jan. 2002), 184–187.

[92] LAMBERT, P. *Capillary Forces in Microassembly: Modeling, Simulation, Experiments, and Case Study*, 2007 edition ed. Springer, October 2007.

[93] LANG, D. *A Study on Micro-gripping Technologies*. PhD thesis, University of Southern Denmark, Denmark, 2008.

[94] LEANG, K., ZOU, Q., AND DEVASIA, S. Feedforward control of piezoactuators in atomic force microscope systems. *IEEE Control Systems 29*, 1 (Feb. 2009), 70–82.

[95] LI, D., ZHAO, T., YANG, Z., AND ZHANG, D. Monolithic integration of a micromachined piezoresistive flow sensor. *Journal of Micromechanics and Microengineering 20* (2010).

[96] LI, M., TANG, H., AND ROUKES, M. Ultrasensitive nems-based cantilevers for sensing, scanned probe and very-high frequency applications. *Nature Nanotechnology 2* (2007), 114120.

[97] LIU, C. *Foundations of MEMS*. Pearson Education, 2012.

[98] LOVE, L., AND BOOK, W. Environment estimation for enhanced impedance control. *IEEE International Conference on Robotics and Automation 2* (21-27 May 1995), 1854–1859.

[99] LOW, T., AND GUO, W. Modeling of a three-layer piezoelectric bimorph beam with hysteresis. *Journal of Microelectromechanical Systems 4*, 4 (Dec. 1995), 230–237.

[100] LU, Z., CHEN, P. C. Y., GANAPATHY, A., ZHAO, G., NAM, J., YANG, G., BURDET, E., TEO, C., MENG, Q., AND LIN, W. A force-feedback control system for micro-assembly. *Journal of Micromechanics and Microengineering 16*, 9 (September 2006), 1861.

[101] LU, Z., CHEN, P. C. Y., AND LIN, W. Force sensing and control in micromanipulation. *IEEE Transactions on Systems, Man, and Cybernetics, Part C: Applications and Reviews 36*, 6 (Nov. 2006), 713–724.

[102] LU, Z., AND GOLDENBERG, A. Robust impedance control and force regulation: Theory and experiments. *The International Journal of Robotics Research 14*, 3 (June 1995), 225–254.

[103] MACKAY, R., LE, H., CLARK, S., AND WILLIAMS, J. Polymer micro-grippers with an integrated force sensor for biological manipulation. *Journal of Micromechanics and Microengineering 23*, 1 (January 2013), 015005.

[104] MAHARBIZ, M., HOWE, R., AND PISTER, K. Batch transfer assembly of micro-components onto surface and soi mems. *Transducers'99 Conference 2* (Sendai, Japan, June 7-10 1999), 1478–1481.

[105] MANZARDO, O. *Micro-sized Fourier Spectrometers*. PhD thesis, cole polytechnique fdrale de Lausanne (EPFL), 2002.

[106] MENCIASSI, A., EISINBERG, A., SCALARI, G., AND ANTICOLI, C. Force feedback-based microinstrument for measuring tissue properties and pulse in microsurgery. *IEEE International Conference on Robotics and Automation (ICRA) 1* (2001), 626 – 631.

[107] MIGNARDI, M., GALE, R., DAWSON, D., AND SMITH, J. *MEMS and MOEMS Technology and Applications : The digital Micromirror Device -A Micro-Optical Electromechanical Device for Display Applications*. SPIE Press, 2001.

[108] MISRA, S., AND OKAMURA, A. Environment parameter estimation during bilateral telemanipulation. *14th Symposium on Haptic Interfaces for Virtual Environment and Teleoperator Systems* (25-26 March 2006), 301–307.

[109] MOKABERI, B., AND REQUICHA, A. A. G. Compensation of scanner creep and hysteresis for afm nanomanipulation. *IEEE Trans. on Automation Science and Engineering 5*, 2 (Apr. 2008), 197–208.

[110] MØLHAVE, K., AND HANSEN, O. Electro-thermally actuated microgrippers with integrated force-feedback. *Journal of Micromechanics and Microengineering 15*, 6 (June 2005), 1265.

[111] MOORE, P., RAKOTONDRABE, M., CLÉVY, C., AND WIENS, G. Development of a modular and compliant micro-assembly platform with integrated force and compliance measurement capabilities. *ICOMM 7th International Conference on MicroManufacturing* (2012).

[112] MUNTWYLER, S., BEYELER, F., AND NELSON, B. Three-axis micro-force sensor with sub-micro-newton measurement uncertainty and tunable force range. *Journal of Micromechanics and Microengineering 20*, 2 (Feb. 2010), 025011.

[113] NICLASS, C., ITO, K., SOGA, M., MATSUBARA, H., AOYAGI, I., KATO, S., AND KAGAMI, M. Design and characterization of a 256x64-pixel single-photon imager in cmos for a mems-based laser scanning time-of-flight sensor. *Optics Express 20*, 11 (May 2012), 11863–11881.

[114] NOELL, W., CLERC, P.-A., DELLMANN, L., GULDIMANN, B., HERZIG, H.-P., MANZARDO, O., MARXER, C., WEIBLE, K., DANDLIKER, R., AND DE ROOIJ, N. Applications of soi-based optical mems. *IEEE Journal of Selected Topics in Quantum Electronics 8*, 1 (Jan/Feb 2002), 148–154.

[115] OCEAN OPTICS. Ocean optics spectrometers. http://www.oceanoptics.com/product/, 2014.

[116] PAN, Y., XIE, H., AND FEDDER, G. Endoscopic optical coherence tomography based on a microelectromechanical mirror. *Optics Letters 26*, 24 (2001), 19661968.

[117] PARK, S., DOLL, J., AND PRUITT, B. Piezoresistive cantilever performancepart i: Analytical model for sensitivity. *Journal of Microelectromechanical Systems 19*, 1 (Feb. 2010), 137–148.

[118] PÉREZ, R., AGNUS, J., CLÉVY, C., HUBERT, A., AND CHAILLET, N. Modeling, fabrication, and validation of a high-performance 2-dof piezoactuator for micromanipulation. *IEEE/ASME Transactions on Mechatronics 10*, 2 (April 2005), 161–171.

[119] PIRIYANONT, B., AND MOHEIMANI, S. Design, modeling, and characterization of a mems micro-gripper with an integrated electrothermal force sensor. *IEEE/ASME International Conference on Advanced Intelligent Mechatronics (AIM)* (9-12 July 2013), 348–353.

[120] PIRIYANONT, B., MOHEIMANI, S., AND BAZAEI, A. Design and control of a mems micro-gripper with integrated electro-thermal force sensor. *3rd Australian Control Conference (AUCC)* (4-5 Nov. 2013), 479–484.

[121] POPA, D. Automated assembly and packaging of mems. *Technical report* (ARRI Institut Texas 2007).

[122] POPA, D., LEE, W., MURTHY, R., DAS, A., AND STEPHANOU, H. High yield automated mems assembly. *IEEE International Conference on Automation Science and Engineering* (22-25 Sept. 2007), 1099–1104.

[123] POPA, D., MURTHY, R., AND DAS, A. M^3 -deterministic, multiscale, multirobot platform for microsystems packaging: Design and quasi-static precision evaluation. *IEEE Transactions on Automation Science and Engineering 6*, 2 (April 2009), 345–361.

[124] PRECISION FORCE GAUGE PCE-FG 50. http://www.industrial-needs.com/technical-data/force-gauge-pce-fg.htm.

[125] PRECISION FORCE GAUGE PGE-FG 1K. http://www.industrial-needs.com/technical-data/force-meter-pce-sh.htm.

[126] PULIAFITO, C., HEE, M., LIN, C., REICHEL, E., SCHUMAN, J., DUKER, J., IZATT, J., SWANSON, E., AND FUJIMOTO, J. Imaging of macular diseases with optical coherence tomography. *Ophthalmology 102*, 2 (1995), 217229.

[127] RABENOROSOA, K., CLEVY, C., CHEN, Q., AND LUTZ, P. Study of forces during microassembly tasks using two-sensing-fingers grippers. *IEEE/ASME Transactions on Mechatronics 17, Issue: 5* (Oct. 2012), 811 – 821.

[128] RABENOROSOA, K., CLÉVY, C., LUTZ, P., GAUTHIER, M., AND ROUGEOT, P. Measurement of pull-off force for planar contact at the microscale. *Micro Nano Letters 4* (2009), 148 –154.

[129] RAIBERT, M., AND CRAIG, J. Hybrid position/force control of manipulators. *Transactions of ASME, Journal of Dynamic Systems, Measurement, and Control 102* (1981), 126–133.

[130] RAJAGOPALAN, J., TOFANGCHI, A., AND SAIF, M. Linear high-resolution biomems force sensors with large measurement range. *Journal of Microelectromechanical Systems 19*, 6 (Dec. 2010), 1380–1389.

[131] RAKOTONDRABE, M. Bouc-wen modeling and inverse multiplicative structure to compensate hysteresis nonlinearity in piezoelectric actuators. *IEEE Transactions on Automation Science and Engineering 8*, 2 (Apr. 2011), 428–431.

[132] RAKOTONDRABE, M., CLÉVY, C., AND LUTZ, P. Complete open loop control of hysteretic, creeped and oscillating piezoelectric cantilever. *IEEE Trans. on Automation Science and Engineering 7*, 3 (July 2010), 440–450.

[133] RAKOTONDRABE, M., CLÉVY, C., RABENOROSOA, K., AND NCIR, K. Presentation, force estimation and control of an instrumented platform dedicated to automated micromanipulation tasks. *IEEE International Conference on Automation Science and Engineering (CASE)* (Toronto, Canada, August 2010), 722 – 727.

[134] RAKOTONDRABE, M., HADDAB, Y., AND LUTZ, P. Quadrilateral modelling and robust control of a nonlinear piezoelectric cantilever. *IEEE Transactions on Control Systems Technology 17*, 3 (May 2009), 528–539.

[135] RAKOTONDRABE, M., AND IVAN, I. Development and force/position control of a new hybrid thermo-piezoelectric microgripper dedicated to micromanipulation tasks. *IEEE Transactions on Automation Science and Engineering 8*, 4 (Oct. 2011), 824–834.

[136] REDDY, A., MAHESHWARI, N., SAHU, D., AND ANANTHASURESH, G. Miniature compliant grippers with vision-based force sensing. *IEEE Transactions on Robotics 26*, 5 (Oct. 2010), 867–877.

[137] SANDNER, T., KENDA, A., DRABE, C., SCHENK, H., AND SCHERF, W. Miniaturized ftir-spectrometer based on optical mems translatory actuator. *Proceedings of SPIE 6466: MOEMS and Miniaturized Systems VI 6466* (2007).

[138] SARIOLA, V., JÄÄSKELÄINEN, M., AND ZHOU, Q. Hybrid microassembly combining robotics and water droplet self-alignment. *IEEE Transactions on Robotics 26*, 6 (Dec. 2010), 965–977.

[139] SERAJI, H. Adaptive admittance control : An approach to explicit force control in compliant motion. *IEEE International Conference on Robotics and Automation 4* (May 1994), 2705–2712.

[140] SERAJI, H. Adaptive admittance control: An approach to explicit force control in compliant motion. In *Jet Propulsion Laboratory California Institute of Technology Pasadena, CA 91109* (1994).

[141] SERAJI, H., AND COLBAUGH, R. Force tracking in impedance control. *The International Journal of Robotics Research 16*, 1 (Feb. 1997), 97–117.

[142] SHEN, Y., XI, N., AND LI, W. J. Contact and force control in microassembly. *Proceedings of the IEEE International Symposium on Assembly and Task Planning* (July 2003), 60–65.

[143] SHEN, Y., XI, N., WEJINYA, U., AND LI, W. High sensitivity 2-d force sensor for assembly of surface mems devices. *Proceedings. IEEE/RSJ International Conference on Intelligent Robots and Systems (IROS 2004) 4* (2004), 3363 – 3368.

[144] SILBERBERG, Y., PERLMUTTER, P., AND BARAN, J. Digital optical switch. *Applied Physics Letters 51* (1987), 1230.

[145] SIMSON, D., ZIEMANN, F., STRIGL, M., AND MERKEL, R. Micropipet-based pico force transducer: In depth analysis and experimental verification. *Biophysical Journal 74*, 4 (April 1998), 2080–2088.

[146] SINGH, G., HORSLEY, D., COHN, M., PISANO, A., AND HOWE, R. Batch transfer of microstructures using flip-chip solder bonding. *Journal of Microelectromechanical Systems 8*, 1 (March 1999), 27–33.

[147] SINGH, S., AND POPA, D. An analysis of some fundamental problems in adaptive control of force and impedance behavior: theory and experiments. *IEEE Transactions on Robotics and Automation 11*, 6 (Dec. 1995), 912–921.

[148] SIVAK, M., KOBAYASHI, K., IZATT, J., ROLLINS, A., UNG-RUNYAWEE, R., CHAK, A., WONG, R., ISENBERG, G., AND WILLIS, J. High-resolution endoscopic imaging of the gi tract using optical coherence tomography. *Gastrointestinal Endoscopy 51*, 4 (2000), 474479.

[149] SLOTINE, J.-J. E. Sliding controller design for non-linear systems. *International Journal of Control 40*, 2 (1984), 421–434.

[150] SMITS, J., DALKE, S., AND COONEY, T. The constituent equations of piezoelectric bimorphs. *Sensors and Actuators A: Physical 28*, 1 (June 1991), 41–61.

[151] SOLF, C., MOHR, J., AND WALLRABE, U. Miniaturized liga fourier transformation spectrometer. *Proceedings of IEEE Sensors 2*, 1 (22-24 Oct. 2003), 773–776.

[152] SRINIVASAN, U., LIEPMANN, D., AND HOWE, R. Microstructure to substrate self-assembly using capillary forces. *Journal of Microelectromechanical Systems 10*, 1 (March 2001), 17–24.

[153] STILES, R. Frequency and displacement amplitude relations for normal hand tremor. *Journal of applied physiology 40*, 1 (Jan. 1976), 44–54.

[154] SU, C.-Y., LEUNG, T. P., AND ZHOU, Q.-J. Force/motion control of constrained robots using sliding mode. *IEEE Transactions on Automatic Control 37*, 5 (May 1992), 668–672.

[155] SUN, Y., FRY, S., POTASEK, D., BELL, D., AND NELSON, B. Characterizing fruit fly flight behavior using a microforce sensor with a new comb-drive configuration. *Journal of Microelectromechanical Systems 14*, 1 (Feb. 2005), 4–11.

[156] SUN, Y., GRAETZEL, C., FRY, S., AND NELSON, B. A mems micro force sensor for drosophila flight characterization. *Robotics and Biomimetics (ROBIO). 2005 IEEE International Conference on* (2005), 505,510.

[157] SUN, Y., AND KIM, K. Mems-based micro and nano grippers with two axis force sensors. *U.S. Patent No 8,623,222* (7 janv. 2014).

[158] SUN, Y., NELSON, B., AND GREMINGER, M. Investigating protein structure change in the zona pellucida with a microrobotic system. *The International Journal of Robotics Research 24*, 2-3 (February 2005), 211–218.

[159] SUN, Y., PIYABONGKARN, D., SEZEN, A., NELSON, B., RAJAMANI, R., SCHOCH, R., AND POTASEK, D. A novel dual-axis electrostatic microactuation system for micromanipulation. *IEEE/RSJ International Conference on Intelligent Robots and Systems 2* (2002), 1796 – 1801.

[160] SYMS, R., AND MOORE, D. Optical mems for telecoms. *Materials Today 5*, 7-8 (Aug. 2002), 2635.

[161] TAMADAZTE, B., PIAT, N., AND DEMBÉLÉ, S. Robotic micromanipulation and microassembly using monoview and multiscale visual servoing. *IEEE/ASME Transactions on Mechatronics 16 , Issue: 2* (April 2011), 277 – 287.

[162] TAN, N. *Calibration of micro and nanorobotic systems : Contribution of influential parameters to the geometric accuracy*. PhD thesis, Université de Franche-Comté, 2013.

[163] THAYSEN, J., BOISEN, A., HANSEN, O., AND BOUWSTRA, S. Atomic force microscopy probe with piezoresistive read-out and a highly symmetrical wheatstone bridge arrangement. *Sensors and Actuators A: Physical 83* (2000), 47–53.

[164] THOMAS, D., AND DUGUID, G. Optical coherence tomographya review of the principles and contemporary uses in retinal investigation. *Eye 18* (2004), 561570.

[165] THOMPSON, J., AND FEARING, R. Automating microassembly with ortho-tweezers and force sensing. *IEEE/RSJ International Conference on Intelligent Robots and Systems 3* (2001), 1327–1334.

[166] TOLFREE, D., AND JACKSON, M. *Commercializing Micro-Nanotechnology Products*. CRC Press, 2006.

[167] TORTONESE, M., BARRETT, R., , AND QUATE, C. Atomic resolution with an atomic force microscope using piezoresistive detection. *Appl. Phys. Lett. 62, no. 8* (1993), 834836.

[168] TRUCK WEIGH. http://www.direct-pesage.net/page.php?lg=fr&rub=02&id_catalogue=382&racine.

[169] TSAI, Y.-C., LEI, S., AND SUDIN, H. Design and analysis of planar compliant microgripper based on kinematic approach. *Journal of Micromechanics and Microengineering 15*, 1 (Jaun. 2005), 143.

[170] TSUI, K., GEISBERGER, A., ELLIS, M., AND SKIDMORE, G. Micromachined endeffector and techniques for directed mems assembly. *Journal of Micromechanics and Microengineering 14*, 4 (April 2004), 542.

[171] UTKIN, V. Variable structure systems with sliding modes. *IEEE Transactions on Automatic Control 22*, 2 (1977), 212–222.

[172] UTKIN, V. Variable structure systems- present and future. *Automation and Remote Control 44*, 9 (1984), 1105–1120.

[173] VOLPE, R., AND KHOSLA, P. A theoretical and experimental investigation of explicit force control strategies for manipulators. *IEEE Transactions on Automatic Control 38*, 11 (Nov. 1993), 1634–1650.

[174] WANG, D., AND MCCLAMROCH, N. Position and force control for constrained manipulator motion: Lyapunov's direct method. *IEEE Transactions on Robotics and Automation 9*, 3 (June 1993), 308–313.

[175] WANG, D., YANG, Q., AND DONG, H. A monolithic compliant piezoelectric-driven microgripper: Design, modeling, and testing. *IEEE/ASME Transactions on Mechatronics 18*, 1 (Feb. 2013), 138–147.

[176] WANG, J., AND LI, X. A single-wafer-based single-sided bulk-micromachining technique for high-yield and low-cost volume production of pressure sensors. *16th International Solid-State Sensors, Actuators and Microsystems Conference (TRANSDUCERS'11)* (June 2011), 410 – 413.

[177] WANG, L., MILLS, J., AND CLEGHORN, W. Automatic microassembly using visual servo control. *IEEE Transactions on Electronics Packaging Manufacturing 31*, 4 (Oct. 2008), 316–325.

[178] WASON, J., WEN, J., GORMAN, J., AND DAGALAKIS, N. Automated multiprobe microassembly using vision feedback. *IEEE Transactions on Robotics 28*, 5 (Oct. 2012), 1090–1103.

[179] WEBER, N., ZAPPE, H., AND SEIFERT, A. A tunable optofluidic silicon optical bench. *Journal of Microelectromechanical Systems 21*, 6 (Dec. 2012), 1357–1364.

[180] WEI, J., MAGNANI, S., AND SARRO, P. Suspended submicron silicon-beam for high sensitivity piezoresistive force sensing cantilevers. *Sensors and Actuators A: Physical 186* (2012), 8085.

[181] WEI, J., PORTA, M., TICHEM, M., STAUFER, U., AND SARRO, P. Integrated piezoresistive force and position detection sensors for micro-handling applications. *Journal of Microelectromechanical Systems 22*, 6 (Dec. 2013), 1310,1326.

[182] WELZEL, J. Optical coherence tomography in dermatology: a review. *Skin Research and Technology 7*, 1 (2001), 19.

[183] WISITSORAAT, A., PATTHANASETAKUL, V., LOMAS, T., AND TUANTRANONT, A. Low cost thin film based piezoresistive mems tactile sensor. *Sensors and Actuators A 139* (2007), 1722.

[184] XIAO, S., AND LI, Y. Modeling and high dynamic compensating the rate-dependent hysteresis of piezoelectric actuators via a novel modified inverse preisach model. *IEEE Transactions on Control Systems Technology 21*, 5 (2013), 1549–1557.

[185] XIE, H., PAN, Y., AND FEDDER, G. Endoscopic optical coherence tomographic imaging with a cmos-mems micromirror. *Sensors and Actuators A 103*, 1-2 (2003), 237241.

[186] XIE, H., AND RÉGNIER, S. Three-dimensional automated micromanipulation using a nanotip gripper with multi-feedback. *Journal of Micromechanics and Microengineering 19*, 7 (July 2009), 075009.

[187] XIE, Y., SUN, D., LIU, C., AND CHENG, S. H. An adaptive impedance force control approach for robotic cell microinjection. *IEEE/RSJ International Conference on Intelligent Robots and Systems* (Sep. 2008), 907–912.

[188] XIE, Y., SUN, D., LIU, C., TSE, H. Y., AND CHENG, S. H. A force control approach to a robot-assisted cell microinjection system. *The International Journal of Robotics Research 29*, 9 (Aug. 2010), 1222–1232.

[189] XIE, Y., SUN, D., TSE, H. Y. G., LIU, C., AND CHENG, S. H. Force sensing and manipulation strategy in robot-assisted microinjection on zebrafish embryos. *IEEE/ASME Transactions on Mechatronics 16*, 6 (Dec. 2011), 1002–1010.

[190] XU, J.-X., AND ABIDI, K. Discrete-time output integral sliding-mode control for a piezomotor-driven linear motion stage. *IEEE Transactions on Industrial Electronics 55*, 11 (Nov. 2008), 3917–3926.

[191] XU, Q. Precision position/force interaction control of a piezoelectric multimorph microgripper for microassembly. *IEEE Transactions on Automation Science and Engineering 10*, 3 (July 2013), 503–514.

[192] XU, Q., AND LI, Y. Model predictive discrete-time sliding mode control of a nanopositioning piezostage without modeling hysteresis. *IEEE Transactions on Control Systems Technology 20*, 4 (July 2012), 983–994.

[193] XU, W., CAI, C., YIN, M., AND ZOU, Y. Time-varying force tracking in impedance control. *IEEE 51st Annual Conference on Decision and Control (CDC)* (2012), 344–349.

[194] YEOW, T., LAW, K., AND GOLDENBERG, A. Mems optical switches. *IEEE Communications Magazine 39*, 11 (Nov. 2001), 158–163.

[195] YONG, Y., APHALE, S., AND MOHEIMANI, S. Design, identification, and control of a flexure-based xy stage for fast nanoscale positioning. *IEEE Transactions on Nanotechnology 8*, 1 (Jan. 2009), 46–54.

[196] ZANDI, K., WONG, B., ZOU, J., KRUZELECKYK, R., JAMROZ, W., AND PETER, Y.-A. In-plane silicon-on-insulator optical mems accelerometer using waveguide fabry-perot microcavity with silicon/air bragg mirrors. *IEEE 23rd International Conference on Micro Electro Mechanical Systems (MEMS)* (24-28 Jan. 2010), 839–842.

[197] ZHANG, R., CHU, J., GUAN, L., LI, S., AND MIN, J. Microgripping force measuring device based on su-8 microcantilever sensor. *Journal of Micro/Nanolithography, MEMS and MOEMS 13*, 1 (Feb. 2014), 013007–013007.

[198] ZHAO, G., TEO, C.-L., HUTMACHER, D.-W., AND BURDET, E. Force-controlled automatic microassembly of tissue engineering scaffolds. *Journal of Micromechanics and Microengineering 20*, 3 (March 2010), 035001.

[199] ZHAO, Y., AND JAYASURIYA, S. Feedforward controllers and tracking accuracy in the presence of plant uncertainties. *ASME Journal of Dynamic Systems, Measurement, and Control 117*, 4 (Dec. 1995), 490495.

[200] ZHEN, R., AND GOLDENBERG, A. Robust position and force control of robots using sliding mode. *IEEE International Conference on Robotics and Automation 1* (May. 1994), 623–628.

[201] ZHOU, Q., AND GAUTHIER, M. Fusion of robotic microassembly and self-assembly for microsystem integration and thin-chip micro-assembly for 3d integration. *IEEE International Conference on Robotics and Automation* (Karlsruhe, Germany 2013).

[202] ZHU, R., CAI, S., DING, H., YANG, Y. J., AND SU, Y. A micromachined gas inertial sensor based on thermal expansion. *Sensors and Actuators A: Physical 212*, 1 (June 2014), 173–180.

[203] ZHU, Y., BAZAEI, A., MOHEIMANI, S., AND YUCE, M. Design, modeling, and control of a micromachined nanopositioner with integrated electrothermal actuation and sensing. *Journal of Microelectromechanical Systems 20*, 3 (June 2011), 711,719.

[204] ZHU, Y., LIU, W., JIA, K., LIAO, W., AND XIE, H. A piezoelectric unimorph actuator based tip-tilt-piston micromirror with high fill factor and small tilt and lateral shift. *Sensors and Actuators A: Physical 167*, 2 (June 2011), 495–501.

[205] ZOU, J., CHEN, J., LIU, C., AND SCHUTT-AINE, J. Plastic deformation magnetic assembly (pdma) of out-of-plane microstructures: Technology and application. *Journal of Microelectromechanical Systems 10*, 2 (June 2001), 302–309.

Appendix **A**

Appendix - Transfer Functions for the Model defined in Chapter 3

The model of the TSFM has been developed in Chapter 3. The final model has been written using Equation (3.34) as follows:

$$F_g = \begin{cases} 0 & \text{if} \quad y_C < y_e \\ H_u(s)\left[d_p U - H_s(U)\right] - H_e(s) Y_e & \text{if} \quad y_C \geq y_e \end{cases}$$

where $H_u(s)$ and $H_e(s)$ are two 4th order transfer functions combining the dynamics of the actuator, force sensor and flexible environment. The two transfer functions can be written as follows:

$$\begin{cases} H_u(s) = \dfrac{a_0 + a_1 s + a_2 s^2 + a_3 s^3}{b_0 + b_1 s + b_2 s^2 + b_3 s^3 + b_4 s^4} \\ H_e(s) = \dfrac{m_0 + m_1 s + m_2 s^2 + m_3 s^3 + m_4 s^4}{b_0 + b_1 s + b_2 s^2 + b_3 s^3 + b_4 s^4} \end{cases} \tag{A.1}$$

The coefficients, a_{ij}, b_{ij} and m_{ij} defined in Equation (A.1) are detailed in the following equation in the next page:

$$
\begin{cases}
a_3 = 2b_s m_e L_a^2 + 4Lb_s m_e L_a \\
a_2 = 2L_a^2 b_e b_s + 2L_a^2 k_s m_e + 4LL_a b_e b_s + 4LL_a k_s m_e \\
a_1 = 2L_a^2 b_e k_s + 2L_a^2 b_s k_e + 4LL_a b_e k_s + 4LL_a b_s k_e \\
a_0 = 2k_e k_s L_a^2 + 4Lk_e k_s L_a \\
b_4 = 2L_a^2 a m_e + 2L_a^2 a m_s \\
b_3 = 2L_a^2 a b_e + 2L_a^2 a b_s + 2L_a^2 b m_e + 2L_a^2 b m_s + 6L^2 b_s m_e s_p + 2L_a^2 b_s m_e s_p + 2L_a^2 b_s m_s s_p + \\
\quad + 6LL_a b_s m_e s_p + 3LL_a b_s m_s s_p \\
b_2 = 2L_a^2 m_e + 2L_a^2 m_s + 2L_a^2 b b_e + 2L_a^2 b b_s + 2L_a^2 a k_e + 2L_a^2 a k_s + 6L^2 b_e b_s s_p + 2L_a^2 b_e b_s s_p + \\
\quad + 8L_a^2 k_s m_e s_p + 2L_a^2 k_s m_s s_p + 6LL_a b_e b_s s_p + 6LL_a k_s m_e s_p + 3LL_a k_s m_s s_p \\
b_1 = 2L_a^2 b_e + 2L_a^2 b_s + 2L_a^2 b k_e + 2L_a^2 b k_s + 6L^2 b_s k_e s_p + 8L_a^2 b_e k_s s_p + 2L_a^2 b_s k_e s_p + \\
\quad + 6LL_a b_e k_s s_p + 6LL_a b_s k_e s_p \\
b_0 = 2L_a^2 k_e + 2L_a^2 k_s + 8L_a^2 k_e k_s s_p + 6LL_a k_e k_s s_p \\
m_4 = 2L_a^2 a k_e m_s \\
m_3 = 2L_a^2 a b_s k_e + 2L_a^2 b k_e m_s + 2L_a^2 b_s k_e m_s s_p + 3LL_a b_s k_e m_s s_p \\
m_2 = 2L_a^2 k_e m_s + 2L_a^2 b b_s k_e + 2L_a^2 a k_e k_s + 2L_a^2 k_e k_s m_s s_p + 3LL_a k_e k_s m_s s_p \\
m_1 = 2L_a^2 b_s k_e + 2L_a^2 b k_e k_s \\
m_0 = 2L_a^2 k_e k_s
\end{cases}
\tag{A.2}
$$

List of Publications

My Ph.D. works have raised several publications. The publications appear in the following way:
- Chapter **2** has been presented in **[2]**,
- Chapter **3** has been presented in **[4] and [8]**,
- Chapter **4** has been presented in **[5], [6] and [9]**,
- Chapter **5** has been presented in **[3], [7] and [9]**.

Journal Papers *(1 collaboration paper)*

[1] - A. Espinosa, X. Zhang, K. Rabenorosoa, C. Clévy, S. R. Samuelson, **B. Komati**, H. Xie, and P. Lutz, “ Piston Motion Performance Analysis of a 3DOF Electrothermal MEMS Scanner for Medical Applications ”, *International Journal of Optomechatronics*, Vol. 8, No. 3, pp. 179-194, June 2014.
[2] - **B. Komati**, J. Agnus, C. Clévy, and P. Lutz, “ Prototyping of a Highly Performant and Integrated Piezoresistive Force Sensor for Microscale Applications ”, *Journal of Micromechanics and Microengineering*, Vol. 24, No. 3, pp. 035018, March 2014.
[3] - **B. Komati**, K. Rabenorosa, C. Clévy, and P. Lutz, “ Automated Guiding Task of a Flexible Micropart Using a Two-Sensing-Fingers Microgripper ”, IEEE Transactions on Automation, Science and Engineering, Vol. 10, No. 3, pp. 515-524, July 2013.

Conference Papers *(2 collaboration papers)*

[4] - **B. Komati**, C. Clévy, M. Rakotondrabe, and P. Lutz, “ Dynamic Force/Position Modeling of a one-DOF Smart Piezoelectric Micro-Finger with Sensorized End-Effector ”, *IEEE/ASME AIM International Conference on Advanced Intelligent Mechatronics (AIM’14)*, Besançon, France, July 2014.
[5] - **B. Komati**, C. Clévy, and P. Lutz, “ Force Tracking Impedance Control with Unknown Environment at the Microscale ”, *IEEE International Conference on Robotics and Automation (ICRA’14)*, Hong Kong, China, June 2014.
[6] - A. Espinosa, X. Zhang, K. Rabenorosoa, C. Clévy, S. R. Samuelson, **B. Komati**, H. Xie, and P. Lutz, “Piston Motion Performance Analysis of a 3DOF Electrothermal MEMS Scanner for Medical Applications ”, *International Symposium on Optomechatronic Technologies (ISOT’13)*, Jeju Island, Korea, October 2013.
[7] - **B. Komati**, M.R. Pac, I. Ranatunga, C. Clévy, D. Popa, and P. Lutz, “ Explicit Force Control v.s. Impedance Control for Micromanipulation ”, *ASME-IDETC International Design Engineering Technical Conferences & Computers and Information in Engineering Conference*, Portland, USA, August 2013.

Journal Papers in progress

[8] - **B. Komati**, C. Clévy, and P. Lutz, " A Piezoelectric Microgripper with Integrated Force Sensors and Position Detection Algorithm for the Grasp of Multistiffness Microcomponents ".
[9] - **B. Komati**, C. Clévy, and P. Lutz, " A Fully and High Dynamic Automated Microassembly Using an Active Microgripper with Integrated Force Sensors and Hybrid Force/Position Control".

Communication skills and oral presentations

[10] - **B. Komati**, C. Clévy, and P. Lutz, " Towards Fully Automated Microassembly Using an Active Microgripper with Integrated Force Sensors and Hybrid Force/Position Control ", oral presentation, *AS2M Department Scientific Day*, Besançon, France, June, 2014.
[11] - **B. Komati**, C. Clévy, and P. Lutz, " Hybrid Force/Position Control for the Microassembly ", oral presentation, *Young Researchers in Robotics Day (JJCR'13)*, Annecy, France, October, 2013.

Résumé :

La thèse propose l'utilisation d'une pince active instrumentée en force pour automatiser l'assemblage des MOEMS 3D hybrides. Chacun des doigts de la pince instrumentée est composé d'un actionneur piézoélectrique et d'un capteur de force piézorésistif intégré. Le capteur de force intégré présente des performances innovantes par rapport aux capteurs existants dans l'état de l'art. Cette pince offre la possibilité de mesurer les forces de serrage appliquées par la pince pour saisir un microcomposant et d'estimer les forces de contact entre le microcomposant et le substrat de micro-assemblage. Un modèle dynamique et non linéaire est développé pour la pince instrumentée. Une commande hybride force/position est utilisée pour automatiser le micro-assemblage. Dans cette commande, certains axes sont commandés en position et les autres sont commandés en force. Pour les axes commandés en force, une nouvelle commande fondée sur une commande en impédance avec suivi de référence est proposée selon un principe de commande non linéaire par mode glissant avec estimation des paramètres en lignes. En utilisant le schéma de commande hybride force/position proposé, une automatisation de toutes les tâches de micro-assemblage est réalisée avec succès, notamment sur un composant flexible à guider dans un rail.

Mots-clés : Microassemblage, microassemblage automatisé, pince instrumentée en force, commande en force, commande en impédance, commande hybride force/position, commande par mode glissant, guidage automatisé par commande en force, prise automatisée, dépose automatisée, MOEMS hybrides, microbanc optique.

Résumé :

This work proposes the use of an active microgripper with sensorized end-effectors for the automation of the microassembly of 3D hybrid MOEMS. Each of the two fingers of the microgripper is composed of a piezoelectric actuator with an integrated piezoresistive force sensor. The integrated force sensor presents innovative performances compared to the existing force sensors in literature. The force sensors provide the ability to measure the gripping forces applied by the microgripper to grasp a microcomponent and estimated the contact forces between the microcomponent and the substrate of microassembly. A dynamic nonlinear model of the microgripper is developed. A hybrid force/position control is used for the automation of the microassembly. In the hybrid force/position control formulation, some axes are controlled in position and others are controlled in force. For the force controlled axes, a new nonlinear force control scheme based on force tracking sliding mode impedance control is proposed with parameter estimation. Using the proposed hybrid force/position control scheme, full automation of the microassembly is performed, notably for the guiding of a flexible component in a rail.

Keywords: Microassembly, automated microassembly, microgripper with sensorized end-effectors, force control, impedance control, hybrid force/position control, sliding mode control, automated guiding using force control, automated grasp, automated release, hybrid MOEMS, micro-optical bench.

■ École doctorale SPIM 16 route de Gray F - 25030 Besançon cedex

■ tél. +33 (0)3 81 66 66 02 ■ ed-spim@univ-fcomte.fr ■ www.ed-spim.univ-fcomte.fr